Watching the Stars go 'Round and 'Round

A Dissertation Presented

by

Scott Joseph Wolk

to

The Graduate School

in Partial Fulfillment of the Requirements

for the Degree of

Doctor of Philosophy

in

Earth and Space Sciences
(Astronomy)

State University of New York
at
Stony Brook

December 1996

State University of New York
at Stony Brook

The Graduate School

Scott Joseph Wolk

We the dissertation committee for the above candidate for the Doctor of Philosophy degree, hereby recommend acceptance of the dissertation.

Frederick M. Walter, Associate Professor
Astronomy Program, Earth and Space Sciences

Michal Simon, Professor
Astronomy Program, Earth and Space Sciences

Jack J. Lissauer, Adjunct Associate Professor
Astronomy Program, Earth and Space Sciences

William Herbst, Professor
Astronomy Department, Wesleyan University

This dissertation is accepted by the Graduate School.

Graduate School

Abstract of the Dissertation

Watching the Stars go 'Round and 'Round

by

Scott Joseph Wolk

Doctor of Philosophy

in

Earth and Space Sciences
(Astronomy)

State University of New York at Stony Brook

1996

I present results from several seasons of photometric observations of X–ray sources in the Orion OB1a and OB1b star formation regions. The initial goal was to measure the rotational periods of several dozen pre–main sequence (PMS) stars. Since the early 1980s, X–rays have been found to be the premier method of identifying PMS stars, especially in highly confused regions. I first describe previous work in rotational studies, beginning with spectrophotographic observations of $v \sin i$ through the modern use of

charge coupled devices to study the rotational modulation of spotted stars. The optical properties of 105 X–ray sources observed as part of my thesis research are discussed in detail next. Based on optical colors, I find that the X–ray sources in both regions lie along a well defined locus above the main sequence. Infrared and optical data confirm that 90% of the X–ray sources are PMS and about 10% of the PMS stars may have disks. Between V magnitudes 12 and 16, I find that the X–ray sources account for 80% of the pre–main sequence population, as determined by location in the H–R diagram. This photometric study also reveals a population of PMS stars to which the X–ray surveys were insensitive. These PMS stars range in mass from Solar mass objects, down to very close to the brown dwarf limit. This photometric method, augmented by spectra, may supplant X–rays as the premier method for identification of PMS sources in regions of star formation. It may also provide a method for observing stars at the low mass end of the initial mass function.

With the PMS nature of these X–ray sources well characterized, I examine the periodic nature of only the stars which were associated with X–ray sources. I use simulated data to demonstrate that for stars with perfectly sinusoidal behavior, accurate periods can be found in a cases of signal to noise greater than 2. that the For more realistic stars, which do not vary in brightness (along our line–of–sight) exactly as a sine wave, the signal to noise must

be higher by a factor of two or more. I also discuss the expected color changes due to spot modulation and find that the allowed variations cover a very limited range in phase space. I find rotation periods for five stars at confidence of greater than 99.9/greater than 99/at much lower confidence.

Finally, the relation between the data presented here and other data is discussed. The sampling rate of the data presented here allows for detection of shorter periods than previously reported for T Tauri stars. I note the bimodal distribution of rotation periods which other authors have reported. I further note that the ratio of slow rotators to fast rotators seems to change as a function of the age of the star forming region. Rotation period and various observables are compared. I find weak correlations between slow rotation and high variability and between slow rotation and IR color excess. Both these correlations support the hypothesis that stars with disks are slow rotators. However, there is also a large fraction of slow rotators which do not show evidence for disks.

For Lillian, Mom, Dad and Joshua

Contents

List of Figures . . . . . **xvi**

List of Tables . . . . . **xviii**

Preface . . . . . **xix**

Acknowledgements . . . . . **xxi**

1 Introduction **1**

1.1 X–ray Activity and PMS Stars. 4

1.2 T Tauri Stars, Naked and Otherwise 4

1.3 Direct Monitoring of Rotational Modulation 6

1.4 Rotation Periods of ZAMS Stars 8

1.5 Rotation Periods of PMS Stars 10

1.6 This Work 12

2 Observational Data **17**

2.1 The Orion OB1 Association 18

2.2 Source Selection 19
2.3 Optical Photometry 24
2.4 Calculation of Extinction from Optical Colors 33
2.4.1 Infrared Data 35
2.4.2 Spectroscopic Data 39
2.5 Fits to Evolutionary Models 44
2.6 Completeness 49
2.6.1 X–ray Quiet PMS Candidates 58
2.6.2 Very Low Mass PMS Objects 61

3 Period Analysis 67
3.1 Period Determination 67
3.1.1 Phase Dispersion Minimization 69
3.1.2 Periodogram 70
3.1.3 False Alarms and Aliasing 71
3.1.4 Windowing 72
3.2 Simulations 76
3.2.1 Synthetic Modulation 76
3.2.2 Starspots 84
3.3 Period Criteria 87

4 Results 90
4.1 Specific Stars 90
4.1.1 TAP 26 91
4.1.2 P1724 93

4.2 Other Stars 94
4.2.1 Stars with Highly Secure Periods 99
4.2.2 Stars with Less Secure Periods 99
4.2.3 Stars without Periods 102

5 Discussion 109
5.1 Biases 109
5.2 Relations 112
5.3 Evolutionary Effects 114
5.4 Rapidly Rotating Stars 117

6 Conclusions 123

A Finding Charts 128

B Lightcurves and Observational Data 154
B.1 Secure Rotation Period Determinations 155
B.2 Period Determinations of Moderate Confidence 159
B.3 Highly Uncertain Period Determinations 172

C The Care and Feeding of the Mount Stony Brook Observatory 186
C.1 Introduction 186
C.2 The Telescope and Dome 187
C.3 The Computer Hardware and Relevant Equipment 188
C.4 CCD Systems and Their Hardware 190

C.4.1 The Lynxx 191
C.4.2 The ST-4 192
C.4.3 The ST-6 194
C.5 Data Acquisition 195
C.5.1 Target Finding 195
C.5.2 Data Acquisition with the Lynxx 196
C.5.3 The ST-4 198
C.5.4 ST-6 Data Collection 200
C.6 Data Storage 202
C.6.1 Data Formats 203
C.6.2 Data Storage Media 205
C.7 Data Processing 206
C.7.1 Quick Look Tools 206
C.7.2 The Lynxx Tools 208
C.7.3 IDL 210
C.7.4 IRAF 214
C.8 A Night At The Telescope 214
C.8.1 The End Of The Night 216
C.9 Training 217
C.9.1 Week 1 217
C.9.2 Week 2 218
C.9.3 Week 3 218
C.9.4 Week 4 218
C.10 Maintenance 219

C.11 Future Improvements 220
C.12 Help Sheets For Operation Of The PC 222
C.12.1 Lynxx Time Sheet 222
C.12.2 PC To VAX FTP Commands 223
C.12.3 14" Telescope Shut Down Check Sheet 225
C.13 IDL Program Help Pages 227

D The Epsilon Auigae Secondary 232
D.1 Introduction 232
D.2 Characteristics of the ϵ Aurigæ System 234
D.3 Vertical Structure of the Secondary: Hydrostatic Model 239
D.4 Eclipse Lightcurves for the Hydrostatic Model 247
D.5 Disk Expansion and Absorption Line Profiles 265
D.6 Summary 270

References 277

List of Figures

1.1 Schematic of period modulation technique 15

1.2 Histogram of all published periods 16

2.1 Color–magnitude diagram for X–ray sources near σ Orionis. . 29

2.2 Color–magnitude diagram for X–ray sources northwest of the belt. 29

2.3 Spectral-type vs. CaI line ratios 41

2.4 Spectral-type vs. FeI line ratios 42

2.5 Luminosity–temperature diagram (reddening corrected) 46

2.6 Color–magnitude diagram for all stars near σ Orionis. 55

2.7 Color–magnitude diagram for all stars NW of the belt 56

2.8 Location of non–X–ray PMS candidates 57

2.9 X–ray count rates near σ Orionis 61

2.10 Luminosity–temperature diagram for all stars near σ Orionis. . 65

2.11 Luminosity–temperature diagram for all stars NW of the belt 66

3.1 Typical window function 74

3.2 The effect of windowing on period analysis 75

3.3 Period analysis on simulated data (simple) 80
3.4 Accuracy of periodogram analysis (simple) 81
3.5 Period analysis on simulated data (complex) 82
3.6 Accuracy of periodogram analysis (complex) 83
3.7 Color change of spot models 86

4.1 TAP 26 as viewed from MTSB 92
4.2 Comparison of different search ranges 95
4.3 Field of P1724 96
4.4 Folded data for P1724 97
4.5 Nightly trend analysis for P1724 98
4.6 Histogram for all periods observed 107
4.7 Evolutionary breakdown of histogram 108

5.1 An example of aliasing 120
5.2 Amplitude modulation vs. rotation period 121
5.3 Spectral type vs. rotation period 121
5.4 Color vs. rotation period 122
5.5 IR–color vs. rotation period 122

A.1 ROSAT sources north of σ Orionis 130
A.2 ROSAT sources south of σ Orionis 131
A.3 ROSAT sources east of σ Orionis 132
A.4 ROSAT sources west of σ Orionis 133
A.5 ROSAT sources northwest of the belt of Orion (region 1) . . . 134

A.6 ROSAT sources northwest of the belt of Orion (region 2) . . . 135
A.7 ROSAT sources northwest of the belt of Orion (region 3) . . . 136
A.8 ROSAT sources northwest of the belt of Orion (region 4) . . . 137
A.9 ROSAT sources northwest of the belt of Orion (region 5) . . . 138
A.10 ROSAT sources northwest of the belt of Orion (region 6) . . . 139
A.11 ROSAT sources northwest of the belt of Orion (region 7) . . . 140
A.12 ROSAT sources northwest of the belt of Orion (region 8) . . . 141
A.13 Other PMS candidates north of σ Orionis 142
A.14 Other PMS candidates south of σ Orionis 143
A.15 Other PMS candidates east of σ Orionis 144
A.16 Other PMS candidates west of σ Orionis 145
A.17 Other PMS candidates northwest of the belt of Orion (region 1) 146
A.18 Other PMS candidates northwest of the belt of Orion (region 2) 147
A.19 Other PMS candidates northwest of the belt of Orion (region 3) 148
A.20 Other PMS candidates northwest of the belt of Orion (region 4) 149
A.21 Other PMS candidates northwest of the belt of Orion (region 5) 150
A.22 Other PMS candidates northwest of the belt of Orion (region 6) 151
A.23 Other PMS candidates northwest of the belt of Orion (region 7) 152
A.24 Other PMS candidates northwest of the belt of Orion (region 8) 153

D.1 Light curve of ϵ Aurigæ, 1982 – 1984 244
D.2 Cartoon of the ϵ Aurigæ system. 245
D.3 Side view of the ϵ Aurigæ system. 246
D.4 Optical depth profile for the disk in the sky plane. 254

D.5 Optical depth profiles (continued). 255
D.6 Synthetic light curves produced by the disk models 256
D.7 Synthetic light curves (continued). 257
D.8 All other light curves. 258
D.9 All other light curves (continued). 259
D.10 All other light curves (continued). 260
D.11 All other light curves (continued). 261
D.12 All other light curves (continued). 262
D.13 All other light curves (continued). 263
D.14 All other light curves (final). 264
D.15 Optical depth profile of the disk in the sky plane 273
D.16 Quasi-hydrodynamic lightcurves 274
D.17 Quasi-hydrodynamic lightcurves (continued) 275
D.18 Quasi-hydrodynamic lightcurves (continued) 276

List of Tables

2.1 X–ray sources near σ Orionis 22

2.2 X–ray sources NW of the belt of Orion 23

2.3 Statistics for observing runs 26

2.4 Colors of X–ray sources near σ Orionis 30

2.5 Colors of X–ray sources near σ Orionis (continued). 31

2.6 Colors of comparison stars. 31

2.7 Colors of X–ray sources NW of the Belt 32

2.8 IR Colors of X–ray near σ Orionis 37

2.9 IR Colors of X–ray near σ Orionis (continued) 38

2.10 Spectroscopic data for standard stars 41

2.11 Spectroscopic data for X–ray sources NW of the Belt of Orion 42

2.12 Spectroscopic data for X–ray sources near σ Orionis 43

2.13 Extinction corrected bolometric magnitudes. 48

2.14 Colors of candidate PMS stars near σ Orionis. 51

2.15 Colors of candidate PMS stars near σ Orionis...cont. 52

2.16 Colors of candidate PMS stars NW of the Belt 53

2.17 Colors of candidate PMS stars NW of the Belt...cont. 54

2.18 Spectroscopic data for candidate PMS stars 59

4.1 Periods measured by this program with high confidence 104

4.2 Periods measured by this program with moderate confidence . 105

4.3 Periods measured by this program with low confidence 106

C.1 Technical Specifications Of The CCD Cameras. 190

C.2 Sample settings for the ST-4 guiding on a 7^{th} magnitude star. 199

C.3 Storage Capacity For Lynxx and ST-6 Images. 205

C.4 Cables fundamental to the operation of Mt. Stony Brook. . . . 220

D.1 Results of disk simulations. 249

D.2 Results of disk simulations (continued). 250

Preface

This dissertation grew up in a hurry. I say that in spite of the fact that it has been five years since its inception. As recently as nine months ago, I thought this work would be like many others, simply the inclusion of all the papers I had previously published on somewhat related topics. There would be some new material too; rotation periods for about a dozen pre–main sequence stars and a guide for using the Mount Stony Brook Observatory. I would use the introduction to justify that, in fact, all the different works were indeed related.

All that began to change last September, when I noticed that the photometric data I had could help to fill in the incompleteness in the x-ray surveys. This focused my attention more clearly on the stars which are discussed here in two ways. First, it motivated me to reduce the rotational data for the bulk of the stars discussed here. Secondly, it caused me to use some of my time during a run at CTIO this winter to experiment with medium deep mapping of regions of star formation. Using this mapping, I looked for non-x-ray emitting pre–main sequence stars. The results given here are very exciting.

In some ways I am sorry I am finishing so soon (which is remarkably

surprising since I have been here long enough to get tenure). What I mean is that it really took me three years to understand what I was doing. I was fortunate that the bulk of my observing during those three years was done either through clouds, rain or snow. Otherwise, I would have been wasting valuable telescope time. But I learned, through the holes in the clouds, the art that went with the science. It has allowed me to produce as much science in the last six months as I did over the previous 5 years.

That is the process which went into the creation of the document you are holding. There are a couple of holdovers from the original plan. These have been placed in the appendix for convenient removal. They are there either to provide a sense of closure (in the case of Mount Stony Brook) or because they were hastily promised in a draft of paper written years ago (ϵ Aurigæ).

–Scott

Stony Brook, May 1996

Acknowledgements

As with any project on this scale, I could not, and did not, do it alone. In fact, I think I employed the help of more people than usual, and it will be impossible for me to name them all here. But I will do my best to cover everyone.

First of all, there are the official acknowledgments. This work was supported in part by the NASA Origins of Solar Systems Program under grant NAGW-3165. The Digitized Sky Survey was produced at the Space Telescope Science Institute under U.S. Government Grant NAGW-2166. I have been a visiting astronomer at the Kitt Peak National Observatory and Cerro Tololo Inter-American Observatory. These are both run by the Association of Universities for Research in Astronomy under contract with the National Science Foundation. I am ever grateful for the help of all the assistants who have helped me over the years, especially Mauricio Navarrete for teaching me IRAF during cloudy nights. I also want to thank Zoran Ninkov for allowing me 10 snowy weeks using the Mees Observatory and Kathy DeGioia-Eastwood for permitting me to use some of her time on the Lowell 31". $\Sigma\Xi$ provided a grant for transportation to the Wise Observatory in Israel where most of the

rotation data were taken. Drora Ianovici helped take data at Wise. I especially want to thank Sara Beck both for offering me the use of this instrument and for her support during my early graduate days.

Closer to home, I would like to thank my advisor Fred Walter for believing in me. He provided me with infinite freedom, a fair amount of resources and taught me to think and operate independently. I may have floundered a bit here and there, but I think the overall quality of my work both in this dissertation and in the future are higher because of it. Deane Peterson and Jim Lattimer have taken (apparently) honest interest in my work and encouraged many of my fruitful intellectual wanderings.

On a personal level, I have had the unwaivering support of my family. I don't think I would have survived a year without the emotional support of my friends here. In the early days, it was Dave, Frank, Don and my lost cat Lynda. More recently Lynn and Lisa have been there to pick me up when my helmet shatters. Saeid helped with his "Illustrator" magic. Tom Mooney provided the thesis TEX template.

Of course, the observers gave me invaluable assistance. They were guinea pigs exposed to freezing cold, faulty equipment and my temper. They deserve more than just simple recognition here and occasional pizza. They include graduate students, undergrads, high school students and amateurs: Nance Adams, Matt Adcock, Hakan Alton, Eric Barnes, Gerbs Bauer, Kevin Brower, Tim Burbage, Tom Clark, Chris Del Russo, Chris Farris, Josh Faber, James Forman, Craig Giles, Bob Gubiak, Salman Hameed, Arthur Hervias, John Janis, George Leussis, Ron Lindenfeld, Mark McHugh, Janette Mallozzi,

Anne-Marie Milner, Mike Mugavero, Dané Orlovic, Dan O'Sullivan, Jim Petreshock, Mike Phillips, Tony Ricci, Scott Schell, Mark Simons, Jon Stalhut, Carlos Tello, Jennifer Thomas, Jo-May Tsang & Sophia Zahariou.

I particularly need to thank Scott Schell, Jim Petreshock, Josh Faber and Dan O'Sullivan with assistance in data reduction. Scott and Jim went above and beyond the call of duty countless times in regard to data reduction, telescope maintenance, proofreading and my sanity. They have taught me as much as I have taught them. I am glad to call them friends.

Finally I want to thank my friend, confidant and partner, Nance. Even though she likes to talk science at inopportune moments, she has kept me on an even keel throughout this long strange trip and has taught me the meaning and the spelling of c-o-m-m-i-t-m-e-n-T.

Chapter 1

Introduction

Since the beginning of the twentieth century, one of the most perplexing problems in our understanding of the development of the Solar System, and stars in general, has been the disposition of angular momentum. It is the only significant observable quantity in the Solar System that the Sun does not dominate. In the early 1970s, it was shown that for stars of mass $M_\star > 1.5$ $M_\odot$, their specific angular momenta fall on the relation $< J/M_\star > \propto M_\star^\alpha$, where $\alpha \sim 2/3$ and J is the specific angular momentum. While the Sun itself and similar low–mass stars fall below this relation by two orders of magnitude, the Solar System as a whole fits this relation (Kraft 1970). This observation was consistent with the independently derived theoretical result that an accretion disk provided a simple mechanism for allowing mass to collect on a central object while controlling the growth of angular momentum (Lynden–Bell and Pringle 1972).

Over the past two decades, the existence of such accretion disks has been clearly demonstrated. As a star forms, not only is its own angular momentum

being determined, but also the angular momentum available for its planetary system. This has made the need to study the evolution of the rotation periods of stars, and hence the angular momentum, very clear. The study of rotation gives us insight into the physical processes inside stars. In the case of low mass pre–main sequence (PMS) stars, we seek to learn whether disks alone determine the angular momentum distribution when stars arrive on the main sequence. It is also likely that the angular momentum loss mechanism varies as the star evolves.

The basics of the evolution of the rotation of a star with fixed angular momentum are fairly straightforward. Assuming that there is no significant loss of angular momentum during a star's evolution following the Hayashi track, spin–up is a result of conservation of angular momentum as the stellar radius decreases. Under these conditions, angular momentum (J) is constant (typically $J \sim 1 \times 10^{50} g\ cm^2\ s^{-1}$; here I am going to be primarily concerned with the magnitude of J and not its vector nature). Since $I\omega \propto J$ and $I = \frac{2}{5}MR^2$ (for the simple case of a uniform density distribution), as R goes down by a factor of 10, ω must go up by a factor of 100. Further, since $R(t) \sim t^{-1/3}$, then $\omega(t) \sim t^{2/3}$.[1] After stars have attained their main–sequence radii, they continue to spin–up as more material settles toward the center of the star. Once stars have achieved their stable main–sequence configurations, they will

[1] $R(t) \sim t^{-1/3}$ can be derived from simple arguments about stars on the Hayashi track. The potential energy given off by stars on this track is GM^2/R, while the stellar luminosity $\propto R^2T^4$. Since the stellar luminosity is the change in energy per unit time, $\frac{-GM^2}{R^2}\frac{dR}{dt} \propto R^2T^4$. Along the convective tracks, temperature is approximately constant. Removing all the constants one gets $\frac{-dR}{dt} \propto R^4$. Integrating leads to $R(t) \propto t^{-1/3}$.

spin–down appreciably during the main sequence lifetime (Skumanich 1972). This is because they will continually lose angular momenta to the stellar wind as shown by Endal & Sofia (1981).

If one assumes that angular momentum is conserved from the natal cloud, then rotation periods exceeding breakup velocity are implied for PMS stars. This conclusion was supported by the earliest measurements of $v \sin i$ for PMS stars (Herbig 1957). However this work was on atypical stars including SU Aurigæ. The first systematic study of the rotational periods of PMS stars was undertaken by Vogel & Kuhi (1981). They studied the rotational velocities of a large sample of stars in the Taurus–Auriga star forming region. They found, for the most part, that there were no rapid rotators among (classical) T Tauri stars. Hartmann et al. (1986) and Bouvier et al. (1986) reached similar results, finding the mean rotational velocity for T Tauri stars (TTs) was about 15 km/s or about 10% of the breakup velocity. These results were surprising, not only for the theoretical reasons just described, but also because main sequence stars show a correlation between activity and rotation period (Noyes et al. 1984). PMS stars are highly active, yet the rotation velocities do not seem well correlated. Evidently, while rotation and activity are linked in main sequence stars, PMS stars either have a non–dynamo activity source, or other mitigating factors, which disconnect the observed activity from the rotational velocity.

1.1 X–ray Activity and PMS Stars.

The advent of X–ray astronomy greatly expanded the number of known PMS stars. The earliest X–ray observations were carried out in the mid–1970s. X–ray luminosities of order $L_x \sim 10^{33}$ erg/sec were detected in the 2-11 keV range in the direction of the Orion star forming region. Imaging observations were later made by the EINSTEIN X–Ray observatory (Ku & Chanan 1979). These observations showed that the O and B stars were the brightest X–ray sources, and that TTs were also associated with emission. Feigleson and Kriss (1981) showed that some of the X–ray sources were associated with PMS stars which had not been previously detected which Hα surveys. Gahm (1980) suggested that the X–ray emission originated in flare-like events. Walter & Kuhi (1981, 1984) showed that about 1/3 of TTs were detected by EINSTEIN and contended that since the derived temperatures of these stars were similar to those of RS CVn type systems, the source of the emission was probably coronal. They argued that the reason only the T Tauri stars with the least veiling were observed was further evidence that the X–rays must come from close to the stellar surface.

1.2 T Tauri Stars, Naked and Otherwise

Pointed EINSTEIN observations of TTs in the Taurus–Auriga star forming region (SFR) detected five serendipitous sources in the field (Feigelson & Kriss 1981 and Walter & Kuhi 1981). Follow–up ground based observations showed

these to be K stars with weak Hα lines and strong Li I 6707Å absorption lines. Lithium absorption lines are indicators of youth because Li is a fairly fragile element and is destroyed at the temperatures experienced at the base of the convection zone. Lithium is depleted in stars as they age (Duncan 1981). Mundt et al. (1983) showed that these serendipitous sources were radial velocity members of the Taurus–Auriga SFR, but did not exhibit the IR excesses previously associated with TTs.

Further observations in Taurus, Ophiuchus, and Corona Australis showed that these five serendipitous sources were not unique. There exists a class of PMS stars, located in SFRs, which have similar space motions, masses and ages to those of TTs. They lack the strong line emission and infrared excesses which made such objects easy to distinguish observationally. Walter (1986) called these objects naked T Tauri stars (nTTs; Walter 1986, Walter et al. 1987). The nTTs are still on their convective tracks and thought to be more evolved than (although coeval with) the other TTs, which are now referred to as classical T Tauri stars (cTTs). Classical T Tauri stars are viewed as composite systems of a stellar photosphere, an accretion zone and a circumstellar disk of cool material (Bertout et al. 1989).

The catalog of Herbig & Bell (1988) distinguished between cTTs and weak–lined T Tauri stars (wTTs) instead of nTTs. Whereas Walter (1986) defined nTTs on a multi-wavelength basis (lack of accretion and disk signatures in the optical and IR), Herbig & Bell defined wTTs as PMS stars with Hα equivalent widths of < 10 Å. While all nTTs are wTTs, the converse is not true. There are two type of wTTs which are not nTTs. Higher mass G stars

have high continuum fluxes which can hide the emission from the Hα line. Also, stars with optically thick passive disks do not necessarily show strong Hα emission, but are not considered nTTs.

1.3 Direct Monitoring of Rotational Modulation

Walter et al. (1988) suggested that $v \sin i$ was higher for nTTs than for cTTs. The measurement of $v \sin i$ is a spectroscopic observation of the Doppler broadening of the stellar spectral lines by the projected rotational velocity. It is fairly straightforward to measure, given sufficient resolution and signal to noise. Since only a single observation of a star is required to measure $v \sin i$, the quantity is known for many stars. However, since only the projected velocities are measured, random projection effects can skew the results of any given star. Young stars may not have randomly distributed rotational axes. Heyer et al. (1987) found that the rotational axes of dark clouds are aligned with the local magnetic field. If this alignment continues down to the stellar level, the $\sin i$ term introduces a systematic bias. However, this finding is not supported by the recent work of Goodman et al. (1992, 1995)

The first attempts to directly measure periodic modulation of T Tauri stars occurred in the early 1980s. Rydgren & Vrba (1983) observed four PMS stars using photoelectric photometry over a period of seven consecutive photometric nights. They found rotation periods ranging from 1.9 to 4.1 days and

amplitudes of about 0.1 magnitudes at V. This confirmed the results of the spectrophotometric study; The TTs are relatively fast rotators, but are not close to their breakup velocities. They further concluded that there was no correlation between rotation period and line emission. Over the next 6 years, rotation periods were measured for about 20 TTs. In general, periods of between one and ten days were found. The slow rate of progress was essentially due to the inherently strict requirements of observing rotation periods which demand runs of at least 10 nights with photometric conditions on most of those nights. Further, even when working in a cluster, the efficiency of photoelectric photometry is limited by the single element nature of the detector.

The development of inexpensive, highly linear, large format charge–coupled devices (CCDs) has made it possible to directly measure the rotation periods of a much larger number of stars, at a much wider expanse of ages, than earlier spectrophotographic or photoelectric techniques. Using wide field CCDs, many nTTs can be observed at a single time and field stars can be used as comparison objects. The multiplexing nature of the CCD is most efficient when used in regions where there are many target stars, along with many possible comparison objects. This allows differential measurements to be made among the target and several comparisons objects, all observed through the same atmospheric conditions.

Detailed models by Bouvier and Bertout (1989) show that large fractions ($> 10\%$) of the photospheres of nTTs are covered with cool starspots. The observational work by Wolk and Walter (1996) verifies these predictions. The work of Vrba et al. (1988) indicates that on active stars, spot lifetimes may

exceed several years. The large covering factor means that the spots can have a noticeable effect on the star's magnitude. Because the spot lifetime is much longer than the rotational period, the observed effect will be a modulation of the light from the star synchronously with the rotation period. Thus, the rotation period can be measured photometrically. Figure 1.1 demonstrates this technique.

1.4 Rotation Periods of ZAMS Stars

Studies using direct detection of periods via rotational modulation have been carried out on stars in several young clusters which are near the zero–age main sequence (ZAMS), including the Hyades, the Pleiades and α Persei (see Radick 1988, Schaller et al. 1992 and Prosser 1992 respectively). The ages of these clusters are about 700, 70 and 50Myr respectively. Comparison of these data leads to the following conclusions (Soderblom 1996):

1. Rotation in ZAMS clusters has a strong mass dependence. High–mass stars tend to rotate much more quickly than the low–mass stars.

2. The two younger clusters, α Persei and the Pleiades, contain ultra–fast rotators (UFRs) with $v \sin\ i > 30$ km/s at all masses.

3. The maximum rotation rate is highest in the youngest cluster, and the fraction of UFRs is also highest in this cluster.

When combining these results with those on TTs, problems develop. If one sets the initial rotation periods, masses and radii observed for TTs and then allows them to evolve forward, the resulting distribution of rotation periods doesn't resemble the distribution of rotation periods observed in young clusters. Barnes and Sofia (1996) argue the UFRs cannot be produced if Skumanich–like spin down occurs on the pre–main sequence. They argue that the magnetic field saturates beyond a threshold rotational velocity and has a very strong dipole. This limits the rate at which angular momentum transfer occurs through the magnetic field and causes UFRs to exist in cases of relatively short disk survival. Once stars reach the main sequence, all stars experience a Skumanich–like slowdown due to angular momentum loss via their winds (Endal & Sofia 1981). Recent work (cf. Barry 1988, Walter & Barry 1991) indicate that the spin–down rate is a function of the mass and is proportional to $e^{At^{0.5}}$ (where A is a constant). The result is that younger stars are expected to spin down more quickly and older stars spin down more slowly than expected with the Skumanich law.

In order to explain the slow down of the UFRs to the rate of the other slower rotators, core–envelope decoupling has been suggested (cf. Li & Collier–Cameron 1993, Strom 1994). In the models, the core decouples from the envelope of a young star. The core is free to spin–up in accordance with $\omega \propto t^{-2/3}$, without a noticeable change to the stellar surface rotation. According to such models, in time, angular momentum in transferred out to the envelope. Meanwhile, all stars slow down due to wind losses. This model is tunable, depending on the coupling between the core and the envelope. Stars on their

radiative tracks can either speed up or slow down their observed rotational velocities. By moving the decoupling radius for stars of various ages and various masses, the observed distributions can be reproduced. This seems to be a case of too many free parameters, and not enough data. The models can be constrained somewhat by including younger stars into the database. These stars will provide fiducial positions for rotation period as a function of age. The data on the young stars will teach us exactly what the usual rotation rate is as a function of mass and age.

1.5 Rotation Periods of PMS Stars

The core–envelope decoupling model was developed out of a desire to reproduce the observed period distribution at 50-500 Myrs of age. Another way to approach this problem is to observe the youngest stars, from < 1 to about 10 Myrs, and try to see how the UFRs are formed. There are currently several groups involved in the studies of the rotation periods of PMS stars. The Van Vleck Observatory (cf. Attridge and Herbst 1992) has concentrated on single band photometry of the Orion Nebula Cluster (ONC) where the stars are expected to be less than a million years old (Brown 1996). Prosser et al. (1993a, 1993b, 1995) have concentrated their work on the somewhat older α Persei and Pleiades clusters, but have monitored a few TTs. Grankin (1993, 1994) and the COYOTES group (Bouvier et al. 1993, 1995) have been primarily concerned with rotation periods of classical T Tauri stars (cTTs), (and to a lesser extent nTTs) in the Taurus–Auriga association.

These works individually focus on specific clusters at specific stages in formation, but taken as a whole they have begun to clarify the evolution of angular momentum in young stars. Overall, there are about 100 rotation periods known for PMS stars. Figure 1.2 shows a summary of the bulk of the published results. The main feature of the figure is the bimodal distribution of the periods. Peaks in the distribution occur near 8 days and 3 days. Furthermore, the stars with periods near 8 days also tend to have infrared excesses which can be interpreted as arising from disks. The distribution is clearly bimodal; there are 20 stars in the "gap" from 4 to 6 days which is about half the number expected for a smooth distribution.

This bimodal distribution can be thought of in two physically distinct ways. The gap may arise either because the distribution has a hole, or because it is made up of two distinct distributions. In the first interpretation, the gap occurs because locking mechanism holds stars at a $\sim$ eight day rotation period. Once the lock is broken, the star is free to spin–up. The stars quickly increase their rotational period. The pile–up observed in the faster peak is the result of probable internal breaking and binning effects. If this is the case, the depth and width of the gap is a function of how fast stars spin up after they lose their disk and how quickly such spin up is halted. The latter interpretation assumes that PMS stars naturally bifurcate into two types, fast rotators and slow rotators. In this case, the dearth of stars from four to six days is a manifestation of the lack of strength in the wings of the two distribution. There are no no evolutionary parameters which can be derived from the depth of the gap.

Edwards et al. (1993) were the first to suggest that the peak in the distribution near eight days is evidence for disk locking. In a cTTs system with an optically thick disk, the star may be magnetically coupled to the disk. Any tendency of the star's rotation period to decrease as the star contracts is mitigated by drag on the stellar magnetic field by the disk. This holds rotation periods at about eight days. Once the disk has dissipated, the star is free to spin–up. At this point the rotation rate of the star quickly increases until its peak rotation rate is reached. This appears to be less than three days for many stars. Königl (1991) showed that if the magnetic field truncated at the inner edge of the accretion disk, the drag of charged particles in the disk on the stellar magnetic field could slow the rotation of the star. Cameron et al. (1994) modeled one such mechanism and found that for a cTTs with a magnetic field strength of a few hundred gauss, the torque of the disk on the star could slow the star's rotation into a quasi–static equilibrium. Further, they found that that the effect is nearly independent of stellar mass and also independent of disk mass above a critical value. Shu et al. (1994) included a similar mechanism into their magnetocentrifugally driven "X–celerator wind" model. They show that a long (eight day) rotation period is a natural consequence of accretion through a magnetically truncated disk using their X-celerator wind.

1.6 This Work

Previous studies of the angular momentum of young stars (Attridge & Herbst 1992; Bouvier et al. 1993,1995; Grankin 1993, 1994; Prosser 1993,

1994, 1995; Adams 1995; Choi & Herbst 1996) cover a wide range of stellar ages, but with exception of the ONC, the nTTs have been underrepresented. The nTTs are of particular interest since they are the youngest stars which are not members of composite systems. In a cTTs, there are three major flux contributors: the star, the disk and the boundary layer between them. Variability in any of these three components can cause a variability in the optical signal. The nTTs have only one primary contributor to the optical signal, the photosphere. This makes causes of variability easier to interpret and lowers the number of sources of possibly conflicting signals. This makes period detection easier, especially under non–ideal conditions. Because some nTTs may have very recently lost their disks, they could be stars undergoing rapid change in their rotational properties. This would make them the most likely stars to occupy the 4 to 6 day gap (see Adams et al. 1996).

In this dissertation, I will discuss the results of observations of nTTs in Orion. Observations were made using both the local facility known as "Mount Stony Brook", and limited time allotments at large observatories. The target stars are primarily in the Orion OB1a and OB1b sub–associations. Estimates of the ages of these subgroups vary, but they are generally thought to be less than 12 Myrs old (Brown 1996). In Orion OB1b, I will concentrate specifically on stars within 11 arc minutes of σ Orionis. This region was chosen for its compactness, which allowed many targets to be observed in a single field. Other nTTs in the Orion OB1a association provide a larger cross–section of the stellar populations between 1 and 10 million years old.

The goal of this thesis is to study the rotational modulations of about 100

X–ray sources and to attempt to understand the effect of rotation on other observable phenomena. Before focusing my efforts on the rotational modulation, I first examine the general optical properties of the X–ray selected sample and introduce 150 new PMS (primarily nTT) stars. About 50 of these 150 stars were not identified as pre–main sequence by their X–ray properties, but instead by their spectra and optical photometry. The rotational data improve our understanding of the evolution of angular momentum among young stars by greatly improving the statistical data base of the youngest stars with unobscured photospheres. In the next section I show that the stars near σ Orionis are truly coeval and the stars in Orion OB1a create a second coeval set. Because of this, interpretive problems introduced by age uncertainties can be minimized. In Chapter 3, I discuss the difficulties inherent in measuring the correct rotational periods of the candidate stars. In Chapter 4, the period distributions and the false alarms in the individual findings are discussed. There are several observables on which angular momentum may be dependent including mass, age and IR–excess. I discuss these, as well as the biases in the data set, in Chapter 5.

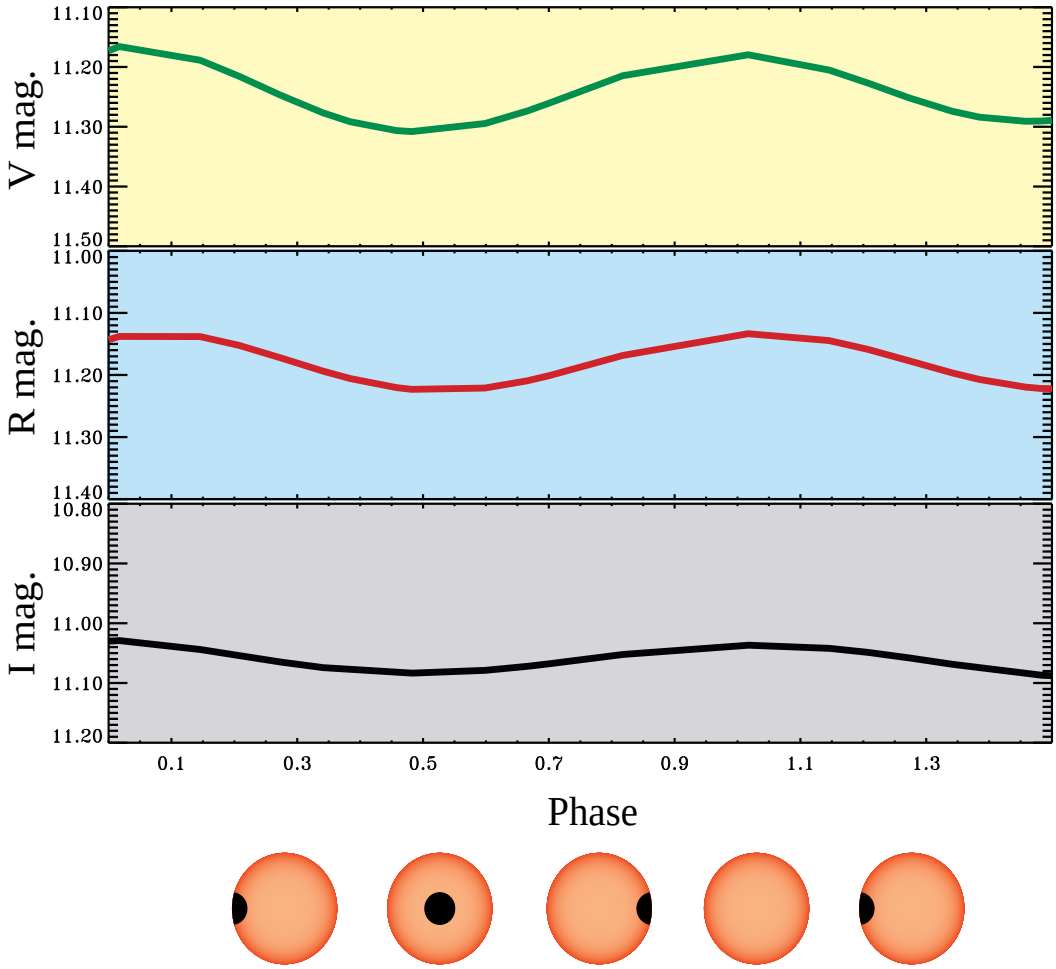

Figure 1.1: Cartoon demonstration of how to measure rotation periods using spot modulation. As the spotted hemisphere of the star comes into view, the flux drops in all bands, but preferentially in the V–band. As the spotted hemisphere moves out of view, the flux increases.

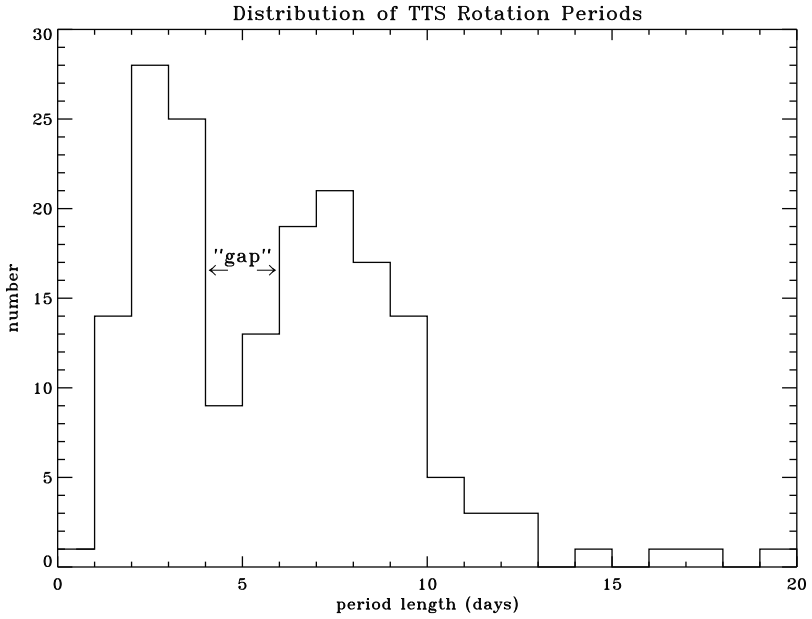

Figure 1.2: Histogram of all published periods for T Tauri stars. Data in this figure is taken from Attridge and Herbst (1992), Bouvier et al. (1993,1995), Grankin (1993, 1994), Adams (1995), Eaton et al. (1995) and Choi and Herbst (1996). The 4 – 6 day "gap" (Attridge and Herbst 1992) is indicated.

Chapter 2

Observational Data

In this chapter, I will define the sample of stars which will be discussed throughout the remainder of the dissertation. I define two coeval sets of PMS stars located in the Orion OB1 association. Once chosen, these stars can be monitored, and their rotational periods can be measured. I start with a brief description of the Orion OB1 association. I then describe the X–ray observations which were used to find the PMS stars in this association. After this, I spend several sections detailing the photometric observations and difficulties in placing objects on the H–R diagram. Once placed on the H–R diagram, the PMS objects are clear. A completeness study, however, shows that the X–ray observations do not detect all the PMS stars in the observed regions. In fact, there are a great number of very low mass objects which are detected photometricly. Some of these may have sub–stellar masses.

2.1 The Orion OB1 Association

Early studies of PMS stars focused on T associations, especially Taurus-Auriga. However, one might expect low mass star formation to be different in OB associations. It is possible for O stars winds to effect the environs. Further, the initial mass functions have been reported to be different in OB association when compared with regions which only form low mass stars (Miller & Scalo 1979). The Orion OB association is among the most interesting of these, owing to its relative closeness and complexity. It contains a large molecular cloud and four sub-complexes of OB stars with different ages, starting with the very youngest of stars and extending beyond 10 million years.

Blaauw (1964) found that OB associations often break down into sub-structures of different ages. He identified Orion OB1a as the stars northwest of the belt. Orion OB1b is composed of the stars near the belt, including the belt stars and σ Orionis. Stars south of the belt are in Orion OB1c and the stars in the immediate vicinity of M42 are in Orion OB1d. Warren & Hesser (1977, 1978) carried out one of the largest surveys of the whole association using $ubvy\beta$ photometry. They divided the Orion OB1b into 3 sub–subgroups arguing that distance increases from west to east.

Ages for the stars in this association have generally been determined by fitting the main sequence turn–off of the O and B stars. One of the most recent studies of this region was performed by Brown (1996). He finds no perceptible distance change within the Orion OB1b association and finds the distance modulus to be 7.8 and 7.9 for Orion OB1a and OB1b respectively.

These distances are about 5% closer than the distances found by Warren & Hesser (1977, 1978). The ages derived for the different sub-associations vary. Brown publishes ages of 11.4, 1.7, 4.6 and <1 Myr for OB1a through OB1d respectively. Warren & Hesser found ages of 7.9, 5.1 3.7 and < 1 Myr, which is somewhat discrepant with Brown in terms of relative ages. Blaauw (1991) revisited these sub–associations and found 12 and 7 Myr for Orion OB1a and OB1b respectively. For the remainder of the dissertation, I will use the most recent values (Brown 1996) when referring to the various sub-associations with the caveat that the correct values are not obvious. The observations which I present will concentrate on Orion OB1a and OB1b.

2.2 Source Selection

The stars examined here were primarily culled from two lists of X–ray sources in Orion. The objects in the lists were detected by pointed observations using the ROSAT X–ray satellite. The observations, made by Walter (1993, 1994, 1995), cover two regions in Orion. One region is six degrees in north–south aspect and ten degrees east–west, centered on the belt of Orion. The second region is two degrees in extent east–west and ten degrees north–south with λ Orionis being near the northern edge. X–ray satellites have been proven to be extremely efficient in finding PMS stars which would have gone unnoticed by other search techniques such as objective prism imaging (Walter 1986). Near the dark clouds of the Taurus–Auriga star forming region, it has been estimated that the nTTs (detected primarily via their X–ray flux) outnumber

cTTs by a ratio of nearly 10 to 1 (Walter et al. 1988). More recent work in Taurus-Auriga gives similar (a ratio of 9:1) results and suggests an age dependence of the ratio (Neuhäuser et al. 1995).

The ROSAT point source lists provided over 800 X–ray sources with fluxes at least three σ above the background located in Orion north of M42. To limit this to a more tractable number, I chose to concentrate on the regions densest in X–ray sources. In this way, the observing program could be very efficient by observing many X–ray sources in every exposure. By selecting the best regions to monitor, I could measure rotational periods for the highest possible number of PMS stars. In the end, two main regions were chosen for monitoring: stars near σ Orionis and stars northwest of the belt of Orion. The group of sources associated with σ Orionis are within the OB1b association. It was chosen since it represented an extreme of compactness with over 50 sources in the central 25 arcminutes. The total area of this region is about 900 minutes of arc. This region was observed by ROSAT during 2 pointed observations. The first of these was 25 Kseconds of exposure time using the Position Sensitive Proportional Counter (PSPC). Supporting ribs obscure part of the PSPC's nominal 1° radius field of view. Problems caused by the obstruction are small, since the central field of view is clear and the ribs move relative to the sky due to spacecraft wobble. A larger problem with the PSPC is scattered light from the bright central X–ray source (σ Orionis), which raises the local background and makes detection of faint sources difficult. A followup 15 Ksecond exposure was obtained by M. Freyberg (1994) using the High Resolution Imager (HRI), which had an unobstructed view of 25 arcminutes centered on σ Orionis

and higher resolution. These data were processed using SASS processing and analyzed using IDL/RX software (Walter 1993). Source extractions were performed using the SEX procedure. Sixty–three sources were identified within $25'$ of σ Orionis.

While both PSPC and HRI data were available, the HRI was the primary source of targets, because it was much more complete near σ Orionis. The HRI detected 18 sources that PSPC missed. Sixteen of these sources are within $6'30''$ of σ Orionis, so they were probably missed due to scattered light. The PSPC identified 22 sources within $15'$ of σ Orionis in addition to the sources listed in Table 2.1, giving a total of 85 X–ray sources in the σ Orionis region. It is not surprising that the PSPC would detect additional sources since it is about 5 times more sensitive than the HRI. Of the 22 sources, 8 had no obvious optical counterpart and one was the bright star SAO 132412. This left 13 sources additional sources to be monitored. All the X–ray sources near σ Orionis with optical counterparts are listed in Table 2.1.

A second region to the northwest of the belt in the OB1a was also chosen because it was expected that this group would represent somewhat more evolved stars. This area was initially observed by the PSPC using a 7 Ksecond exposure. The data were analyzed in a similar manner to those near σ Orionis. One PSPC field covers over 3000 arcminutes of field. This is too much to monitor with the same time resolution as the σ Orionis field. The area of analysis was limited to the 1350 arcminutes which was densest in X–ray sources. These sources are listed in Table 2.2

X-ray Sources Near σ Orionis

Source ID	RA (J2000.)	Dec (J2000.)	Count Rate
R053751-0235	5 37 51.5	-2 35 25	1.49e-03± 6.60e-04
R053752-0240	5 37 52.1	-2 40 40	1.20e-03± 5.86e-04
R053752-0233	5 37 52.7	-2 33 33	1.34e-02± 1.13e-03
R053754-0239	5 37 53.9	-2 39 27	1.82e-02± 1.57e-03
R053755-0245	5 37 55.4	-2 45 07	2.24e-02± 1.67e-03
R053755-0245	5 37 55.7	-2 45 16	2.24e-02± 1.56e-03
R053756-0245	5 37 56.0	-2 45 12	2.35e-02± 1.67e-03
R053807-0231	5 38 07.5	-2 31 27	6.31e-03± 8.48e-04
R053808-0235	5 38 08.0	-2 35 50	1.14e-03± 6.28e-04
R053827-0242	5 38 27.7	-2 42 58	2.25e-03± 6.42e-04
R053828-0236	5 38 28.8	-2 36 00	9.50e-04± 6.09e-04
R053831-0235	5 38 31.4	-2 35 04	8.49e-04± 4.21e-04
R053832-0235	5 38 32.7	-2 35 35	3.20e-03± 7.85e-04
R053833-0236	5 38 33.7	-2 36 25	3.57e-04± 6.90e-04
R053834-0234	5 38 34.2	-2 34 16	1.60e-03± 7.29e-04
R053834-0234	5 38 34.1	-2 34 18	9.23e-04± 6.40e-04
R053835-0231	5 38 35.2	-2 31 48	8.23e-03± 9.51e-04
R053835-0230	5 38 35.7	-2 30 39	3.52e-03± 7.65e-04
R053838-0236	5 38 38.1	-2 36 38	3.44e-03± 7.62e-04
R053838-0234	5 38 38.3	-2 34 51	1.21e-02± 1.07e-03
R053839-0230	5 38 39.8	-2 30 17	2.51e-03± 7.49e-04
R053841-0237	5 38 41.2	-2 37 20	3.03e-03± 7.25e-04
R053843-0233	5 38 43.3	-2 33 20	1.23e-03± 7.26e-04
R053844-0240	5 38 44.0	-2 40 18	6.10e-03± 8.40e-04
R053844-0232	5 38 44.1	-2 32 30	7.49e-03± 9.18e-04
R053844-0235	5 38 44.6	-2 35 58	1.20e-01± 2.99e-03
R053845-0241	5 38 45.3	-2 41 58	1.59e-03± 6.34e-04
R053845-0236	5 38 45.4	-2 36 00	1.30e-01± 3.76e-03
R053847-0235	5 38 47.0	-2 35 35	8.33e-03± 1.03e-03
R053847-0227	5 38 47.6	-2 27 09	4.28e-03± 9.26e-04
R053847-0237	5 38 47.6	-2 37 18	2.34e-03± 7.99e-04
R053849-0238	5 38 49.0	-2 38 21	6.40e-03± 8.66e-04
R053851-0236	5 38 51.3	-2 36 15	2.65e-03± 4.96e-04
R053851-0246	5 38 51.8	-2 46 41	5.39e-03± 9.79e-04
R053852-0238	5 38 52.7	-2 38 56	1.91e-03± 6.16e-04
R053852-0243	5 38 52.9	-2 43 47	2.88e-03± 8.27e-04
R053853-0233	5 38 53.2	-2 33 20	1.20e-02± 1.08e-03
R053854-0249	5 38 54.2	-2 49 27	4.03e-03± 8.95e-04
R053900-0239	5 39 00.4	-2 39 35	6.51e-04± 8.18e-04
R053901-0238	5 39 01.3	-2 38 54	5.96e-03± 9.04e-04
R053905-0232	5 39 05.3	-2 32 24	2.75e-03± 7.32e-04
R053907-0232	5 39 07.4	-2 32 33	3.20e-03± 7.49e-04
R053911-0235	5 39 11.6	-2 35 58	1.67e-03± 6.93e-04
R053914-0228	5 39 14.8	-2 28 27	1.48e-03± 6.17e-04
R053918-0229	5 39 18.2	-2 29 27	3.02e-03± 7.81e-04
R053932-0239	5 39 32.7	-2 39 40	3.35e-03± 7.36e-04
R053936-0242	5 39 36.4	-2 42 17	1.69e-02± 1.42e-03
R053937-0242	5 39 36.8	-2 42 19	1.45e-02± 1.26e-03
R053947-0232	5 39 47.4	-2 32 22	4.96e-04± 9.55e-04
R053947-0226	5 39 47.6	-2 26 05	2.54e-03± 6.83e-04
R053806-0230	5 38 06.8	-2 30 30	1.01e-03± 4.72e-04
R053813-0234	5 38 13.9	-2 34 57	1.80e-03± 4.17e-04
R053814-0236	5 38 14.6	-2 36 37	5.97e-04± 1.39e-04
R053820-0237	5 38 20.3	-2 37 47	2.01e-03±4.66e-04
R053859-0244	5 38 59.1	-2 44 59	3.65e-03±8.47e-04
R053901-0240	5 39 01.6	-2 40 57	9.67e-04±2.24e-04
R053902-0229	5 39 02.6	-2 29 47	2.61e-03±6.06e-04
R053908-0239	5 39 08.7	-2 39 54	8.09e-04±1.88e-04
R053911-0230	5 39 11.3	-2 30 59	1.89e-03±4.38e-04
R053916-0233	5 39 16.8	-2 33 03	7.74e-04±1.79e-04
R053919-0230	5 39 19.5	-2 30 36	2.95e-03±6.84e-04
R053923-0233	5 39 23.1	-2 33 33	5.46e-03±1.27e-03
R053930-0238	5 39 30.4	-2 38 20	1.85e-03±4.29e-04

Table 2.1: Locations and fluxes of X–ray sources near σ Orionis.

X-ray Sources Northwest of the Belt

Source ID	RA (J2000.)	Dec (J2000.)	Count Rate
J052321+0107	5 23 21.6	1 07 46.6	0.00348 ± 0.000803
J052325+0100	5 23 25.2	1 00 44.7	0.00233 ± 0.000538
J052325+0059	5 23 25.2	0 59 28.0	0.00423 ± 0.000977
J052329+0115	5 23 29.5	1 15 59.1	0.00590 ± 0.001362
J052330+0112	5 23 30.8	1 12 39.3	0.00543 ± 0.001254
J052347+0103	5 23 47.1	1 03 58.9	0.00169 ± 0.000390
J052350+0056	5 23 50.0	0 56 56.4	0.00151 ± 0.000348
J052351+0100	5 23 51.8	1 00 26.7	0.02788 ± 0.006440
J052354+0055	5 23 54.7	0 55 15.1	0.00295 ± 0.000681
J052358+0116	5 23 58.7	1 16 23.4	0.01159 ± 0.002677
J052401+0056	5 24 01.8	0 56 51.1	0.00202 ± 0.000466
J052408+0108	5 24 08.9	1 08 02.7	0.03909 ± 0.009029
J052410+0111	5 24 10.7	1 11 32.1	0.00755 ± 0.001744
J052418+0102	5 24 18.1	1 02 02.8	0.02289 ± 0.005287
J052422+0100	5 24 22.3	1 00 12.0	0.00349 ± 0.000806
J052425+0152	5 24 25.4	0 52 04.0	0.00480 ± 0.001108
J052426+0108	5 24 26.0	1 08 11.1	0.00519 ± 0.001198
J052426+0126	5 24 26.6	1 26 50.2	0.00579 ± 0.001337
J052426+0118	5 24 26.8	1 18 13.3	0.00282 ± 0.000651
J052429+0127	5 24 29.0	1 27 34.6	0.00208 ± 0.000480
J052435+0110	5 24 35.8	1 10 11.4	0.01269 ± 0.002931
J052435+0110a	5 24 35.8	1 10 17.4	0.00217 ± 0.000501
J052439+0121	5 24 39.9	1 21 42.4	0.00200 ± 0.000462
J052443+0134	5 24 43.1	1 34 12.8	0.00103 ± 0.000237
J052446+0131	5 24 46.5	1 31 25.1	0.03737 ± 0.008632
J052447+0136	5 24 47.9	1 36 36.2	0.00280 ± 0.000646
J052453+0124	5 24 53.9	1 24 12.9	0.00400 ± 0.000924
J052457+0138	5 24 57.5	1 38 29.0	0.06685 ± 0.015442
J052459+0138	5 24 59.8	1 38 30.3	0.02181 ± 0.005038
J052503+0120	5 25 03.2	1 20 53.8	0.00820 ± 0.001894
J052503+0133	5 25 03.2	1 33 10.5	0.00200 ± 0.000462
J052505+0120	5 25 05.1	1 20 46.3	0.05202 ± 0.012016
J052505+0121	5 25 05.8	1 21 12.2	0.00225 ± 0.000519
J052511+0136	5 25 11.3	1 36 04.4	0.00301 ± 0.000695
J052515+0133a	5 25 11.6	1 33 35.0	0.00155 ± 0.000358
J052515+0133	5 25 15.8	1 33 39.2	0.00283 ± 0.000653
J052521+0121	5 25 21.5	1 21 40.8	0.00066 ± 0.000152
J052529+0124a	5 25 29.3	1 24 15.2	0.00357 ± 0.000824
J052531+0124	5 25 31.0	1 24 35.4	0.02201 ± 0.005084
J052536+0121	5 25 36.6	1 21 25.2	0.00144 ± 0.000332
J052540+0125	5 25 40.0	1 25 50.0	0.00192 ± 0.000443

Table 2.2: Locations and fluxes of X–ray sources northwest of the belt of Orion.

2.3 Optical Photometry

Optical photometric data were taken of fields encompassing all these sources during a total of seven telescope runs. The facilities used were the Kitt Peak National Observatory (KPNO), the Cerro Tololo Inter–American Observatory (CTIO), the Lowell Observatory, the Florence and George Wise Observatory (WISE) and the Mount Stony Brook Observatory (MTSB; see Appendix C for details.) With the exception of the CTIO run and part of the KPNO run, photometric conditions were not encountered. The CCD detectors used were Photometrics 512 and 1K arrays, two Tektroniks 2K arrays and a Santa Barbara Instrument Group ST–6 camera. Johnson U, B, V and Kron–Cousins R and I band filters were used. These details are summarized in Table 2.3.

The initial goal of the photometric observations is to follow up the X–ray sources, assign them colors in a standard system, so that the observed objects can be placed on a color–magnitude diagram. This can be used to verify that the X–ray sources are indeed PMS stars. In many cases, more than one star falls within the X–ray error circle (nominally about $15''$). The photometric data are very useful in selecting out the probable X–ray source from among the several possibilities. The optical colors can be combined with infrared and spectral data so that the stars can be placed on the H–R diagram. Once on the H–R diagram, they can be fit to evolutionary tracks so that ages and masses can be measured for individual sources.

Raw CCD frames were debiased and flat fielded using the CCDRED pack-

age in IRAF.[1] In addition, for the data taken with the Photometrics detectors, a dark correction was applied between the debiasing and the flatfielding. Aperture photometry was performed using the APPHOT package in IRAF. The apertures used varied from run to run due to changes in the seeing and focus at the individual sites. The apertures averaged about four arcseconds in radius. Sky background was measured in an annulus with a five arcsecond inner radius and a seven arcsecond outer radius. The product of this phase of the reductions was an instrumental magnitude for every star of interest.

[1]The Image Reduction and Analysis Facility is distributed by the National Optical
Astronomy Observatories.

History of all runs

RUN ID	D93a	D93b	N94	J95	O95	J96
Observatory	KPNO	Lowell	MTSB	Wise	MTSB	CTIO
Telescope	0.9m	0.8m	0.35m	1.0m	0.35m	0.9m
Detector	Tek2K	Phot512	ST6	Phot1K	ST6	Tek2K
Dates	Dec 93	Dec 93	Oct/Nov 94	Jan 95	Oct/Nov 95	Jan 96
Weather	Some photometric conditions	8 nights useful	15 nights useful	10 nights useful	17 nights useful	5 nights photometric
extraction aperatures	4”	4”	8”	5”	8”	3”
sky apertures	7”	7”	11”	7”	11”	6”

Table 2.3: Statistics for all observing runs associated with this dissertation.

The instrumental magnitudes were converted to the standard Johnson (U, B, V; 1963) Kron–Cousins(R, I; Cousins 1980) system using the IRAF/PHOTCAL package. Data used for these observations were taken from only the three best photometric nights: 8 December 1992, 29 January 1996 and 2 February 1996. For target stars, there were usually two observations made in all filters, except for the U band in which only one observation was made due to time constraints. Calibration stars were taken from Landolt (1992). Standard star field observations were made approximately once every 90 minutes. Airmasses of standard stars varied between 1.1 and 2.4. Airmasses of target stars were between 1.1 and 1.3 for calibrated observations. Since the Landolt fields are very dense in standard stars, there were more than 100 standard measurements made in each filter on each night. Internal errors were less than 0.01 magnitudes. Sky variability limited the overall accuracy of the data. Overall errors were about 0.02 magnitude in the V band at 16th magnitude in a two–minute exposure. Errors were somewhat higher in the B and U bands.

The measured colors and magnitudes for all X–ray sources observed in Orion OB1b (stars nears σ Orionis) and OB1a (stars NW of the belt) are listed in Tables 2.4 through 2.7. The errors given in these tables are the deviation of the standards to the fit at the magnitude of the target star. If more than one observation was made, the standard deviations of the mean of the measurements is listed instead. In most cases, this latter value is much larger than the deviation of the fit and gives an indication of the intrinsic variability of the star. In Figures 2.1 and 2.2, the V magnitude is plotted against the R−I color for stars near σ Orionis and those northwest of the belt

respectively. A line representing the location of the main sequence at 380 pc has been added to the figure. The bulk of the X–ray sources lie above this line. These are probably PMS stars (assuming that they are at 380 pc). Other objects in this plot are most likely background or foreground objects which were within the error ellipse of the X–ray source. Overall, about 85% of the X–ray sources with measurable V, R and I band fluxes appear to be PMS stars. In about ten cases, there were multiple targets with V$>$ 16 inside the error circle. In these cases, both objects are plotted on the H-R diagram. Although the extinctions have not been calculated for the X–ray sources shown in these figures, conclusions about the PMS nature of these sources is not effected since the reddening vector runs roughly parallel to the main sequence.

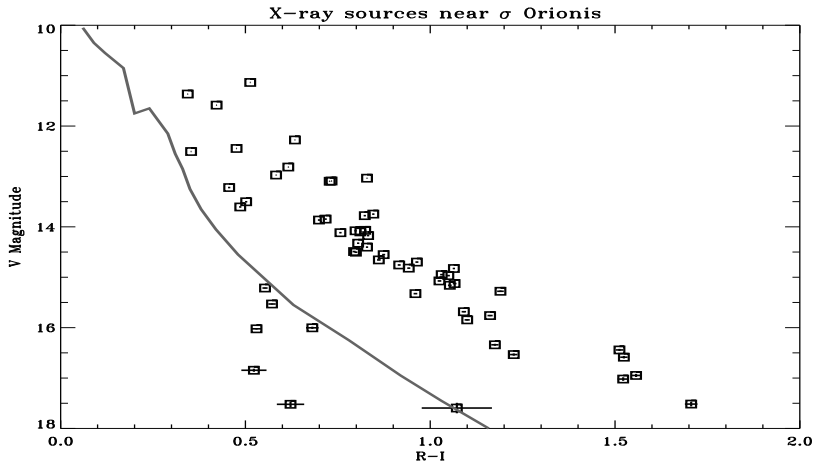

Figure 2.1: V magnitude plotted against the R−I color for X–ray sources near σ Orionis. The thick line is the main sequence at a distance of 380 pc. The mean error bars are indicated.

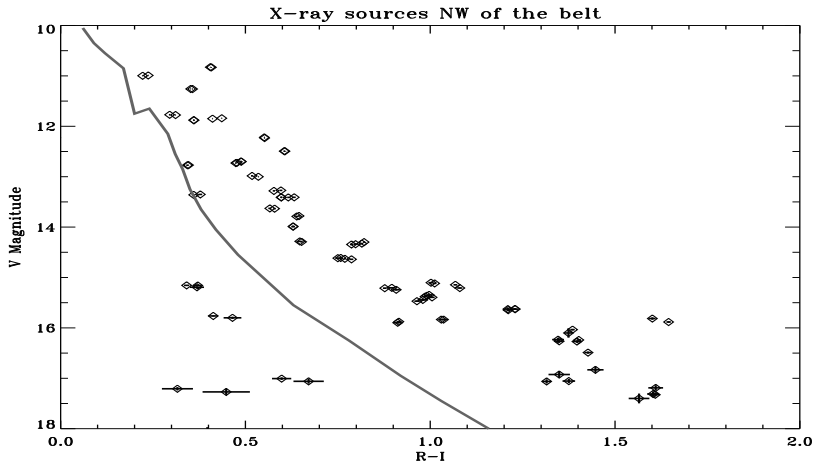

Figure 2.2: V magnitude plotted against the R−I color for X–ray sources northwest of the belt. In this case, each observation is plotted. The thick line is the location of the main sequence. Error bars are plotted.

Optical photometry of X–ray sources near σ Orionis

Star	R.A. (J2000.)	Dec. (J2000.)	U−B	B−V	V	V−R	R−I	No.
R053751-0235	5 37 51.5	-2 35 26.0	0.71 0.08	1.40 0.03	15.630 0.010	1.07 0.01	1.21 0.00	1
4771 0775	5 37 52.9	-2 33 34.4	0.27 0.00	0.78 0.00	11.565 0.001	0.46 0.01	0.42 0.01	1
4771 0921	5 37 54.2	-2 39 29.8	0.54 0.00	0.94 0.00	11.113 0.001	0.56 0.01	0.51 0.01	1
R053802-0224	5 38 02.2	-2 24 24.0	-0.12 0.24	1.10 0.15	17.607 0.059	0.61 0.07	0.51 0.05	1
4771 0950	5 38 06.3	-2 28 49.4	0.28 0.14	1.19 0.19	14.825 0.111	0.95 0.05	0.97 0.04	3(2)
4771 0947	5 38 06.6	-2 30 22.8	0.19 0.07	0.68 0.05	15.224 0.024	0.44 0.02	0.50 0.02	3(2)
4771 0854	5 38 06.9	-2 31 17.4	0.69 0.07	1.08 0.02	12.718 0.064	0.63 0.03	0.64 0.02	3(2)
R053807-0231	5 38 07.7	-2 31 31.4	-0.60 0.29	0.61 0.30	17.101 0.136	0.87 0.13	0.52 0.08	1
R053808-0235	5 38 08.1	-2 35 56.1	0.66 0.02	0.95 0.12	15.190 0.038	0.65 0.02	0.56 0.03	3(2)
R053808-0235	5 38 08.4	-2 35 40.8	-0.29 0.38	1.42 0.33	16.170 0.166	0.95 0.21	1.36 0.04	3(2)
R053810-0232	5 38 10.6	-2 32 54.3	1.14 0.27	1.44 0.02	14.455 0.063	0.80 0.03	0.73 0.03	2
R053812-0232	5 38 12.5	-2 32 59.5	1.22 0.02	1.27 0.08	13.924 0.027	0.75 0.01	0.65 0.01	2
R053813-0230	5 38 13.1	-2 30 33.3	0.79 0.02	1.14 0.01	14.659 0.022	0.64 0.01	0.61 0.03	2
R053814-0235	5 38 14.0	-2 35 05.3	0.44 0.06	0.94 0.05	16.012 0.230	0.58 0.18	0.56 0.05	3(1)
R053820-0238	5 38 20.1	-2 38 01.3	-0.18 0.38	0.88 0.32	17.030 0.121	0.64 0.12	0.26 0.11	1
R053827-0242	5 38 27.1	-2 42 59.7	0.38 0.38	1.41 0.20	16.340 0.114	1.33 0.12	1.35 0.01	2
R053828-0242	5 38 28.1	-2 42 55.3	1.21 0.43	1.00 0.12	16.407 0.052	0.83 0.06	0.61 0.10	2
R053829-0236	5 38 29.0	-2 36 02.4	1.40 0.06	1.08 0.44	16.096 0.193	0.91 0.16	1.12 0.05	3(1)
R053829-0223	5 38 29.8	-2 23 38.1	0.27 0.07	0.77 0.05	13.135 0.058	0.43 0.03	0.43 0.02	3(2)
R053830-0241	5 38 30.5	-2 41 19.5	0.39 0.03	0.90 0.02	14.001 0.010	0.47 0.01	0.47 0.01	1
R053831-0235	5 38 31.4	-2 35 14.9	1.35 0.15	1.44 0.03	15.658 0.011	1.05 0.01	1.09 0.01	1
R053832-0235	5 38 32.5	-2 35 03.9	1.16 0.39	1.41 0.15	15.145 0.406	0.92 0.10	1.08 0.17	3(2)
R053832-0235	5 38 32.8	-2 35 39.0	0.97 0.27	1.25 0.03	14.548 0.072	0.84 0.02	0.83 0.03	3(2)
R053833-0236	5 38 33.9	-2 36 37.5	1.09 0.46	1.03 0.24	16.403 0.180	1.15 0.17	1.54 0.02	4(3)
R053834-0234	5 38 34.2	-2 34 59.7	0.14 0.05	0.70 0.03	14.726 0.018	0.42 0.02	0.43 0.01	1
R053834-0234	5 38 34.4	-2 34 18.1						0
R053835-0231	5 38 35.3	-2 31 31.3	1.17 0.02	1.27 0.06	14.025 0.058	0.78 0.05	0.79 0.02	4(3)
R053835-0230	5 38 35.7	-2 30 42.2	2.53 1.49	0.21 0.15	16.731 0.096	0.65 0.10	0.27 0.09	1
4771 1097	5 38 35.7	-2 30 43.3	0.86 0.18	1.11 0.07	13.951 0.110	0.73 0.05	0.79 0.012	3(2)
R053836-0236	5 38 36.7	-2 36 44.3	0.80 0.40	1.28 0.04	14.089 0.056	0.85 0.07	0.85 0.030	3(2)
R053838-0236	5 38 38.0	-2 36 38.4	0.73 0.31	1.30 0.04	14.053 0.007	0.82 0.02	0.86 0.035	3(2)
R053838-0234	5 38 38.2	-2 34 54.7	0.89 0.00	1.18 0.20	12.244 0.013	0.71 0.02	0.65 0.027	2
4771 1147	5 38 38.3	-2 34 55.2	0.68 0.02	1.18 0.08	13.713 0.078	0.76 0.01	0.76 0.007	3(2)
R053838-0226	5 38 38.3	-2 26 44.3	0.76 0.20	1.15 0.04	14.679 0.014	0.70 0.00	0.65 0.014	2
R053840-0230	5 38 40.1	-2 30 18.5	0.73 0.36	1.32 0.13	14.650 0.003	0.91 0.01	0.94 0.02	3(2)
R053840-0230	5 38 40.2	-2 30 19.0	0.82 0.12	1.19 0.07	13.956 0.119	0.74 0.06	0.78 0.019	3(2)
R053841-0227	5 38 41.1	-2 27 22.6	0.95 0.11	1.36 0.00	14.582 0.071	0.94 0.08	0.87 0.009	1
R053843-0240	5 38 43.6	-2 40 33.9	0.70 0.03	1.06 0.17	15.414 0.136	0.71 0.14	0.69 0.054	2
4771 1051	5 38 44.1	-2 40 20.1	0.87 0.45	1.20 0.10	13.935 0.189	0.81 0.09	0.79 0.008	3(2)
4771 1055	5 38 44.3	-2 32 41.7	1.09 0.09	1.29 0.06	13.741 0.018	0.84 0.01	0.86 0.020	3(2)
R053844-0240	5 38 44.5	-2 40 30.5						0
R053845-0241	5 38 45.1	-2 41 58.9	0.63 0.44	1.44 0.21	15.593 0.155	1.03 0.12	1.35 0.01	3(2)
R053847-0237	5 38 47.7	-2 37 19.6	0.21 0.12	1.22 0.06	15.982 0.022	0.84 0.02	0.68 0.01	1
4711 0899	5 38 47.9	-2 27 14.1	0.87 0.08	1.18 0.05	12.899 0.099	0.73 0.03	0.82 0.01	3(2)
R053848-0244	5 38 48.4	-2 44 20.0	0.17 0.01	0.79 0.01	13.215 0.005	0.52 0.01	0.52 0.01	1
R053849-0238	5 38 49.0	-2 38 21.4	1.15 0.02	1.33 0.10	14.838 0.194	0.96 0.08	1.00 0.05	4
R053851-0236	5 38 51.3	-2 36 21.1	0.20 0.45	1.00 0.19	17.68 0.087	1.50 0.09	1.77 0.03	1
4771 0080	5 38 51.9	-2 46 43.6	1.02 0.04	1.36 0.01	14.483 0.004	0.90 0.01	0.80 0.01	1
R053852-0238	5 38 52.9	-2 38 50.3	1.24 0.07	1.42 0.09	14.816 0.102	1.00 0.09	1.05 0.01	3
R053852-0238	5 38 52.9	-2 38 53.8	1.27 0.06	1.38 0.09	14.534 0.269	0.92 0.01	0.95 0.15	2
R053853-0243	5 38 53.0	-2 43 52.3	1.13 0.15	1.23 0.28	15.653 0.258	1.03 0.16	1.08 0.08	3(1)
4771 1049	5 38 53.2	-2 33 23.3	0.84 0.08	1.15 0.05	13.021 0.044	0.72 0.02	0.73 0.01	3(2)
R053853-0233	5 38 53.2	-2 33 24.0	0.63 0.57	1.31 0.14	15.130 0.034	0.93 0.02	1.11 0.04	3(2)
4771 0119	5 38 53.9	-2 49 29.7	0.72 0.00	1.03 0.00	12.954 0.002	0.64 0.01	0.58 0.01	1
R053856-0231	5 38 56.9	-2 31 25.1	0.20 0.05	0.70 0.01	12.914 0.009	0.40 0.01	0.40 0.02	2
R053859-0247	5 38 59.0	-2 47 12.8	1.06 0.02	1.21 0.00	13.845 0.003	0.79 0.01	0.69 0.01	1
R053859-0332	5 38 59.0	-2 33 51.3	0.83 0.08	1.16 0.06	13.021 0.044	0.72 0.01	0.73 0.01	3(2)
4771 0026	5 38 59.4	-2 45 07.8	0.06 0.14	0.59 0.04	12.386 0.090	0.36 0.06	0.34 0.03	3(2)
R053901-0240	5 39 01.6	-2 40 57.0	-0.24 0.09	1.15 0.06	16.441 0.026	1.10 0.03	1.32 0.01	1
4771 901	5 39 11.4	-2 31 06.4	-0.15 0.82	1.00 0.48	16.406 0.564	1.11 0.04	1.09 0.10	3(2)
4771 1038	5 39 11.5	-2 36 03.0	1.24 0.14	1.17 0.05	14.514 0.078	0.83 0.09	0.90 0.02	2(1)

Table 2.4: Colors of X–ray sources near σ Orionis.

Photometry of X–ray sources near σ Orionis...(cont.)

Star	R.A. (J2000.)	Dec. (J2000.)	U−B	B−V	V	V−R	R−I	No.
R053911-0236	5 39 11.7	-2 36 03.7	1.26 0.06	1.37 0.01	14.792 0.005	0.91 0.01	0.94 0.01	1
R053916-0232	5 39 16.8	-2 32 55.5	1.84 1.59	1.10 0.23	18.157 0.094	0.82 0.11	0.72 0.06	1
4771 598	5 39 17.9	-2 29 28.9						0
R053918-0229	5 39 18.4	-2 29 31.1	0.54 0.01	0.93 0.01	12.423 0.001	0.54 0.01	0.47 0.00	1
4771 910	5 39 18.7	-2 30 53.3	1.22 0.04	1.44 0.01	14.344 0.004	0.92 0.01	0.84 0.01	1
R053922-0233	5 39 22.7	-2 33 32.9	1.55 0.37	1.41 0.07	16.508 0.022	1.12 0.02	1.23 0.01	1
4771 0579	5 39 30.2	-2 35 06.5	0.75 0.02	1.28 0.01	14.227 0.004	0.78 0.01	0.74 0.01	1
R053930-0238	5 39 30.4	-2 38 26.3	1.02 0.76	1.55 0.20	17.631 0.057	0.95 0.06	1.51 0.03	1
R053930-0238	5 39 30.4	-2 38 27.1						0
R053931-0239	5 39 31.5	-2 39 30.0						0
R053932-0239	5 39 32.4	-2 39 44.1						0
R053936-0242	5 39 36.4	-2 42 17.0	1.18 0.02	1.37 0.00	13.653 0.002	0.87 0.01	0.84 0.01	1
4771 1075	5 39 05.3	-2 32 30.1	0.89 0.30	1.31 0.08	14.414 0.032	0.88 0.01	0.87 0.03	3(2)
R053906-0232	5 39 06.5	-2 32 33.2	1.19 0.03	1.39 0.01	14.376 0.004	0.88 0.01	0.83 0.01	1
R053907-0228	5 39 07.7	-2 28 16.0	-0.04 0.20	1.55 0.11	16.886 0.031	1.05 0.03	1.45 0.01	1
R053907-0232	5 39 07.7	-2 32 39.2	0.81 0.02	1.32 0.01	14.299 0.004	0.86 0.01	0.80 0.01	1
4771 1056	5 39 00.5	-2 39 38.0	0.50 0.05	0.87 0.05	13.469 0.086	0.55 0.06	0.49 0.01	4(3)
R053901-0238	5 39 01.4	-2 38 55.6	— —	— —	— —	— —	— —	0
R053902-0241	5 39 02.5	-2 41 20.1	1.32 0.33	1.14 0.12	15.720 0.127	0.70 0.15	0.66 0.08	2
R053902-0229	5 39 02.6	-2 29 55.8	0.98 1.22	1.27 0.33	16.998 0.201	1.10 0.20	1.55 0.05	4(2)
R053902-0241	5 39 02.8	-2 41 26.9	-0.24 0.09	1.15 0.06	16.329 0.159	1.12 0.10	1.31 0.02	2(1)
4771 1092	5 39 07.4	-2 32 39.3	0.44 0.05	1.19 0.03	14.118 0.015	0.79 0.01	0.80 0.01	2(1)
4771 1094	5 39 07.6	-2 40 10.5	0.35 0.02	0.76 0.11	15.448 0.094	0.53 0.07	0.60 0.05	3(2)

Table 2.5: Colors of X–ray sources near σ Orionis (continued).

Photometry of stars used as comparison objects

Star	R.A. (J2000.)	Dec. (J2000.)	U−B	B−V	V	V−R	R−I	No.
C053802-0229	5 38 02.0	-2 29 55.7	-0.13 0.64	1.38 0.19	15.859 0.112	0.55 0.05	0.56 0.01	2
C053834-0228	5 38 34.3	-2 28 48.3	0.20 0.13	0.98 0.04	15.354 0.025	0.60 0.02	0.59 0.03	2
C053842-0227	5 38 42.2	-2 27 08.2	-0.24 0.08	0.20 0.01	11.297 0.016	0.15 0.01	0.18 0.01	2
C053845-0243	5 38 45.9	-2 43 46.0	1.02 0.16	1.54 0.06	14.562 0.014	0.77 0.01	0.75 0.01	1
C053859-0242	5 38 59.3	-2 42 19.5	0.23 0.02	0.81 0.01	13.877 0.007	0.45 0.00	0.53 0.01	1
C053900-0237	5 39 00.5	-2 37 32.3	1.41 0.84	0.95 0.23	16.272 0.136	0.71 0.06	0.65 0.10	2(1)
C053903-0237	5 39 03.1	-2 37 27.2	0.12 0.34	0.84 0.13	15.264 0.026	0.58 0.06	0.58 0.02	2
C053918-0236	5 39 18.3	-2 36 53.4	0.35 0.02	0.98 0.01	14.752 0.005	0.62 0.01	0.60 0.01	1

Table 2.6: Colors of stars used as comparison objects near σ Orionis.

Optical photometry of X–ray sources NW of the belt

Star	R.A. (J2000.)	Dec. (J2000.)	U−B	B−V	V	V−R	R−I	No.
101 0518	5 23 21.6	1 07 51.2	0.15 0.01	0.67 0.01	11.878 0.002	0.37 0.00	0.36 0.01	2(1)
J052324-0059	5 23 24.9	0 59 33.0	1.12 0.18	1.43 0.02	15.220 0.021	0.62 0.51	2.25 2.72	4(1)
J052325-0100	5 23 25.7	1 00 37.7	0.23 0.64	0.25 0.77	18.291 0.320	0.52 0.34	0.46 0.09	2(1)
J052329-0116	5 23 29.5	1 16 13.0	— —	2.38 1.03	16.249 0.023	1.13 0.00	1.34 0.01	2(0)
101 0807	5 23 29.6	1 12 40.8	— —	1.08 0.01	12.993 0.012	0.57 0.00	0.52 0.01	2(0)
J052347-0104	5 23 47.3	1 04 02.2	0.56 0.18	1.57 0.27	17.307 0.087	1.32 0.09	1.59 0.02	4(2)
J052350-0057	5 23 50.1	0 57 01.9	-0.01 0.01	0.48 0.02	15.169 0.021	0.31 0.00	1.51 2.31	4(1)
101 2495	5 23 51.6	1 03 25.3	1.12 0.20	1.26 0.03	14.624 0.013	0.80 0.00	0.76 0.01	4(2)
J052351-0100	5 23 51.7	1 00 31.2	-0.56 0.45	0.92 0.89	17.012 0.063	0.73 0.33	0.99 0.42	4(2)
J052354-0055	5 23 54.6	0 55 21.6	0.78 0.13	1.43 0.01	15.834 0.000	0.99 0.00	1.03 0.01	2(1)
J052357-0116	5 23 57.8	1 16 40.6	— —	2.09 0.89	15.849 0.049	1.29 0.00	1.62 0.03	2(0)
J052402-0056	5 24 02.2	0 56 59.5	0.83 0.17	1.54 0.04	15.887 0.015	0.92 0.03	0.91 0.01	2(1)
101 0537	5 24 08.7	1 08 11.0	0.69 0.01	1.04 0.01	13.410 0.003	0.61 0.00	0.59 0.01	2(1)
J052410-0111	5 24 10.5	1 11 39.0	0.90 0.13	1.41 0.12	15.626 0.003	1.05 0.00	1.23 0.01	4(1)
101 0594	5 24 11.8	1 22 03.0	3.70 0.37	1.07 0.01	13.632 0.004	0.63 0.00	0.57 0.01	2(1)
101 1156	5 24 17.6	1 02 15.8	0.49 0.02	1.19 0.01	14.312 0.021	0.79 0.02	0.81 0.01	2(1)
101 2447	5 24 18.9	1 01 51.8	0.38 0.01	0.86 0.01	12.727 0.004	0.50 0.00	0.47 0.01	2(1)
J052417-0124	5 24 17.7	1 24 39.8	0.04 0.01	0.55 0.01	11.774 0.004	0.31 0.00	0.30 0.01	2(1)
J052422-0100	5 24 22.7	1 00 01.2	0.78 0.02	1.09 0.01	12.225 0.008	0.58 0.00	0.55 0.01	2(1)
J052424-0052	5 24 24.9	0 52 08.7	0.11 0.11	0.36 0.17	17.239 0.044	0.30 0.08	0.38 0.09	2(1)
J052426-0108	5 24 26.9	1 08 02.6	0.06 0.01	0.58 0.01	12.771 0.001	0.34 0.00	0.34 0.01	2(1)
J052426-0126	5 24 26.4	1 26 48.9	0.13 0.01	0.64 0.01	11.260 0.001	0.37 0.00	0.35 0.01	2(1)
J052426-0118	5 24 26.5	1 18 14.5	—- —-	1.42 0.07	15.110 0.010	0.98 0.01	1.00 0.01	2(1)
J052429-0127	5 24 29.0	1 27 32.1	— —	1.17 0.01	14.288 0.006	0.72 0.00	0.65 0.01	2(0)
J052435-0120	5 24 35.5	1 20 44.8	0.24 0.45	— –	— —	0.80 0.24	0.71 0.07	1
J052435-0120	5 24 35.6	1 20 55.0	— —	1.52 0.31	16.832 0.060	4.37 4.40	1.46 0.02	1(0)
J052436-0120	5 24 36.4	1 20 48.3	-1.69 1.10	0.36 0.71	18.826 0.386	0.37 0.50	0.61 0.39	1
J052435-0110	5 24 35.6	1 10 18.9	0.51 0.01	0.92 0.01	12.699 0.003	0.52 0.00	0.48 0.01	1
J052442-0134	5 24 42.6	1 34 09.5	0.76 0.03	1.17 0.01	13.410 0.001	0.70 0.00	0.62 0.01	2(1)
J052446-0131	5 24 46.2	1 31 28.9	0.13 0.00	0.78 0.01	11.845 0.006	0.42 0.00	0.42 0.01	2(1)
J052447-0136	5 24 47.7	1 36 29.2	1.00 0.35	1.48 0.06	15.457 0.018	0.91 0.00	0.97 0.01	2(1)
J052453-0124	5 24 53.9	1 24 10.2	0.76 0.03	1.08 0.02	13.784 0.006	0.68 0.00	0.64 0.01	2(1)
J052500-0138	5 25 00.1	1 38 32.6	-0.10 0.01	0.41 0.01	10.994 0.004	0.22 0.00	0.23 0.01	2(1)
J052501-0138	5 25 01.0	1 38 32.6	0.01 0.01	0.69 0.01	13.357 0.006	0.38 0.01	0.36 0.01	2(1)
J052502-0133	5 25 02.7	1 33 04.6	— –	— –	— —	— —	1.43 1.03	1
101 0719	5 25 03.1	1 20 52.3	0.83 0.01	1.14 0.01	12.494 0.001	0.67 0.00	0.60 0.01	2(1)
J052504-0120	5 25 04.6	1 20 51.5	— —	0.45 0.07	17.062 0.042	1.33 0.33	1.31 0.01	2(0)
101 2429	5 25 05.7	1 21 10.2	0.85 0.15	1.42 0.05	15.177 0.045	0.99 0.03	1.07 0.01	2(1)
J052510-0135	5 25 10.5	1 35 58.6	0.56 0.02	1.03 0.02	13.277 0.007	0.59 0.00	0.58 0.01	2(1)
J052511-0133	5 25 11.4	1 33 29.1	-0.03 0.01	0.20 0.01	9.912 0.001	0.04 0.00	0.11 0.01	1
J052515-0133	5 25 15.5	1 33 37.9	0.54 0.07	1.28 0.01	14.342 0.004	0.80 0.00	0.79 0.01	2(1)
J052521-0121	5 25 21.4	1 21 39.2	0.16 0.00	0.70 0.01	10.828 0.002	0.40 0.00	0.40 0.01	2(1)
J052529-0124	5 25 29.3	1 24 14.5	0.83 0.03	1.10 0.01	13.988 0.005	0.67 0.00	0.62 0.01	2(1)
J052532-0124	5 25 32.0	1 24 48.7	—- —-	0.80 0.08	15.781 0.026	0.42 0.01	0.43 0.03	2(1)
J052536-0121	5 25 36.2	1 21 25.0	— —	1.44 0.10	16.490 0.022	1.13 0.02	1.41 0.01	2(0)
J052539-0125	5 25 39.7	1 25 48.8	— —	3.34 3.02	16.068 0.047	1.19 0.03	1.38 0.01	2(1)

Table 2.7: Colors of X–ray sources NW of the Belt.

2.4 Calculation of Extinction from Optical Colors

In theory, the application of a reddening correction should be straightforward. For example, one method is to derive the spectral energy distribution (SED) for a target star and compare it to the SED of a dereddened standard star. One can multiply the standard SED by various extinction coefficients (A_V), so the residual of the target with respect to standard is minimized. However, since I only have five filter bands to work with and the U band data are very noisy, I lack sufficient leverage to use this method. Nonetheless, B through I data can still be useful. Temperature can be determine via the B−V color (Gilliland 1985):

$$\log(T_{eff}) = 3.9255 - 0.31661(B-V) + 0.11780(B-V)^2 - 0.049392(B-V)^3. \tag{2.1}$$

Likewise, the R−I color can be converted to temperature (Laird 1985):

$$\Theta_{eff} = 0.993(R-I) + 0.539. \tag{2.2}$$

Here Θ_{eff} is defined in the usual way ($\Theta_{eff} = 5040/T_{eff}$). The relations are both valid for dwarfs between 4000K and 7000K. PMS stars are sub giants, a luminosity class which is not well understood. The spectral type assigned to a star of a given temperature can differ by 3 subtypes, depending on luminosity class, with the largest differences being seen for G stars. However, the difference in color index between luminosity classes III and V for a given temperature is less than 0.03 for B−V and R−I. The spectral subtype I derived

here is based on the observed color index. The difference in the color temperatures thus obtained is a function of the reddening. By adjusting the reddening to minimize the difference between the B−V and R−I color temperatures, an estimate to extinction can be made. The extinction is determined to be the A_V needed to make to B−V and R−I temperatures the same. This methodology was tested against the background stars in the Orion OB1a fields. The results produced small extinctions to the background stars of between $A_V = 0.1$ and $A_V = 0.4$. However, when the same techniques were applied to the X–ray data, very unusual results were obtained. Extinctions of $A_V > 8$ or < 0 were not uncommon. These results are considered spurious and were likely the effect of photospheric contamination by the active chromosphere. Such unusual extinctions could be the result of chromospheric activity which was primarily detected in the B band and therefore made the star appear warmer in the blue than in the red. The high extinctions could be the result of strong chromospheric Hα line emission which is observed in the R–band and can make the R−I color temperature artificially high. Given coverage into the infrared, temperature and be independently derived from the V−K color so long as the stars lack any near-IR excess (Carney 1983). Alternatively, spectral typing gives an independent assessment of temperature. The most accurate extinction calculation requires both IR and spectral data.

2.4.1 Infrared Data

Near–infrared observations were made on 5–6 February 1996 at CTIO using the CIRIM imager. CIRIM is a 256×256 HgCdTe array sensitive to near infrared wavelengths. At the focus of the CTIO 1.5 meter, the pixels are $1.16''$ on a side. The field of view was about $5' \times 5'$, and J, H and K filters were used. Sixteen fields near σ Orionis were observed. Exposure times averaged about 10 seconds in each filter with six coadds per exposure. In the infrared, the sky background is high relative to the dynamic range of the detector. This effect is mild at J–Band, but it limits K–band exposures to under 10 seconds. It is desirable to coadd several exposures together. The nominal seeing at the CTIO 1.5 meter was about 0.8 arcseconds. Since the pixel size was larger than the nominal size of a seeing disk, it was necessary to move the telescope several times during the exposure sequence to get an accurate flux measurement. This process is called dithering. Five dithered exposures were taken of each field. As the first step in the reduction, all frames had a linearity correction applied (Elston 1994). Afterward, the individual frames were dark–subtracted and flatfielded. The dithered frames, thus reduced, were then added together to create a composite frame and median filtered to create a sky background frame. This sky background frame was multiplied by five and then subtracted from the composite frame to produce a final frame.

Photometry was carried out only on those sources for which a possible (not necessarily confirmed) optical counterpart to an X–ray source had been identified. The IRAF/APPHOT package was used in a similar manner to the optical

data with a similar 4" radius aperture. In some cases, the dithering procedure caused stars to overlap with other stars on the final frame. In these cases, corrected single star frames were measured using IRAF/APPHOT. Comparisons stars were taken from the UKIRT faint standards (Casali & Hawarden 1992). Standard stars were observed between five and nine times at each airmass; airmasses ranged from 1.2 to 2.2. The solution for each night was accurate to about 5% in each color. These analyses lead to five measurements of each target star in each filter. The results were averaged and are listed in Table 2.8. The errors given are the standard deviations among the five measurements.

IR photometry of X–ray sources

Object ID	K	Err K	H-K	Err H-K	J-H	Err J-H
R053806-0228	9.76	0.03	0.05	0.03	0.28	0.02
R053807-0231	14.76	0.30	-0.02	0.24	0.81	0.25
R053807-0231	9.80	0.05	0.09	0.03	0.70	0.04
R053808-0235	11.41	0.03	0.34	0.11	0.69	0.17
R053808-0235b	12.51	0.09	0.13	0.08	0.55	0.14
R053815-0236	13.69	0.11	0.17	0.16	0.39	0.31
R053827-0242	11.33	0.11	0.11	0.07	0.74	0.04
R053828-0242	13.46	0.06	0.14	0.16	0.56	0.12
R053829-0223	11.18	0.03	0.05	0.03	0.46	0.04
R053829-0236	11.78	0.07	0.10	0.13	0.81	0.08
R053832-0235	10.61	0.02	0.52	0.01	0.97	0.02
R053832-0235	10.85	0.05	0.08	0.06	0.76	0.06
R053833-0236	11.10	0.03	0.16	0.02	0.79	0.06
R053833-0236	11.09	0.04	0.24	0.07	0.70	0.07
R053834-0231	11.15	0.03	—	—	0.44	0.27
R053834-0234	12.91	0.06	0.18	0.09	0.28	0.06
R053835-0230	14.57	0.20	-0.08	0.28	0.73	0.30
R053835-0231	12.52	2.37	0.16	0.04	1.02	0.33
R053836-0236	10.61	0.06	0.16	0.01	0.80	0.11
R053838-0234	9.14	0.01	0.13	0.01	0.69	0.01
R053838-0236	10.35	0.03	0.11	0.09	0.76	0.06
R053840-0230	10.52	0.06	0.23	0.04	0.83	0.03
R053840-0230	10.57	0.04	0.17	0.03	0.98	0.05
R053840-0230	10.54	0.05	0.11	0.04	0.73	0.02
R053844-0232	10.08	0.05	0.22	0.12	0.50	0.27
R053844-0240	11.32	1.10	0.41	0.39	0.37	0.53
R053845-0241	11.06	0.02	0.19	0.03	0.82	0.03
R053847-0237	10.61	0.04	0.21	0.04	0.88	0.04

Table 2.8: IR Colors of X–ray near σ Orionis.

IR photometry of X–ray sources (continued)

Object ID	K	Err K	H-K	Err H-K	J-H	Err J-H
R053849-0238	10.60	0.02	0.41	0.13	0.30	0.44
R053849-0238	10.60	0.05	0.13	0.05	0.74	0.05
R053852-0238	10.86	0.05	0.12	0.04	0.68	0.03
R053852-0238	10.96	0.07	0.25	0.07	0.57	0.09
R053853-0233	9.72	0.03	0.10	0.02	0.71	0.05
R053853-0243	11.33	0.08	0.19	0.06	0.81	0.02
R053859-0247	10.50	0.03	0.16	0.04	0.74	0.03
R053900-0239	11.16	0.07	0.00	0.06	0.51	0.04
R053901-0238	8.09	0.03	0.12	0.00	-0.04	0.04
R053902-0229	14.03	0.24	-0.11	0.27	0.69	0.38
R053902-0229	11.80	0.08	0.25	0.09	0.43	0.28
R053902-0241	11.81	0.89	0.67	0.09	0.22	0.10
R053902-0241b	12.47	0.19	0.52	0.21	0.13	0.34
R053907-0240	13.54	0.18	0.27	0.29	0.17	0.28
R053916-0232	14.68	0.08	-0.01	0.11	0.81	0.13
R053922-0233	13.72	0.29	0.00	0.37	0.47	0.11
4771 0026	10.83	0.05	0.08	0.02	0.30	0.05
4771 0080	10.62	0.06	0.25	0.02	0.89	0.02
4771 0598	10.15	0.12	0.05	0.16	0.48	0.10
4771 0899	9.35	0.05	0.22	0.00	0.95	0.02
4771 0901	11.06	0.14	0.32	0.16	0.92	0.07
4771 0947	13.16	0.08	0.08	0.13	0.45	0.07
4771 0950	10.57	0.03	0.46	0.05	0.99	0.03
4771 1056	11.31	0.14	0.11	0.16	0.45	0.06
4771 1075	10.69	0.15	0.17	0.24	0.84	0.06
4771 1092	10.31	0.09	0.22	0.15	0.80	0.09
4771 1097	10.50	0.02	0.10	0.02	0.80	0.02
4771 1147	10.41	0.09	0.11	0.05	0.74	0.02

Table 2.9: IR Colors of X–ray near σ Orionis (continued).

2.4.2 Spectroscopic Data

F. Walter (1996) obtained WIYN/HYDRA queue observations of stars in both the σ Orionis field and the field NW of the belt. The targets fell in two categories: **A.** Stars which are likely counterparts of the X–ray sources. These were identified by visual inspection of optical images. **B.** Stars with magnitudes and colors comparable to those selected as likely X–ray counterparts. Observations were in the 5850–6800Å band at 1Å resolution (Grating 860). The integration time was an hour on each field. This yielded S/N of about 100 per pixel in the continuum for V=14, and S/N of about 40 at V=16.

The spectra were trimmed, debiased and overscan and flat–field corrected using the IRAF/DOHYDRA package. The wavelength calibration was also performed using this package. All subsequent analysis was performed using the IDL/ICUR package (Walter 1992). The spectra were not flux calibrated. To correct for wavelength dependent detector effects, spectra of three bright stars were combined, heavily smoothed and fitted with a third order polynomial. The fits were then normalized with respect to the maxima. Data analysis were mostly performed by undergraduate student James Petreshock under my supervision.

Equivalent widths of Ca I absorption lines at 6122Å, 6162Å, and 6494Å and Fe I at 6103Å, 6200Å, and 6574Å were measured for several spectral standards. All spectral observations were made with the KPNO 2.1 meter telescope using the GOLDCAM. The spectral standards were observed several time per nights so that spectra at different airmasses could be sampled. The

spectral types of the target stars were determined by comparing source line ratios to those of standard stars. Line ratios were used as an indicator of spectral type. The ratios were obtained from the three Ca I absorption lines: 6122/6494, 6162/6494, and 6122/6162. As shown in Figures 2.3 and 2.4, the Ca I lines show a strong dependence upon spectral type over the range of spectral type we were expecting to observe. The majority of the spectra showed that the Fe I line at 6574 was filled in by Hα emission and therefore would not be an accurate indicator. Also, the Fe I lines were generally weaker than the Ca I lines. In Figures 2.3 and 2.4, the solid line represents a third order polynomial fit to the observed data. The standard deviation to this fit is about 1.5 spectral sub–types. I take this to be the error in the final spectral type determination of the target stars. The standard used are given in Table 2.10 It was not possible to classify sources with an average count rate below 100 photons/pixel. The results of the spectral classification are shown in Tables 2.12 through 2.11. The uncertainty in the spectral type is about one and a half sub–types. For stars with S/N of greater than 100, the deviation was usually less than one spectral subtype. However, in the cases of high noise observations, the deviation was up to three subtypes.

All but one of the bright X–ray sources near σ Orionis shows a Li absorption feature and six (out of 49 = 12.3%) show strong (>10Å) Hα emission lines. Northwest of the belt, again all but one source shows Li in absorption, but only one star (out of 13 = 7.7%) shows an Hα emission line. The data verify that the X–ray emission is a good indicator of youth.

Results of WIYN observations of spectral standards

Name	Sp Type	Ca I 6122/ 6162	Ca I 6122/ 6494	Ca I 6162/ 6494	Fe I 6103/ 6200	Fe I 6103/ 6574	Fe I 6200/ 6574
SAO 82868	F5	0.340	0.148	0.383	7.611	—	—
HD 115043	G1	0.333	0.220	0.548	4.630	19.364	4.182
HD 69830	G7.5	0.317	0.262	0.773	3.710	14.222	3.833
HD 131156A	G8	0.327	0.248	0.718	4.726	12.739	2.696
HD 124752	K0	0.361	0.340	0.953	3.753	6.549	1.745
HD 124750	K0	0.391	0.378	0.866	2.978	8.839	2.968
HD 142091	K1	0.276	0.227	0.699	1.695	3.263	1.925
HD 109011	K2	0.384	0.456	1.147	3.083	4.139	1.343
HD 110463	K3	0.457	0.563	1.212	2.791	3.084	1.105
HD 128165	K3	0.415	0.538	1.109	3.061	3.041	0.993
HD 113156B	K5	0.457	0.848	1.790	3.172	3.854	1.215
HD 237903	K7	0.382	0.818	—	3.539	2.161	0.611

Table 2.10: Ca I and Fe I absorption lines ratios as a function of spectral type for observed standards.

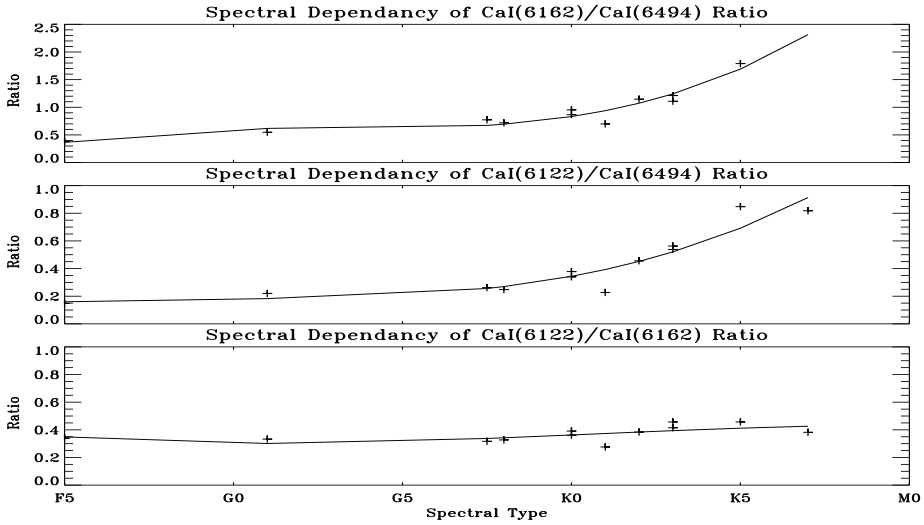

Figure 2.3: Ca I absorption lines ratios 6122/6494Å, 6162/6494Å and 6122/6162Å as a function of spectral type. The 6162/6494Å and 6122/6494Å ratios show a fairly monotonic correspondence with spectral type. The solid lines represent third order polynomial fits to the observed data.

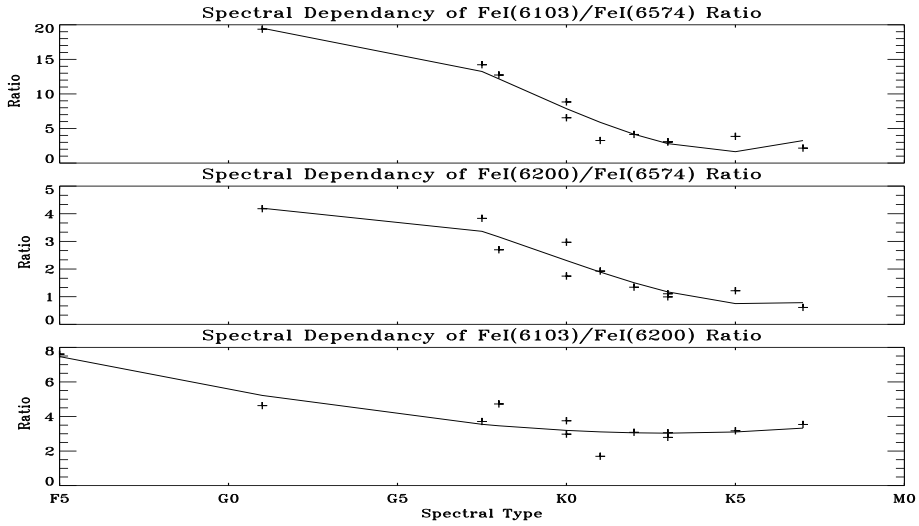

Figure 2.4: Fe I absorption lines ratios 6103/6574Å, 6200/6574Å and 6103/6200Å as a function of spectral type. Although the 6103/6574Å and 6200/6574Å ratios have fairly monotonic correspondence with spectral type and are somewhat steeper, the 6574Å line is often blended with Hα 6563Å. The solid lines represent third order polynomial fits to the observed data.

Results of WIYN observations of X–ray sources NW of the belt

Name	Sp Type	Ca I 6122/ 6495	Ca I 6162/ 6494	Ca I 6122/ 6162	Fe I 6103/ 6574	Hα 6563	Li I 6707	notes
R052329+0115	–	—	—	—	—	0.000	0.000	f
R052426+0108	–	—	—	—	—	0.000	0.000	f
R052435+0110	M1	2.185	3.055	0.715	-23.198	0.000	1.320	
R052505+0120	M1	1.449	0.000	—	—	0.000	0.519	f
R052510+0105	–	—	—	—	—	0.000	0.000	f
R052645+0104	–	—	—	—	—	0.000	0.000	f
GSC 101 518	G0	0.726	3.066	0.237	—	0.000	0.790	
GSC 101 537	K0	0.941	2.876	0.327	0.000	0.169	1.310	
GSC 101 843	G8	0.755	4.287	0.176	96.170	0.016	0.562	
GSC 101 1156	K0	0.784	2.787	0.281	4.430	0.130	0.938	
GSC 101 1544	F5	0.925	3.159	0.293	95.000	0.000	0.495	
GSC 101 1579	K7	1.950	4.521	0.431	-3.240	0.225	1.110	
GSC 101 2447	K7/M0	2.968	4.317	0.688	-4.238	0.000	0.216	f

Notes:
f – Faint spectra

Table 2.11: Spectroscopic data for X–ray sources NW of the Belt of Orion.

Results of WIYN observations of σ Orionis X–ray sources

Name	Sp Type	Ca I 6122/ 6495	Ca I 6162/ 6494	Ca I 6122/ 6162	Fe I 6103/ 6574	Hα 6563	Li I 6707	notes
R053752-0233	K7	3.605	6.879	1.908	—	-3.690	0.000	f
R053807-0235	–	—	—	—	—	0.000	0.000	f
R053820-0237	M0	—	—	—	—	-7.010	0.562	f
R053833-0236	K5	—	—	—	—	-24.460	2.160	f
R053844-0240c	K5	—	—	3.961	—	-7.340	1.660	f
R053849-0238	K5	0.878	0.860	0.980	—	-5.870	0.000	f
R053851-0236	K5	—	—	—	—	-86.290	0.000	f
R053851-0246	K7	0.595	0.598	1.006	—	-3.840	0.247	f
R053853-0243	–	3.069	2.332	0.760	—	-4.220	0.000	f
R053923-0233	K7	1.320	3.058	2.316	—	-5.070	1.180	f
R053932-0239	–	—	—	—	—	0.000	0.000	f
R053751-0235b	M0	1.421	0.228	0.161	—	-6.410	0.315	
R053807-0235a	K5	1.277	2.078	1.627	—	-15.220	0.219	
R053828-0235	K5	1.643	8.307	5.056	—	-5.800	0.350	
R053831-0235	K7	0.828	2.917	3.524	—	-5.710	4.030	
R053834-0234	K0	0.999	1.029	1.031	—	1.030	0.851	
R053835-0231	K5	0.343	0.244	0.711	—	-1.330	0.299	
R053838-0234	K5	0.503	0.923	1.836	—	-1.340	0.389	
R053838-0236	K5	0.660	1.186	1.798	—	-3.640	0.391	
R053840-0230a	M0	0.607	1.428	2.352	—	-2.080	0.409	
R053841-0237	K3	0.370	1.068	2.890	—	-7.760	0.316	
R053844-0240b	K3	1.142	0.424	0.371	—	2.640	0.000	
R053847-0237	K5	0.787	5.654	7.181	—	-9.560	0.263	
R053853-0239	M1	1.105	1.505	1.362	—	-0.274	0.028	
R053902-0229	K7	0.188	2.385	12.662	—	-5.320	0.177	B
GSC 4771 579	K2	0.000	0.935	—	—	1.750	0.0007	f
GSC 4771 751	K0	0.251	0.918	3.656	10.182	1.460	0.195	
GSC 4771 775	K0	0.220	0.805	3.657	—	-9.420	0.188	
GSC 4771 899	K3	0.322	1.761	5.470	1.522	-1.680	0.256	
GSC 4771 901	K5	0.857	1.536	1.792	—	-13.800	0.571	f
GSC 4771 910	K3	0.800	2.121	2.652	3.451	-11.850	0.472	
GSC 4771 921	K0	0.285	0.948	3.323	3.654	0.521	0.417	
GSC 4771 947	–	1.728	3.811	2.205	—	-31.380	0.689	
GSC 4771 950	K0	0.268	0.458	1.707	—	4.900	0.030	
GSC 4771 953	K5	3.757	7.992	2.127	3.372	-1.520	0.557	
GSC 4771 1038	K5	0.537	2.246	4.183	5.826	-2.520	0.492	
GSC 4771 1049	K5	0.692	1.708	2.469	1.511	-2.270	0.450	
GSC 4771 1051	K5	0.837	2.009	2.399	1.832	-5.540	0.429	
GSC 4771 1056	K1	0.315	0.987	3.132	2.524	0.520	0.107	
GSC 4771 1075	K5	0.444	1.410	3.175	2.113	-1.550	0.354	
GSC 4771 1092	K3	0.663	1.554	2.345	3.537	-9.070	0.533	
GSC 4771 1097	K5	0.672	1.595	2.374	1.691	-1.920	0.457	
GSC 4771 1147	K0	0.586	1.456	2.483	1.922	-1.440	0.311	B

Notes:
B – Double lines, binary.
f – Faint spectra

Table 2.12: Spectroscopic data for X–ray sources near σ Orionis.

2.5 Fits to Evolutionary Models

With knowledge of the spectral types and IR colors, T_{eff} could be calculated for a subset of the stars. Since B−V colors are not useful, one instead works from V−K as well as R−I (Carney 1983). For those stars with spectra, the intrinsic colors for a given spectral type are taken from Bessell (1979) and Bessell and Brett (1988). The Seaton (1979) extinction curve is used for reddening. Extinction is solved for by dereddening the stars, so that the dereddened colors match the observed spectral type. By varying the spectral class and spectral type (by one class and one subtype respectively), I calculate the extinction (A_v) for each color. The best fit A_v was then used to deredden the colors. Extinction was calculated for all of the colors. However, A_v determined from the R-I color was used preferentially in the dereddening procedure because it would be least affected by chromospheric activity. Dereddened colors could only be obtained for those stars with either IR data or spectra. The dereddened colors for those stars are given in Table 2.13.

To determine luminosity, one can simply integrate the dereddened SED and assume a blackbody law beyond the range of the photometric coverage. Alternatively, if one assumes the stars have normal photospheres, then the bolometric flux, in units of ergs/cm^2/s, is given by:

$$f_{bol} = 2.48 \times 10^5 \times 2.512^{-(m_V+BC)}. \tag{2.3}$$

In equation 2.3, m_V is the dereddened V magnitude and BC is the bolometric correction. The bolometric correction is taken from Lang (1994). The bolometric correction is dependent on spectral classification, the value of the

correction tabulated in Lang varies by up to 10% between luminosity classes III and V, with class V sources having lower values than class III sources. Walter et al. (1994) explicitly solved for the bolometric correction of luminosity class IV objects. These value are systematically lower than the Lang values for class V stars by 5 – 10%. The estimation of the bolometric correction based on tables from Lang for class V sources introduces an error of about 5%. The bolometric flux thus obtained was divided by the solar value (Allen 1973) at a distance of 380 pc to produce the luminosity given in the table.

Figure 2.5 shows the photometric data from all Orion OB1 stars for which extinctions were calculated in this manner overplotted with evolutionary tracks from D'Antona and Mazzitelli (1994). Many authors (e.g., D'Antona and Mazzitelli 1994, Swenson 1996, Vandenberg 1985) have recently published evolutionary models for low–mass PMS stars. These models generally attempt to reproduce the temperature and luminosity of a PMS star as a function of time. The D'Antona and Mazzitelli tracks employ mixing length theory and convection (following the prescription of Canuto and Mazzitelli 1990). High temperature opacities are taken from Rogers and Iglesias (1992) and low temperature opacities are from Alexander et al. (1989). In general, it is difficult to use such evolutionary models to obtain exact ages for PMS sources because of difficulty in setting the zero point. This difficulty mainly arises because it is unclear how stars form in the natal stages. Most authors assume that these stages move very quickly, so the exact starting point is unimportant. D'Antona and Mazzitelli (1994) begin their calculations when the core temperature in hydrostatic equilibrium reaches 6×10^5K. Some young stars sit at the birth-

line (Stahler 1983) for an extended period of time while still accreting material (e.g., the stars in Upper Scorpius; Walter et al. 1994). It is not appropriate to start the model evolving until after the star has started down the Hayashi track, at this point the evolution of the star is treated as a function of the mass of the star alone, and the disk is discounted. Other differences among the models, such as the treatment of convection and opacities can generate age differences of up to 40%.

The models can be used to measure relative parameters of the samples in the two sub–associations examined. The data given in Table 2.13 indicate that, in general, the redding of the stars near σ Orionis is small ($A_v < 2$). Based on this observation, and the data in Figures 2.1 and 2.2, the X–ray sources in Orion OB1a are about 0.5 dex older than the stars near σ Orionis. The stars

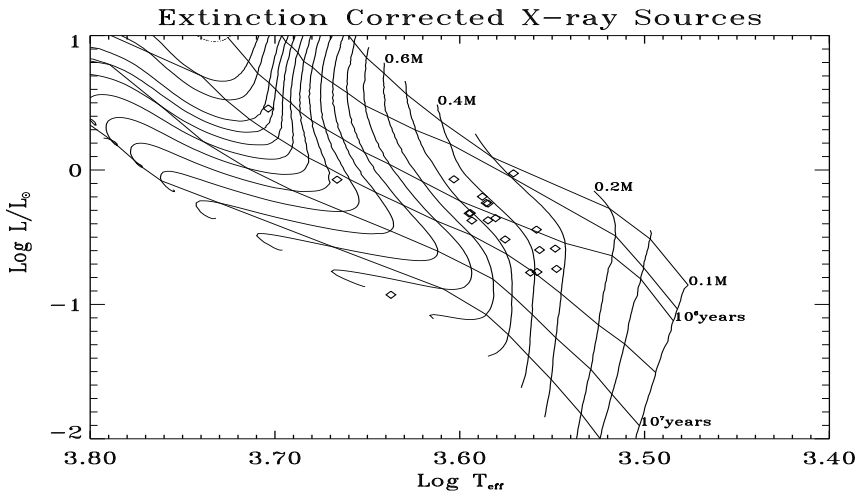

Figure 2.5: Luminosity–temperature diagram for all X–ray sources for which extinctions could be calculated based on optical plus either IR or spectral data. The evolutionary tracks used are described in the text.

near σ Orionis also have a much narrower age dispersion. In both cases, the X–ray sources are less than 1.5 $M_{\odot}$. Both samples show some sources which appear to be far younger than the rest of the sample. One explanation for these stars may be that they are part of binary systems. Binary systems of stars occupy higher positions on the H–R diagram than single stars since the magnitudes of the two components are combined (Simon et al. 1993).

Extinction corrections

Star	A_V	V	T_{eff}	BC	L_{bol}
R053751-0235	1.51	14.12	3534	1.93	0.260
R053808-0235	0.21	14.98	4337	0.84	0.117
R053829-0223	1.95	14.14	3604	1.78	0.254
R053831-0235	1.89	13.76	3618	1.76	0.360
R053838-0236	0.78	13.27	3852	1.34	0.568
R053840-0230	0.70	13.95	3762	1.49	0.304
R053841-0227	1.30	13.28	3843	1.36	0.563
R053852-0238	0.25	14.56	3645	1.70	0.172
R053922-0233	2.01	14.49	3528	1.95	0.183
4771 0775	0.05	11.51	5054	0.66	2.868
4771 0901	1.85	14.55	3615	1.76	0.174
4771 0910	1.19	13.15	3870	1.32	0.633
4771 0950	2.10	12.72	3723	1.56	0.944
4771 1038	0.96	13.55	3807	1.41	0.438
4771 1049	0.19	12.83	4010	1.13	0.853
4771 1051	0.47	13.46	3935	1.23	0.475
4771 1056	0.63	12.83	4638	0.70	0.847
4771 1075	0.82	13.59	3843	1.36	0.422
4771 1092	0.52	13.59	3921	1.25	0.421
4771 1097	0.49	13.46	3928	1.24	0.477

Table 2.13: Extinction corrected bolometric magnitudes for those stars with sufficient spectral or IR data.

2.6 Completeness

The X–ray selected PMS candidates may not constitute a complete list. The primary factor is the sensitivity limit, complicated by the vignetting in the field of the PSPC which was used to make the source list. The vignetting causes the sensitivity function to vary over the field, so one cannot quote a single sensitivity limit. In order to better understand the completeness of the X–ray data, photometry of every star in both regions was undertaken. The star identification was performed in the R–band frames using the DAOFIND task in the IRAF/APPHOT package. This task is fairly robust in rejecting objects with non–stellar point spread functions. The source positions thus identified were recentered on the individual frames using the CENTER task. Photometry and standardization were performed identically to the other stars in this study. The optical completeness, as determined by number counts, was V of 18.5 with some stars as faint as magnitude V=20 detected in at least three colors. More than 4000 stars were detected over a total of 2200 arcminutes^2 of sky observed. The results (with X–ray sources removed) are overlayed with the X–ray sources in Figures 2.6 and 2.7. The figures show that the data bifurcate into two distinct groups. There is a set of background stars below the main sequence (for an assumed distance of 400 pc). This set includes probable giant branch stars which can most clearly be seen in Figure 2.7 as a group of stars near V = 14 and R−I = 0.5 which lie in between the background and the PMS stars. The second set of stars are co–spatial with the X–ray sources. Since reddening is not known for the bulk of the stars in the group, the temperature

is measured simply by interpolating R−I using translations given by Bessell (1990). The V magnitude was converted to luminosity by using the same formulation as used in the previous section. Data on these additional PMS candidates are summarized in Tables 2.14 and 2.16.

In Figures 2.6 and 2.7, the X–ray quiet stars, in the PMS region of the color–magnitude diagram between magnitudes V=11 and V=16, are about 50% of the total number of sources. This result is not an artifact of vignetting in the X–ray observations. Observations were made using both the ROSAT HRI and the ROSAT PSPC. While both of the instruments have strong sensitivity variations across the field, regions generally obscured to one camera are not obscured in the other. There is no positional correlation with the locations of the X–ray sources and the HRI sensitivity function. The X–ray quiet sources are distributed evenly across the field (see Figure 2.8).

Non X-ray PMS stars near σ Orionis

Star	R.A. (J2000.)	Dec. (J2000.)	U−B	B−V	V	V−R	R−I
P053752-0233	5 37 52.1	-2 33 38.1	1.93 0.62	1.30 0.09	16.792 0.031	1.04 0.03	1.33 0.01
4771 0775	5 37 52.9	-2 33 34.3	0.27 0.01	0.78 0.01	11.565 0.001	0.46 0.01	0.42 0.01
P053754-0241	5 37 54.7	-2 41 08.2	0.94 0.77	0.64 0.28	18.750 0.163	1.62 0.17	1.72 0.04
P053758-0241	5 37 58.3	-2 41 25.7	— —	1.47 0.51	18.607 0.149	1.49 0.16	1.79 0.04
4771 0720	5 37 58.9	-2 41 00.3	0.44 0.01	0.77 0.01	11.601 0.000	0.44 0.01	0.37 0.01
4771 0961	5 38 02.0	-2 29 55.8	1.33 0.05	1.45 0.01	14.499 0.004	0.82 0.01	0.69 0.01
P053805-0240	5 38 05.5	-2 40 17.8	0.26 0.05	0.44 0.03	16.437 0.021	1.11 0.02	1.23 0.01
P053808-0235	5 38 08.2	-2 35 56.1	-0.01 0.10	1.46 0.05	16.187 0.017	1.10 0.02	1.32 0.01
4771 0706	5 38 10.5	-2 32 57.5	1.21 0.02	1.33 0.01	13.943 0.003	0.74 0.01	0.65 0.01
P053816-0238	5 38 16.0	-2 38 05.5	— —	0.52 0.16	18.300 0.109	1.49 0.12	1.60 0.03
P053817-0240	5 38 17.8	-2 40 48.7	— —	0.66 0.18	18.283 0.105	1.43 0.11	1.86 0.03
P053820-0238	5 38 20.1	-2 38 02.1	0.60 0.45	1.45 0.16	17.430 0.047	1.37 0.05	1.72 0.01
P053820-0234	5 38 20.5	-2 34 11.0	-2.14 0.37	1.07 0.32	18.542 0.131	1.29 0.14	1.83 0.04
P053822-0245	5 38 22.8	-2 45 30.9	— —	1.22 0.24	18.022 0.084	0.91 0.10	1.33 0.05
P053822-0236	5 38 22.8	-2 36 49.1	-0.22 0.66	1.45 0.38	18.331 0.112	1.09 0.12	1.56 0.04
P053823-0225	5 38 23.0	-2 25 34.3	-0.64 0.26	0.81 0.20	18.218 0.102	1.20 0.11	1.49 0.04
P053823-0244	5 38 23.1	-2 44 14.4	-0.54 0.58	1.70 0.37	17.996 0.091	1.19 0.10	1.57 0.03
P053823-0241	5 38 23.5	-2 41 29.6	-0.30 0.67	1.74 0.42	18.108 0.089	1.22 0.10	1.73 0.03
4771 1021	5 38 26.2	-2 34 29.3	0.21 0.01	0.81 0.01	13.103 0.002	0.50 0.01	0.50 0.01
4771 0041	5 38 27.1	-2 45 10.0	0.44 0.02	1.24 0.01	14.561 0.005	0.92 0.01	0.82 0.01
P053827-0235	5 38 27.4	-2 35 03.8	0.31 0.20	1.07 0.08	17.087 0.037	1.24 0.04	1.50 0.01
P053831-0236	5 38 31.3	-2 36 32.3	-1.09 0.03	0.72 0.03	16.303 0.018	1.21 0.02	1.29 0.01
P053833-0236	5 38 33.3	-2 36 17.0	0.83 0.16	1.58 0.04	15.866 0.013	1.13 0.01	1.26 0.01
4771 1095	5 38 33.5	-2 44 14.4	1.08 0.01	1.38 0.01	13.201 0.002	0.92 0.01	0.81 0.01
P053833-0241	5 38 33.7	-2 41 09.4	— —	1.46 0.28	17.871 0.081	1.73 0.08	1.43 0.02
P053834-0222	5 38 34.1	-2 22 56.5	0.66 0.01	1.27 0.01	13.802 0.003	0.78 0.01	0.76 0.01
P053834-0239	5 38 34.6	-2 39 29.1	— —	1.83 0.01	14.155 0.004	1.20 0.01	1.05 0.01
P053834-0239	5 38 34.7	-2 39 29.1	2.13 0.10	1.83 0.01	14.065 0.003	1.11 0.01	1.04 0.01
P053834-0232	5 38 34.7	-2 32 53.1	0.70 0.01	1.07 0.01	11.919 0.001	0.63 0.01	0.54 0.01
4771 1097	5 38 35.7	-2 30 43.3	0.97 0.02	1.25 0.01	14.080 0.003	0.79 0.01	0.81 0.01
4771 1026	5 38 35.7	-2 43 51.3	1.10 0.01	1.30 0.01	13.563 0.003	0.85 0.01	0.72 0.01
P053836-0244	5 38 36.5	-2 44 13.0	0.83 0.42	1.04 0.15	17.649 0.060	1.56 0.06	1.76 0.02
P053836-0236	5 38 36.7	-2 36 44.3	— —	0.70 0.23	18.427 0.123	1.67 0.13	1.80 0.03
P053838-0245	5 38 38.8	-2 45 32.9	0.77 0.38	1.31 0.14	17.263 0.043	1.34 0.04	1.33 0.01
4771 0740	5 38 39.4	-2 26 49.3	0.82 0.01	1.02 0.01	13.150 0.002	0.59 0.01	0.52 0.01
P053839-0240	5 38 39.6	-2 40 20.2	0.20 0.87	0.99 0.42	18.943 0.178	1.67 0.19	1.77 0.05
P053840-0233	5 38 40.4	-2 33 27.2	— —	1.25 0.17	17.638 0.061	1.45 0.06	1.63 0.02
P053840-0232	5 38 40.7	-2 32 58.3	0.19 0.47	1.53 0.22	17.645 0.064	1.44 0.07	1.67 0.02
P053841-0236	5 38 41.2	-2 36 39.3	-0.58 0.61	1.49 0.22	17.206 0.050	1.33 0.05	1.36 0.02
P053841-0230	5 38 41.4	-2 30 28.7	— —	1.63 0.14	17.022 0.037	1.16 0.04	1.44 0.01
P053842-0237	5 38 42.1	-2 37 18.4	0.62 0.10	1.37 0.02	15.080 0.007	1.01 0.01	1.00 0.01
P053842-0238	5 38 42.8	-2 38 51.9	— —	1.34 0.11	17.064 0.035	1.02 0.04	1.11 0.01
P053843-0232	5 38 43.3	-2 32 02.2	0.60 0.45	1.37 0.16	17.461 0.052	1.57 0.05	1.74 0.01
P053843-0237	5 38 43.7	-2 37 04.0	— —	0.97 0.21	17.928 0.081	1.33 0.09	1.78 0.03
P053844-0240	5 38 44.4	-2 40 30.5	— —	1.55 0.34	18.114 0.098	1.47 0.10	1.59 0.03
4771 1030	5 38 44.6	-2 33 59.2	0.81 0.01	1.24 0.01	12.458 0.001	0.70 0.01	0.67 0.01
P053845-0245	5 38 45.8	-2 45 27.9	-3.37 0.98	1.16 0.86	19.434 0.339	2.11 0.36	1.82 0.05
4771 1090	5 38 45.9	-2 43 47.7	1.10 0.05	1.36 0.01	14.740 0.006	0.88 0.01	0.74 0.01
P053847-0234	5 38 47.1	-2 34 50.0	-0.31 0.24	0.81 0.14	17.356 0.088	1.26 0.10	1.45 0.03
P053847-0247	5 38 47.4	-2 47 30.4	— —	0.12 0.13	18.239 0.105	-0.19 0.18	1.42 0.15
P053847-0230	5 38 47.5	-2 30 35.6	-1.49 0.80	1.41 0.64	18.933 0.196	1.50 0.21	1.99 0.05
P053847-0247	5 38 47.5	-2 47 27.0	— —	1.37 0.04	16.106 0.016	1.33 0.01	1.50 0.01
4771 0638	5 38 47.7	-2 24 55.0	0.35 0.01	0.66 0.01	13.433 0.002	0.41 0.01	0.42 0.01
4771 1057	5 38 48.4	-2 44 18.0	0.42 0.01	0.86 0.01	13.358 0.002	0.60 0.01	0.51 0.01
P053848-0235	5 38 48.5	-2 35 24.0	-1.58 0.17	0.97 0.18	14.799 0.135	0.84 0.16	0.97 0.08
P053848-0235	5 38 48.7	-2 35 09.0	-1.23 0.13	0.43 0.23	15.417 0.233	1.48 0.26	0.98 0.08
P053849-0241	5 38 49.0	-2 41 24.6	— —	0.12 0.13	18.239 0.105	-0.19 0.18	1.42 0.15

Table 2.14: Coordinates and colors of candidate non–X–ray PMS stars near σ Orionis.

Non X-ray PMS stars near σ Orionis... (cont.)

Star	R.A. (J2000.)	Dec. (J2000.)	U−B	B−V	V	V−R	R−I
P053849-0241	5 38 49.1	-2 41 24.9	— —	1.37 0.04	16.106 0.016	1.33 0.01	1.50 0.01
P053849-0241	5 38 49.1	-2 41 26.6	0.90 0.14	1.44 0.04	15.982 0.013	1.24 0.01	1.49 0.01
P053849-0245	5 38 49.6	-2 45 28.0	— —	1.61 0.08	16.482 0.022	1.10 0.02	1.23 0.01
P053849-0241	5 38 49.8	-2 41 23.3	— —	1.56 0.12	16.973 0.035	1.39 0.03	1.37 0.01
P053850-0237	5 38 50.0	-2 37 35.5	1.14 0.62	0.50 0.17	18.172 0.107	1.65 0.11	1.69 0.03
P053850-0226	5 38 50.2	-2 26 49.6	1.53 0.44	1.37 0.08	16.792 0.028	1.21 0.03	1.47 0.01
P053850-0236	5 38 50.3	-2 36 37.7	— —	1.46 0.15	15.448 0.103	1.20 0.12	0.87 0.05
P053854-0240	5 38 54.2	-2 40 03.4	— —	0.92 0.36	18.730 0.173	1.10 0.19	1.58 0.07
P053854-0228	5 38 54.8	-2 28 57.2	1.35 4.70	1.71 0.87	18.996 0.209	1.80 0.22	1.70 0.04
P053855-0241	5 38 55.2	-2 41 28.4	1.33 0.24	1.49 0.04	16.113 0.015	1.16 0.01	1.40 0.01
P053855-0241	5 38 55.2	-2 41 28.4	— —	1.38 0.05	16.280 0.018	1.31 0.02	1.38 0.01
4771 1071	5 38 56.8	-2 31 25.9	0.24 0.01	0.72 0.01	12.921 0.002	0.42 0.01	0.40 0.01
P053859-0233	5 38 59.1	-2 33 51.3	-0.39 0.06	0.78 0.04	16.532 0.023	0.81 0.02	1.13 0.01
P053859-0233	5 38 59.1	-2 33 51.3	-0.45 0.05	0.72 0.03	16.451 0.021	0.73 0.02	1.13 0.01
P053901-0236	5 39 01.0	-2 36 39.6	—- —-	-0.84 0.80	20.477 0.837	-0.31 1.47	1.84 1.12
P053902-0238	5 39 02.3	-2 38 35.6	0.89 0.14	1.75 0.03	15.151 0.008	-0.21 0.01	1.67 0.01
P053902-0229	5 39 02.5	-2 29 54.9	1.61 0.62	1.39 0.11	17.001 0.036	1.25 0.04	1.55 0.01
P053902-0222	5 39 02.7	-2 22 40.7	— —	— —	17.899 0.086	0.35 0.11	1.37 0.07
P053902-0241	5 39 02.8	-2 41 28.6	-0.12 0.08	1.10 0.05	16.407 0.020	1.14 0.02	1.38 0.01
P053902-0241	5 39 02.8	-2 41 28.6	-0.24 0.09	1.18 0.05	16.412 0.025	1.18 0.02	1.30 0.01
P053903-0246	5 39 03.3	-2 46 26.0	-0.01 0.13	0.96 0.07	16.957 0.032	1.19 0.03	1.41 0.01
P053904-0226	5 39 04.9	-2 26 21.1	0.07 0.59	1.23 0.32	18.323 0.115	0.96 0.13	1.54 0.06
P053905-0232	5 39 05.0	-2 32 59.1	— —	— —	18.034 0.099	1.40 0.09	1.61 0.03
4771 1075	5 39 05.2	-2 32 30.4	1.09 0.03	1.39 0.01	14.376 0.004	0.88 0.01	0.84 0.01
P053905-0226	5 39 05.6	-2 26 15.9	0.07 0.59	1.23 0.32	18.323 0.115	0.96 0.13	1.54 0.06
P053907-0228	5 39 07.4	-2 28 21.9	-0.04 0.20	1.55 0.11	16.886 0.031	1.05 0.03	1.45 0.01
4771 1092	5 39 07.4	-2 32 39.3	0.79 0.02	1.28 0.01	14.296 0.004	0.86 0.01	0.82 0.01
P053907-0228	5 39 07.9	-2 28 42.1	0.39 0.49	0.76 0.23	18.411 0.125	0.85 0.15	1.69 0.06
P053908-0232	5 39 08.0	-2 32 27.6	— —	0.73 0.33	18.833 0.186	1.27 0.20	1.80 0.06
4771 0135	5 39 08.1	-2 49 46.2	1.15 0.01	1.26 0.01	13.402 0.002	0.79 0.01	0.66 0.01
4771 0645	5 39 09.7	-2 25 47.5	0.95 0.01	1.06 0.01	13.222 0.002	0.61 0.01	0.50 0.01
4771 0668	5 39 11.1	-2 25 49.2	0.35 0.01	0.91 0.01	12.901 0.002	0.57 0.01	0.57 0.01
P053911-0227	5 39 11.6	-2 27 39.5	-0.24 0.75	1.85 0.45	18.030 0.084	1.26 0.09	1.60 0.03
P053912-0229	5 39 12.9	-2 29 56.9	-0.43 0.58	1.58 0.37	18.118 0.097	1.57 0.10	1.85 0.02
4771 0955	5 39 25.1	-2 38 22.1	0.09 0.01	1.22 0.01	14.487 0.004	0.94 0.01	0.91 0.01
P053925-0231	5 39 25.1	-2 31 44.2	1.51 0.18	1.71 0.03	15.426 0.009	0.87 0.01	0.81 0.01
4771 0767	5 39 26.6	-2 33 37.6	0.10 0.01	0.67 0.01	12.728 0.001	0.39 0.01	0.37 0.01
4771 0579	5 39 30.3	-2 35 07.5	0.75 0.02	1.28 0.01	14.227 0.004	0.78 0.01	0.74 0.01
P053933-0236	5 39 33.2	-2 36 41.8	0.45 0.01	1.02 0.01	14.018 0.003	0.65 0.01	0.64 0.01
P053938-0233	5 39 38.1	-2 33 06.0	0.24 0.01	0.85 0.01	13.438 0.002	0.55 0.01	0.54 0.01
P053939-0231	5 39 39.6	-2 31 20.6	-0.84 0.01	0.89 0.01	14.531 0.005	0.88 0.01	0.76 0.01

Table 2.15: Coordinates and colors of candidate non–X–ray PMS stars near σ Orionis ....continued

Photometry of other candidate PMS stars NW of the Belt

Star	R.A. (J2000.)	Dec. (J2000.)	U−B	B−V	V	V−R	R−I
P052312+0110	5 23 12.04	1 10 47.5	— —	— —	19.424 0.388	-1.14 1.14	1.90 0.98
P052313+0110	5 23 13.26	1 10 50.3	-0.11 0.40	0.21 0.22	18.400 0.141	1.31 0.15	1.27 0.04
P052315+0106	5 23 15.59	1 06 25.7	— —	1.70 0.58	18.060 0.100	0.98 0.11	1.61 0.04
P052316+0049	5 23 16.16	0 49 45.6	— —	0.94 0.23	17.498 0.075	-2.64 0.78	1.37 0.76
P052317+0106	5 23 17.50	1 06 28.5	0.47 0.82	1.36 0.27	17.454 0.059	1.12 0.06	1.25 0.02
0101 0518	5 23 21.67	1 07 51.0	0.15 0.01	0.67 0.01	11.877 0.000	0.38 0.01	0.36 0.00
P052324+0059	5 23 24.90	0 59 33.0	1.23 0.20	1.40 0.03	15.211 0.008	0.90 0.01	0.87 0.00
P052329+0116	5 23 29.45	1 16 12.9	— —	1.53 0.11	16.242 0.022	1.11 0.02	1.35 0.01
P052334+0051	5 23 34.59	0 51 22.9	— —	— —	17.640 0.090	1.28 0.09	1.67 0.02
0101 1252	5 23 35.31	1 01 16.5	0.41 0.01	0.93 0.01	12.356 0.001	0.51 0.01	0.50 0.00
0101 1252	5 23 35.31	1 01 16.5	— —	0.91 0.01	12.403 0.001	0.54 0.01	0.50 0.00
P052336+0054	5 23 36.00	0 54 36.8	— —	1.19 0.15	16.627 0.041	0.71 0.04	1.86 0.02
P052337+0112	5 23 37.67	1 12 34.3	-0.29 0.68	1.28 0.34	17.679 0.081	0.80 0.09	1.38 0.04
P052341+0114	5 23 41.16	1 14 33.5	0.55 0.43	1.15 0.13	16.721 0.033	0.93 0.03	1.09 0.01
P052341+0111	5 23 41.75	1 11 53.7	1.01 0.20	1.36 0.04	15.473 0.010	0.89 0.01	0.83 0.00
P052341+0112	5 23 41.78	1 12 00.0	0.08 0.01	0.59 0.01	13.327 0.002	0.33 0.01	0.34 0.00
P052342+0051	5 23 42.45	0 51 06.0	— —	0.24 0.28	19.050 0.176	0.74 0.21	1.33 0.09
P052342+0104	5 23 42.49	1 04 06.6	-0.21 0.46	0.68 0.27	18.692 0.119	0.92 0.13	1.35 0.05
0101 1151	5 23 42.50	0 49 17.0	— —	1.28 0.02	14.357 0.005	0.71 0.01	0.63 0.00
P052342+0102	5 23 42.50	1 02 21.8	— —	1.87 0.86	18.822 0.135	1.27 0.15	1.45 0.04
P052342+0102	5 23 42.50	1 02 21.8	0.50 1.02	1.00 0.35	18.114 0.106	0.52 0.13	1.45 0.06
0101 1242	5 23 42.90	0 52 44.7	4.67 0.81	1.27 0.01	12.953 0.002	0.83 0.01	0.73 0.00
P052344+0111	5 23 44.97	1 11 32.5	— —	1.41 0.05	15.486 0.012	0.86 0.01	0.85 0.00
0101 0497	5 23 45.26	1 07 20.9	0.94 0.05	1.29 0.01	14.170 0.003	0.67 0.01	0.61 0.00
0101 1191	5 23 46.02	0 52 27.3	3.14 0.26	1.02 0.01	13.593 0.003	0.57 0.01	0.52 0.00
P052347+0104	5 23 47.25	1 04 02.0	0.53 0.89	1.59 0.28	17.309 0.053	1.29 0.05	1.61 0.01
P052349+0050	5 23 49.71	0 50 10.5	— —	1.30 0.32	17.417 0.068	1.29 0.07	1.64 0.02
P052350+0100	5 23 50.39	1 00 51.7	-0.34 0.70	2.14 0.40	17.044 0.041	1.05 0.04	1.36 0.01
P052350+0100	5 23 50.39	1 00 51.7	-0.75 0.45	1.57 0.28	17.080 0.051	1.07 0.05	1.36 0.02
P052352+0101	5 23 52.62	1 01 52.6	— —	0.47 1.16	19.957 0.564	0.25 0.77	1.65 0.47
P052353+0105	5 23 53.92	1 05 55.7	-0.85 0.84	0.91 0.62	19.401 0.238	1.21 0.26	1.53 0.08
P052354+0055	5 23 54.57	0 55 21.6	1.38 0.55	1.32 0.07	15.830 0.016	0.97 0.01	1.02 0.00
P052355+0104	5 23 55.26	1 04 22.7	— —	0.43 0.19	17.910 0.098	0.48 0.12	1.51 0.06
P052355+0108	5 23 55.32	1 08 45.9	— —	— —	18.647 0.126	1.18 0.14	1.33 0.05
0101 1235	5 23 55.60	1 01 31.0	— —	0.61 0.01	11.779 0.001	0.38 0.01	0.35 0.00
0101 1235	5 23 55.60	1 01 31.5	0.10 0.01	0.62 0.01	11.723 0.000	0.35 0.01	0.35 0.00
P052355+0049	5 23 55.87	0 49 04.8	— —	0.98 0.77	18.738 0.234	-1.72 1.13	1.57 1.06
P052356+0053	5 23 56.39	0 53 50.3	— —	— —	19.509 0.226	-2.78 3.19	1.69 2.98
P052356+0109	5 23 56.66	1 09 57.6	-0.87 0.59	1.12 0.42	18.195 0.129	0.72 0.15	1.21 0.07
0101 0429	5 23 57.13	1 06 07.4	0.23 0.01	0.73 0.01	13.111 0.001	0.41 0.01	0.40 0.00
0101 0429	5 23 57.15	1 06 07.9	0.26 0.01	0.74 0.01	13.109 0.002	0.40 0.01	0.37 0.00
P052359+0102	5 23 59.95	1 02 35.7	-0.30 0.75	1.44 0.41	18.487 0.100	1.38 0.11	1.35 0.03
0101 0666	5 24 01.20	1 10 32.5	— —	1.16 0.01	14.331 0.004	0.64 0.01	0.60 0.00
P052404+0114	5 24 04.27	1 14 06.0	— —	0.43 0.19	17.910 0.098	0.48 0.12	1.51 0.06
P052404+0116	5 24 04.95	1 16 15.7	— —	1.17 0.09	16.430 0.027	1.01 0.03	1.15 0.01
P052405+0058	5 24 05.17	0 58 05.9	— —	— —	20.124 0.433	1.53 0.47	1.36 0.12
P052406+0057	5 24 06.48	0 57 42.6	— —	— —	18.597 0.104	-2.99 1.62	1.32 1.60
P052406+0108	5 24 06.89	1 08 55.5	0.64 0.29	1.53 0.08	16.621 0.018	1.00 0.02	1.22 0.01
P052406+0108	5 24 06.89	1 08 55.5	0.82 0.72	1.46 0.16	16.671 0.034	1.09 0.03	1.21 0.01
P052407+0129	5 24 07.02	1 29 20.7	— —	— —	18.023 0.107	1.20 0.11	1.43 0.03
P052407+0129	5 24 07.02	1 29 20.7	0.78 0.29	1.44 0.06	15.770 0.014	0.95 0.01	0.97 0.00
P052407+0104	5 24 07.30	1 04 52.6	— —	— —	18.048 0.068	1.13 0.07	1.41 0.02
P052407+0117	5 24 07.47	1 17 57.8	— —	0.76 0.84	19.230 0.334	-0.98 0.88	1.38 0.78
0101 0410	5 24 07.64	1 23 48.7	4.74 0.90	1.16 0.01	13.552 0.002	0.70 0.01	0.60 0.00
P052407+0055	5 24 07.73	0 55 10.9	— —	0.26 0.20	18.758 0.130	1.10 0.14	1.33 0.05
0101 1205	5 24 07.91	1 01 52.1	1.13 0.01	1.28 0.01	12.361 0.000	0.68 0.01	0.62 0.00
0101 0717	5 24 10.31	1 27 13.4	0.64 0.01	1.02 0.01	12.795 0.001	0.55 0.01	0.52 0.00
P052411+0118	5 24 11.66	1 18 30.4	-0.56 0.64	1.34 0.38	17.772 0.095	0.93 0.11	1.30 0.04
P052413+0102	5 24 13.60	1 02 05.9	-1.02 0.43	0.53 0.35	19.137 0.165	0.09 0.26	1.58 0.18
P052414+0054	5 24 14.97	0 54 54.8	0.15 1.15	0.83 0.52	19.281 0.198	1.19 0.22	1.43 0.07
0101 0539	5 24 15.75	1 22 33.5	— —	1.13 0.01	14.356 0.004	0.70 0.01	0.58 0.00
0101 1184	5 24 16.76	0 52 24.9	0.48 0.01	0.91 0.01	13.161 0.001	0.50 0.01	0.47 0.00
0101 0652	5 24 16.77	1 26 51.6	— —	1.01 0.01	14.030 0.003	0.57 0.01	0.52 0.00
0101 0423	5 24 17.87	1 06 03.2	0.67 0.01	1.03 0.01	14.074 0.002	0.54 0.01	0.54 0.00
P052418+0121	5 24 18.30	1 21 46.3	— —	— —	18.622 0.172	-1.41 0.64	1.75 0.57
P052418+0124	5 24 18.58	1 24 36.5	0.05 0.01	0.54 0.01	11.776 0.000	— —	0.53 0.09
P052420+0110	5 24 20.31	1 10 52.8	0.73 0.02	1.08 0.01	14.177 0.003	0.58 0.01	0.55 0.00
0101 0556	5 24 20.43	1 22 23.5	0.35 0.01	0.84 0.01	11.094 0.000	0.46 0.01	0.44 0.00
P052420+0124	5 24 20.81	1 24 05.9	1.27 0.31	1.26 0.04	15.596 0.012	0.97 0.01	0.97 0.00
P052422+0101	5 24 22.01	1 01 41.0	— —	0.80 0.83	19.859 0.360	0.85 0.42	1.37 0.18
P052422+0100	5 24 22.17	1 00 22.8	0.14 0.12	1.33 0.05	16.290 0.014	1.19 0.01	1.37 0.00
0101 0534	5 24 22.30	1 26 03.8	0.20 0.01	0.69 0.01	11.021 0.000	0.38 0.01	0.36 0.00
P052424+0102	5 24 24.57	1 02 42.9	— —	2.14 0.59	18.154 0.074	1.19 0.08	1.16 0.02

Table 2.16: Coordinates and colors of candidate non–X–ray PMS stars NW of the Belt.

Other candidate PMS stars NW of the Belt...(cont.)

Star	R.A. (J2000.)	Dec. (J2000.)	U−B	B−V	V	V−R	R−I
0101 0596	5 24 25.89	1 09 22.2	0.84 0.00	1.04 0.00	12.791 0.001	0.59 0.00	0.51 0.00
P052426+0128	5 24 26.77	1 28 45.3	— —	1.72 0.28	17.044 0.045	1.14 0.05	1.32 0.02
0101 1166	5 24 27.08	1 02 10.4	— —	— —	18.411 0.107	1.21 0.10	1.28 0.04
P052427+0103	5 24 27.91	1 03 20.4	— —	0.83 0.44	19.203 0.185	1.28 0.20	1.40 0.06
P052429+0058	5 24 29.19	0 58 14.1	0.85 0.98	0.96 0.26	18.386 0.092	1.29 0.10	1.24 0.03
P052429+0100	5 24 29.94	1 00 27.0	— —	— —	19.630 0.292	1.08 0.33	1.52 0.12
P052431+0101	5 24 31.21	1 01 22.1	0.99 0.13	1.41 0.03	15.661 0.008	0.88 0.00	0.84 0.00
P052432+0123	5 24 32.88	1 23 50.2	-1.55 1.15	2.16 0.93	17.962 0.098	-2.58 0.95	1.86 0.88
P052433+0129	5 24 33.89	1 29 37.1	— —	— —	17.830 0.104	1.23 0.10	1.51 0.03
0101 0296	5 24 36.05	1 39 41.5	0.29 0.01	0.81 0.00	13.301 0.002	0.41 0.00	0.38 0.00
P052437+0133	5 24 37.33	1 33 44.6	-0.33 0.58	0.24 0.33	18.342 0.196	0.66 0.23	1.68 0.10
P052437+0129	5 24 37.98	1 29 51.0	— —	— —	17.954 0.101	1.07 0.11	1.21 0.04
0101 0746	5 24 39.05	1 32 58.2	0.53 0.00	1.02 0.00	12.255 0.001	0.52 0.00	0.49 0.00
0101 0638	5 24 40.28	1 10 07.2	0.42 0.00	0.85 0.00	13.551 0.002	0.48 0.00	0.47 0.00
P052440+0110	5 24 40.99	1 10 55.5	-1.18 0.86	1.63 0.68	18.696 0.120	1.23 0.13	1.76 0.04
0101 0889	5 24 41.05	1 31 00.4	0.49 0.03	1.03 0.01	13.914 0.004	0.55 0.00	0.50 0.00
P052441+0132	5 24 41.12	1 32 15.6	— —	0.07 0.43	18.741 0.272	1.76 0.29	1.53 0.05
P052441+0134	5 24 41.19	1 34 31.3	— —	0.23 0.29	18.242 0.176	0.56 0.21	1.31 0.10
P052449+0129	5 24 49.68	1 29 39.4	— —	0.77 0.25	17.907 0.095	0.98 0.11	1.57 0.04
P052449+0129	5 24 49.68	1 29 39.4	— —	0.61 0.33	17.961 0.137	1.03 0.15	1.64 0.05
P052450+0125	5 24 50.75	1 25 16.1	— —	1.42 0.39	17.709 0.080	1.32 0.08	1.48 0.02
0101 0320	5 24 52.26	1 38 43.5	0.75 0.04	1.21 0.01	13.686 0.003	0.73 0.00	0.66 0.00
0101 0381	5 24 53.81	1 24 09.4	0.77 0.03	1.09 0.00	13.777 0.003	0.67 0.00	0.64 0.00
P052454+0134	5 24 54.09	1 34 02.3	0.72 —	— —	17.770 0.117	1.32 0.12	1.41 0.03
P052454+0140	5 24 54.20	1 40 03.2	— —	1.79 0.17	16.104 0.024	0.99 0.02	1.08 0.01
0101 0780	5 24 54.72	1 20 14.7	0.03 0.00	0.58 0.00	13.135 0.002	0.34 0.00	0.34 0.00
0101 0300	5 24 55.02	1 39 23.0	0.00 0.00	0.66 0.00	11.257 0.000	0.36 0.00	0.36 0.00
P052455+0127	5 24 55.02	1 27 02.4	-1.19 0.72	1.55 0.53	17.961 0.101	1.32 0.11	1.36 0.03
P052455+0141	5 24 55.14	1 41 46.0	— —	1.45 0.51	17.582 0.093	1.11 0.10	1.58 0.03
P052457+0141	5 24 57.69	1 41 42.7	— —	— —	17.952 0.134	1.43 0.14	1.59 0.04
P052458+0125	5 24 58.80	1 25 18.6	— —	1.08 0.89	19.016 0.268	1.25 0.29	1.79 0.08
P052500+0139	5 25 00.99	1 39 43.8	— —	— —	18.252 0.192	1.46 0.19	1.58 0.04
P052501+0140	5 25 01.28	1 40 52.2	— —	— —	18.179 0.161	0.77 0.18	1.19 0.08
P052501+0134	5 25 01.87	1 34 56.7	0.79 1.36	1.43 0.31	17.097 0.062	1.19 0.06	1.44 0.02
P052501+0137	5 25 01.97	1 37 21.3	0.06 0.36	1.63 0.14	16.082 0.023	0.97 0.02	1.30 0.01
0101 2527	5 25 02.27	1 31 49.9	— —	-0.26 0.83	19.619 0.674	1.54 0.73	1.72 0.15
0101 0932	5 25 03.63	1 30 14.1	0.35 0.01	0.94 0.00	12.775 0.002	0.53 0.00	0.48 0.00
0101 0514	5 25 03.72	1 22 50.7	0.14 0.01	0.67 0.00	13.554 0.004	0.37 0.00	0.39 0.00
P052505+0136	5 25 05.01	1 36 54.0	-0.43 0.60	1.69 0.33	16.959 0.055	1.27 0.06	1.46 0.01
0101 0431	5 25 05.36	1 36 38.6	0.13 0.01	0.81 0.00	13.637 0.003	0.43 0.00	0.42 0.00
P052507+0134	5 25 07.47	1 34 24.8	-1.30 0.43	2.13 0.33	16.390 0.031	1.19 0.03	1.39 0.01
0101 0876	5 25 07.89	1 31 15.6	0.61 0.02	1.10 0.00	12.985 0.002	0.57 0.00	0.52 0.00
P052511+0129	5 25 11.29	1 29 25.9	— —	0.64 0.99	19.131 0.396	0.73 0.47	1.94 0.20
0101 0716	5 25 11.57	1 20 53.0	0.68 0.00	1.00 0.00	11.843 0.001	0.54 0.00	0.51 0.00
0101 0977	5 25 11.79	1 29 08.8	0.68 0.01	1.08 0.00	12.608 0.002	0.56 0.00	0.49 0.00
0101 0977	5 25 11.79	1 29 08.8	0.78 0.01	1.07 0.00	12.628 0.002	0.57 0.00	0.52 0.00
P052513+0136	5 25 13.32	1 36 15.9	— —	0.73 0.69	18.720 0.266	1.59 0.28	1.56 0.06
P052514+0138	5 25 14.30	1 38 39.0	— —	0.03 0.46	18.828 0.308	-0.73 0.64	1.32 0.55
P052514+0122	5 25 14.95	1 22 44.9	— —	0.14 0.37	18.431 0.242	1.95 0.26	1.46 0.04
0101 0600	5 25 16.48	1 21 56.7	0.01 0.00	0.52 0.00	13.131 0.003	0.32 0.00	0.34 0.00
0101 0712	5 25 16.50	1 27 13.5	— —	0.88 0.22	17.240 0.081	1.24 0.09	1.46 0.03
P052516+0116	5 25 16.66	1 16 16.1	-0.60 0.51	2.22 0.39	16.452 0.040	1.13 0.04	1.39 0.01
P052517+0128	5 25 17.54	1 28 30.0	— —	— —	19.007 0.350	1.59 0.37	1.42 0.08
0101 0433	5 25 20.34	1 23 37.1	0.47 0.00	0.92 0.00	12.718 0.002	0.52 0.00	0.51 0.00
0101 2518	5 25 20.63	1 23 35.5	0.19 0.01	0.67 0.00	13.369 0.004	0.39 0.00	0.39 0.00
0101 0685	5 25 21.04	1 33 41.0	-0.01 0.01	0.67 0.00	13.401 0.003	0.37 0.00	0.35 0.00
P052525+0129	5 25 25.70	1 29 50.7	-0.50 0.67	1.35 0.37	17.403 0.082	1.26 0.09	1.54 0.02
P052527+0141	5 25 27.62	1 41 47.2	— —	— —	17.544 0.094	1.13 0.10	1.44 0.03
0101 0369	5 25 28.07	1 37 17.8	0.90 0.07	1.27 0.01	14.020 0.004	0.76 0.00	0.69 0.00
0101 0873	5 25 29.15	1 28 30.2	— —	1.10 0.01	13.796 0.004	0.58 0.00	0.55 0.00
0101 0873	5 25 29.15	1 28 30.2	0.70 0.02	1.06 0.01	13.786 0.005	0.59 0.00	0.54 0.00
0101 0443	5 25 30.18	1 23 22.4	0.12 0.00	0.66 0.00	11.525 0.001	0.36 0.00	0.36 0.00
0101 0579	5 25 30.96	1 26 30.3	0.69 0.00	1.04 0.00	11.142 0.001	0.55 0.00	0.51 0.00
P052533+0122	5 25 33.87	1 22 31.0	-0.30 0.12	0.99 0.09	16.129 0.029	0.23 0.03	1.43 0.02
P052535+0128	5 25 35.58	1 28 23.2	2.10 0.42	1.26 0.05	15.357 0.016	0.94 0.01	0.86 0.01
P052537+0127	5 25 37.64	1 27 18.8	— —	1.30 0.81	18.194 0.195	1.20 0.21	1.42 0.07
P052541+0126	5 25 41.41	1 26 44.9	— —	1.68 0.52	17.282 0.088	1.26 0.09	1.28 0.03
P052541+0123	5 25 41.80	1 23 48.2	0.93 0.26	1.18 0.09	16.058 0.029	0.95 0.03	1.13 0.01
0101 0697	5 25 46.47	1 21 04.7	0.06 0.00	0.62 0.00	11.201 0.001	0.35 0.00	0.34 0.00
0101 0718	5 25 50.30	1 27 19.2	0.86 0.00	1.03 0.00	11.522 0.001	0.56 0.00	0.48 0.00

Table 2.17: Coordinates and colors of candidate non–X–ray PMS stars NW of the Belt. (continued)

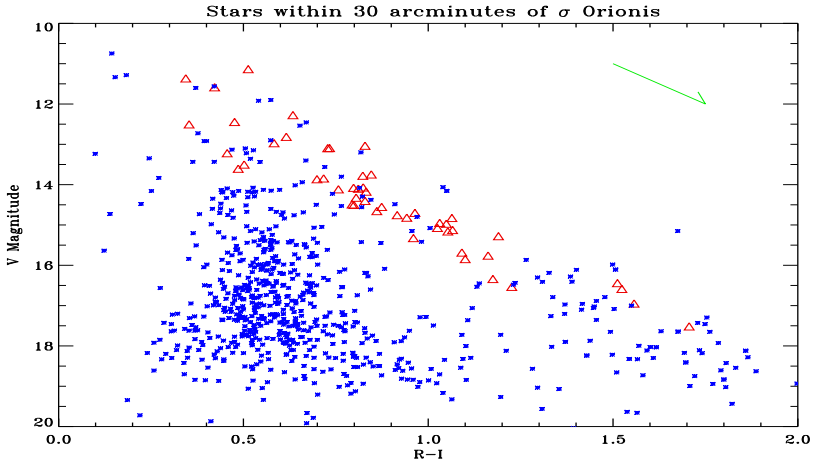

Figure 2.6: A color–magnitude diagram for all stars in 900 square arcminutes nearest to σ Orionis. Triangles indicate X–ray sources. The smaller dots indicate background sources. A one magnitude reddening vector is shown.

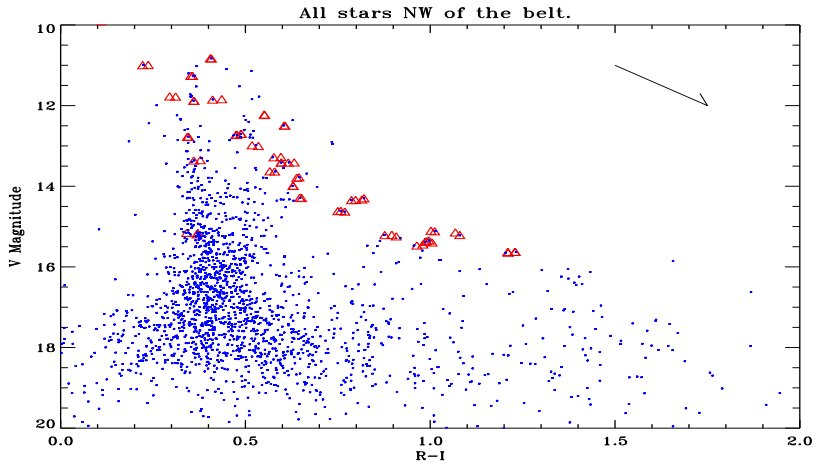

Figure 2.7: A color–magnitude diagram for all stars in 1350 square arcminutes which were observed during observations of X–ray sources northwest of the belt of Orion. Triangles indicate X–ray sources, two observations of each X–ray source are displayed in the figure. All other symbols are the same as the previous figure.

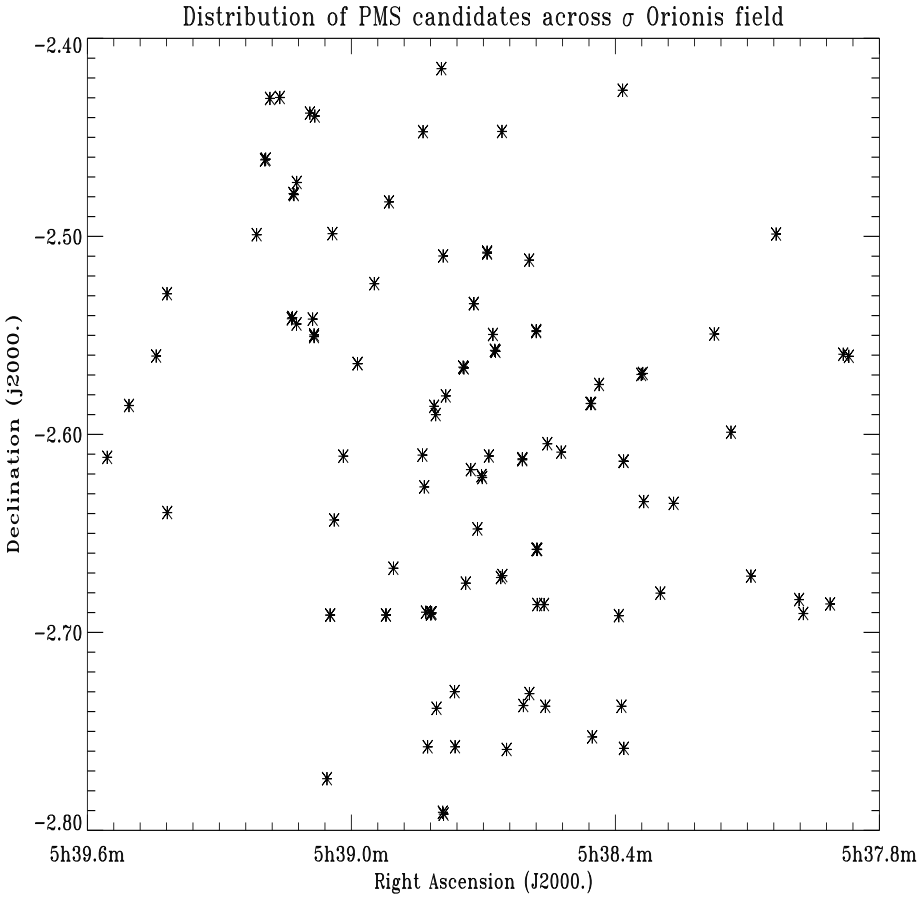

Figure 2.8: The locations of non–X–ray PMS candidates near σ Orionis. The sources cover the field uniformly. There are no sources in the corners of the region displayed since no data were taken in these regions.

2.6.1 X–ray Quiet PMS Candidates

There are several explanations for these X–ray quiet PMS stars. To examine the explanations, it is proper to divide the PMS stars into three groups: those bluer than R−I = 0.7, those redder than the X–ray sources (R−I > 1.25) and those with colors similar to the X–ray sources. For the first group, contamination by background stars is a problem. The peak in the distribution of background stars appears at R−I of 0.5. At this color, it is possible that dozens background stars are occupying the same region of the H-R diagram as PMS stars. However, since this group is also the brightest, we were able to obtain spectra for many of these objects.

A total of 26 of the non–X–ray detected PMS candidates had spectra taken. They were part of the control sample of non–X–ray emitting stars which was drawn drawn for the Guide Star Catalog (Lasker et al. 1990). The results are given in in Table 2.18. Strong (EW > 0.200 Å) Li I absorption features were found in absorption in 19 of them. Of the 19 confirmed PMS stars, nine were near σ Orionis. Two of these had strong Hα emission lines associated with cTTs. A preliminary result is that 73% ± 15% of the PMS candidates identified solely through their optical colors, are indeed PMS.

As stars get redder, there is a clear gap between the background sources and the PMS candidates. The bifurcation between the background group and the X–rays sources is almost a magnitude for stars redder the R−I = 0.7 and increases in the redward direction. These stars were too dim to be observed with the spectroscopic survey. To estimate contamination for the stars near

Results of WIYN observations of X–ray quiet GSC stars

Name	Sp Type	Ca I 6122/ 6495	Ca I 6162/ 6494	Ca I 6122/ 6162	Fe I 6103/ 6574	Fe I 6200/ 6574	Hα 6563	Li I 6707
101 410	K5	2.006	4.308	0.466	—	—	0.211	1.440
101 443	K0	0.563	2.534	0.222	178.095	0.000	0.000	0.584
101 518	K0	0.709	3.112	0.228	—	—	0.077	0.750
101 638	G8	1.149	3.490	0.329	—	—	0.062	1.060
101 666	K2	0.411	2.740	0.150	—	—	0.158	1.050
101 697	K0	0.768	3.000	0.256	113.704	0.000	0.017	0.584
101 780	–	—	—	—	—	—	0.000	0.000
101 977	K1	0.772	3.713	0.208	—	—	0.139	0.888
101 1151	G8	1.379	3.757	0.367	—	—	0.000	1.180
101 1166	K3	0.970	3.188	0.304	61.786	0.000	0.000	0.152
101 2518	K0	0.698	2.842	0.246	103.235	0.000	0.028	0.589
101 2527	G8	0.732	2.204	0.332	225.385	0.000	0.074	0.618
4771 41	K5	0.634	2.240	0.283	—	—	-45.60	0.387
4771 135	K5	0.639	1.634	0.391	—	—	0.662	0.000
4771 579	–	0.000	0.000	—	—	—	1.890	0.000
4771 638	F5	0.109	0.473	0.231	—	—	6.750	0.060
4771 720	G1	0.135	0.991	0.136	—	—	3.290	0.000
4771 740	K2	0.705	1.950	0.361	—	—	0.809	0.000
4771 767	G8	0.285	0.847	0.337	—	—	4.240	0.000
4771 775	K1	0.319	1.300	0.245	—	—	-1.090	0.208
4771 1026	K3	0.407	1.132	0.360	—	—	-1.280	0.333
4771 1071	G8	0.195	0.926	0.210	—	—	4.230	0.054
4771 1075	K5	0.227	1.495	0.152	—	—	-2.370	0.456
4771 1092	K5	0.706	1.895	0.373	—	—	-8.640	0.566
4771 1095	K5	0.489	1.308	0.374	—	—	-24.42	0.404
4771 1097	K5	0.541	1.876	0.289	—	—	-2.130	0.514

Table 2.18: Spectroscopic data for optically selected candidate PMS stars.

σ Orionis, I divided the color–magnitude diagram of from R−I of 0.7 to 1.25 into 4 bins. The bins were defined by lines running parallel to the reddening vector, and passing through R−I = 0.7 and V magnitudes of 14 through 18. (See 2.6 for more details.) The group of stars below the bottom line was ignored since this bin is incomplete. In the lowest bin there are 63 stars, in the bin above that there are 24, in the next bin (the once that most closely fills the gap between the background sources and the PMS stars) there are 10 sources. A fit to these data projects 3–4 background sources to be found in the top bin. If I had accounted for the incompleteness in the bottom two bins, this number would be even smaller. Excluding X–ray sources, there are a total of 22 sources in the top bin. Based on the above argument, I expect about 85% ± 10% of these to be PMS stars.

The existence non–X–ray detected PMS stars implies one of two conclusions. The first possibility is there are X–ray quiet PMS stars. It is possible that these stars are relatively slow rotators, so that the dynamo for generating the activity is not as powerful. The second possibility is that the activity rates in stars change with time. Figure 2.9 shows the X–ray count rate of all but the brightest detected X-ray sources near σ Orionis. The bottom 12 sources in the figure are within 3 σ of the detection limit. Given that the observed X–ray variability of PMS stars in Taurus is up to a factor of five (Walter et al. 1988), many of the sources observed could be missing in later observations and many stars not observed here may be seen in future observations. The X–ray flux changes may be secular in nature or could indicate stellar activity cycles in these stars, similar to those of the Sun and older stars (cf. Dorren 1995). However, Walter et al. (1988) note that of Taurus–Auriga stars observed in X–rays more than once, 25% of them have significant source variability which led to non–detections during at least one observation. Between V=14 and V=16, I find 25 stars which are X–ray sources and estimate 19 non–X–ray PMS stars. Based on their colors the non–X–ray detected stars are PMS.

The group of stars which are redder than the X–ray sources, R$-$I > 1.25, is probably composed of stars similar to the X–ray sources, except that their smaller mass leads to a smaller surface area. Assuming a constant X–ray flux per unit surface area, the lower mass stars are X–ray dim. Consequently, they fall below the ROSAT detection limit.

2.6.2 Very Low Mass PMS Objects

In Figures 2.10 and 2.11, the color-magnitude data from Figures 2.6 and 2.7, have been moved onto a luminosity–temperature plot using the following steps. First the color was converted to a temperature, using tables from Bessell (1990). Then the bolometric correction, appropriate for these temperatures was applied to the observed V magnitudes. Bolometric magnitude was then compared to the bolometric magnitude of the Sun at 380 pc. Since the reddening found for the stars in Table 2.13 was small, no reddening correction was attempted. The evolutionary tracks of D'Antona and Mazzitelli (1994) have been overplotted. Note the addition of seven diamonds at the lower right–hand corner of the plot. These diamonds indicate the positions of very low mass, 3 Myr old, objects from the work of Burrows et al. (1993). These

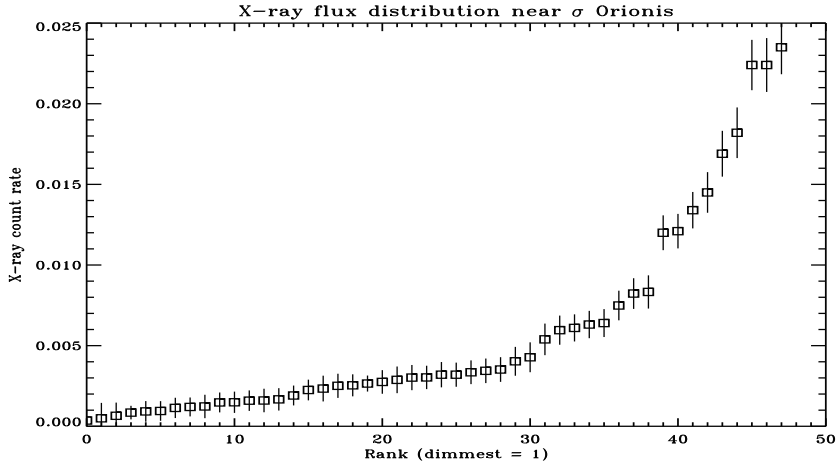

Figure 2.9: The X–ray count rates of all but the brightest HRI sources near σ Orionis. One sigma error bars are indicated.

models are similar to those mentioned above except that they focus particular attention to absorption of H_2 molecules and Coulomb corrections due to free electrons in cool stellar atmospheres. Consequently these models are expected to be more accurate than other models in the cool regime. The diamonds represent objects of masses from 0.2 $M_\odot$ to 0.05 $M_\odot$. From the figure, it is clear that masses determined using the Burrows et al. tracks are higher than those with the D'Antona and Mazzitelli tracks. Nonetheless, there are still a significant number of PMS sources cooler than the 0.08 $M_\odot$ hydrogen burning limit. These objects are candidate brown dwarfs.

As stated above, no reddening correction was applied to the sources. Since the reddening vector runs in the redward direction along the main sequence, it is possible that these objects are simply highly reddened PMS stars. JHK data will aid in determining the reddening and temperatures of these objects. Spectral line diagnostics of these stars will give a more complete picture of their nature. It has been suggested (Stauffer, private communication) that there may be a dust sheet behind the σ Orionis cluster, and that the extremely red sources are simply embedded in the cloud. However, this is considered unlikely based on the comparison of Figures 2.6 and 2.7. From these figures, one can calculate the mean color of the background populations. The means are R$-$I = 0.55 and R$-$I = 0.4 for σ Orionis stars and stars northwest of the belt respectively. While there is difference in the overall extinction beyond the two groups, it is only about 0.15 in R$-$I, which translates to an extinction of only 0.5 in V. Global extinction probably does not exceed 0.8 magnitudes at V.

The number of stars near the brown dwarf cutoff may betray the existence of many more. The completeness limit of the diagram is approximately V magnitude 18.5. Note that in Figures 2.6 and 2.7, the density of sources in the PMS group decreases only slightly as this limit is approached. This seems to imply the existence of additional stars redward of those in the figure. These sources would either be subject to extreme reddening ($A_V > 2$) or be below the hydrogen burning limit. In either event, the data do indicate a plethora of extremely low mass objects.

This optical V versus R−I scheme is a very powerful method of detecting very low mass (VLM) objects. The usual method of finding young brown dwarfs is to use deep infrared mapping of star formation regions (cf. Comeron et al. 1993, Stauffer et al. 1994 and references therein). The advantage of infrared mapping is that very low mass stars are expected to be brightest in these colors. As one moves toward the optical, flux falls off rapidly since cool objects have their flux peak well into the near–IR (although for a sufficiently cool temperature, absorption dominates and objects appear bluer as their effective temperature drops). When one looks at young stars (< 2 Myr in the case of σ Orionis), there is no discernible break in the luminosity function as one moves below the hydrogen burning limit (Burrows et al. 1989). Because of this, young brown dwarfs are intrinsically no more difficult to observe in the optical than low mass stars at the age of σ Orionis. Although 2 Myr old brown dwarfs have less flux by in optical wavelengths than the IR, it appears that this effect is outweighed by the wide field and low background of optical CCDs with respect to IR arrays. The ability to identify a complete population of

PMS stars is very important to our understanding of these objects. Previous samples used to study the binary fraction have been naturally biased toward stars with strong emission lines or X–ray emission. The capacity to identify PMS stars independent of their activity levels will greatly aid us in the pursuit of understanding the nature of these objects.

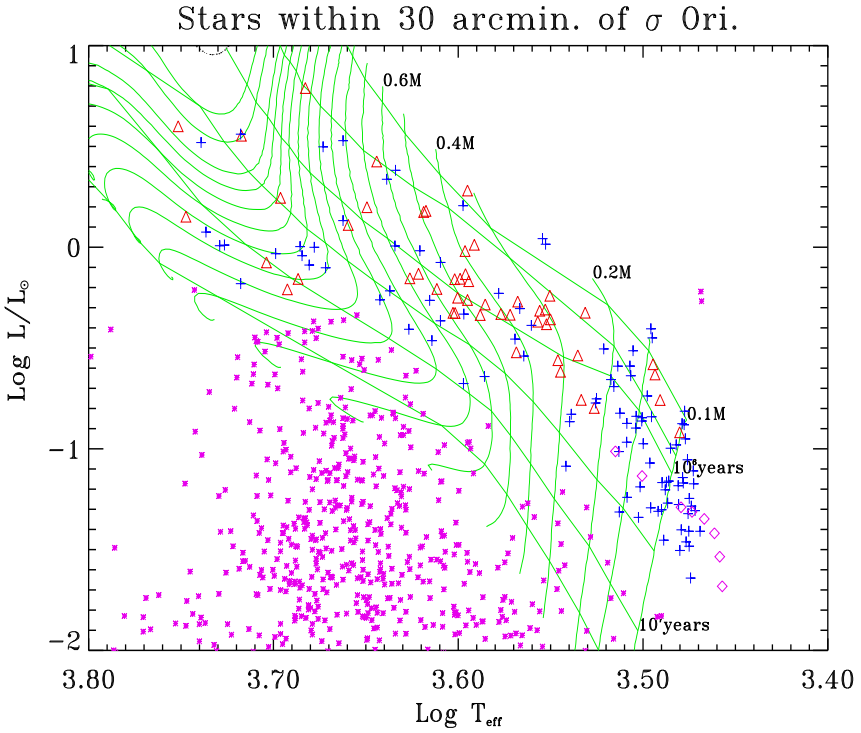

Figure 2.10: A luminosity–temperature diagram for all stars in 900 square arcminutes nearest to σ Orionis. Triangles indicate X–ray sources. The smaller dots indicate background sources. Diamonds indicate the locations of 3 Myr stars (0.1 – 0.06 $M_\odot$ (Burrows et al. (1993) No reddening corrections have been applied. Isochrones are taken from D'Antona and Mazzitelli (1993) using opacities from Alexander et al. (1989).

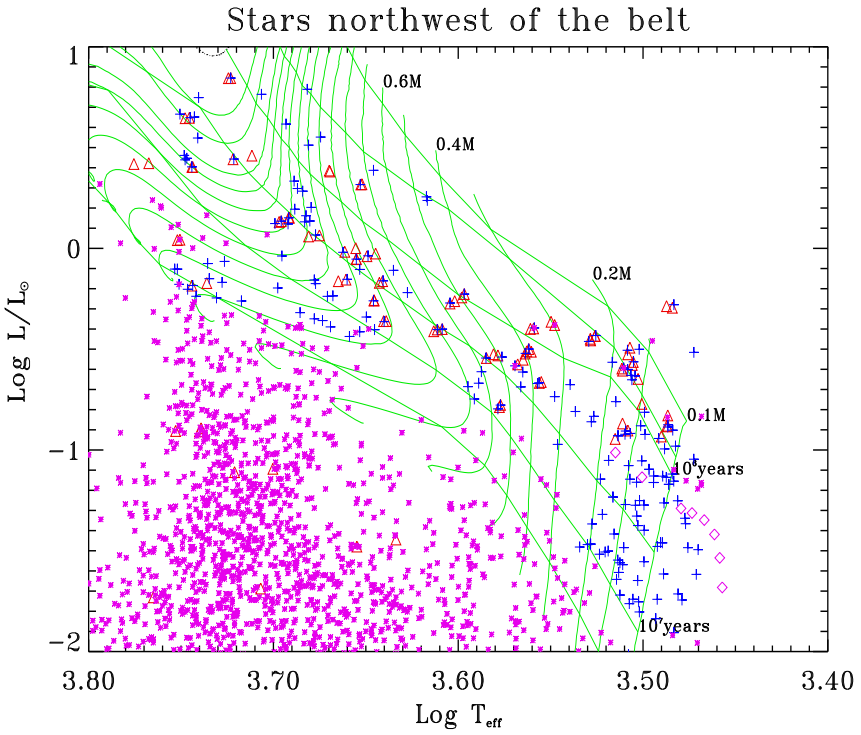

Figure 2.11: A luminosity–temperature diagram for all stars in 1350 square arcminutes which were observed during observations of X–ray sources northwest of the belt of Orion. Triangles indicate X–ray sources, two observations of each X–ray source are displayed in the figure. All other symbols are the same as the previous figure.

Chapter 3

Period Analysis

The combination of the X–ray and photometric observations have produced two samples of low mass PMS stars. At the time that the stars were monitored for rotational modulation, their photometric and spectroscopic properties were not yet known. For this reason, only the stars in each sample which were coincident with X–ray sources and randomly chosen comparison stars had their photometric data extracted and analyzed. By measuring the rotational periods of the stars in the two samples, one can separate out the effects of age on the rotation period from those of other factors such as mass.

3.1 Period Determination

Period determination for short period stars is performed by observing target fields several times per night for several consecutive, or closely spaced, nights. Data are reduced to instrumental magnitudes in a similar manner to that described in Section 2.2. First the individual frames are debiased and

flat–fielded, then fluxes within a four arcsecond aperture around each star (targets and randomly chosen background stars) are extracted. The nominal seeing was about 1.5 arcseconds at both the Wise observatory and at Lowell. An annulus with an inner radius of five arcseconds and an outer radius of seven arcseconds is used for background subtraction. The relative fluxes are put on a magnitude scale with the zero–point set to 25. Since the goal of the program is differential photometry, nightly airmass and color solutions are not needed. In any event, the sky conditions under which these data were taken were not photometric.

After instrumental magnitudes were calculated for the stars observed during the run, several comparison stars are chosen. These comparison stars were then compared among themselves, and the four most stable in each field were chosen as field standards. Differential magnitudes were then measured between the target stars each field standard star. For any single target star, there are usually three to four observations per night and four field standard stars per observation. The longest continuous run was at the Wise Observatory. It contained 11 nights of data. Counting each comparison star separately and removing unusable frames, each target had about 100 data points per filter. Observations made from MTSB had many more observations.

The first step in period searches involves trimming highly discrepant points, those that vary from the mean magnitude by more than six standard deviations. Normally, one or two highly deviant points were removed this way. Usually, such deviations occurred to many objects in the same field and were caused by either filter misalignment or terrestrial clouds. Then, two

separate numerical period searching routines are used. One is a phase dispersion minimization (PDM) method (Stellingwerf 1978) and periodogram (Scargle 1982).

3.1.1 Phase Dispersion Minimization

In the PDM method, the period producing the least possible scatter about the derived light curve is chosen. One does this by minimizing the sum of the squares of the differences in the ordinate from one data point to the next. The period resulting in the smallest sum is taken to be the true periods. Conceptually, this has been referred to as the "shortest string" connecting all the data points (Dworetsky 1983). More rigorously, any set of observations can be represented by the ordered pair (x_i, t_i) where x_i, t_i represent the magnitude and time. of the ith observation. Given N observations, the variance of x is defined as:

$$\sigma^2 = \frac{\sum(x_i - \bar{x})}{N-1}. \tag{3.1}$$

For this case, $\bar{x}$ is the mean magnitude. One can calculate such a variance for any given sample range. One is interested in minimizing the variance of the data with respect to the mean value of the lightcurve. To do this, one chooses a test period. Modular division of the observation times by this test period assigns a phase to each data point. The observations are then grouped into bins of roughly the same phase. The variance in each bin can now be calculated. The overall variance is the sum of the variance of the samples: The data are explicitly folded of each test period until the total variance is

minimized. PDM is well suited to small and randomly spaced samples. This method has no preference for a particular shape (e.g., sinusoidal) for the curve.

3.1.2 Periodogram

The other period search technique is the periodogram which is based on the prescriptions of Lomb (1976) and Horne & Balinas (1986). The periodogram is essentially a discrete Fourier transform of the input data. Any function of time can be written as a function of frequency:

$$H(f) = \int_{-\infty}^{\infty} h(t) e^{2\pi i f t} dt \quad or \quad h(t) = \int_{-\infty}^{\infty} H(f) e^{-2\pi i f t} df \tag{3.2}$$

This transformation conserves power:

$$\text{Power} = \int_{-\infty}^{\infty} |h(t)|^2 dt = \int_{-\infty}^{\infty} |H(f)|^2 df \tag{3.3}$$

Decomposition of a regularly sampled signal into its Fourier components is straightforward. The difficulty that arises in astronomical data is that weather and daylight usually render even sampling impossible. The classical periodogram is defined as a discrete sum:

$$P_x(f) = \frac{1}{N_0} \left| \sum_{j=1}^{N_0} h(t_j) e^{-2\pi i f t_j} \right|^2 \tag{3.4}$$

The periodogram provides an approximation to the power spectrum. In this respect, the procedure breaks down the signal into sine wave components across a frequency range. The residuals of the least squares fit to the data are then summed. The period is chosen by minimization of this sum.

3.1.3 False Alarms and Aliasing

One major advantage of the periodogram method is that it generates a value called the power. The power can be converted to the probability that the period found is not true, the false alarm probability (FAP). Scargle (1982) showed that the probability distribution returned by this method is exponential, and thus the probability of a false alarm is defined as $P \equiv 1 - (1 - e^z)^N$, where z is the power at a given frequency and N is the number of frequencies sampled. Unfortunately, the formulation for calculating the FAP is only valid in the case where the data are not clumped in their sampling. The data reported here are clumpy since up to four observations are taken per night, but none during the day.

To overcome this problem, Eaton et al. (1995) have suggested calculating the power of the most likely period in a set of data created by randomizing the night number associated with observations of a given star. By calculating the maximum power on a large number of randomized data, the conversion from power to FAP can be individually determined for each set of observations in a statistical manner. However, it is still possible to have several possible periods with less than 1% probability of being true. This is due to aliasing in the dataset. Aliasing is caused by periodicity in the timing observations being coupled with the periodic nature of the source. The sampling theorem shows that if the frequency of a continuous function $h(t)$ (in this case the amplitude) is less than half the sampling frequency (the Nyquist frequency) the original signal can be recovered. Given a sampling time interval Δ, one can identify

individual observations at time t as the n^{th} observations. If one were to observe an infinite number of times, one would obtain:

$$h(t) = \Delta \sum_{n=0}^{\infty} h_n \frac{\sin[2\pi f_c(t - n\Delta)]}{\pi(t - n\Delta)} \tag{3.5}$$

where: $f_c = 1/2\Delta$ is the Nyquist frequency. This has an unfortunate side effect, Two waves, f_1 and f_2 give the same samples if they differ by $1/\Delta$. This implies than any given sample can be reconstructed into an infinite number of original signals all separated by n/Δ in frequency space. Any power in the spectral density which exists outside the search range is moved into the search range. Two periods $p1$ and $p2$ will give the same samples, and thus be indistinguishable, if they differ by the inverse of the sampling frequency. The problem is complicated by the two sampling frequencies in the data, the diurnal cycle and the $\approx$ three hours between samples each night. The aliasing causes several peaks in the periodogram analysis to appear at similar power.

3.1.4 Windowing

The term "spectral window" is used to describe the response of the data analysis system to a perfect sine wave. If one observes a non-variable object with finite signal–to–noise each night at exactly the same time (equivalently an object with a one day period), the periodogram analysis on it will return a power spectrum that is peaked at 1 day. This means that there is energy is the sampling frequency itself. The observing times define a window. This window, convolved with the signal, determines the periodogram (Deeming

1975). The sampling frequency enters because you can define a period that oscillates wildly, yet hits all the observed points.

Figure 3.1 shows a typical analysis, including the window function. This demonstrates the main features of the window function. First there is a narrow central peak with width $\approx 2\pi/N$ where N equals the number of samples. The number of samples taken places a fundamental limit on the accuracy of the period measurement. Second, there are roughly evenly spaced side lobes. These side lobes contain spectral leakage due to high frequency components in the Fourier transform of the original signal. Third, the total power in the peak of the window function is greater than the power of the true signal by a factor of a few. Finally, there are large peaks on either side of the main lobe displace by one rotation per day. This is due to the one day periodicity in the observations. The windowing can cause a problem with period determination since periods very close to one day and very long periods and appear similar to the null signal case. Careful study of Figure 3.2 reveals difference between the window function and periodograms of these signals. Even with only 30 samples, periods deviating from a day by 1% are detectable. For convincing results though, the periodogram requires the aid of other data analysis. This usually consists of visual inspection of the raw data and the phased data. To gain a better understanding of how the observational data behave, simulations were run using synthetic data.

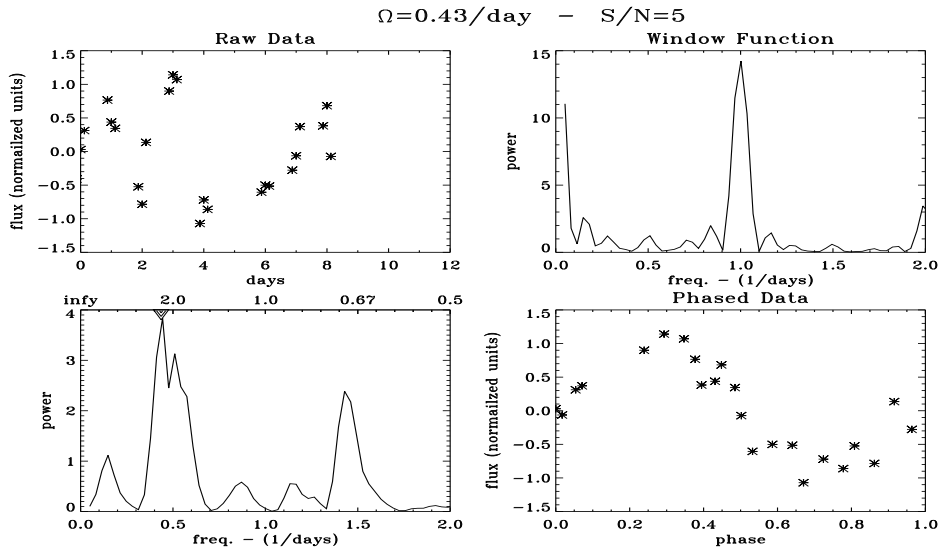

Figure 3.1: Typical period analysis. The top left panel show the raw "observed" data. The top right panel shows the results of running using periodogram analysis of a non–varying signal observed at the same time as the data. The lower left panel shows the periodogram analysis on the data. The small triangle near the top of this frame shows the expected location of the input period. The lower right panel shows the data folded over the measured period. In this and the following figures, the "flux" is normalized relative to the mean value for the input signal (i.e $flux = signal - mean\ flux$). Data shown in this example are simulated as a single sine wave with noise as described in section 3.2. The input period is 2.32 days, data were taken on 8 of 11 nights and the S/N of the data is 5. The window function here is similar to those shown in figure 3.2. Note the strong main lobe with adjacent side lobes. Large peaks are visible at the zero and two rotations per day.

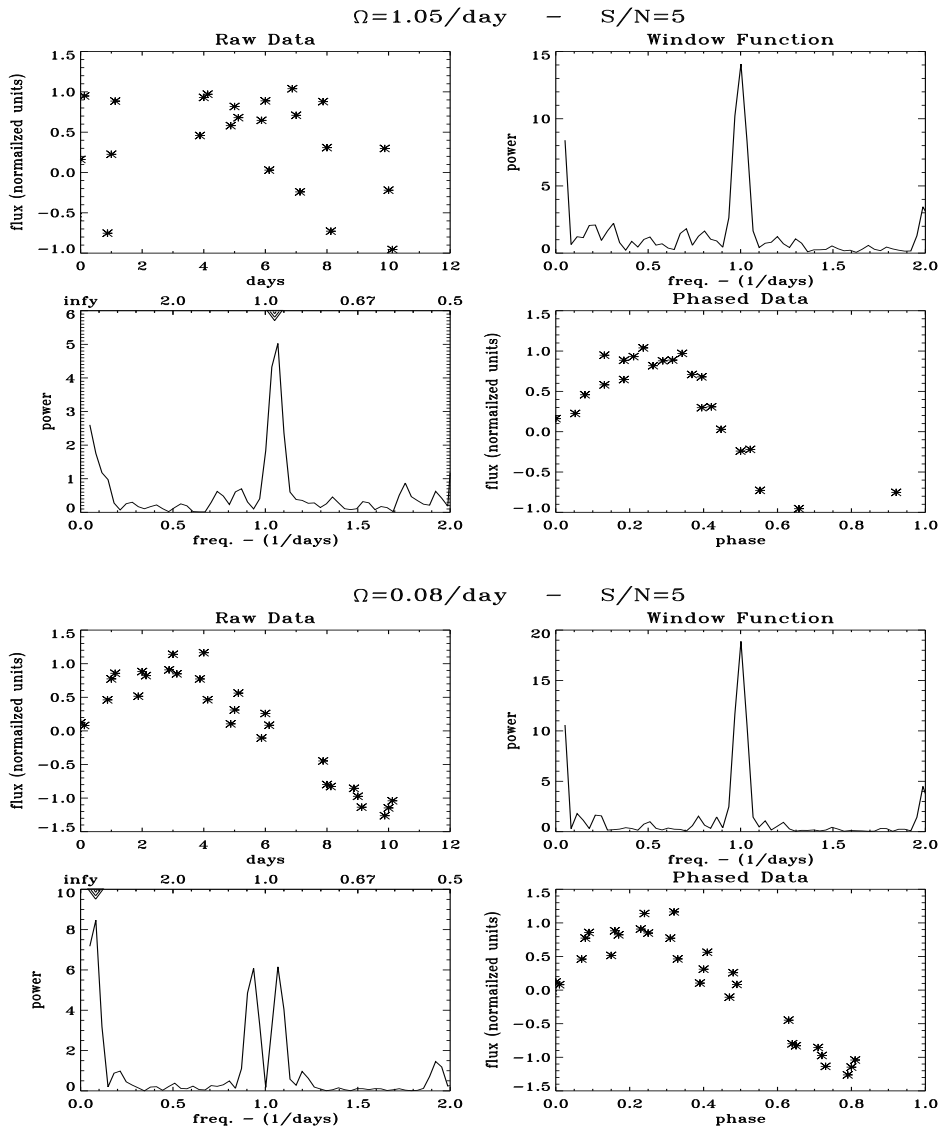

Figure 3.2: The effect of windowing on period analysis. In these cases, the periodogram of the data with signal looks very similar to the non–varying case. When the data are folded over the measured period however, the modulation becomes apparent. Panels are the same as in the previous figure. The input periods are 0.95 days and 12.5 days for the top and bottom figures respectively, S/N of the data is 5.

3.2 Simulations

3.2.1 Synthetic Modulation

Since the bulk of the data for rotational modulation were taken during short (< 11 night) runs, there is a great deal of variation in the sensitivity to periods, depending on the length of the period. The searches are much more sensitive to short periods than to longer ones. To test the sensitivity in a quantitative way, I made numerical simulations of the photometric data. For the simulation, the input data was a pure sine wave. Poisson noise was added so that the signal to noise ratio (S/N) varied from 5:1 to 1:1.[1] The run was simulated to be 11 nights long with anywhere from one to seven nights randomly removed to simulate bad weather. The data were sampled, three times a night, roughly at 9 p.m., midnight and 3 a.m. to simulate the nominal sampling. The sampled data were then processed through the periodogram routine. Forty–eight sets of input parameters were used, eight different periods each with six different signal to noise settings. Each parameter set was simulated 1000 times. An example of a simulation with an input period of 5.4 days is shown in Figure 3.3.

From this figure, both the strengths and the weakness of period finding become apparent. The strength is that in all cases, even down to signal to noise levels of one, a large percentage of the power can be found in the correct

[1]The usage of S/N in this context is not the same as in standard photometry. "Noise" has the same meaning, but here "signal" refers to the intrinsic strength of the modulation. If a star is measured to 2% accuracy and has at 10% modulation (0.2 magnitudes peak to peak), the S/N is 5.

period. Weaknesses are noted in the two aliased peaks near 1.18 days and 0.82 days. $1/(1.18-1) = 1/(1-.82) \approx 5.4$. A similar pair of peaks is present either side of 0.5 days (frequency = 2). Such families of solutions are a result of the uneven and clumped sampling. The aliased peaks can be as strong or stronger than the correct peak. In the example, the correct peak is given some additional power due to its low frequency. The lowest frequency peak covers a very large portion of the search window. In the highest S/N case, the full width half maximum of the 5.4 day peak ranges from about 4 days to about 6.5 days. The low spectral resolution at lower frequencies can inflate the strengths of these peaks. Also, note that in one of the high S/N cases, the sampling causes a split the normal family of solutions into two narrower families.

The overall results of the simulation are given in Figure 3.4. The main lessons found here are:

- No matter how high the S/N and how short the period, 5% of all stars will not have the correct period found. In the cases of the strongest sources, aliases are found instead.

- Accuracy better than 5% can be found only for the $<$ one day periods or S/N higher than 5. To some extent, this is a function of the periodogram parameters, which can be set for any degree of accuracy at a geometrically increasing cost in CPU time. However, it is also an indication of limitations incurred due to the short duration of the run and the small number of samples.

- For periods less than half the run, length S/N of 4 is sufficient to get the FAP below 10%.
- As periods approach the length of the run, the exact period found becomes increasingly less accurate. Signal to noise > 2 is sufficient, but the FAP averages 70%.
- For periods longer than the length of the run, there is still a possibility of finding the correct period, but S/N must be high and the resulting FAP is high as well.

In reality, it is hard to imagine a spot modulation being perfectly sinusoidal. If a star has a single spot, or spotted region, on its surface the observed variation will be constant (bright) for the time that the spot is on the far side. A slow fall (rise) will be observed as the spot rotates into (out of) view. The flux will be nearly constant (dim) in between since the projected area of the spot does not change. Further, there is no reason to expect that any given star will have only one spot. In fact, Doppler imaging of active stars usually indicates more than one spotted region, and none of the spotted regions are round (cf. Strassmeier et al. 1994). To simulate this more realistic case, the above model was modified so that the input signal was the sum of three sine waves. The sine waves are assigned random strength. The phases are assigned with a random fluctuation with a standard deviation of one about phase 0 so that two spots do not cancel each other. Of course in the real universe, two spots may cancel each other so this simulation still overestimates the ability of the periodogram to detect periods. Also, input signals are still initially

sine waves and other possibilities such as differential rotation have not been explored. With these caveats in mind, the results are shown in Figures 3.5 and Figure 3.6. Not surprisingly, the results are far more complicated than the single spot case. The power peaks can develop side lobes and the bifurcation of a family of solutions into two or more is common, even at high S/N. In general, higher S/N is required to detect any given period and the FAP is higher.

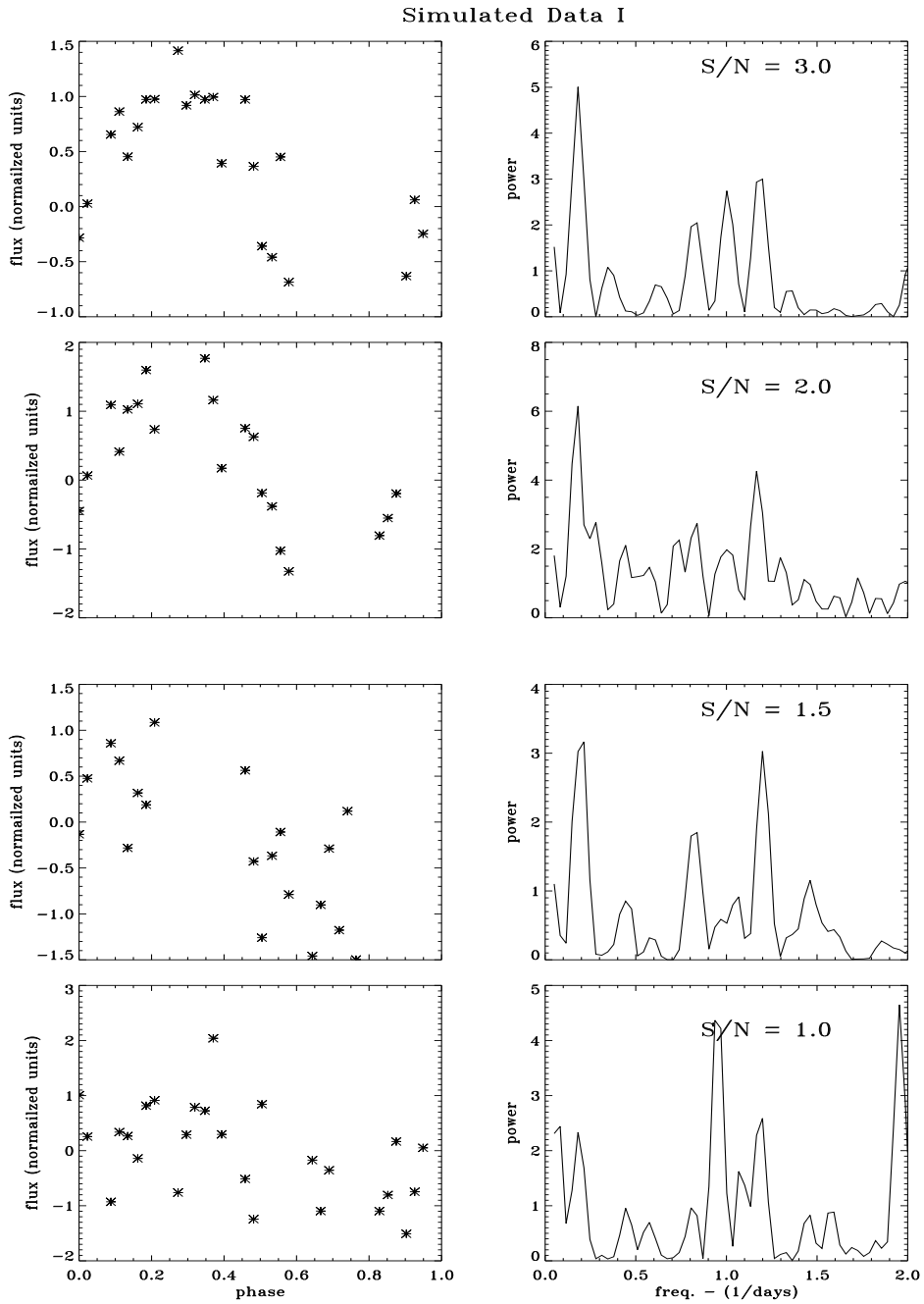

Figure 3.3: Period analysis of simulated data. The panels on the left hand side show the input data folded over the 5.4 day period ($\Omega = 0.19$). The panels on the right hand side show the results of the periodogram analysis. The S/N ratio is 3 in the top panels and lowers to 2, 1.5 and 1 in the lower panels.

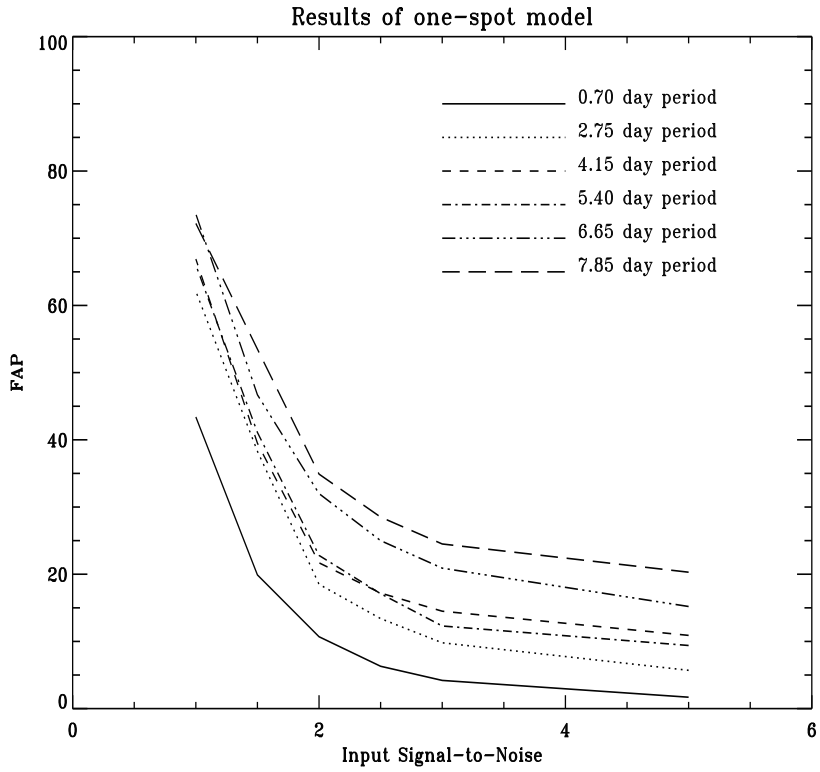

Figure 3.4: Results of period searches on simulated data with one input sinusoidal signal. As the signal to noise drops, it becomes rapidly more difficult to detect the correct period. In the high signal to noise regime, as the period becomes longer by one–tenth the observing window, FAP increase by about 4%.

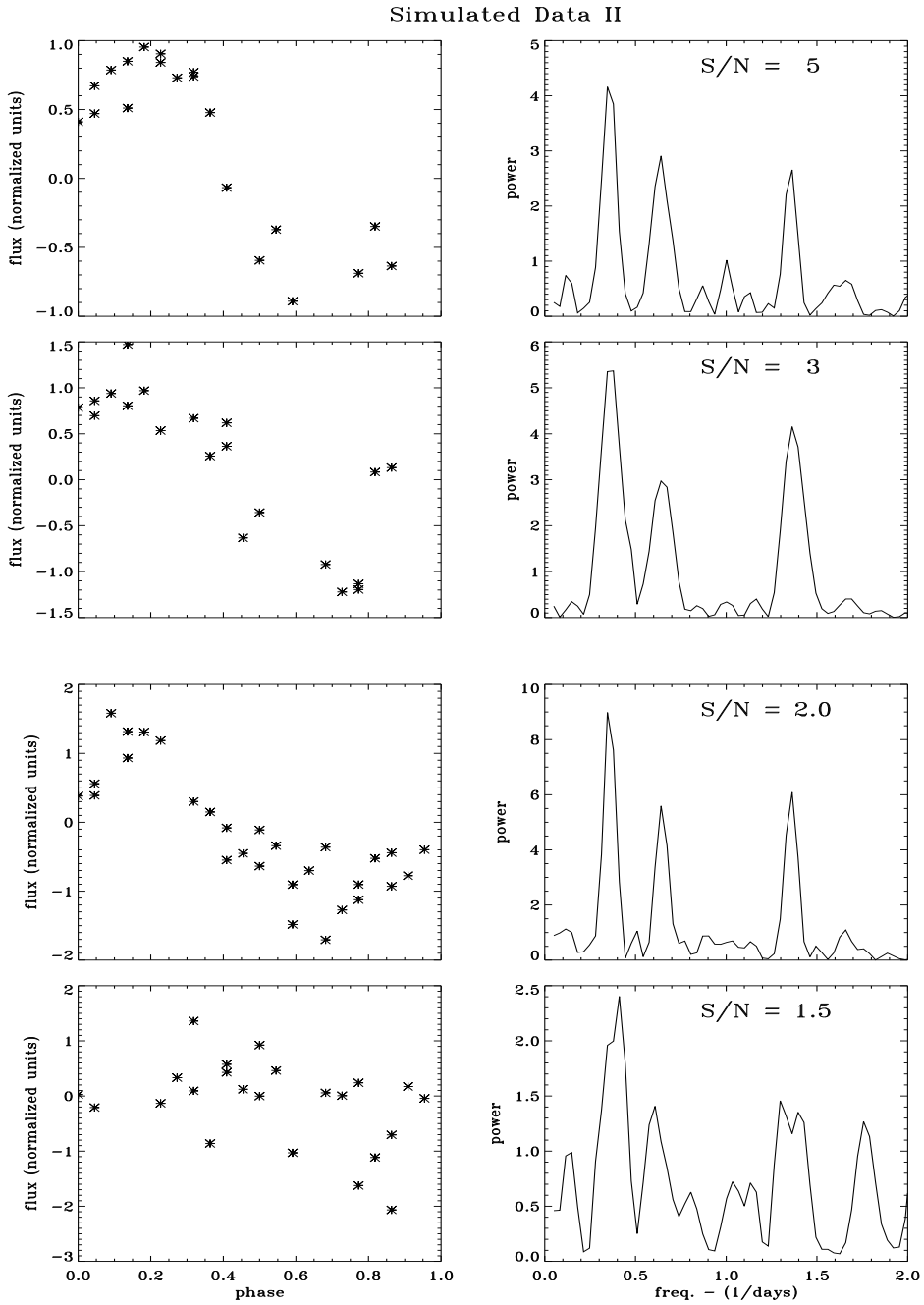

Figure 3.5: Same as Figure 3.3 except that this simulation features three sine curves are different amplitudes and phases. The input signal had a 2.75 day period ($\Omega = 0.36$) S/N ratios of 5, 3, 2 and 1.5 are shown.

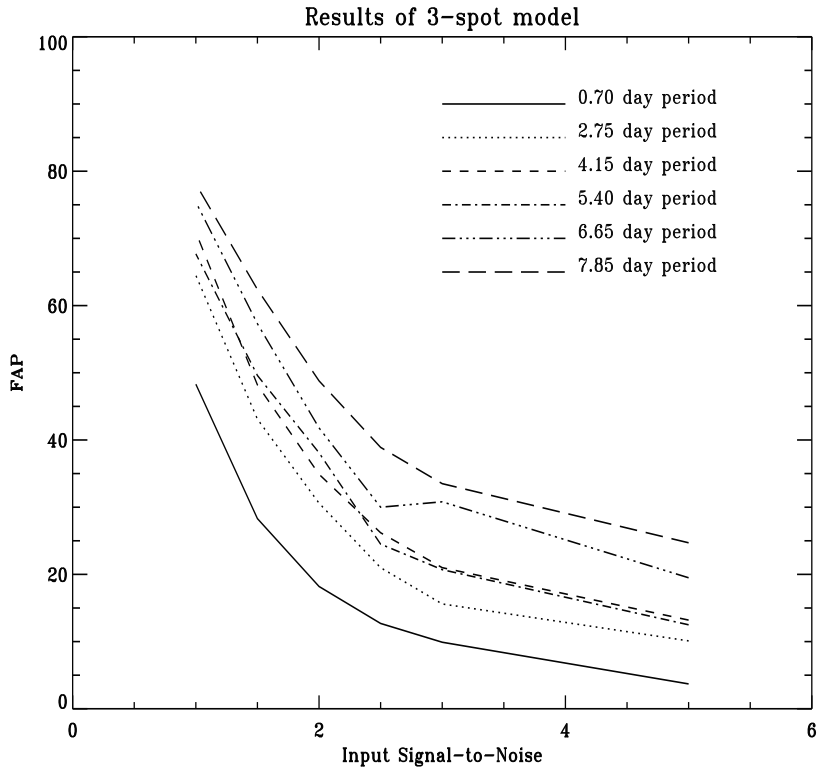

Figure 3.6: Results of period searches on simulated data with three input sinusoidal signals. Results are similar to Figure 3.4 except that FAPs are about 7% higher

3.2.2 Starspots

Simulations were also carried out to quantify the range in parameter space which could be filled by stars varying in accordance with the spot hypothesis. Spotted stars were modeled in a two step process. First, an unspotted star was produced. To do this, colors of a given spectral type (taken from Bessell and Brett 1992) were converted to fluxes for a normalized distance. The flux was summed over 100 grid locations to represent a 100% filling factor. In this model, each portion of the star's surface is weighted evenly and limb darkening is not accounted for. No correction was applied for spectral class IV relative to spectral class V since the goal of the simulation was to gain a qualitative understanding of the expected result. As a test, summation over the 100 grid locations returns the original colors. To simulate spots, between five and 40 of the grid locations were refilled with values corresponding to temperatures between 100K and 1000K cooler than the photosphere. Summation over this grid returns the colors of the spotted star. The original and final colors are subtracted to produce ΔV, ΔR and ΔI.

All spectral types between K0 and M5 were simulated. The change in the colors for each given band, the observable quantity, was calculated. For any given waveband, the flux change for spots with a spot filling factor of about 20% (assuming spots 500K cooler than the ambient photosphere) is about 10%. The largest change in any given color was about half a magnitude. This was for a spot 1500K cooler than the photosphere covering 40% of the observable surface. There have been some stars in the literature with reported

spot modulation of over one magnitude. For example, DR Tau has had several reported periods ranging from 2.8 to 9 days (Bouvier et al. 1995). Its peak to peak variation ranges from 1.5 magnitudes at I to 3 magnitudes at U. It is not possible to produce such large and color sensitive variation using cool spots. Bouvier et al. conclude that, in this case, the modulation is caused by hot spots, presumably due to accretion. Herbst et al. (1994) suggest more generally that variations between 0.5 and three magnitudes are usually the result of hot spots, variable accretion or variable circumstellar obscuration. Eaton et al. (1995) discuss large amplitude variables (LAVs) and found similar results.

In Figure 3.7, the results of the simulation are displayed in terms of the change observed in R and I relative to change in V. One can see that these values are all ≤ 1. Values close to unity indicate stars with very cool spots relative to their photosphere. It is interesting to note that spotted stars occupy a fairly small triangle of parameter space. The right–hand side of the triangle is defined by the M4 stars, the left–hand side by the K0 stars, and the bottom by stars with spots just slightly cooler than their photosphere and large spot filling factors. Another result is the apparent uniqueness of any given point in the parameter space. Each point on the plot corresponds to exactly one combination of spectral type, spot temperature and filling factor (the uniqueness breaks down as ΔV, ΔR and ΔI approach unity). While this uniqueness quality provides hope for the future determination of spot properties based solely on photometric data, it should be pointed out that this would require signal to noise in the modulation of about 100, which is a factor of 20 better

than were obtained. Also, the model uses only a single spot temperature which is a vast over–simplification. The color behavior is an important criterion for period determination. The change in the bluer color must be greater than or equal to the change in the redder color. The details are far too subtle any useful study to be made with the data here due to insufficient signal to noise.

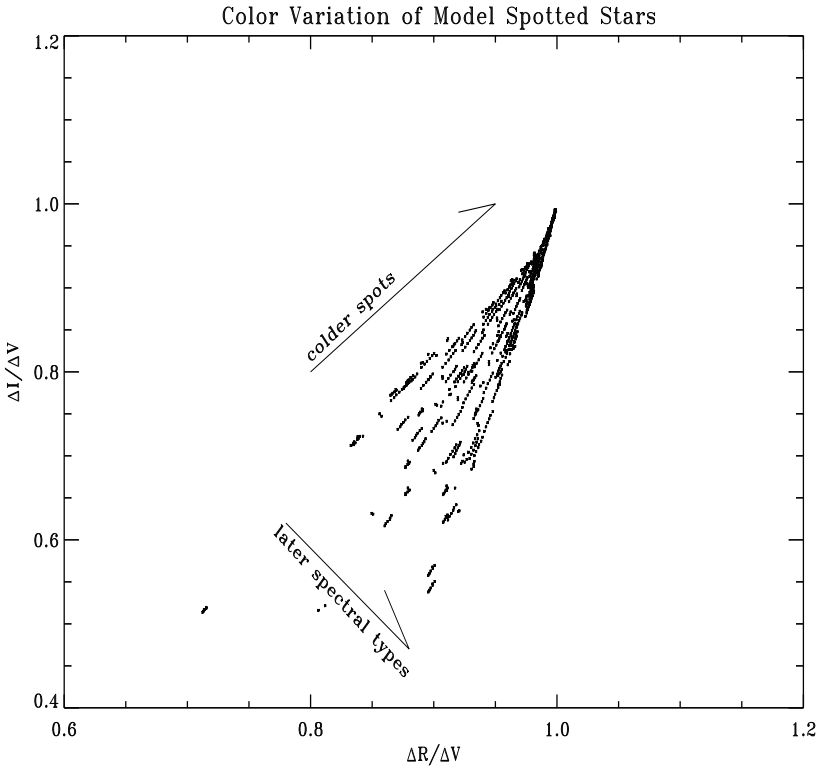

Figure 3.7: Plot showing the ratio of the variations in color generated by simulating spots on a rotating star. Spectral types K0–M5 were used for the photosphere, spectral type K1–M6 were used for the spots. Spot filling factor was varied between 5% and 40% in steps of 5%.

3.3 Period Criteria

Actual stars are expected to be more complicated than these simulations. For example, if a star is inclined and has a nearly polar spot, the variation will be far more complicated. The spot may be entirely visible most of the time (one would observe a prolonged flux minimum low), and then part of it may disappear over the horizon briefly and then return (slow rise and then fall back to constant level). In this case, the observed modulation is actually a brightening from the base signal. Flares on stars are even more troublesome, since they usually occur near spotted regions. When the photosphere is becoming dimmer, there can be a very bright group of data points. In these realistic cases, it would be very difficult to determine the correct period without high S/N and additional information. With the set of observations taken here, I have information available from several comparison stars and color information. I use four consistency criteria to mitigate against noise, and two additional criteria to fight aliasing.

1. **The same period must be found using both period finding techniques.** The rule that was used here was that a peak in the power distribution of the periodogram had to coincide with a local minimum of the PDM code.

2. **The same period must be found using multiple comparison stars.** This is an obvious criterion which is used to remove variable comparison stars.

3. **The same period must be found in the V, R and I filters.** If the periodic behavior does not have the same period in the three filters, it is probably not due to rotation. Five percent deviation is considered acceptable to allow for measurement errors in the time of observation and in the sampling grid used by the period search routines. As is shown in the Figures 3.1, 3.2, 3.3 and 3.5. The full width half maximum of the peaks in the periodogram functions are quite wide. This width is caused by the low number of sample used in the simulation, and the actual data sets.

4. **The same phase must be found in the three filters.** This criterion is similar to the previous one. Again five percent errors are considered acceptable.

5. **The period found must be consistent with the data from any given night.** One way to test whether a true period or an alias has been found is to compare the fit to the period with the data for a given night. For example, if the fit to the data predict that on a given night the target star should be getting fainter, yet the data for that night show that star is getting significantly brighter, the period is discarded.

6. **The color changes observed are consistent with the starspot hypothesis.** All the period measurements rest on the initial hypothesis that the observed modulations are induced by the rotation of spotted regions of the star onto and off of the side of the star facing the Earth. This hypothesis has fundamental predictions for the observed color changes

that should be observed. For a star with very cold spots, the spots appear black relative to the star and the same color variation is observed in all colors. For a star with warmer spots, 300K cooler than the photosphere, more flux is removed from the V band than the I band, therefore the observed variations are greater in V than in R, and greater in R than in I. If the behavior differs from this prediction by more than the observed noise in the signal, the period is discarded.

Before discussing the results, a few cautionary notes should be made clear. Even with these criteria, there is no method available to completely prevent false period detections. The statistical FAP calculation should be looked upon as a relative measure for comparing different results and not an absolute measure. It is also very difficult to distinguish between periods that are aliases of each other and are also close to one day, which is a fairly common occurrence. In the following section, I present the most probable periods that are consistent with the criteria that have been discussed. The data are separated into two main sections, those with FAPs below 1% which are expected to be very secure, and those with FAPs between 1% and 20% which are far less certain.

Chapter 4

Results

Overall, 105 PMS stars were monitored in an attempt to measure their rotational period. Analysis began with periodogram and PDM searches in each passband to locate the most likely periods. The data were then folded over the candidate periods so that the other criteria could be evaluated. The criteria left one "best–fit" period. The quality of the best–fit varied.

4.1 Specific Stars

While the bulk of these stars were located in the Orion OB1a and OB1b fields, two stars of particular interest were monitored from our Mount Stony Brook Observatory. One of these stars was TAP 26 (NTTS 041559+1716, HBC 376). This star, located in Taurus, had a measured rotational period which was inconsistent with its $v \sin i$. The other star was P1724, located near Orion OB1d, for which x–ray periodicity had been observed.

4.1.1 TAP 26

TAP 26 was first reported by Feigelson et al. (1987) as a K7 PMS star. Walter et al. (1988) found a relatively high $v \sin i$ of about 70 km/s. It was first monitored for rotational modulation by Bouvier et al. (1993). They reported a 2.5 day rotation period for this star which they confirmed with their 1995 results (Bouvier et al. 1995). While acknowledging that their derived equatorial velocity was only 28 km/s, they suggested that they were seeing the orbital motion of a binary system. Mathieu et al. (1989) observed this star, yet did not report it as a spectroscopic binary. Prosser et al. (1995) were suspicious that Bouvier et al. may have missed the true period due to the fact that their sampling rate was not high enough. Since Bouvier et al. only averaged one measurement per night, they were not sensitive to periods of < 2 days. Prosser et al. monitored TAP 26 during a six day period in which they observed the star 12 times. They reported a 13 hour period. However, they noted that the confidence in the period was low because they did not obtain sufficient data.

TAP 26 was monitored from MTSB on 15 nights. On average, five observations were made of the star each night in each of three filters, V, R and I. During three of these 15 nights, the filter wheel failed and approximately 17 observations were made of the star, all in the I filter. From these data, I derived a 0.715 day period for the star. The MTSB data are displayed in Figure 4.1. The MTSB data indicate that the previously published period is an alias of the true, shorter, period. In Figure 4.2, MTSB data are compared

with those of Bouvier et al. (1995). If one confines the period search range for the MTSB data to be greater than one day, the results are nearly identical to those for the data presented by Bouvier et al. Further, the Prosser et al. results are consistent with one of the aliases of our periodogram result, as expected in the case of insufficient data. Combining the period of TAP 26, with the published radius (1.1 $R_{\odot}$; Walter et al. 1988) one derives the sine of the inclination to Earth to be $\approx .93$ or about 68°.

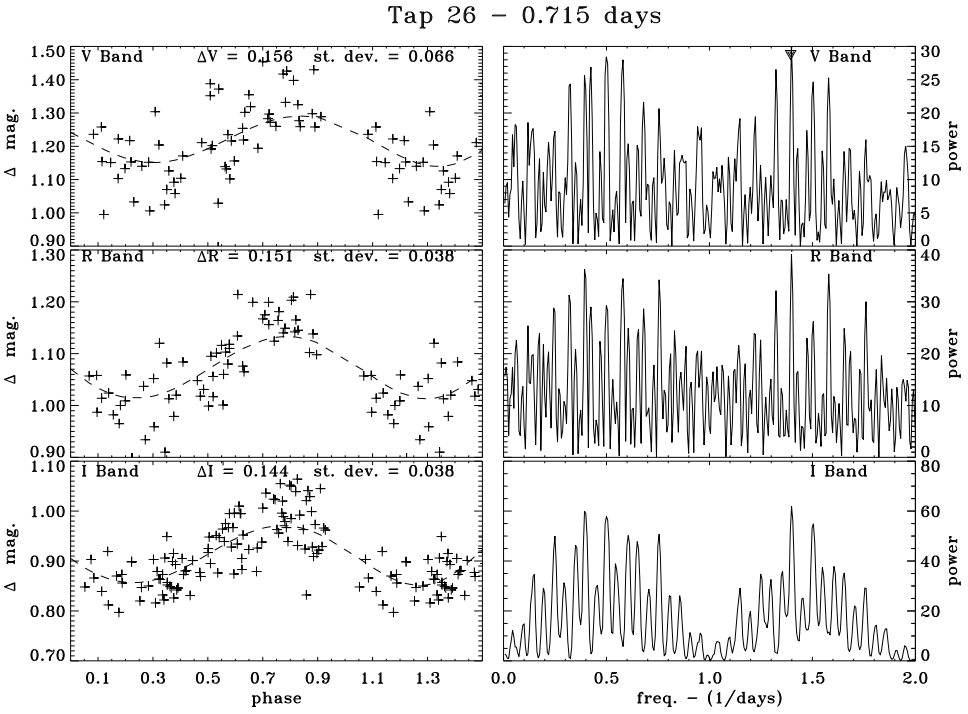

Figure 4.1: Results of data analysis for TAP 26 based on observations made from the Mount Stony Brook Observatory located atop the E.S.S. Building at SUNY Stony Brook. The period search was limited to be greater than 0.5 days. The right hand side shows the results of the periodogram analysis. The pluses on the left–hand panels are the data folded on a 0.715 day period.

4.1.2 P1724

P1724 is a recently reported, X–ray active PMS star (Preibisch et al. 1995). Neuhäuser et al. (1995) found an X–ray variability with modulation on a $\sim$ 20 hour time scale in the star and speculated that the variability was the result of rotational modulation. P1724 was monitored from MTSB on 17 nights over a six week period. About five observations were made per night using V, R and I filters. Three field stars were used for comparison (see Figure 4.3). The results of these observations are shown in Figure 4.4. One can see from the figure the effects of aliasing. There is a family of several periods indicated by the periodogram. The preferred frequency is 1.18 rotations per day (a 0.85 day long period), but the power at this peak is not particularly stronger than the three other strong peaks. However, the 1.21 day period (0.826 rotations per day) is excluded by the nightly trend analysis. In this case, the trend of the data is opposite to the direction of the fit (see Figure 4.5). Evaluation of the 5.5 day period is more difficult. The dispersion of the data in any given night is only 10% greater than that of the 0.85 day solution. However, when the data are fit to the 5.5 day period, each given night has the mild trend, expected from the shorter period. Only one field standard star was available for the TAP 26 field. This, and the fact that the signal to noise is higher for P1724, are the reasons for the much cleaner results of the P1724 periodogram with respect to that of TAP 26.

4.2 Other Stars

Similar analyses were carried out on all the sources monitored during the observing run at the Wise observatory in January 1995. Stars were analyzed without knowledge of color or location so that human biases could be minimized. Usually, the PDM and periodogram codes returned several candidate periods. In many of these cases, more than one period satisfied the criteria given in Chapter 3. In these situations, the folded data were fit to a high–order polynomial function. The use of the polynomial fit adds a smoothness criteria to the method used by the PDM code, which simply tries to connect the data points using the shortest possible "string". The standard deviation of the data to the fit was then measured. If more than one period was found, the one with the lowest standard deviation was chosen. To keep computation times reasonable, the periodogram code has a limited number of bins, thus it has limited temporal resolution. Because of this, standard deviation minimization was also used to fine tune the period.

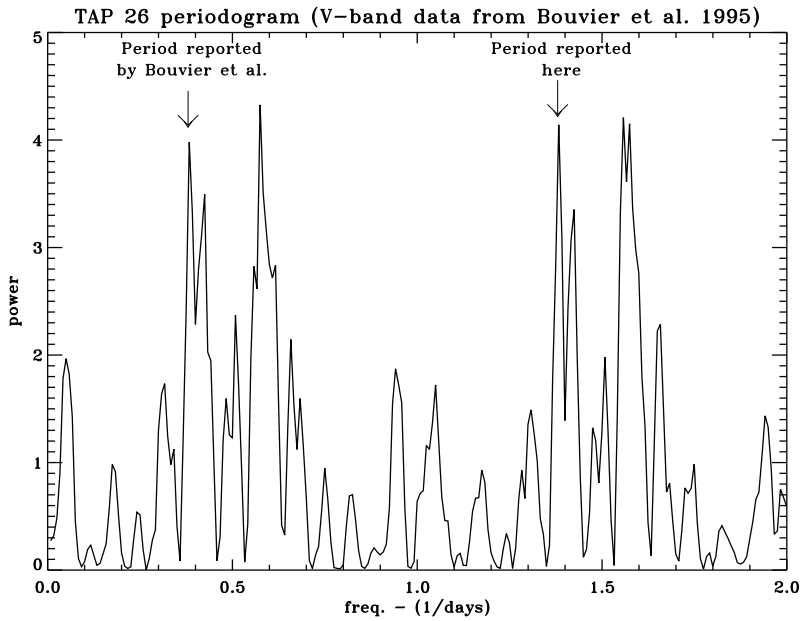

Figure 4.2: Results of data analysis for data from Bouvier et al. (1995) for TAP 26. Note that if the search range included periods less than 1 day, a second family of solutions appears. The periods indicated by the arrows are separated by exactly one in frequency space. The peak at a frequency of 0.58 was not discussed in Bouvier et al. and is not considered likely based on the data shown in Figure 4.1.

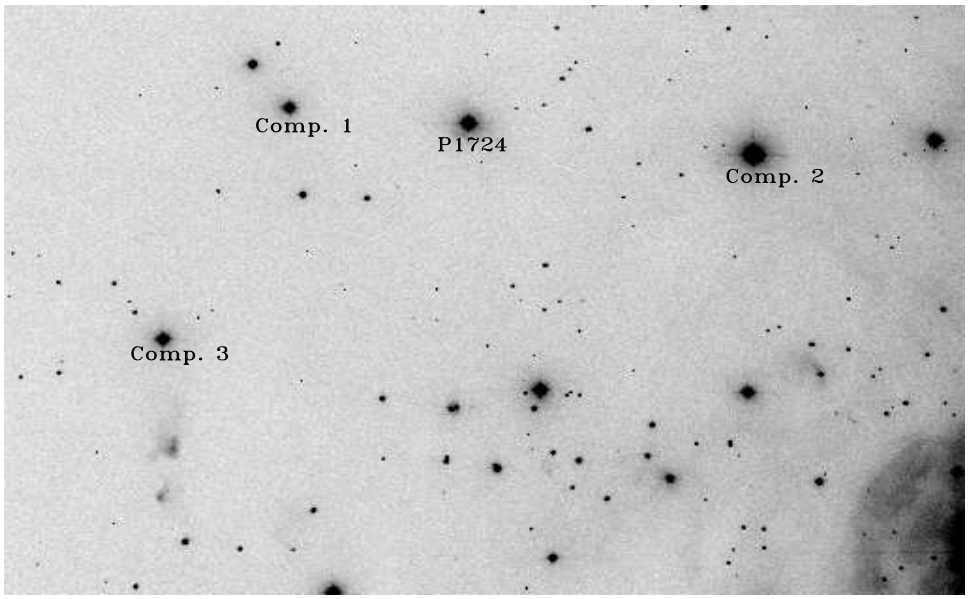

Figure 4.3: The field of P1724. This image is a I–band exposure, the target star and field standard stars are indicated.

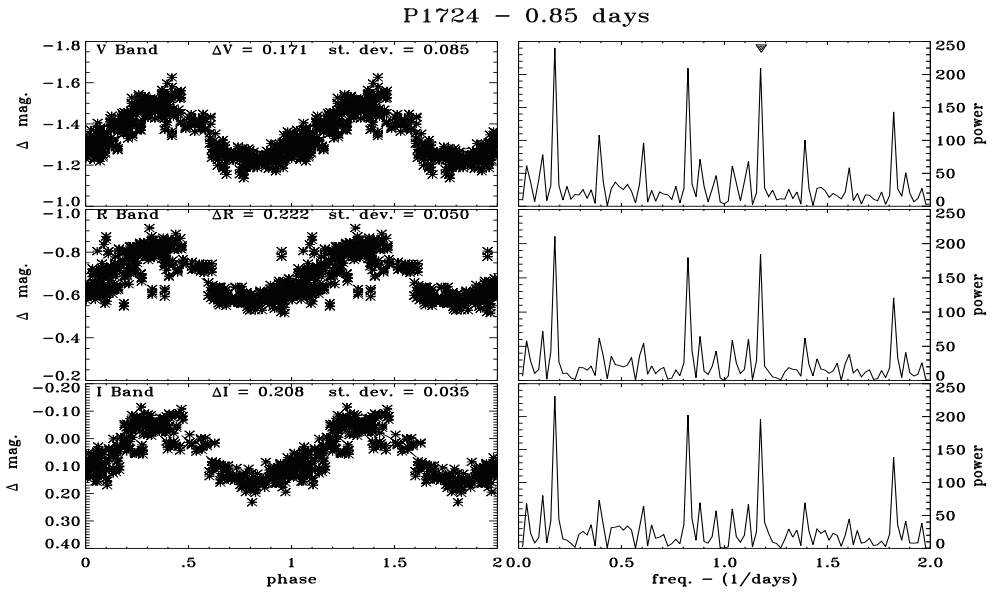

Figure 4.4: Results of data analysis for P1724. Panels are like those in Figure 4.1, the data are folded over a 0.85 day period. All data presented here were taken from MTSB.

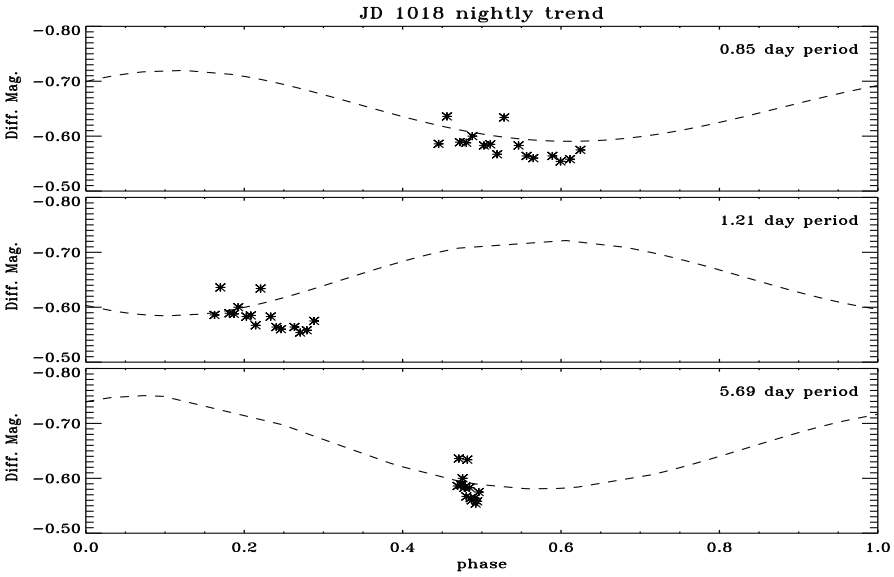

Figure 4.5: Nightly trend analysis for P1724. R–band data from a single night, Julian Date 2,450,018, for P1724 are shown. The dotted lines indicate the fit to the whole data set. The top panel shows the data compared to the fit for a 0.85 day period; both the data and the fit decrease by about 0.04 magnitudes during the night. The middle panel shows the data compared to the 1.21 day fit; note that the data decrease while the fit increases with increasing phase. The bottom panel shows a 5.69 day period. Clearly, the slope of the data in the 0.85 day panel is much closer to the fit than it is for the longer periods.

4.2.1 Stars with Highly Secure Periods

There were 105 stars in Orion OB1b and OB1d sub-association which were analyzed in this way. About 30 observations were made of each star in each of the three filters. The observations occurred near dusk and again each three hours until the stars had fallen below 2.5 airmasses. The results for all 12 stars for which periods were determined which had false alarm probabilities of less than 1% are summarized in Table 4.1. A comment is needed regarding two of these stars, 0101 2447 and 4771 1097. Both of these stars have periods very close to one day, thus they fill–in only a small portion of their light curves and because of the problems with the window function. However, the shape of the periodograms of these stars (see Appendix A) is consistent with Figure 3.2 and other simulations of period very close to 1 day. For this reason, I believe that FAP is very low.

4.2.2 Stars with Less Secure Periods

Periods could be determined for many other stars. However, due to lower signal to noise their periods are less secure. The results are subdivided into two groups, 21 have FAPs between 1% and 5%, 26 have FAPs between 5% and 20%. These results are summarized in Tables 4.2 and 4.3. I expect that of the 47 periods listed in these tables, up to ten of them deviate from the true period by more than 5%. Figure 4.6 is a histogram of all the periods observed by this program. The darker regions indicate the stars with the more secure period determinations. In the histogram, the stars with the less

secure period determinations trace the other stars well. While specific stars may be wrong, the trends seem consistent between the more secure and less secure periods. Note the large clumping of periods at the rapidly rotating end of the diagram, with a small hump near 8 days. This could be interpreted as a continuous distribution with statistically insignificant deviations which give the appearance of gaps or a real gap. The continuous distribution peaks sharply at 2 days, and then is fit with long Lorentzian shoulders. Such a fit expects between one and two stars in the five and six day bins. The peak at 0 – 2 days is not as abrupt as it first appears. This height of this peak is an artifact of the binning. Since the duration of the rotation period is an observable, the data are binned by period length in days. However, periods of less than two days cover the bulk of the rotational phase space. All stars with rotational velocities greater than about 50 km/s are put in one of these two bins. Stars with rotational velocities less than this are spread among all the other bins.

In Figure 4.7, the data from the stars in the Orion OB1a association are shown separately from the stars near σ Orionis. Data from the ONC (Choi & Herbst 1996) are also shown. As displayed, the data show an evolution in time from less than 1 Myr in the top panel through about 2 Myr in the middle panel to about 10 Myr in the third panel. There is a trend which shows a bimodal distribution at early time with a fast rotator (FR) to slow rotator (SR) ratio of about 1:2 moving to a bimodal distribution with FR:SR=2:1 in about half a dex. At an age of about 10 million years, most of the SR group is gone.

A two–sided Kolmogrov–Smirnov (KS) test of the distribution of the ONC data with all the stars measured in this study shows a probability of $< 0.1\%$ of the sets being drawn from the same distribution. This indicates that the distributions are not at all similar. It should be noted that the comparison of the two data sets is not entirely fair. This is because the data set presented here and those from the ONC have different edge conditions. The data here are sensitive to periods below a day and insensitive to periods longer than 13 days. When the distributions of periods less than four days are compared, the KS test gives a higher probability of the distributions being drawn from the same parent population, but the probability is still $< 1\%$. However, the ONC data have a different low–end cut off than the data reported here. When the distributions of periods greater five days are compared for the ONC stars and those near σ Orionis the KS test gives a 47% probability of these distributions being drawn from the same population.

The distribution of the slow rotators looks similar. Differences in the high end distribution are accounted for by the duration of the J95 run which limited the longest measurable period to about 13 days. The Choi & Herbst data have a much longer observing run and are sensitive to longer periods. If long periods do exist among the PMS stars in Orion, I am not sensitive to them here. The Choi & Herbst data were monitored irrespective of colors or X–ray and spectral properties. However, they limit their sample to objects in the Jones & Walker (1988) catalog of proper motion ONC cluster members. Differences in the selection criteria may be important for the fast rotators.

The distributions of the fast rotators look somewhat different. This is

probably a function of our high speed sampling. The period searches conducted on this data were sensitive to periods up to four times faster than those in the surveys summarized in Figure 1.2. However, the data presented here show a dearth of three and four day rotators. Undoubtedly, some of the fast rotators indicated here (especially the ones with higher FAPs) are high frequency aliases of the true period. It is also likely that many rotational periods in the literature are low–frequency aliases. In these cases, the FAP or power measured would not be a proper measurement of the likelihood since the range of the true period was excluded from the calculation.

4.2.3 Stars without Periods

While periods were detected on 59 of 105 stars monitored only 12, ten in Orion OB1a and OB1b plus TAP 26 and P1724, had detections with FAP's below 1%. This seems consistent with results from the Van Vleck Observatory. At the Van Vleck observatory, they obtain data about 35 nights a year over the entire winter season, but they have a somewhat smaller aperture than the 1 meter used for the bulk of the results presented here. The Van Vleck Observatory has reported periods for 75 stars (Choi & Herbst 1996) and variability has been seen in 186 stars (Attridge & Herbst 1992) over four years. In general, they report that they can only measure rotation periods for about 10% of their target stars in any given season (Herbst 1996). It is unclear what fraction 186 is of the total number of Jones & Walker (1988) objects in their fields.

Several factors contributed in keeping the ratio of monitored stars to detected periods low. First of all, as demonstrated in the previous section, the variability of the stars can be complicated, especially when inclination effects and flares are included. Some stars had very little signal; at least 20% of the X–ray sources monitored exhibited variations which were less than the mean noise level in the field standard stars.[1] Exposures were calculated so that the brightest X–ray sources, usually about 11th magnitude at V, would be well exposed. Unfortunately, this causes fairly large errors in dimmer stars. The brightest X–ray sources themselves usually showed very little variability since the bulk of these stars are G7 and earlier. At the other end of the scale, some of the sources showed huge variability of well over a magnitude. These could be early–type T Tauri stars (ETTS; Herbst et al. 1994) or cTTs with highly variable accretion.

[1]The sensitivity limit varied from field to field on the basis on the brightest available field standard star. The mean noise level in the field standards was about 5%.

Stars with secure rotation period determinations

Star	< V >	Δ V	Δ R	Δ I	Period	FAP
TAP 26	—	0.16	0.15	0.14	0.715	< 0.1%
P1724	—	0.17	0.22	0.21	0.85	< 0.01%
4771 1049	12.92	0.14	0.13	0.07	1.57	< 1%
4771 1097	14.03	0.17	0.15	0.08	0.98	< 0.1%
4771 0901	15.45	0.53	0.43	0.22	8.10	< 1%
0101 2447	15.22	0.31	0.28	0.18	1.05	< 0.1%
J052426+0118	15.18	0.12	0.11	0.08	1.09	< 1%
0101 0756	14.28	0.16	0.12	0.10	1.26	< 0.1%
R053904-0229	16.97	0.41	0.20	0.12	1.10	< 1%
4771 0947	14.77	0.30	0.27	0.31	1.12	< 1%

Table 4.1: Periods measured by this program with high confidence. The table lists the mean magnitudes of each star measured relative to the reference stars. The Δ magnitude value is one–half of the peak to peak amplitude of the polynomial fit. The false alarm probability is also listed.

Periods of stars measured with lower confidence

Star	< V >	Δ V	Δ R	Δ I	Period	FAP
4771 1051	13.62	0.19	0.18	0.12	12.2	< 1.5%
R053849-0238	14.53	0.17	0.15	0.15	12.9	< 1.5%
R053835-0231	14.15	0.12	0.13	0.09	9.1	< 2%
R053840-0230	14.79	0.17	0.13	0.12	1.16	< 2%
4771 0899	12.93	0.18	0.11	0.16	1.12	< 2%
R053859-0247	14.74	0.68	0.64	0.40	7.40	< 2%
R053853-0243	15.49	0.32	0.29	0.14	8.22	< 5%
4771 0854	12.62	0.08	0.09	0.10	3.40	< 5%
R053834-0235	13.58	0.17	0.11	0.08	2.27	< 2%
R053832-0235	14.62	0.09	0.06	0.04	1.08	< 5%
R053828-0236	16.10	0.18	0.15	0.11	4.80	< 5%
R053838-0236	13.92	0.19	0.14	0.05	1.23	< 5%
R053833-0236	16.30	0.10	0.14	0.16	1.30	< 5%
0101 1156	12.72	0.08	0.08	0.07	0.82	< 2%
J052422+0100	16.33	0.27	0.12	0.07	1.25	< 2%
0101 0657	12.70	0.08	0.06	0.09	1.29	< 2%
0101 0594	13.69	0.09	0.16	0.17	0.82	< 2%
J052439+0121	15.35	0.12	0.15	0.08	0.88	< 2%
J052505+0121	15.11	0.15	0.20	0.17	1.41	< 5%
0101 1579	14.50	0.08	0.10	0.13	3.60	< 2%
J052402+0057	15.95	0.25	0.40	0.12	1.21	< 2%
J052354+0055	15.09	0.13	0.09	0.05	1.16	< 5%
0101 0687	14.29	0.10	0.07	0.02	0.61	< 2%

Table 4.2: Periods measured by this program with medium confidence. The table headings are the same as in the previous table.

Highly uncertain period determinations

Star	< V >	Δ V	Δ R	Δ I	Period	FAP
R053844-0232	13.73	0.08	0.11	0.10	0.76	< 10%
4771 0080	14.74	0.49	0.57	0.37	0.90	< 10%
R053845-0241	15.51	0.04	0.16	0.12	1.13	< 10%
4771 0598	12.31	0.09	0.14	0.10	1.31	< 20%
R053922-0233	16.41	0.40	0.23	0.12	7.10	< 20%
4771 1092	13.89	0.12	0.12	0.11	1.30	< 20%
4771 1075	14.27	0.10	0.10	0.05	1.30	< 20%
R053931-0239	17.84	0.66	0.15	0.40	0.84	< 20%
4771 0543	13.59	0.12	0.13	0.08	0.88	< 20%
4771 1094	15.42	0.11	0.07	0.09	2.73	< 20%
4771 1056	13.34	0.04	0.05	0.06	1.28	< 20%
R053853-0238	14.67	0.04	0.04	0.06	3.64	< 20%
4771 1038	14.51	0.06	0.13	0.07	8.70	< 20%
4771 0945	15.24	0.07	0.06	0.18	1.45	< 10%
R053808-0235	16.12	0.15	0.10	0.11	0.91	< 10%
R053832-0235	14.62	0.09	0.06	0.04	1.08	< 10%
R053831-0235	15.32	0.49	0.48	0.33	7.28	< 10%
0101 1353	12.19	0.03	0.08	0.04	1.16	< 10%
0101 0636	13.80	0.07	0.05	0.10	1.30	< 10%
J052539+0125	16.13	0.08	0.12	0.06	0.66	< 20%
J052401+0056	15.88	0.17	0.13	0.05	1.12	< 10%
0101 1611	15.12	0.06	0.05	0.03	1.26	< 10%
0101 0496	16.30	0.19	0.11	0.03	0.55	< 10%
0101 0416	13.29	0.06	0.11	0.06	1.81	< 10%
0101 2437	13.59	0.15	0.15	0.07	1.28	< 10%
0101 0854	11.80	0.05	0.06	0.04	1.43	< 10%

Table 4.3: Periods measured by this program with relatively low confidence. The table headings are the same as in the previous tables.

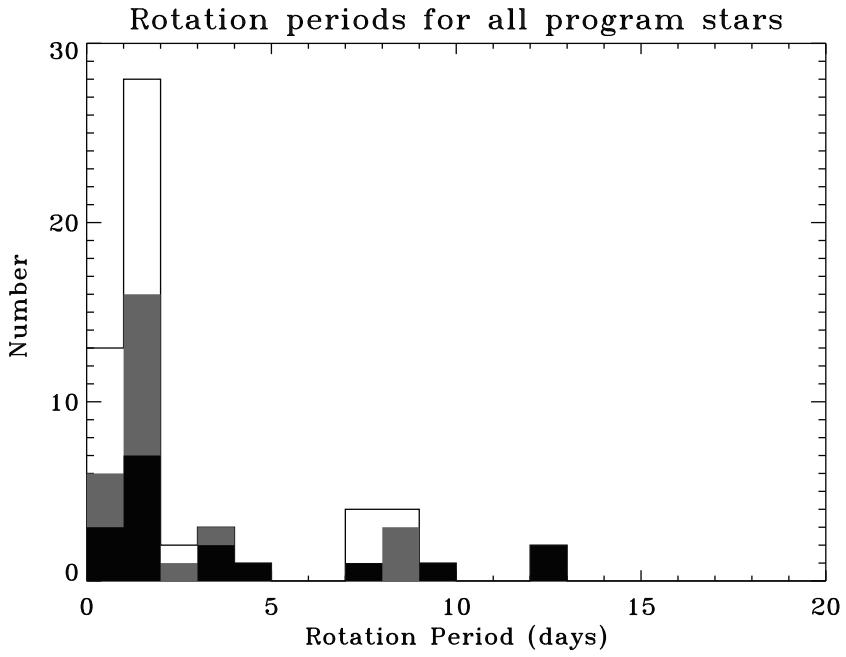

Figure 4.6: Histogram displaying all periods observed during the program. The darkened region represents those stars with FAP $< 2\%$. The more lightly shaded region represents stars with FAPs between 2% and 5%. The unshaded region represents stars with FAPs between 5% and 20%.

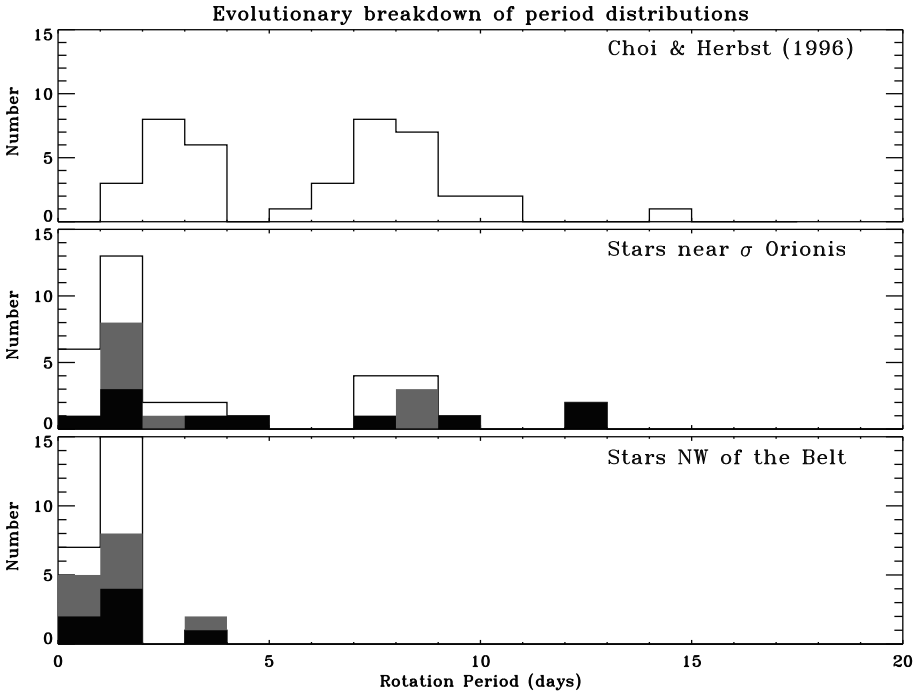

Figure 4.7: The three panels show histograms of rotational periods from three samples. The top sample are stars in Orion OB1d taken from Choi & Herbst (1996). The middle panel is the σ Orionis sample and the bottom panel is the Orion OB1a sample. In the lower two panels, the darkened region indicates stars with FAPs $< 2\%$, the shaded region indicates stars with FAPs between 2% and 5%. The unshaded region represents stars with FAPs between 5% and 20%.

Chapter 5

Discussion

Based on the data presented in Figure 4.7, I can suggest several conclusions about the evolution of young stars. The results of the Kolmogorov–Smirnov (KS) tests with the data presented here and those of Choi & Herbst (1996) on similar regions of the histogram indicate that there is something which holds stars near eight day periods. Stars in different regions also seem to share a similar mechanism which regulates the fast rotators. Further, it seems that stars migrate from the slow rotating (SR) group to the fast rotating (FR) group as a function of time. To gain the most information out of the data presented here one can combine these data with those of other authors. Before that can be done, one should first discuss the biases in the data sets.

5.1 Biases

The only criterion used for inclusion of a star in the monitoring program was that the star had to be an X–ray source. As such, there may be a bias

against observing stars with disks, since the disk might tend to obscure X–rays. This criterion is a very significant bias if there is a relationship between rotation and activity as has been suggested by several authors. Bouvier (1990) found a power law relation between the X–ray luminosity and the rotational velocity. He also found a similar relation between rotation period and X–ray flux. These relations hold for both cTTs and weak–lined T Tauri stars (wTTs). Bouvier used this to argue that the source of the X–rays is the same in both types of stars. However, the relationship between X–ray flux and rotational period is not clearly established. Walter (1996) points out that this perceived relation between X–ray luminosity and rotation may not be the result of physical connection, but instead it may be the result of an X–ray flux dependence on surface area which is a function of mass. In this case, the smaller (in radius) a star is, the less it radiates in X–rays. Since radius is a monotonic function of mass on the Hayashi track, as mass drops, so does X–ray luminosity. If period is a function of mass, a perceived relation between X–rays and rotation may not tell us anything about the dynamo mechanism.

In addition to the selection effects, several observational biases affect the final results. First of all, in any given field there were several target stars. The exposure times were designed to properly expose the brightest target in the field, usually 11th magnitude at V, so that 0.5% photometry would be possible. Generally, noise induced by fairly poor seeing and humidity conditions, lowered accuracy on the brightest sources to 1%. This means that the accuracy of the measurement of a 15th magnitude star in the same field is less than 10%. The detection of a period on a 0.5 $M_{\odot}$ star requires almost 10 times the variability

level as a 1.0 $M_{\odot}$ star. Thus, one is more likely to find periods for either more massive or more active stars.

Another observational bias is set by the duration of the observing runs. With the exception of the two stars monitored from Mount Stony Brook, all stars were monitored over an 11 night time interval. Because of this, the data are not very sensitive to periods longer than 11 days. The two that are found (R053844-0240 and R053849-0238), are extrapolations based on available data. Simulations with three observations per night demonstrated that a star with a period less than six days could be detected at a signal to noise level of about 2.5. Stars with periods of between six and 12 days required a S/N of about four. Stars with periods longer than 12 days required a S/N > 5 to detect the period. Thus, as the period of the star gets longer, one can only measure periods of heavily spotted stars.

To compensate for these short runs, several observations (3–4) were made of each star each night. Therefore, these data are sensitive to periods of less than one day. I include periods from 2 days down to 0.5 days (the length of the night) in my search window. Such periods were explicitly excluded from period search routines of Bouvier et al. (1993, 1995). This could account for the difference in the period of TAP 26. Period searches below two days were also generally excluded from the data presented in Eaton et al. (1995), Attridge & Herbst (1994) and Choi & Herbst (1996). This is one of the reasons that the KS test gave a very low probability of the data presented here and those from Choi & Herbst being drawn from the same parent distribution. Additionally, due to diurnal aliasing properties of the data, it is very hard to distinguish

between periods near a day and an alias of that period. Figure 5.1 shows an example of this for R053844-0240. The data folded on the 1.09 and 0.91 day peaks in the periodogram show almost as strong a sinusoidal behavior as those folded on the 12.2 day peak. The 12.2 day period was chosen as the correct one since it has a smaller deviation from the fit than the shorter ones. Taking these biases as a whole, some of the higher FAP periods listed as just below one day may be just above one day. Also, some 2–4 day periods published by other authors may in fact be < 2 days. The two data sets presented here have identical selection effects. The data from the SFRs in the σ Orionis region and those in Orion OB1a seem similar in spite of the large age difference.

5.2 Relations

Mindful of these biases, I can now explore the relations between the measured rotation periods and various other observables. The hypothesis behind monitoring stellar variability is that active stars have asymmetric spot distributions on their photospheres. It has been argued (Bouvier 1990) that if the magnetic field is a function of a dynamo, then the faster rotators should be more active. Taking this to its logical extension, the stronger the activity, the greater the spot coverage, and thus the stronger the observed variability should be, so long as the spot filling factor does not exceed 50%. Choi & Herbst (1996) were surprised to note the opposite effect. They found that only stars with rotation periods greater than seven days show variations greater than 0.4 magnitudes at I. Bouvier et al. (1995) found that wTTs they observed did not

vary by more than half a magnitude in B or V while the cTTs varied by over a magnitude. In Figure 5.2, a plot of rotation period versus observed variability is shown. V–band is plotted because of its greater sensitivity to spots. Almost 30% of the slow rotators show variability of greater than 0.4 magnitudes at V-band, while only 2 rapidly rotating stars show such variability. Both of those stars had very high FAPs. Overall, the mean value of the V-band modulation of the stars with rotation periods < 4 days is 0.14 ± 0.11 magnitudes, while the modulation for the slower rotators is 0.32 ± 0.18 magnitudes. If I assume that the stars which are more slowly rotating still have or recently lost their disks, the trend in these results, while not as strong, is in agreement with analysis of Herbst et al. (1994). Among PMS stars without disks, they found that the observed variability had a mean of 0.32 ± 0.2 magnitudes in the V-band. They find the cTTs with larger amplitude variations, a mean $0.89\pm$ 0.66 magnitudes.

I did not observe objects as variable as those in the study of Herbst et al. (1994). This may be due to selection effects. The optical sources of variability on cTTs seem to be related to the disk and accretion (Herbst et al. 1994). X–ray selection not only selects out the most X–ray active stars, it also singles out the more massive, G and K stars, ignoring the M stars. Prosser et al. (1993a) demonstrated a relation between X–ray flux and spectral type in ZAMS stars. As shown in Figure 5.3, this dependence does not translate itself into a simple relation between rotation period and spectral type for the PMS stars. Since spectral data for most of the stars with rotation periods are not available, R−I color was taken to be a proxy for spectral type (Figure 5.4).

R−I color was chosen since it was available for all stars and it is least affected by both from reddening extinction effects (which attenuate blue wavelengths more strongly than red wavelengths) and by confusion caused by an active chromosphere (which is a high temperature effect and thus is more apparent in blue wavelengths). There is no apparent direct relation between rotation and spectral type.

That the highest mass stars are rotating most quickly may be an evolutionary effect. Such stars evolve more quickly than low mass stars. Thus, they may lose their disks more quickly, so that there are no slowly rotating high mass stars left to observe by the age of Orion OB1b. However, Figure 5.4 does not confirm this. The bias towards monitoring only X–ray active sources confuses any possible interpretation. Note that in the Pleiades, while stars later than about K0 appear to have saturated X–ray luminosities, in earlier types the relative X–ray luminosity decreases as mass increases (Prosser et al. 1993). In Orion OB1a and b, the most evolved of these stars are starting on their radiative tracks, so they are no longer fully convective.

5.3 Evolutionary Effects

Edwards et al. (1993) noted that stars with near–IR flux excess have longer rotation periods than stars with more normal photospheric IR colors. They attributed this to a mechanism which regulated stellar angular momentum through the accretion disk. More recently, Shu et al. (1994) have incorporated this into their model for bipolar flows from disk winds. In Figure 5.5,

rotation periods are plotted against H−K color for the stars near σ Orionis. The result here is similar to that of Figure 5.2. While none of the rapidly rotating stars have H−K greater than 0.4, over 3 of the 9 slower rotators do.[1] The lack or presence of disks seems to be primarily responsible for the bimodal distribution of rotation periods first noted by Attridge & Herbst (1992).

Although many slow rotators show H−K excesses, many do not. This is true also in the results presented by Edwards et al. (1993). This means that while the existence of optically thick disk material might be linked to slow rotation periods, it is *not* necessary. Since the IR data presented here have large measurement errors, any estimate of evolutionary rates would be extremely rough. One can say that at an age of 2 Myr, 70% of the slow rotators do not have large disk signatures. The data presented here also show a dearth of periods from 3–7 days. While some of this may be due to sampling effects, the data seem to indicate that after a star loses its disk, either it continues its slow rotation for a period of time and then a rapid increase in rotation rate commences or spin up does not necessarily follow the loss of the disk.

If stars maintain their disks for a very long time, then by the time they lose their disks they have achieved their final internal configuration, and no additional spin–up occurs. There are two competing effects to consider here: contraction which leads to an increased rotation rate and core formation which can act as a brake. In the case of contraction, the star gets smaller and the rotation rate must increase to maintain the star's angular momentum. This

[1]Edwards et al. (1993) uses H-K=0.2 as their cut off for stars without disks. I use 0.4 as an upper limit because the errors in H-K can be ± 0.1.

assumes that the star is rigidly rotating. Once a star forms a relatively massive core, the envelope is freed from this constraint. If the core contains the bulk of the mass, it will spin–up to maintain angular momentum, but the stellar photosphere, which is what is observed, does not have to follow suit since it contains relatively little mass and thus little angular momentum. If the star loses its disk after core formation, it may be too late for photospheric spin–up to occur. Angular momentum will still be transferred from the core to the photosphere, but the rate at which the photosphere accelerates is a strong function of the strength of the coupling between the core and the envelope, which is not well determined.

When one compares the histograms shown in Figure 4.7, one is comparing three temporal epochs, < 1 Myr, ~ 2 Myr and ~ 10 Myr. It seems likely that the difference among the three plots is evolutionary in nature. It follows that younger stars are more likely to have disks, and as the stars evolve, they lose their disks and spin–up. There is a great deal of evidence that stars lose their disks as function of time. While evidence for disks is observed around all cTTs, no low mass main sequence star has ever been observed to possess an optically thick disk. The transient nature of disks around stars was first noted by Herbig (1978) who suggested that there should exist a population of stars between the main sequence and what are now called cTTs. More recently the data of Sterzik et al. (1995) show the ratio of nTTs to cTTs increases with increasing distance from dark clouds. The difference in IR colors between the FR and SR is indicative of disk involvement. The change in the ratio of FR to SR may be a manifestation of young stars losing their disks in time.

5.4 Rapidly Rotating Stars

Once a star loses its disk, it appears to be free to spin–up. In Chapter 1, it was demonstrated that $R \propto t^{-1/3}$, therefore, for a fully convective star, during a period of free spin–up, $P_\star \propto t^{-2/3}$. Here, t is the time that the star has spent on the Hayashi track. This implies that the fundamental time scale for determining the rotational period at the ZAMS is the disk survival time, T_{DS}. For example, if a 2 Myr old star is rotating at 8.25 days when loses its disk, it will be a 4 day rotator in 6 Myr. But, if the star is 0.5 Myr old star when it loses its disk, then, it will be a 4 day rotator in 1.5 Myr. (Both cases assume the star is freely spinning up after disk loss.) A star crosses the four to six day gap in the same time as T_{DS}. Choi & Herbst (1996) show that for star's rotation rate to increase from 8 to 2.5 days, the mean of their FR distribution, is $\sim 6T_{DS}$. By the time a star reaches the $\sim$ 1 day periods seen in some stars in Orion OB1a and b it must have lost their disk a relatively long time ago, and have spent only 5% of their post–birthline, PMS lifetime with a disk.

Many of the stars in the σ Orionis cluster have rotation periods of about one day and are about about 2 Myr old. This means that these stars must have lost their disk at an age of about 100,000 years, with a few losing their disks as early as 50,000 years after t_0 (the initial time for the tracks.) This is quite consistent with disk survival times measured in the Taurus–Auriga T association (cf. Walter et al. 1988; Skrutskie et al. 1989; Wolk & Walter 1996) using both IR and spectral methods of disk detection.

Stars in the Orion OB1a sample do not show a markedly

different distribution among the fast rotators. These stars are roughly 10 Myr old. Applying the same arguments to these stars as were applied to stars near σ Orionis, we arrive at the conclusion that the rapid rotators here lost their disks in at most 500,000 years. The most rapid rotation period among the Orion OB1a stars is about 0.7 days, which means that such a star would have lost its disk at an age of no older than 250,000 years. This is a factor of five higher than the similar number for the younger Orion OB1b stars. Another way to state this result is that stars which rotate with the same period as stars which are five times older must have held on to their disks five times longer. But this is a just a manifestation of the increased age of the cluster. It is surprising that the FR distributions look as similar as they do. If stars continue free spin–up for the duration of their convective tracks, (all but five X–ray active stars in the Orion OB1a sample are still on their convective tracks) then the Orion OB1a stars should show much faster periods than the Orion OB1b sample. This is not the case. Assuming this model is correct, it is hard to understand why the physical conditions of these stars would be different in exactly the right way so that the rotation period distribution of the slow rotators looks the same in two associations of different age. The point is, the simple free spin–up after disk loss model does not quite work and the other mechanisms must come into play.

Observational biases should not account for this discrepancy since both the Orion OB1a and OB1b samples were subject to the same criteria. Nor is there evidence for an intrinsic difference between the star formation mechanisms in Orion OB1a and those in Orion OB1b and the Taurus T association.

Instead, these data are suggestive of an internal braking mechanism which prevents stars at certain evolutionary epochs from exceeding a certain spin rate. It is unclear as of yet how such braking mechanism would work, but it should be pointed out that stars of greater than 0.5 $M_{\odot}$ develop radiative cores while still on their convective tracks (Barnes 1996). It is possible for internal braking to occur between the convective and radiative zones of stars still on their putative convective tracks. Barnes & Sofia (1996) argue for a saturation of angular momentum loss beyond a threshold speed. If the magnetic field is proportional to some power of the rotational period ($B_o \propto \Omega^a$, Linsky et al. 1983), and the magnetic field is subject to saturation, this will naturally slow the acceleration of the rotational period. The models of Barnes & Sofia were designed to explain UFRs to which the data presented here are not sensitive. However, their results show that angular momentum saturation does brake stars at an age of 70 Myr. In their model, such braking commences at an age of 2 Myr and has a significant effect by the age of 10 Myr. Therefore angular momentum saturation could be the cause of the similarity among the distributions of the fast rotators.

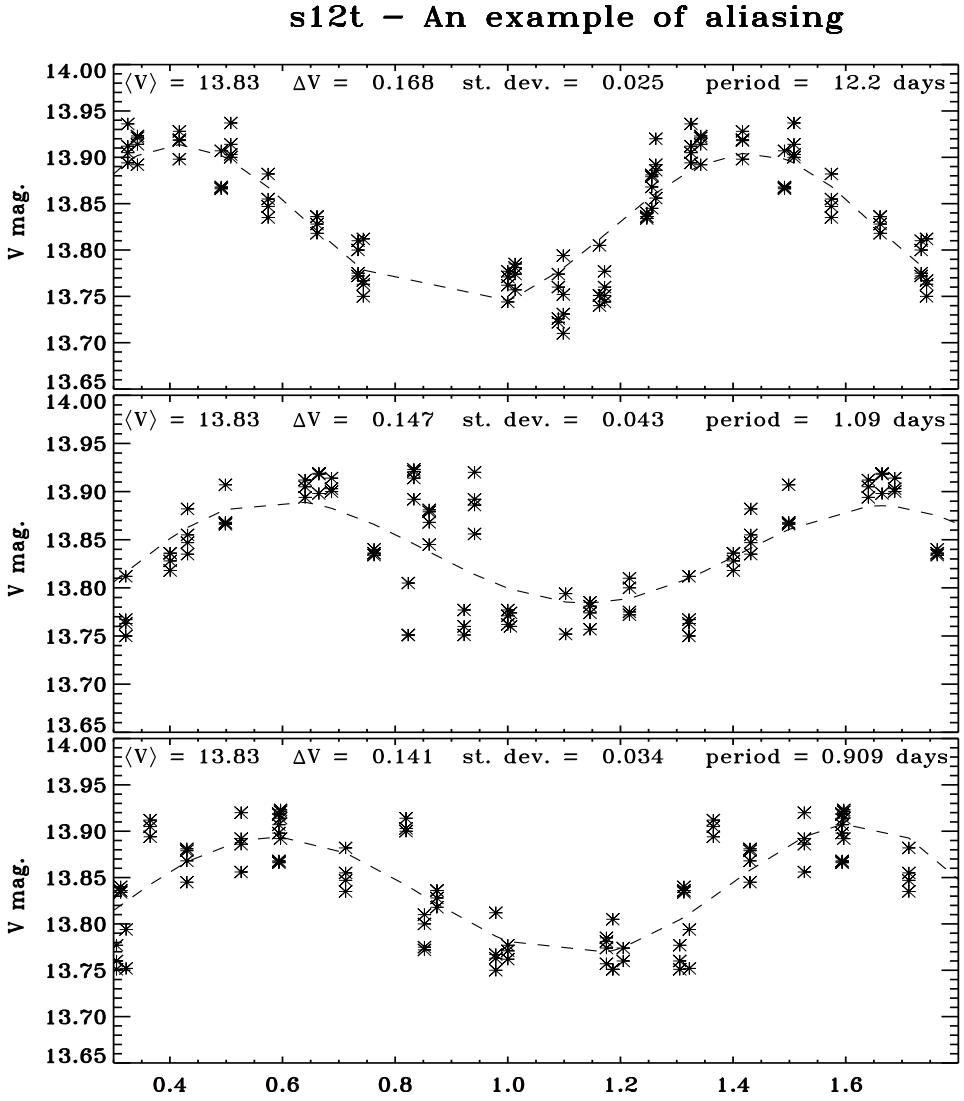

Figure 5.1: An example of aliasing. V–band data for R053844-0240 folded on 3 different periods. Comparison of the deviations to the fit indicates that the longest period is correct. The full 3–band lightcurves are given in Appendix B.

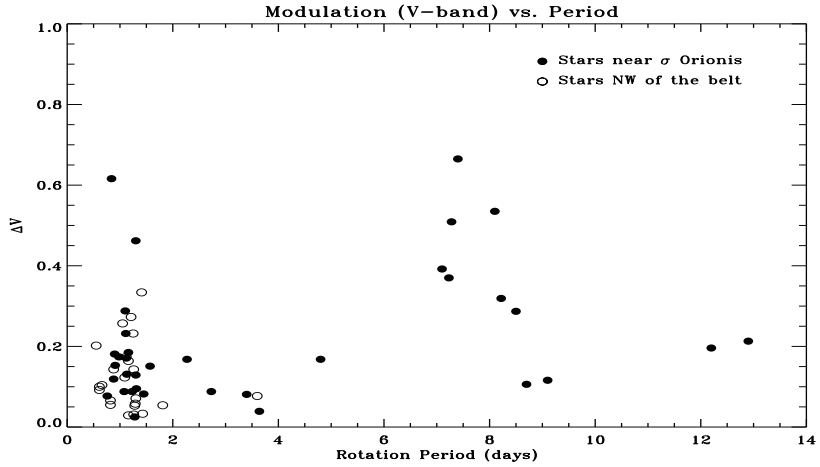

Figure 5.2: Amplitude in the modulation of the V magnitude, plotted vs. period. Filled circles represent stars near σ Orionis, open circles indicate stars northwest of the belt of Orion.

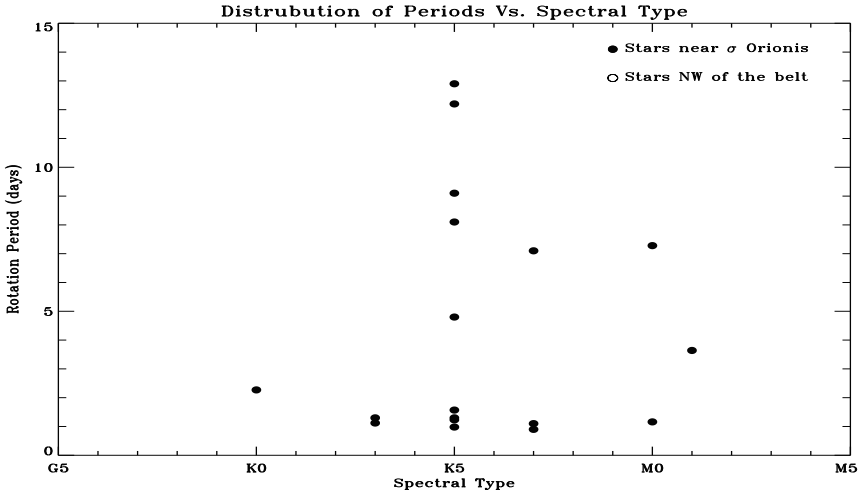

Figure 5.3: Spectral type of stars plotted vs. period for all stars with observed spectra and rotation periods.

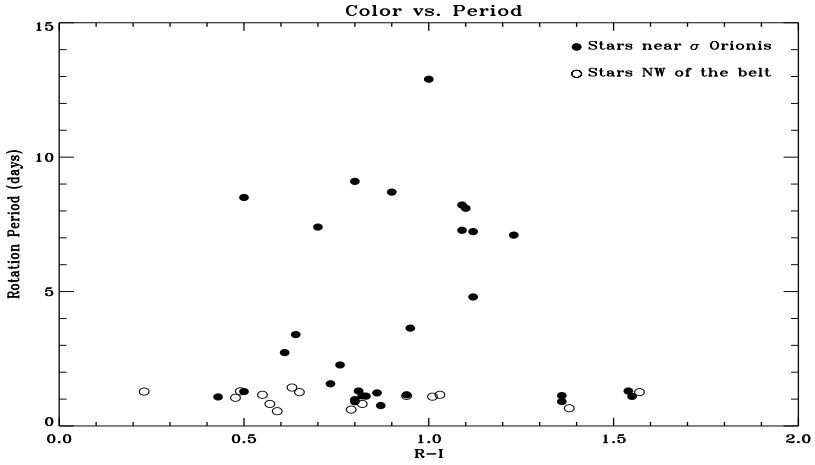

Figure 5.4: R−I color vs. period for all stars with observed rotational periods. Filled circles represent stars near σ Orionis, open circles indicate stars northwest of the belt of Orion.

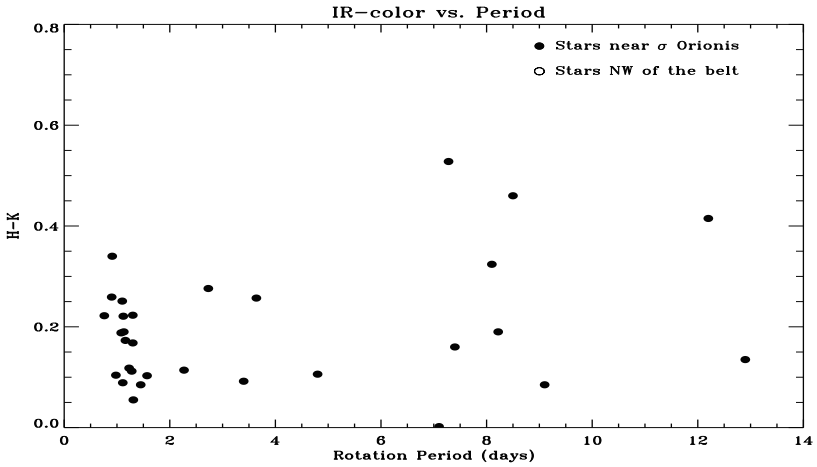

Figure 5.5: Infrared color vs. period for stars near σ Orionis.

Chapter 6

Conclusions

I began this dissertation with a discussion of the status of our understanding of the rotational evolution of young stars. The existence of UFRs at the ZAMS is a quandary for the understanding of the theoretical development of young stars. By studying the rotation of PMS stars in Orion OB1a and OB1b, I hoped to gather some insights to the evolution of rotation in young stars.

In Chapter 2, I laid the groundwork for the rotational investigation by performing optical follow-up to X–ray observations in regions of star formation. First, optical photometry showed that the X–ray sources lay in a well-defined locus, about a magnitude and a half above the main sequence. Infrared photometry and optical spectroscopy were available for a small subset of stars for which I was able to measure extinctions and luminosities. The small size of the data set which could be processed this way and the large variations within the dereddened group made age determination difficult, but showed that the Orion OB1b stars are about 0.5 dex older than the Orion OB1a stars. In an effort to understand the incompleteness of my data, I carried out optical photometry

on every star in the observed region of the two X–ray fields. I discovered that, in addition to the background stars, there exists a population of X–ray quiet stars which occupy the same region of the color–magnitude diagram as the X–ray sources. While a distance estimate is required to demonstrate that any given star is PMS, follow–up spectroscopy among the brightest of these stars indicates that many of them are PMS. Thus, the photometric techniques may give us a method of identifying all the PMS stars in a given region. It may also provide a method of selecting PMS stars for future investigations which is independent of their physical properties. Additionally, the X–ray quiet PMS population occupies all mass ranges from 1.0 $M_{\odot}$ down to the brown dwarf limit. The magnitude limit on the optical observations was such that it prevented the unambiguous detection of brown dwarfs. The are not data sufficient to prove a change in the slope of the initial mass function at very low mass. The main results of the photometric study include:

- Roughly 150 newly found PMS stars are introduced. For the most part, these stars are considered PMS solely on the basis of their colors. In the case of sources for which we do have spectra, the spectra verify their PMS nature. These data indicate that between 70% and 90% of PMS stars near σ Orionis are nTTs. A somewhat higher fraction of stars in Orion OB1a are nTTs. For some of the stars in Orion OB1b infrared colors have been measured.

- X–ray observations in regions of star formation are efficient in detecting PMS stars. However, X–ray studies are not complete. At the sensitivity

limit of ROSAT deep (25 Ksec) X–ray pointings, about one–third of the PMS stars are not X–ray sources. Additionally, there are almost as many PMS stars below the X–ray sensitivity limit as were detected by their X–ray emission. Such X–ray quiet stars extend down to, and perhaps below, the brown dwarf limit.

Once the PMS nature of the X–ray sources was established, I tested my ability to detect periods on stars observed during the 11 night run at the WISE observatory. I found that the periodogram code needs fairly high signal to noise to work effectively on such a short data set. In addition, the non–sinusoidal nature of the stellar signals makes period detection even more difficult. To make period detection more robust, I describe the criteria which I use to determine the validity of periods which are detected. The main results of the rotational study are:

- Rotation periods were measured for 63 X–ray selected PMS stars. A bimodal distribution is observed for the rotation periods of the stars in Orion OB1b, but not for the stars in Orion OB1a. This is probably not due to observational biases since those are the same for both samples. In concurrence with prior works, these results are suggestive of disk regulation of stellar spin–up. As the stars evolve, the bimodal nature of the distribution ceases. There are several possible aspects to this change.

    1. This type of evolution is predicted by the disk-braking model. If all the stars in a given observation have lost their disks at a time in the sufficiently distant past, then all should be fast rotators.

2. However, both here and in Edwards et al. (1993) there are many young stars which are slow rotators and yet show no IR disk signatures. Some stars may maintain their disks so long that by the time the braking mechanism has been removed the stellar core is close its final configurations. Such stars are unable to spin–up.

- Similarities in the distribution of the slow rotators observed here and those observed in other star forming regions indicate that a similar mechanism controls the rotation of the slow rotators in all star forming regions. Data suggest a link between existence of disks and the slow rotation. It is unclear how to account for slow rotators without disks, and the dearth of stars with rotation periods of between 4 – 6 days.

- Similarities in the distribution of the rotation periods of the fast rotators, independent of age, indicate that PMS stars are not subject to an indefinite period of spin–up after they lose their disks. Therefore, some self–regulation mechanism must come into play. While it is possible that stars in Orion OB1b have no internal braking, stars in Orion OB1a are almost certainly under the influence of such a mechanism. Threshold saturation as proposed by Barnes & Sofia (1996) has the proper time scale to be relevant.

The data presented here represent the start of the first systematic study of the evolution of low mass stars in the Orion OB1a and OB1b sub–associations. The data provide some of the most convincing evidence to date that the nTTs represent an evolutionary stage between cTTs and ZAMS stars, as well as

strong support for disk braking of spin–up. The data have also demonstrated deficiencies with the reliance on X–ray surveys to find nTTs. While more sensitive X–ray pointing will be available in the future using Advanced X–ray Analysis Facility (AXAF), wide–field optical photometry supplemented with multi–object spectroscopy has now surpassed X–rays as the premier method of detecting PMS stars. This new knowledge will allow future work to escape the selection effects which have hampered our understanding of how stars form.

Future work should concentrate on the rotation periods of the non–X–ray detected PMS stars. Many of these stars were subject to monitoring, but these data were excluded from the period searches since there was originally no reason to suspect any unusual behavior by these stars. I will more generally study the recently unveiled population of PMS stars with masses below about 0.5 $M_{\odot}$ as well as the spectral properties of the X–ray quiet PMS stars. Future planned observations also include deeper mapping of regions of star formation in V, R and I bands. Such data may allow us to search for the low end of the IMF and determine whether such an end exists. This would tell us how low mass an object can be and still form like a star or if there is some limit on the minimum mass dictated by the physics of star formation.

Appendix A

Finding Charts

This section contains finding charts for all X–ray sources and candidate PMS stars. The charts are separated into two sections. The first is devoted to identification of the X–ray sources. The second is devoted to the identification of non–X–ray detected PMS stars. There are 12 finding charts in each section, the first four surround σ Orionis. The other eight are located in Orion OB1a, northwest of the belt stars. The images are taken from the Digitized Sky Survey (1993).

In most cases the stellar ID is derived from the coordinates of the source. The exceptions to this rule are the guide stars. In the first 12 charts, the overlays on the charts and the coordinates indicate the position of the X–ray source. If a Guide Star Catalog ID is given, the GSC source is considered a likely optical counterpart, the coordinates listed are the coordinates of the X–ray source. Note that in some cases single X–ray sources were identified with multiple GSC stars. In other cases, a single GSC star can be associated with more than one ROSAT source. This ambiguity does not exist in the final

12 charts, since these sources were originally identified optically.

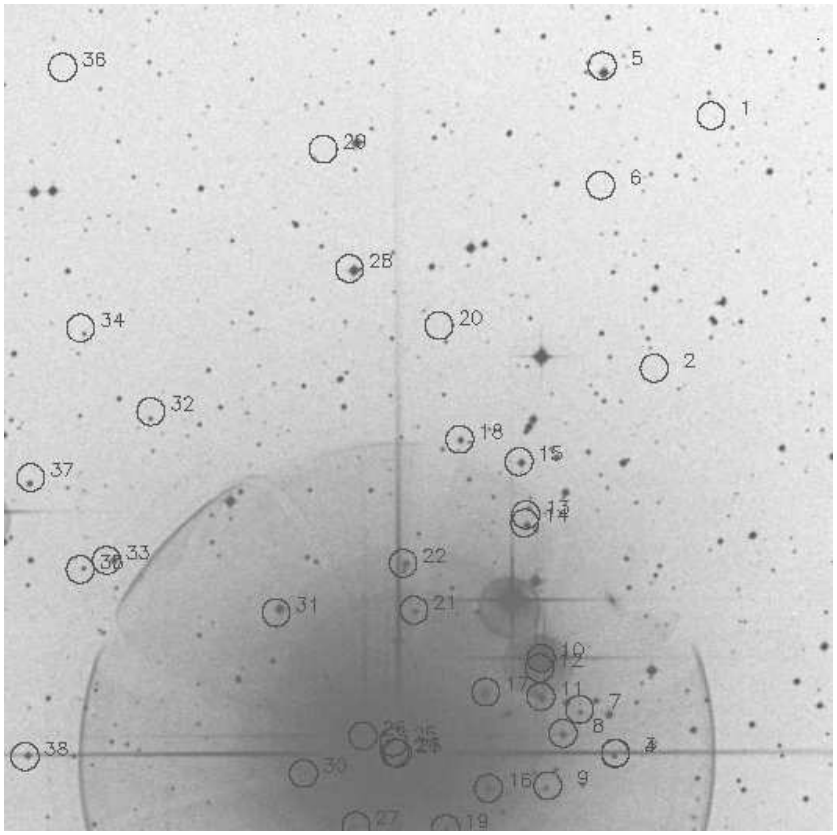

Figure A.1: ROSAT sources north of σ Orionis.

Number	ID	RA(2000)	DEC(2000)	Number	ID	RA(2000)	DEC(2000)
1	R053822-0224	5 38 22.0	-2 24 24.0	2	R053826-0228	5 38 26.1	-2 28 59.0
3	R053828-0235	5 38 28.9	-2 35 58.0	4	R053828-0235	5 38 28.9	-2 35 59.0
5	4771 0751	5 38 29.9	-2 23 30.0	6	R053830-0225	5 38 30.0	-2 25 40.0
7	R053831-0235	5 38 31.5	-2 35 11.0	8	R053832-0235	5 38 32.7	-2 35 37.0
9	R053833-0236	5 38 33.8	-2 36 34.0	10	4771 1133	5 38 34.3	-2 34 15.0
11	R053834-0234	5 38 34.3	-2 34 57.0	12	4771 1133	5 38 34.4	-2 34 26.0
13	R053835-0231	5 38 35.4	-2 31 39.0	14	R053835-0231	5 38 35.5	-2 31 48.0
15	4771 1097	5 38 35.9	-2 30 41.0	16	R053838-0236	5 38 38.1	-2 36 37.0
17	4771 1147	5 38 38.3	-2 34 52.0	18	R053840-0230	5 38 40.2	-2 30 17.0
19	R053841-0237	5 38 41.2	-2 37 21.0	20	R053841-0228	5 38 41.7	-2 28 13.0
21	R053843-0233	5 38 43.5	-2 33 23.0	22	R053844-0232	5 38 44.3	-2 32 32.0
23	SIGMA ORI.	5 38 44.7	-2 35 59.0	24	SIGMA ORI.	5 38 44.9	-2 35 58.0
25	SIGMA ORI.	5 38 45.0	-2 35 47.0	26	R053847-0235	5 38 47.2	-2 35 40.0
27	R053847-0237	5 38 47.7	-2 37 18.0	28	4771 0899	5 38 48.2	-2 27 11.0
29	R053850-0225	5 38 50.1	-2 25 1.0	30	R053851-0236	5 38 51.5	-2 36 21.0
31	4771 1049	5 38 53.5	-2 33 26.0	32	R053902-0229	5 39 2.6	-2 29 47.0
33	4771 1075	5 39 5.8	-2 32 29.0	34	R053907-0228	5 39 7.7	-2 28 16.0
35	4771 1092	5 39 7.7	-2 32 39.0	36	R053909-0223	5 39 9.0	-2 23 32.0
37	4771 0901	5 39 11.3	-2 30 59.0	38	4771 1038	5 39 11.7	-2 36 3.0

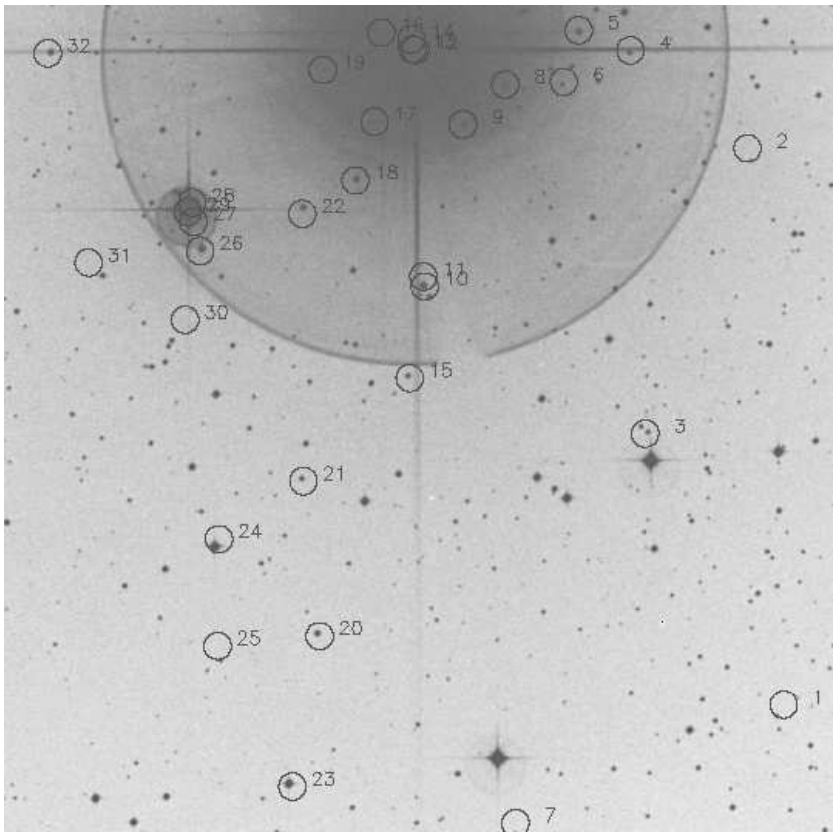

Figure A.2: ROSAT sources south of σ Orionis.

Number	ID	RA(2000)	DEC(2000)	Number	ID	RA(2000)	DEC(2000)
1	R053817-0248	5 38 17.6	-2 48 1.0	2	R053820-0237	5 38 20.3	-2 37 47.0
3	R053827-0243	5 38 27.8	-2 43 2.0	4	R053828-0235	5 38 28.9	-2 35 59.0
5	R053832-0235	5 38 32.7	-2 35 37.0	6	R053833-0236	5 38 33.8	-2 36 34.0
7	R053837-0250	5 38 37.3	-2 50 12.0	8	R053838-0236	5 38 38.1	-2 36 37.0
9	R053841-0237	5 38 41.2	-2 37 21.0	10	R053844-0240	5 38 44.0	-2 40 20.0
11	4771 1051	5 38 44.1	-2 40 9.0	12	SIGMA ORI.	5 38 44.7	-2 35 59.0
13	SIGMA ORI.	5 38 44.9	-2 35 58.0	14	SIGMA ORI.	5 38 45.0	-2 35 47.0
15	R053845-0242	5 38 45.1	-2 42 1.0	16	R053847-0235	5 38 47.2	-2 35 40.0
17	R053847-0237	5 38 47.7	-2 37 18.0	18	R053849-0238	5 38 49.1	-2 38 23.0
19	R053851-0236	5 38 51.5	-2 36 21.0	20	4771 0080	5 38 51.7	-2 46 46.0
21	4771 1078	5 38 52.9	-2 43 55.0	22	R053853-0239	5 38 53.0	-2 39 0.0
23	R053853-0249	5 38 53.7	-2 49 32.0	24	R053859-0244	5 38 59.1	-2 44 59.0
25	R053859-0246	5 38 59.2	-2 46 57.0	26	4771 1056	5 39 0.5	-2 39 41.0
27	4771 1103	5 39 1.0	-2 39 9.0	28	4771 1103	5 39 1.1	-2 38 48.0
29	4771 1103	5 39 1.4	-2 38 58.0	30	R053901-0240	5 39 1.6	-2 40 57.0
31	R053908-0239	5 39 8.7	-2 39 54.0	32	4771 1038	5 39 11.7	-2 36 3.0

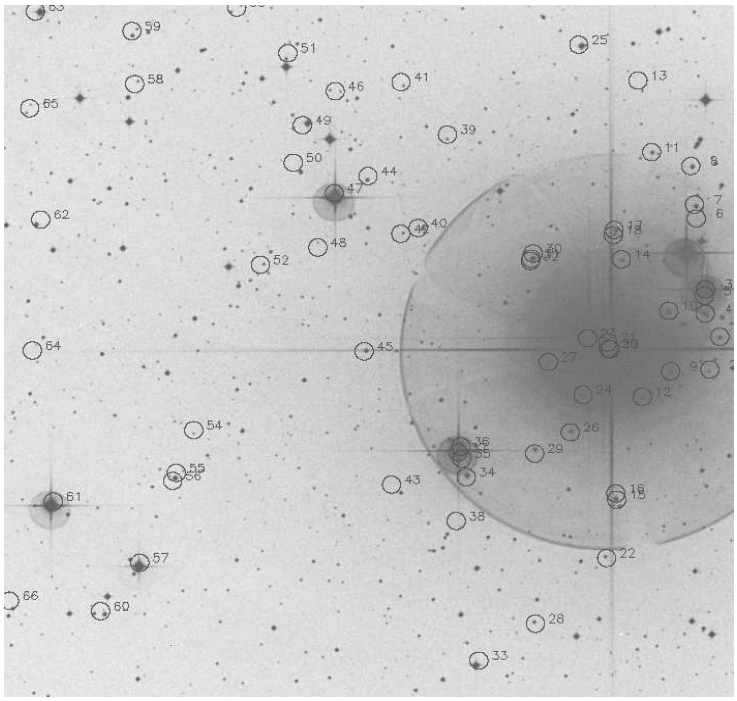

Figure A.3: ROSAT sources east of σ Orionis.

Number	ID	RA(2000)	DEC(2000)
1	R053832-0235	5 38 32.7	-2 35 37.0
3	4771 1133	5 38 34.3	-2 34 15.0
5	R053834-0234	5 38 34.4	-2 34 26.0
7	R053835-0231	5 38 35.5	-2 31 48.0
9	R053838-0236	5 38 38.1	-2 36 37.0
11	R053840-0230	5 38 40.2	-2 30 17.0
13	R053841-0228	5 38 41.7	-2 28 13.0
15	R053844-0240	5 38 44.0	-2 40 20.0
17	R053844-0232	5 38 44.3	-2 32 32.0
19	SIGMA ORI.	5 38 44.7	-2 35 59.0
21	SIGMA ORI.	5 38 45.0	-2 35 47.0
23	R053847-0235	5 38 47.2	-2 35 40.0
25	4771 0899	5 38 48.2	-2 27 11.0
27	R053851-0236	5 38 51.5	-2 36 21.0
29	R053853-0239	5 38 53.0	-2 39 0.0
31	R053853-0233	5 38 53.4	-2 33 22.0
33	4771 0026	5 38 59.1	-2 44 59.0
35	4771 1103	5 39 1.0	-2 39 9.0
37	4771 1103	5 39 1.4	-2 38 58.0
39	R053902-0229	5 39 2.6	-2 29 47.0
41	R053907-0228	5 39 7.7	-2 28 16.0
43	R053908-0239	5 39 8.7	-2 39 54.0
45	4771 1038	5 39 11.7	-2 36 3.0
47	4771 1073	5 39 15.0	-2 31 29.0
49	4771 0598	5 39 18.5	-2 29 31.0
51	R053920-0227	5 39 20.1	-2 27 26.0
53	R053925-0226	5 39 25.7	-2 26 7.0
55	4771 0953	5 39 32.3	-2 39 34.0
57	4771 0543	5 39 36.3	-2 42 10.0
59	R053937-0226	5 39 37.2	-2 26 48.0
61	4771 0685	5 39 45.8	-2 40 24.0
63	4771 0957	5 39 47.8	-2 26 14.0
65	R053948-0229	5 39 48.4	-2 29 2.0

Number	ID	RA(2000)	DEC(2000)
2	R053833-0236	5 38 33.8	-2 36 34.0
4	R053834-0234	5 38 34.3	-2 34 57.0
6	R053835-0232	5 38 35.3	-2 32 12.0
8	4771 1097	5 38 35.9	-2 30 41.0
10	4771 1147	5 38 38.3	-2 34 52.0
12	R053841-0237	5 38 41.2	-2 37 21.0
14	R053843-0233	5 38 43.5	-2 33 23.0
16	R053844-0240	5 38 44.1	-2 40 9.0
18	R053844-0232	5 38 44.4	-2 32 41.0
20	SIGMA ORI.	5 38 44.9	-2 35 58.0
22	R053845-0242	5 38 45.1	-2 42 1.0
24	R053847-0237	5 38 47.7	-2 37 18.0
26	R053849-0238	5 38 49.1	-2 38 23.0
28	R053852-0243	5 38 52.9	-2 43 55.0
30	R053853-0233	5 38 53.2	-2 33 13.0
32	R053853-0233	5 38 53.5	-2 33 26.0
34	4771 1056	5 39 0.5	-2 39 41.0
36	4771 1103	5 39 1.1	-2 38 48.0
38	R053901-0240	5 39 1.6	-2 40 57.0
40	4771 1075	5 39 5.8	-2 32 29.0
42	4771 1020	5 39 7.7	-2 32 39.0
44	4771 0901	5 39 11.3	-2 30 59.0
46	R053914-0228	5 39 14.9	-2 28 32.0
48	R053916-0233	5 39 16.8	-2 33 3.0
50	4771 0910	5 39 19.5	-2 30 36.0
52	R053923-0233	5 39 23.1	-2 33 33.0
54	R053930-0238	5 39 30.4	-2 38 20.0
56	4771 0953	5 39 32.7	-2 39 48.0
58	R053936-0228	5 39 36.9	-2 28 20.0
60	R053940-0243	5 39 40.6	-2 43 34.0
62	R053947-0232	5 39 47.2	-2 32 15.0
64	R053948-0236	5 39 48.1	-2 36 2.0
66	R053950-0243	5 39 50.6	-2 43 16.0

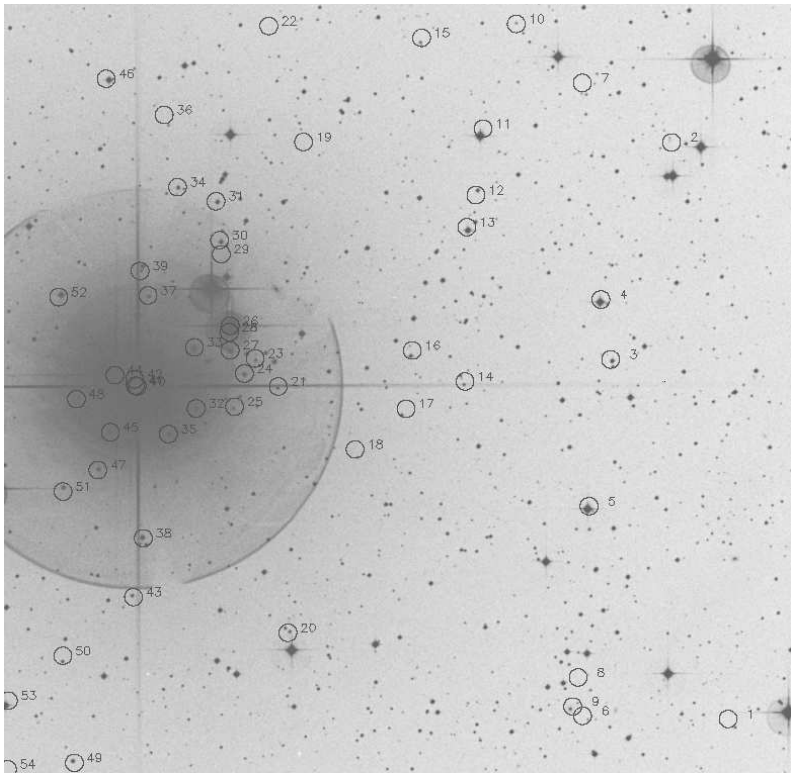

Figure A.4: ROSAT sources west of σ Orionis.

Number	ID	RA(2000)	DEC(2000)	Number	ID	RA(2000)	DEC(2000)
1	R053738-0245	5 37 38.5	-2 45 29.0	2	R053744-0228	5 37 44.9	-2 28 59.0
3	R053751-0235	5 37 51.7	-2 35 12.0	4	4771 0775	5 37 52.8	-2 33 29.0
5	4771 0921	5 37 54.1	-2 39 24.0	6	R053754-0245	5 37 54.8	-2 45 24.0
7	R053754-0227	5 37 54.9	-2 27 17.0	8	R053755-0244	5 37 55.3	-2 44 18.0
9	R053755-0245	5 37 55.9	-2 45 8.0	10	R053802-0225	5 38 2.3	-2 25 36.0
11	4771 0950	5 38 6.0	-2 28 36.0	12	4771 0947	5 38 6.8	-2 30 30.0
13	4771_0854	5 38 7.8	-2 31 25.0	14	R053808-0235	5 38 8.0	-2 35 50.0
15	R053812-0226	5 38 12.9	-2 26 0.0	16	4771 1069	5 38 13.9	-2 34 57.0
17	R053814-0236	5 38 14.6	-2 36 37.0	18	R053820-0237	5 38 20.3	-2 37 47.0
19	R053826-0228	5 38 26.1	-2 28 59.0	20	R053827-0243	5 38 27.8	-2 43 2.0
21	R053828-0235	5 38 28.9	-2 35 59.0	22	R053830-0225	5 38 30.0	-2 25 40.0
23	R053831-0235	5 38 31.5	-2 35 11.0	24	R053832-0235	5 38 32.7	-2 35 37.0
25	R053833-0236	5 38 33.8	-2 36 34.0	26	4771 1133	5 38 34.3	-2 34 15.0
27	R053834-0234	5 38 34.3	-2 34 57.0	28	4771 1133	5 38 34.4	-2 34 26.0
29	R053835-0232	5 38 35.3	-2 32 12.0	30	R053835-0231	5 38 35.5	-2 31 48.0
31	4771 1097	5 38 35.9	-2 30 41.0	32	R053838-0236	5 38 38.1	-2 36 37.0
33	4771 1147	5 38 38.3	-2 34 52.0	34	R053840-0230	5 38 40.2	-2 30 17.0
35	R053841-0237	5 38 41.2	-2 37 21.0	36	R053841-0228	5 38 41.7	-2 28 13.0
37	R053843-0233	5 38 43.5	-2 33 23.0	38	4771 1051	5 38 44.0	-2 40 20.0
39	R053844-0232	5 38 44.4	-2 32 41.0	40	SIGMA ORI.	5 38 44.7	-2 35 59.0
41	SIGMA ORI.	5 38 44.9	-2 35 58.0	42	SIGMA ORI.	5 38 45.0	-2 35 47.0
43	R053845-0242	5 38 45.1	-2 42 1.0	44	R053847-0235	5 38 47.2	-2 35 40.0
45	R053847-0237	5 38 47.7	-2 37 18.0	46	4771 0899	5 38 48.2	-2 27 11.0
47	R053849-0238	5 38 49.1	-2 38 23.0	48	R053851-0236	5 38 51.5	-2 36 21.0
49	4771 0080	5 38 51.7	-2 46 46.0	50	R053853-0243	5 38 53.0	-2 43 42.0
51	R053853-0239	5 38 53.0	-2 39 0.0	52	4771 1049	5 38 53.5	-2 33 26.0
53	4771 0026	5 38 59.1	-2 44 59.0	54	R053859-0246	5 38 59.2	-2 46 57.0

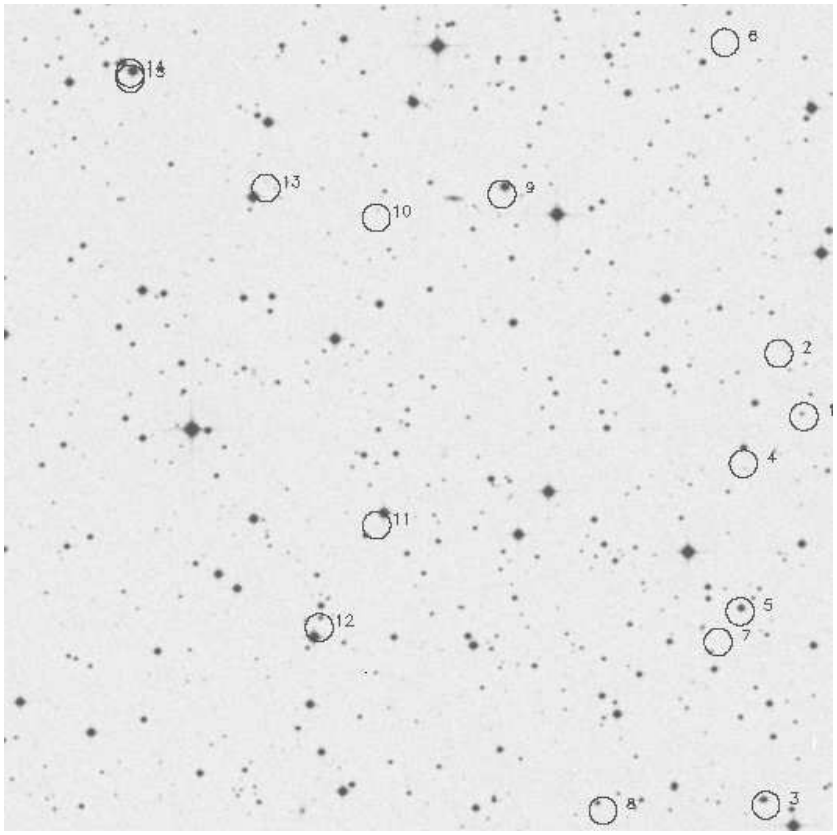

Figure A.5: ROSAT sources northwest of the belt of Orion (region 1)

Number	ID	RA(2000)	DEC(2000)	GSC	RA(2000)	DEC(2000)
1	J052347+0103	5 23 47.10	1 3 59.0			
2	J052348+0105	5 23 48.90	1 5 8.0			
3	J052350+0056	5 23 50.00	0 56 56.0	0101_01611	05 23 50.15	+00 57 1.5
4	J052351+0103	5 23 51.50	1 3 8.0			
5	J052351+0100	5 23 51.80	1 0 27.0	0101_01291	05 23 51.72	+01 00 30.1
6	J052352+0110	5 23 52.70	1 10 47.0			
7	J052353+0059	5 23 53.40	0 59 54.0			
8	J052401+0056	5 24 1.80	0 56 51.0			
9	J052408+0108	5 24 8.90	1 8 3.0	0101_00508	05 24 4.96	+01 07 40.5
10	J052418+0107	5 24 18.00	1 7 38.0			
11	J052418+0102	5 24 18.10	1 2 3.0	0101_01156+	05 24 17.56	+01 02 15.5
12	J052422+0100	5 24 22.30	1 0 12.0	0101_01336	05 24 22.71	+01 00 0.8
13	J052426+0108	5 24 26.00	1 8 11.0	0101_00522	05 24 26.97	+01 08 0.6
14	J052435+0110	5 24 35.80	1 10 17.0	0101_00657	05 24 35.61	+01 10 19.1
15	J052435+0110	5 24 35.80	1 10 11.0	0101_00657	05 24 35.61	+01 10 19.1

+ 0101_02447 05 24 18.95 +01 01 51.8 is also within the error circle.

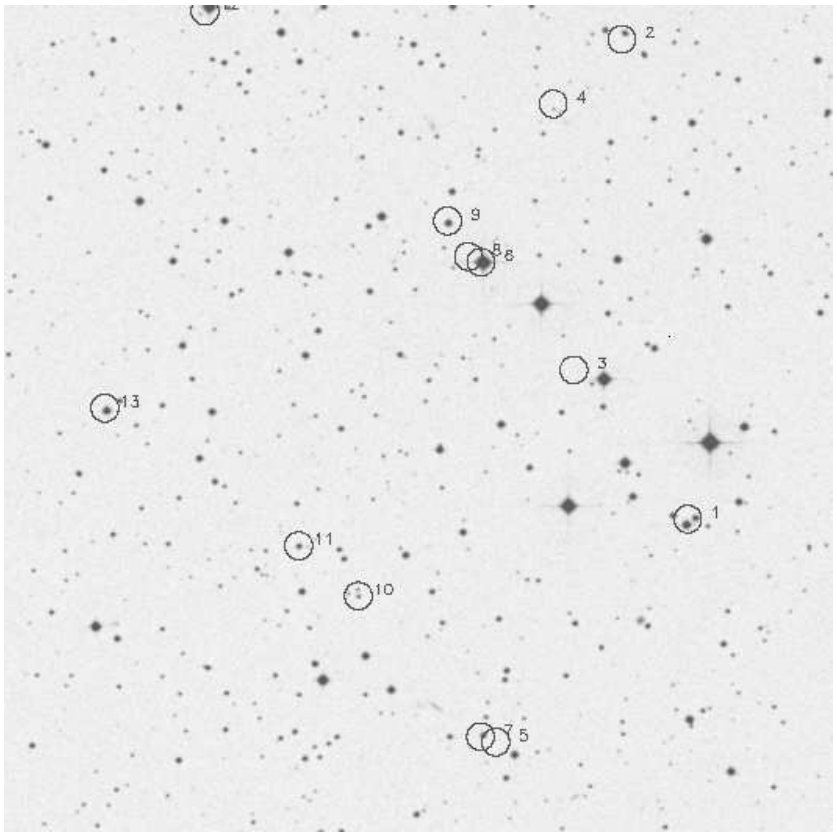

Figure A.6: ROSAT sources northwest of the belt of Orion (region 2)

Number	ID	RA(2000)	DEC(2000)	GSC	RA(2000)	DEC(2000)
1	J052411+0122	5 24 11.70	1 22 9.0	0101_00594	05 24 11.83	+01 22 2.3
2	J052416+0130	5 24 16.30	1 30 52.0			
3	J052419+0124	5 24 19.90	1 24 52.0			
4	J052421+0129	5 24 21.30	1 29 42.0			
5	J052425+0118	5 24 25.70	1 18 7.0			
6	J052426+0126	5 24 26.60	1 26 50.0			
7	J052426+0118	5 24 26.80	1 18 13.0			
8	J052427+0126	5 24 27.50	1 26 56.0	0101_00636	05 24 26.43	+01 26 49.0
9	J052429+0127	5 24 29.00	1 27 35.0	0101_00756	05 24 28.94	+01 27 32.1
10	J052435+0120	5 24 35.60	1 20 47.0			
11	J052439+0121	5 24 39.90	1 21 42.0			
12	J052446+0131	5 24 46.50	1 31 25.0	0101_00854	05 24 46.22	+01 31 28.7
13	J052453+0124	5 24 53.90	1 24 13.0	0101_00381	05 24 53.78	+01 24 9.3

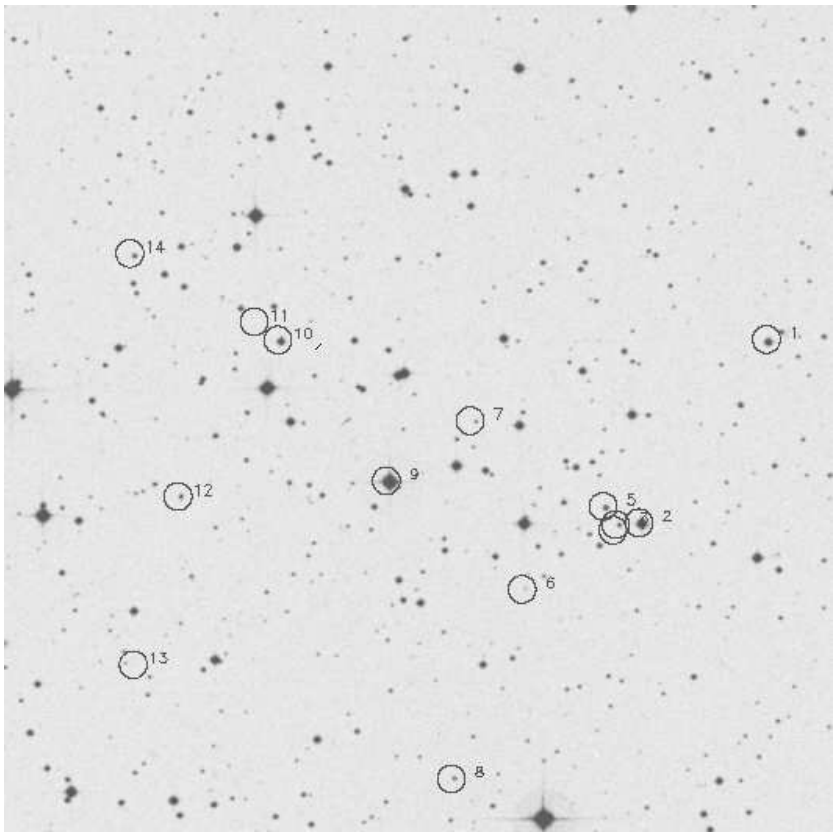

Figure A.7: ROSAT sources northwest of the belt of Orion (region 3)

Number	ID	RA(2000)	DEC(2000)	GSC	RA(2000)	DEC(2000)
1	J052453+0124	5 24 53.90	1 24 13.0	0101_00381	05 24 53.78	+01 24 9.3
2	J052503+0120	5 25 3.20	1 20 54.0	0101_00719	05 25 3.01	+01 20 52.6
3	J052504+0120	5 25 4.90	1 20 52.0			
4	J052505+0120	5 25 5.10	1 20 46.0			
5	J052505+0121	5 25 5.80	1 21 12.0	0101_02429	05 25 5.62	+01 21 10.1
6	J052511+0119	5 25 11.70	1 19 42.0			
7	J052515+0122	5 25 15.40	1 22 46.0			
8	J052516+0116	5 25 16.90	1 16 16.0			
9	J052521+0121	5 25 21.50	1 21 41.0	0101_00645	05 25 21.23	+01 21 38.8
10	J052529+0124	5 25 29.30	1 24 15.0	0101_00372	05 25 29.08	+01 24 13.1
11	J052531+0124	5 25 31.00	1 24 35.0			
12	J052536+0121	5 25 36.60	1 21 25.0			
13	J052539+0118	5 25 39.90	1 18 22.0			
14	J052540+0125	5 25 40.00	1 25 50.0			

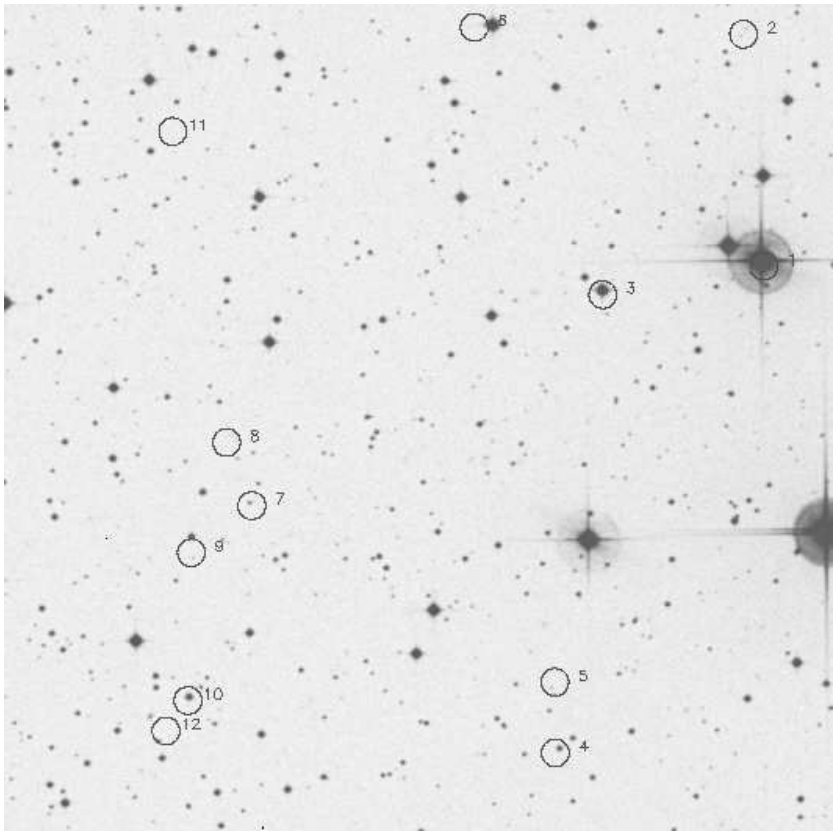

Figure A.8: ROSAT sources northwest of the belt of Orion (region 4)

Number	ID	RA(2000)	DEC(2000)	GSC	RA(2000)	DEC(2000)
1	J052309+0108	5 23 9.90	1 8 17.0	0101_02345+	05 23 10.07	+01 08 22.3
2	J052311+0112	5 23 11.30	1 12 30.0			
3	J052321+0107	5 23 21.60	1 7 47.0	0101_00518	05 23 21.66	+01 07 51.0
4	J052325+0059	5 23 25.20	0 59 28.0			
5	J052325+0100	5 23 25.20	1 0 45.0			
6	J052330+0112	5 23 30.80	1 12 39.0			
7	J052347+0103	5 23 47.10	1 3 59.0			
8	J052348+0105	5 23 48.90	1 5 8.0			
9	J052351+0103	5 23 51.50	1 3 8.0			
10	J052351+0100	5 23 51.80	1 0 27.0	0101_01291	05 23 51.72	+01 00 30.1
11	J052352+0110	5 23 52.70	1 10 47.0			
12	J052353+0059	5 23 53.40	0 59 54.0			
				+AKA	0101_00544	05 23 10.27 +01 08 23.1

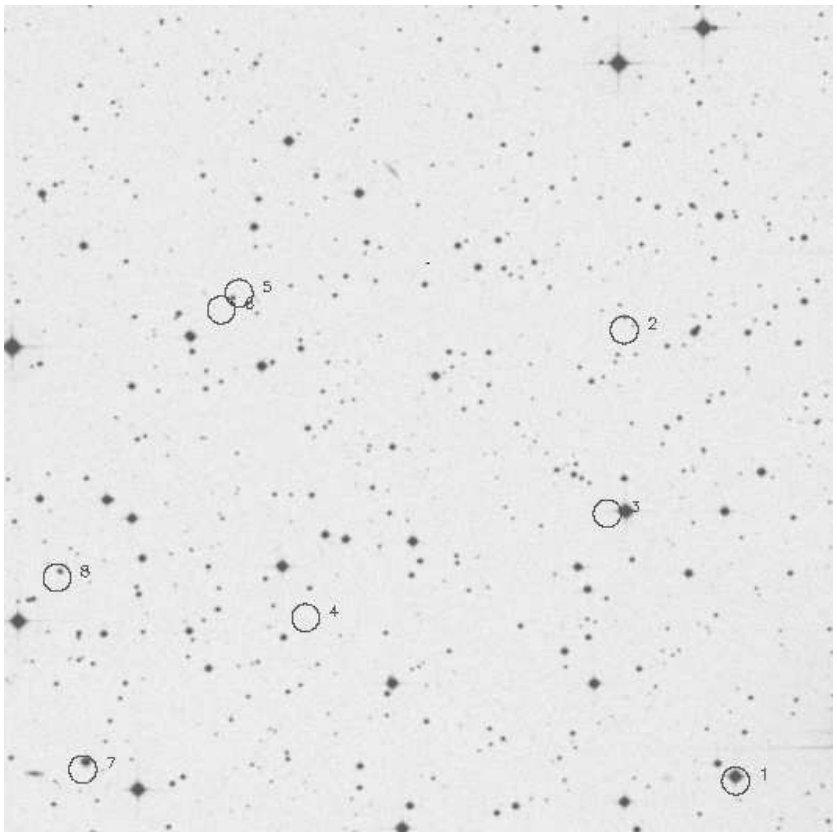

Figure A.9: ROSAT sources northwest of the belt of Orion (region 5)

Number	ID	RA(2000)	DEC(2000)	GSC	RA(2000)	DEC(2000)
1	J052321+0107	5 23 21.60	1 7 47.0	0101_00518	05 23 21.66	+01 07 51.0
2	J052329+0115	5 23 29.50	1 15 59.0			
3	J052330+0112	5 23 30.80	1 12 39.0	0101_00807	05 23 29.56	+01 12 41.0
4	J052352+0110	5 23 52.70	1 10 47.0			
5	J052357+0116	5 23 57.40	1 16 41.0			
6	J052358+0116	5 23 58.70	1 16 23.0			
7	J052408+0108	5 24 8.90	1 8 3.0	0101_00537	05 24 8.67	+01 08 10.6
8	J052410+0111	5 24 10.70	1 11 32.0			

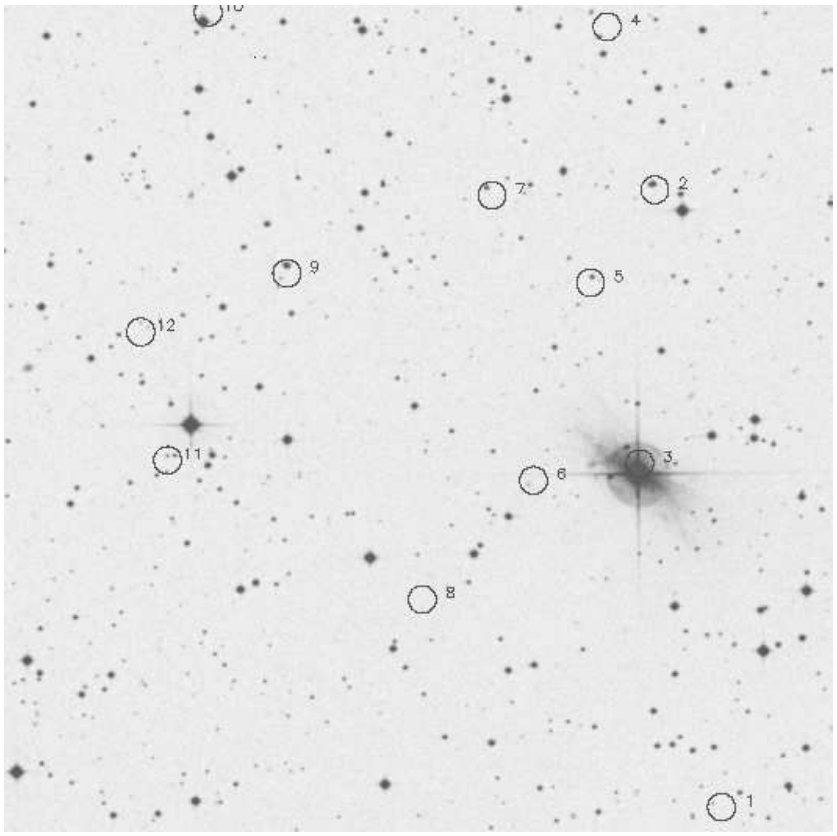

Figure A.10: ROSAT sources northwest of the belt of Orion (region 6)

Number	ID	RA(2000)	DEC(2000)	GSC	RA(2000)	DEC(2000)
1	J052345+0045	5 23 45.40	0 45 43.0			
2	J052350+0056	5 23 50.00	0 56 56.0	0101_01611	05 23 50.15	+00 57 1.5
3	J052351+0051	5 23 51.20	0 51 58.0			
4	J052353+0059	5 23 53.40	0 59 54.0			
5	J052354+0055	5 23 54.70	0 55 15.0			
6	J052358+0051	5 23 58.90	0 51 40.0			
7	J052401+0056	5 24 1.80	0 56 51.0			
8	J052407+0049	5 24 7.00	0 49 31.0			
9	J052416+0055	5 24 16.70	0 55 27.0	0101_01579	05 24 16.73	+00 55 35.4
10	J052422+0100	5 24 22.30	1 0 12.0	0101_01336	05 24 22.71	+01 00 0.8
11	J052425+0052	5 24 25.40	0 52 4.0			
12	J052427+0054	5 24 27.30	0 54 24.0			

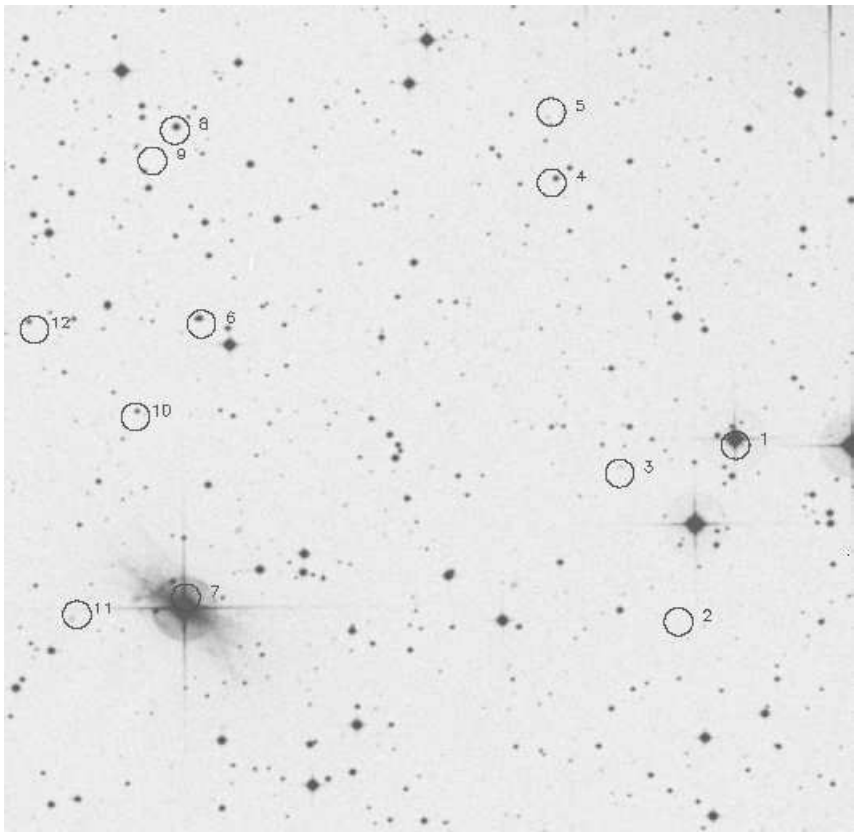

Figure A.11: ROSAT sources northwest of the belt of Orion (region 7)

Number	ID	RA(2000)	DEC(2000)	GSC	RA(2000)	DEC(2000)
1	J052312+0054	5 23 12.30	0 54 41.0	0101_01516	05 23 12.41	+00 54 47.5
2	J052316+0051	5 23 16.40	0 51 29.0			
3	J052320+0054	5 23 20.50	0 54 11.0			
4	J052325+0100	5 23 25.20	1 00 44.7			
5	J052325+0100	5 23 25.20	1 0 45.0			
6	J052350+0056	5 23 50.00	0 56 56.0	0101_01611	05 23 50.15	+00 57 1.5
7	J052351+0051	5 23 51.20	0 51 58.0			
8	J052351+0100	5 23 51.80	1 0 27.0	0101_01291	05 23 51.72	+01 00 30.1
9	J052353+0059	5 23 53.40	0 59 54.0			
10	J052354+0055	5 23 54.70	0 55 15.0			
11	J052358+0051	5 23 58.90	0 51 40.0			
12	J052401+0056	5 24 1.80	0 56 51.0			

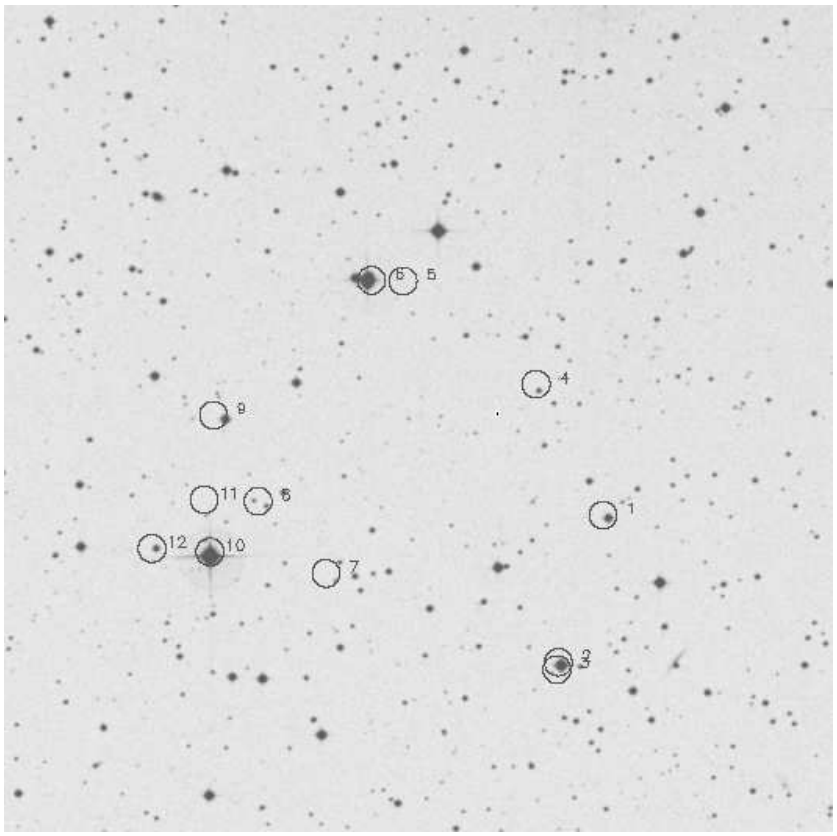

Figure A.12: ROSAT sources northwest of the belt of Orion (region 8)

Number	ID	RA(2000)	DEC(2000)	GSC	RA(2000)	DEC(2000)
1	J052443+0134	5 24 43.10	1 34 13.0	0101_00637	05 24 42.77	+01 34 9.3
2	J052446+0131	5 24 46.40	1 31 33.0	0101_00854	05 24 46.22	+01 31 28.7
3	J052446+0131	5 24 46.50	1 31 25.0	0101_00854	05 24 46.22	+01 31 28.7
4	J052447+0136	5 24 47.90	1 36 36.0			
5	J052457+0138	5 24 57.50	1 38 29.0			
6	J052459+0138	5 24 59.80	1 38 30.0	0101_00321	05 25 0.15	+01 38 29.2
7	J052503+0133	5 25 3.20	1 33 11.0			
8	J052508+0134	5 25 8.10	1 34 30.0			
9	J052511+0136	5 25 11.30	1 36 4.0	0101_00496	05 25 10.50	+01 35 59.1
10	J052511+0133	5 25 11.60	1 33 35.0	0101_00696	05 25 11.66	+01 33 29.7
11	J052512+0134	5 25 12.00	1 34 32.0			
12	J052515+0133	5 25 15.80	1 33 39.0	0101_00687	05 25 15.46	+01 33 38.2

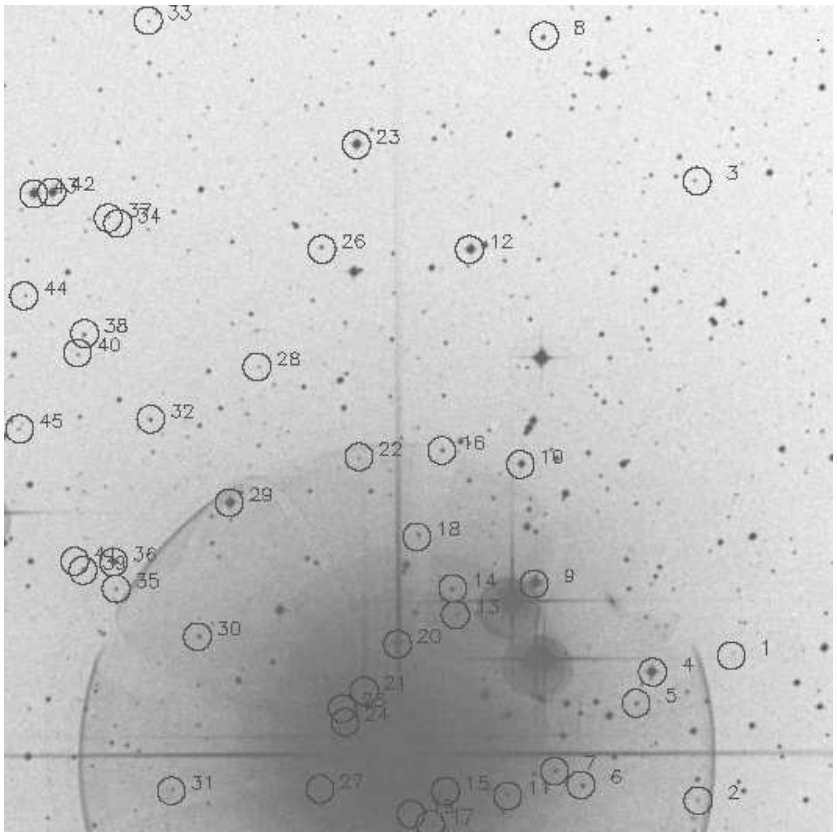

Figure A.13: Non x–ray PMS candidates north of σ Orionis.

Number	ID	RA(2000)	DEC(2000)
1	P053820-0234	5 38 20.5	-2 34 11.0
3	P053823-0225	5 38 23.0	-2 25 34.0
5	P053827-0235	5 38 27.4	-2 35 3.0
7	P053833-0236	5 38 33.3	-2 36 17.0
9	4771 1138	5 38 34.8	-2 32 53.0
11	P053836-0236	5 38 36.7	-2 36 44.0
13	P053840-0233	5 38 40.5	-2 33 27.0
15	P053841-0236	5 38 41.2	-2 36 39.0
17	P053842-0237	5 38 42.3	-2 37 15.0
19	P053843-0237	5 38 43.7	-2 37 4.0
21	P053847-0234	5 38 47.1	-2 34 50.0
23	4771 0638	5 38 47.7	-2 24 55.0
25	P053848-0235	5 38 48.7	-2 35 9.0
27	P053850-0236	5 38 50.3	-2 36 37.0
29	4771 1071	5 38 56.9	-2 31 25.0
31	P053901-0236	5 39 1.1	-2 36 39.0
33	P053902-0222	5 39 2.8	-2 22 40.0
35	P053905-0232	5 39 5.1	-2 32 59.0
37	P053905-0226	5 39 5.7	-2 26 15.0
39	4771 1092	5 39 7.5	-2 32 39.0
41	P053908-0232	5 39 8.1	-2 32 29.0
43	4771 0668	5 39 11.1	-2 25 49.0
45	P053912-0230	5 39 12.1	-2 30 5.0

Number	ID	RA(2000)	DEC(2000)
2	P053822-0236	5 38 22.9	-2 36 49.0
4	4771 1147	5 38 26.2	-2 34 29.0
6	P053831-0236	5 38 31.4	-2 36 32.0
8	P053834-0222	5 38 34.1	-2 22 56.0
10	4771 1097	5 38 35.8	-2 30 43.0
12	4771 0740	5 38 39.5	-2 26 49.0
14	P053840-0232	5 38 40.7	-2 32 58.0
16	P053841-0230	5 38 41.5	-2 30 28.0
18	P053843-0232	5 38 43.3	-2 32 2.0
20	P053844-0233	5 38 44.7	-2 33 59.0
22	P053847-0230	5 38 47.5	-2 30 35.0
24	P053848-0235	5 38 48.5	-2 35 24.0
26	P053850-0226	5 38 50.2	-2 26 49.0
28	P053854-0228	5 38 54.9	-2 28 57.0
30	P053859-0233	5 38 59.2	-2 33 51.0
32	P053902-0229	5 39 2.6	-2 29 54.0
34	P053905-0226	5 39 5.0	-2 26 21.0
36	4771 1075	5 39 5.3	-2 32 30.0
38	P053907-0228	5 39 7.4	-2 28 21.0
40	P053907-0228	5 39 7.9	-2 28 42.0
42	4771 0645	5 39 9.8	-2 25 47.0
44	P053911-0227	5 39 11.8	-2 27 40.0

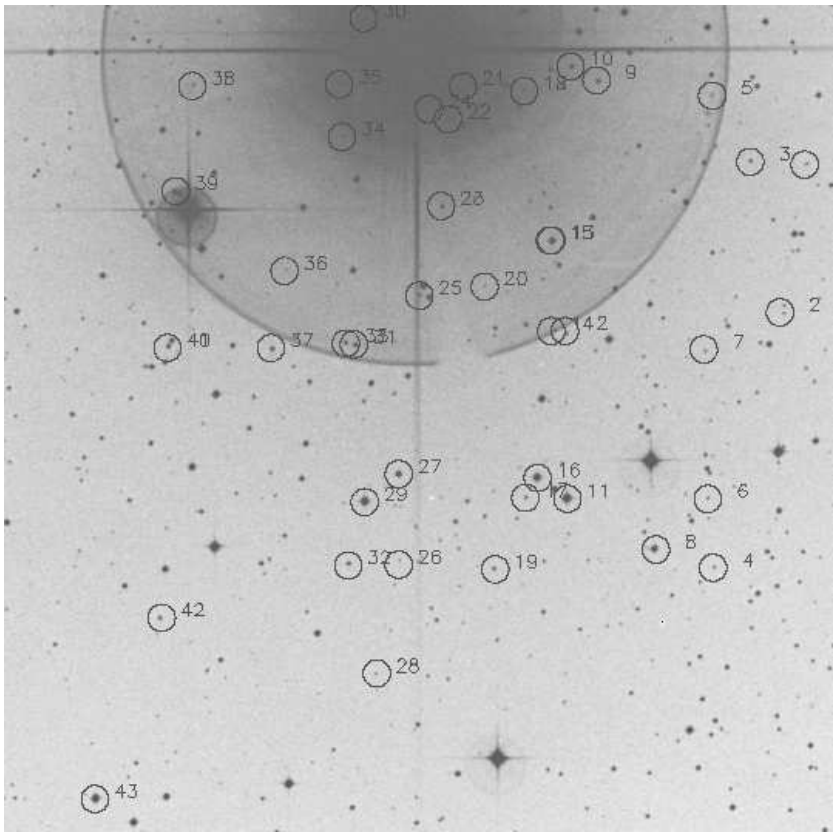

Figure A.14: Non x–ray PMS candidates south of σ Orionis.

Number	ID	RA(2000)	DEC(2000)
1	P053816-0238	5 38 16.1	-2 38 5.0
3	P053820-0238	5 38 20.1	-2 38 2.0
5	P053822-0236	5 38 22.9	-2 36 49.0
7	P053823-0241	5 38 23.5	-2 41 29.0
9	P053831-0236	5 38 31.4	-2 36 32.0
11	4771 1095	5 38 33.5	-2 44 14.0
13	P053834-0239	5 38 34.7	-2 39 29.0
15	P053834-0239	5 38 34.8	-2 39 29.0
17	P053836-0244	5 38 36.6	-2 44 13.0
19	P053838-0245	5 38 38.8	-2 45 32.0
21	P053841-0236	5 38 41.2	-2 36 39.0
23	P053842-0238	5 38 42.8	-2 38 51.0
25	4771 1051	5 38 44.4	-2 40 30.0
27	4771 1090	5 38 45.9	-2 43 47.0
29	4771 1057	5 38 48.4	-2 44 18.0
31	P053849-0241	5 38 49.2	-2 41 24.0
33	P053849-0241	5 38 49.8	-2 41 23.0
35	P053850-0236	5 38 50.3	-2 36 37.0
37	P053855-0241	5 38 55.3	-2 41 28.0
39	P053902-0238	5 39 2.3	-2 38 35.0
41	P053902-0241	5 39 2.9	-2 41 28.0
43	P053908-0249	5 39 8.2	-2 49 46.0

Number	ID	RA(2000)	DEC(2000)
2	P053817-0240	5 38 17.9	-2 40 48.0
4	P053822-0245	5 38 22.8	-2 45 30.0
6	P053823-0244	5 38 23.2	-2 44 14.0
8	4771 0041	5 38 27.0	-2 45 10.0
10	P053833-0236	5 38 33.3	-2 36 17.0
12	P053833-0241	5 38 33.7	-2 41 9.0
14	P053834-0241	5 38 34.7	-2 41 9.0
16	4771 1026	5 38 35.7	-2 43 51.0
18	P053836-0236	5 38 36.7	-2 36 44.0
20	P053839-0240	5 38 39.6	-2 40 20.0
22	P053842-0237	5 38 42.3	-2 37 15.0
24	P053843-0237	5 38 43.7	-2 37 4.0
26	P053845-0245	5 38 45.9	-2 45 27.0
28	P053847-0247	5 38 47.5	-2 47 27.0
30	P053848-0235	5 38 48.5	-2 35 24.0
32	P053849-0245	5 38 49.6	-2 45 28.0
34	P053850-0237	5 38 50.1	-2 37 35.0
36	P053854-0240	5 38 54.3	-2 40 3.0
38	P053901-0236	5 39 1.1	-2 36 39.0
40	P053902-0241	5 39 2.9	-2 41 28.0
42	P053903-0246	5 39 3.3	-2 46 26.0

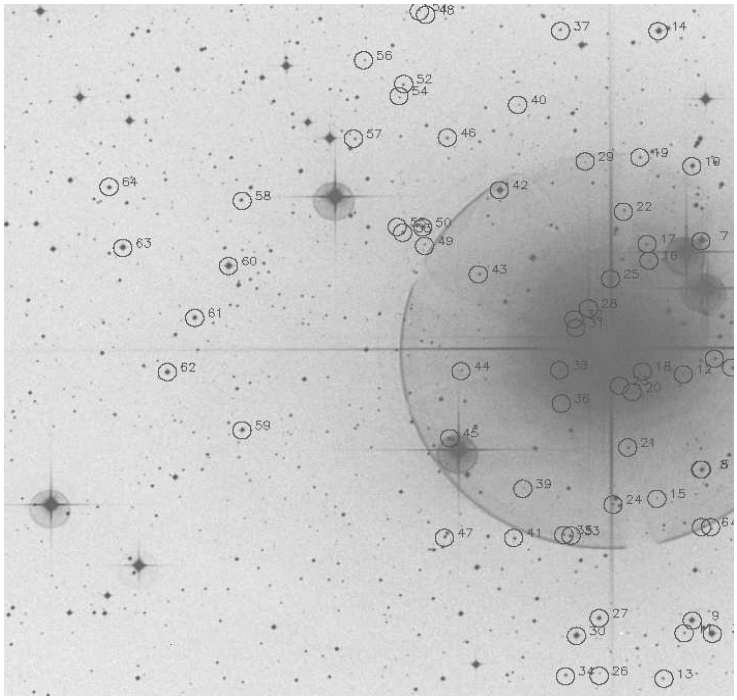

Figure A.15: Non x–ray PMS candidates east of σ Orionis.

Number	ID	RA(2000)	DEC(2000)
1	P053831-0236	5 38 31.4	-2 36 32.0
3	4771 1095	5 38 33.5	-2 44 14.0
5	P053834-0239	5 38 34.7	-2 39 29.0
7	4771 1138	5 38 34.8	-2 32 53.0
9	4771 1026	5 38 35.7	-2 43 51.0
11	P053836-0244	5 38 36.6	-2 44 13.0
13	P053838-0245	5 38 38.8	-2 45 32.0
15	P053839-0240	5 38 39.6	-2 40 20.0
17	P053840-0232	5 38 40.7	-2 32 58.0
19	P053841-0230	5 38 41.5	-2 30 28.0
21	P053842-0238	5 38 42.8	-2 38 51.0
23	P053843-0237	5 38 43.7	-2 37 4.0
25	P053844-0233	5 38 44.7	-2 33 59.0
27	4771 1090	5 38 45.9	-2 43 47.0
29	P053847-0230	5 38 47.5	-2 30 35.0
31	P053848-0235	5 38 48.5	-2 35 24.0
33	P053849-0241	5 38 49.0	-2 41 24.0
35	P053849-0241	5 38 49.8	-2 41 23.0
37	P053850-0226	5 38 50.2	-2 26 49.0
39	P053854-0240	5 38 54.3	-2 40 3.0
41	P053855-0241	5 38 55.3	-2 41 28.0
43	P053859-0233	5 38 59.2	-2 33 51.0
45	P053902-0238	5 39 2.3	-2 38 35.0
47	P053902-0241	5 39 2.9	-2 41 28.0
49	P053905-0233	5 39 5.1	-2 33 2.0
51	P053905-0226	5 39 5.7	-2 26 15.0
53	4771 1092	5 39 7.5	-2 32 39.0
55	P053908-0232	5 39 8.1	-2 32 29.0
57	P053912-0229	5 39 12.9	-2 29 56.0
59	P053925-0238	5 39 25.1	-2 38 22.0
61	4771 0579	5 39 30.3	-2 35 7.0
63	4771 0737	5 39 38.2	-2 33 6.0

Number	ID	RA(2000)	DEC(2000)
2	P053833-0236	5 38 33.3	-2 36 17.0
4	P053833-0241	5 38 33.7	-2 41 9.0
6	P053834-0241	5 38 34.7	-2 41 9.0
8	P053834-0239	5 38 34.8	-2 39 29.0
10	4771 1097	5 38 35.8	-2 30 43.0
12	P053836-0236	5 38 36.7	-2 36 44.0
14	4771 0740	5 38 39.5	-2 26 49.0
16	P053840-0233	5 38 40.5	-2 33 27.0
18	P053841-0236	5 38 41.2	-2 36 39.0
20	P053842-0237	5 38 42.3	-2 37 15.0
22	P053843-0232	5 38 43.3	-2 32 2.0
24	4771 1051	5 38 44.4	-2 40 30.0
26	P053845-0245	5 38 45.9	-2 45 27.0
28	P053847-0234	5 38 47.1	-2 34 50.0
30	4771 1057	5 38 48.4	-2 44 18.0
32	P053848-0235	5 38 48.7	-2 35 9.0
34	P053849-0245	5 38 49.6	-2 45 28.0
36	P053850-0237	5 38 50.1	-2 37 35.0
38	P053850-0236	5 38 50.3	-2 36 37.0
40	P053854-0228	5 38 54.9	-2 28 57.0
42	4771 1071	5 38 56.9	-2 31 25.0
44	P053901-0236	5 39 1.1	-2 36 39.0
46	P053902-0229	5 39 2.6	-2 29 54.0
48	P053905-0226	5 39 5.0	-2 26 21.0
50	4771 1075	5 39 5.3	-2 32 30.0
52	P053907-0228	5 39 7.4	-2 28 21.0
54	P053907-0228	5 39 7.9	-2 28 42.0
56	P053911-0227	5 39 11.8	-2 27 40.0
58	P053925-0231	5 39 25.1	-2 31 44.0
60	4771 0767	5 39 26.6	-2 33 37.0
62	4771 0975	5 39 33.3	-2 36 41.0
64	4771 0851	5 39 39.7	-2 31 20.0

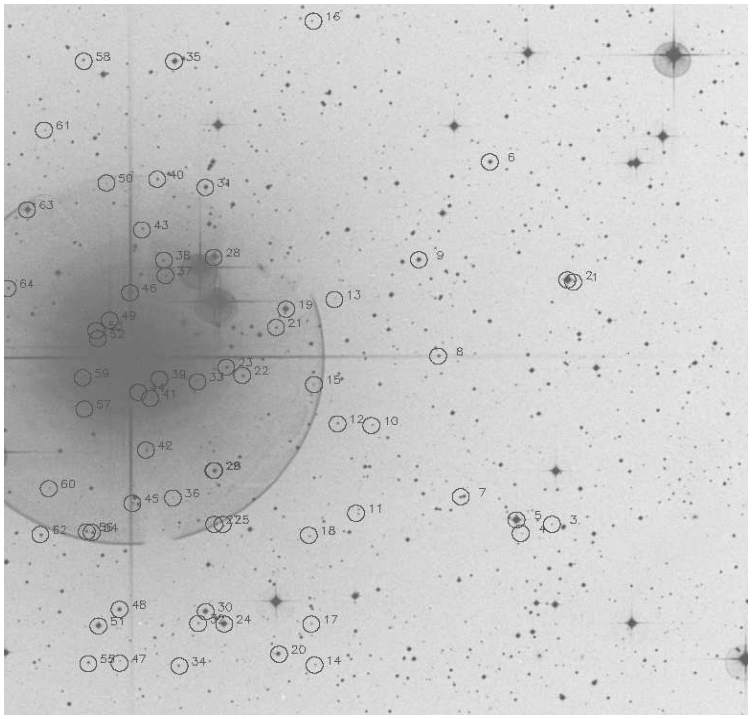

Figure A.16: Non x–ray PMS candidates west of σ Orionis.

Number	ID	RA(2000)	DEC(2000)	Number	ID	RA(2000)	DEC(2000)
1	P053752-0233	5 37 52.2	-2 33 38.0	2	4771 0775	5 37 52.9	-2 33 34.0
3	P053754-0241	5 37 54.7	-2 41 8.0	4	P053758-0241	5 37 58.4	-2 41 25.0
5	4771 0720	5 37 58.9	-2 41 0.0	6	P053802-0229	5 38 2.1	-2 29 55.0
7	4771 0619	5 38 5.5	-2 40 17.0	8	P053808-0235	5 38 8.2	-2 35 56.0
9	4771 0706	5 38 10.5	-2 32 57.0	10	P053816-0238	5 38 16.1	-2 38 5.0
11	P053817-0240	5 38 17.9	-2 40 48.0	12	P053820-0238	5 38 20.1	-2 38 2.0
13	P053820-0234	5 38 20.5	-2 34 11.0	14	P053822-0245	5 38 22.8	-2 45 30.0
15	P053822-0236	5 38 22.9	-2 36 49.0	16	P053823-0225	5 38 23.0	-2 25 34.0
17	P053823-0244	5 38 23.2	-2 44 14.0	18	P053823-0241	5 38 23.5	-2 41 29.0
19	4771 1021	5 38 26.2	-2 34 29.0	20	4771 0041	5 38 27.0	-2 45 10.0
21	P053827-0235	5 38 27.4	-2 35 3.0	22	P053831-0236	5 38 31.4	-2 36 32.0
23	P053833-0236	5 38 33.3	-2 36 17.0	24	4771 1095	5 38 33.5	-2 44 14.0
25	P053833-0241	5 38 33.7	-2 41 9.0	26	P053834-0239	5 38 34.7	-2 39 29.0
27	P053834-0241	5 38 34.7	-2 41 9.0	28	4771 1138	5 38 34.8	-2 32 53.0
29	P053834-0239	5 38 34.8	-2 39 29.0	30	4771 1026	5 38 35.7	-2 43 51.0
31	4771 1097	5 38 35.8	-2 30 43.0	32	P053836-0244	5 38 36.6	-2 44 13.0
33	P053836-0236	5 38 36.7	-2 36 44.0	34	P053838-0245	5 38 38.8	-2 45 32.0
35	4771 0740	5 38 39.5	-2 26 49.0	36	P053839-0240	5 38 39.6	-2 40 20.0
37	P053840-0233	5 38 40.5	-2 33 27.0	38	P053840-0232	5 38 40.7	-2 32 58.0
39	P053841-0236	5 38 41.2	-2 36 39.0	40	P053841-0230	5 38 41.5	-2 30 28.0
41	P053842-0237	5 38 42.3	-2 37 15.0	42	P053842-0238	5 38 42.8	-2 38 51.0
43	P053843-0232	5 38 43.3	-2 32 2.0	44	P053843-0237	5 38 43.7	-2 37 4.0
45	P053844-0240	5 38 44.4	-2 40 30.0	46	P053844-0233	5 38 44.7	-2 33 59.0
47	P053845-0245	5 38 45.9	-2 45 27.0	48	4771 1090	5 38 45.9	-2 43 47.0
49	P053847-0234	5 38 47.1	-2 34 50.0	50	P053847-0230	5 38 47.5	-2 30 35.0
51	4771 1057	5 38 48.4	-2 44 18.0	52	P053848-0235	5 38 48.5	-2 35 24.0
53	P053848-0235	5 38 48.7	-2 35 9.0	54	P053849-0241	5 38 49.2	-2 41 24.0
55	P053849-0245	5 38 49.6	-2 45 28.0	56	P053849-0241	5 38 49.8	-2 41 23.0
57	P053850-0237	5 38 50.1	-2 37 35.0	58	P053850-0226	5 38 50.2	-2 26 49.0
59	P053850-0236	5 38 50.3	-2 36 37.0	60	P053854-0240	5 38 54.3	-2 40 3.0
61	P053854-0228	5 38 54.9	-2 28 57.0	62	P053855-0241	5 38 55.3	-2 41 28.0
63	4771 1071	5 38 56.9	-2 31 25.0	64	P053859-0233	5 38 59.2	-2 33 51.0

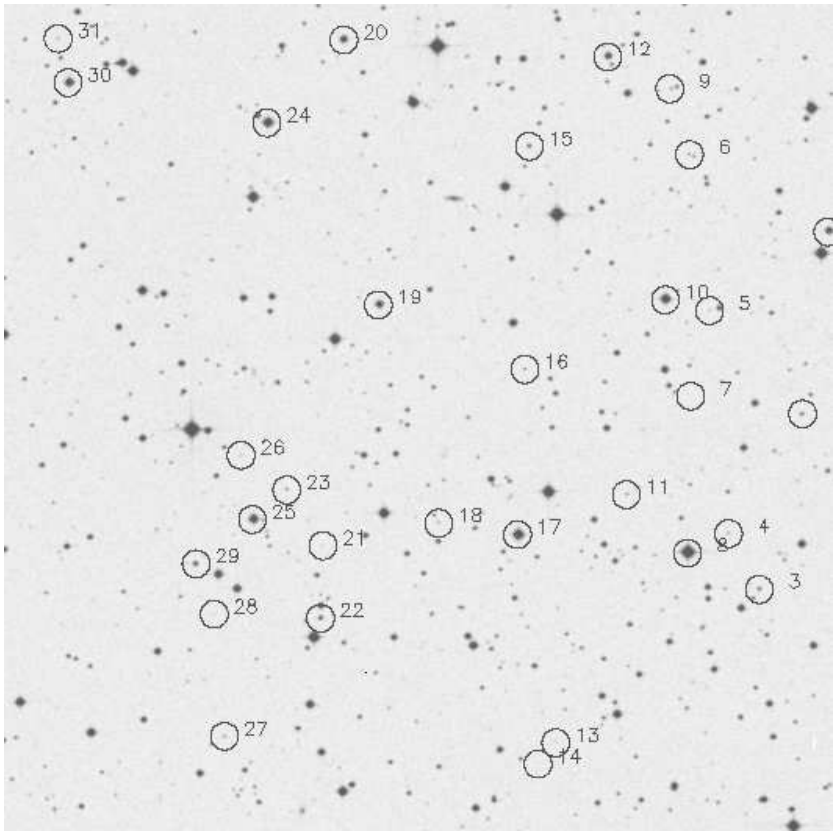

Figure A.17: PMS candidates which are not x-ray sources, located northwest of the belt of Orion (region 1).

Number	ID	RA(2000)	DEC(2000)	Number	ID	RA(2000)	DEC(2000)
1	0101 0497	5 23 45.3	1 7 20.0	2	P052347+01	5 23 47.2	1 4 2.0
3	P052350+01	5 23 50.4	1 0 51.0	4	P052352+01	5 23 52.6	1 1 52.0
5	P052353+01	5 23 53.9	1 5 55.0	6	P052355+01	5 23 55.3	1 8 45.0
7	P052355+01	5 23 55.3	1 4 22.0	8	0101 1235	5 23 55.6	1 1 31.0
9	P052356+01	5 23 56.7	1 9 57.0	10	0101 0429	5 23 57.1	1 6 7.0
11	P052360+01	5 23 60.0	1 2 35.0	12	0101 0666	5 24 1.2	1 10 32.0
13	P05245+00	5 24 5.2	0 58 5.0	14	P05246+00	5 24 6.5	0 57 42.0
15	P05246+01	5 24 6.9	1 8 55.0	16	P05247+01	5 24 7.3	1 4 52.0
17	0101 1205	5 24 7.9	1 1 52.0	18	P052413+01	5 24 13.6	1 2 5.0
19	0101 0423	5 24 17.9	1 6 3.0	20	P052420+01	5 24 20.3	1 10 52.0
21	P052422+01	5 24 22.0	1 1 41.0	22	P052422+01	5 24 22.2	1 0 22.0
23	P052424+01	5 24 24.6	1 2 42.0	24	0101 0596	5 24 25.9	1 9 22.0
25	0101 1166	5 24 27.1	1 2 10.0	26	P052427+01	5 24 27.9	1 3 20.0
27	P052429+00	5 24 29.2	0 58 14.0	28	P052429+01	5 24 29.9	1 0 27.0
29	P052431+01	5 24 31.2	1 1 22.0	30	0101 0638	5 24 40.3	1 10 7.0
31	P052441+01	5 24 41.0	1 10 55.0				

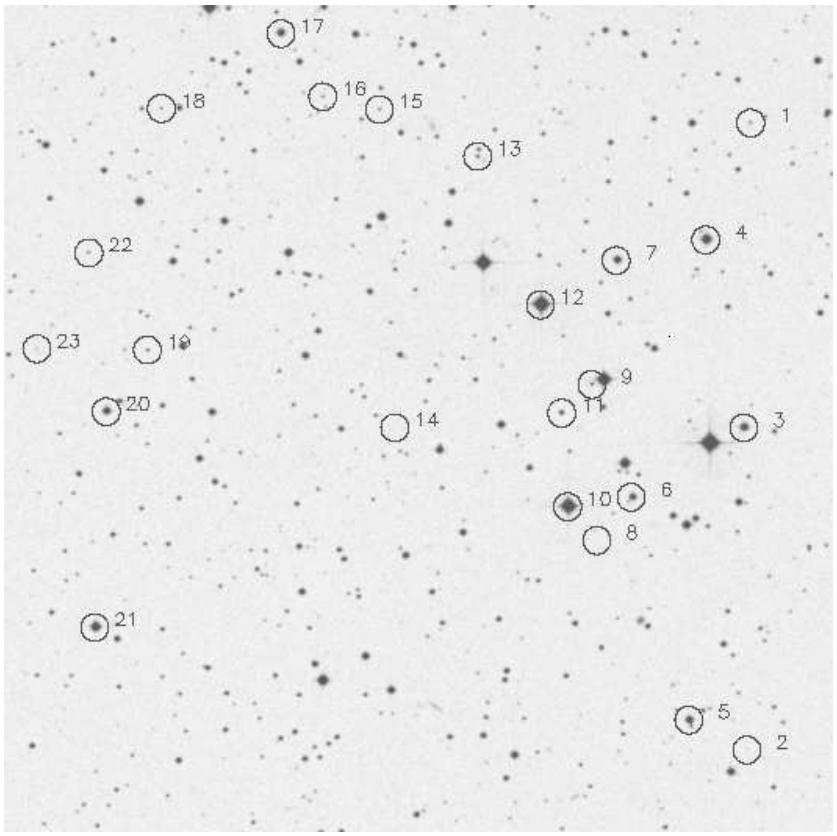

Figure A.18: PMS candidates which are not x-ray sources, located northwest of the belt of Orion (region 2).

Number	ID	RA(2000)	DEC(2000)	Number	ID	RA(2000)	DEC(2000)
1	P05247+01	5 24 7.0	1 29 20.0	2	P05247+01	5 24 7.5	1 17 57.0
3	0101 0410	5 24 7.6	1 23 48.0	4	0101 0717	5 24 10.3	1 27 13.0
5	P052411+01	5 24 11.7	1 18 30.0	6	0101 0539	5 24 15.8	1 22 33.0
7	0101 0652	5 24 16.8	1 26 51.0	8	P052418+01	5 24 18.3	1 21 46.0
9	P052418+01	5 24 18.6	1 24 36.0	10	0101 0556	5 24 20.4	1 22 23.0
11	P052420+01	5 24 20.8	1 24 5.0	12	0101 0534	5 24 22.3	1 26 3.0
13	P052426+01	5 24 26.8	1 28 45.0	14	P052432+01	5 24 32.9	1 23 50.0
15	P052433+01	5 24 33.9	1 29 37.0	16	P052438+01	5 24 38.0	1 29 51.0
17	0101 0889	5 24 41.0	1 31 0.0	18	P052449+01	5 24 49.7	1 29 39.0
19	P052450+01	5 24 50.8	1 25 16.0	20	0101 0381	5 24 53.8	1 24 9.0
21	0101 0780	5 24 54.7	1 20 14.0	22	P052455+01	5 24 55.0	1 27 2.0
23	P052458+01	5 24 58.8	1 25 18.0				

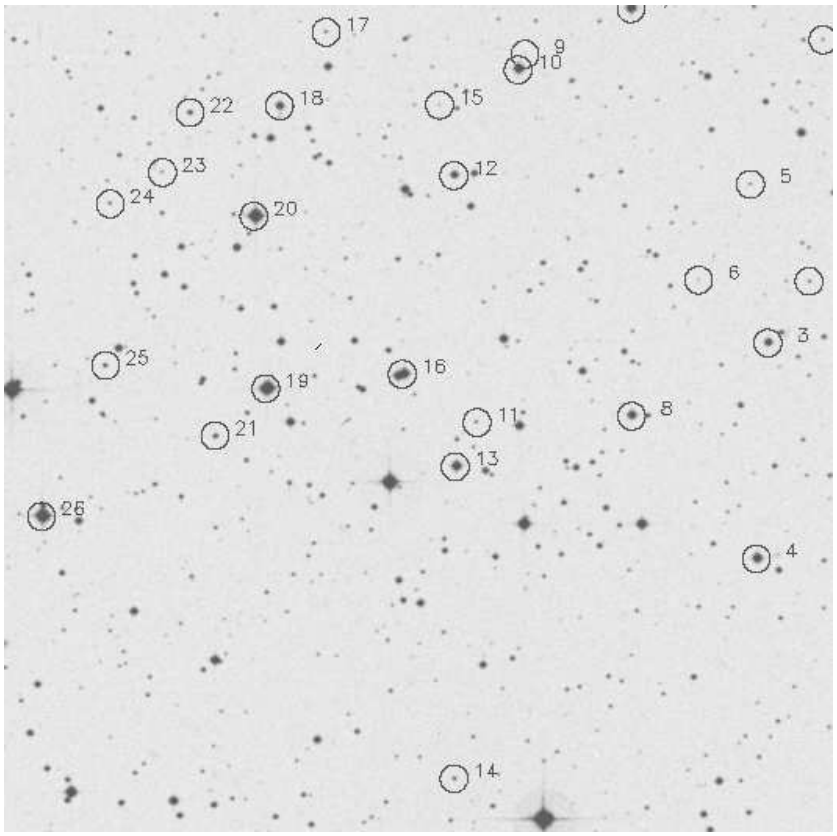

Figure A.19: PMS candidates which are not x-ray sources, located northwest of the belt of Orion (region 3).

Number	ID	RA(2000)	DEC(2000)	Number	ID	RA(2000)	DEC(2000)
1	P052449+01	5 24 49.7	1 29 39.0	2	P052450+01	5 24 50.8	1 25 16.0
3	0101 0381	5 24 53.8	1 24 9.0	4	0101 0780	5 24 54.7	1 20 14.0
5	P052455+01	5 24 55.0	1 27 2.0	6	P052458+01	5 24 58.8	1 25 18.0
7	0101 0932	5 25 3.6	1 30 14.0	8	0101 0514	5 25 3.7	1 22 50.0
9	P052511+01	5 25 11.3	1 29 25.0	10	0101 0977	5 25 11.8	1 29 8.0
11	P052514+01	5 25 14.9	1 22 44.0	12	0101 0712	5 25 16.5	1 27 13.0
13	0101 0600	5 25 16.5	1 21 56.0	14	P052516+01	5 25 16.7	1 16 16.0
15	P052517+01	5 25 17.5	1 28 30.0	16	0101 0433	5 25 20.3	1 23 37.0
17	P052525+01	5 25 25.7	1 29 50.0	18	0101 0873	5 25 29.1	1 28 30.0
19	0101 0443	5 25 30.2	1 23 22.0	20	0101 0579	5 25 31.0	1 26 30.0
21	P052533+01	5 25 33.9	1 22 31.0	22	P052535+01	5 25 35.6	1 28 23.0
23	P052537+01	5 25 37.6	1 27 18.0	24	P052541+01	5 25 41.4	1 26 44.0
25	P052541+01	5 25 41.8	1 23 48.0	26	0101 0697	5 25 46.5	1 21 4.0

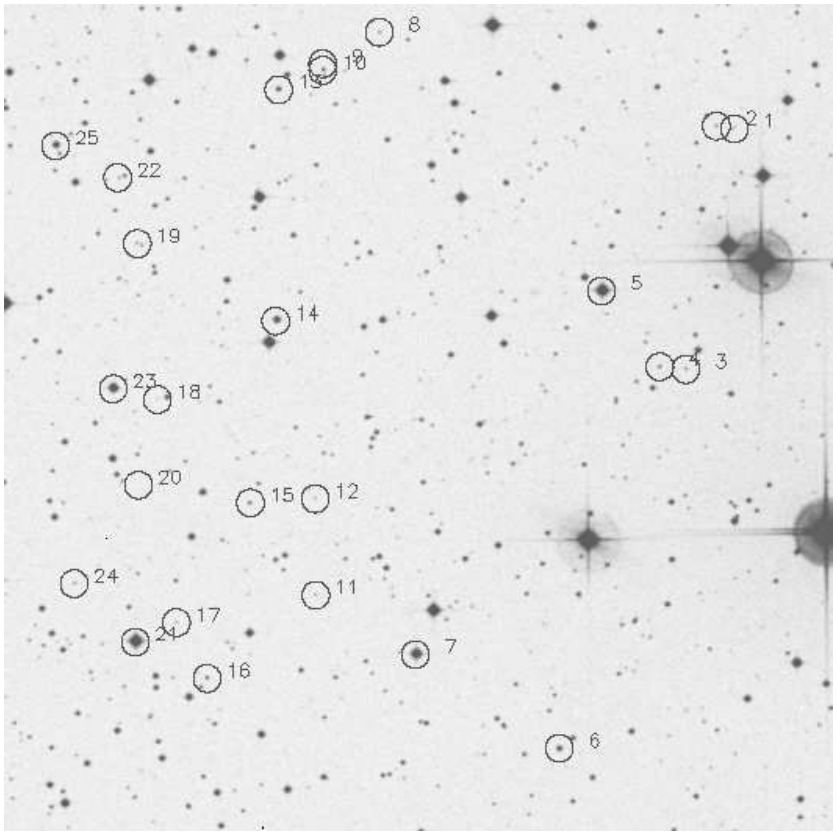

Figure A.20: PMS candidates which are not x-ray sources, located northwest of the belt of Orion (region 4).

Number	ID	RA(2000)	DEC(2000)	Number	ID	RA(2000)	DEC(2000)
1	P052312+01	5 23 12.0	1 10 47.0	2	P052313+01	5 23 13.3	1 10 50.0
3	P052315+01	5 23 15.6	1 6 25.0	4	P052317+01	5 23 17.5	1 6 28.0
5	0101 0518	5 23 21.7	1 7 51.0	6	P052324+00	5 23 24.9	0 59 33.0
7	0101 1252	5 23 35.3	1 1 16.0	8	P052337+01	5 23 37.7	1 12 34.0
9	P052341+01	5 23 41.8	1 12 0.0	10	P052341+01	5 23 41.8	1 11 53.0
11	P052342+01	5 23 42.5	1 2 21.0	12	P052342+01	5 23 42.5	1 4 6.0
13	P052345+01	5 23 45.0	1 11 32.0	14	0101 0497	5 23 45.3	1 7 20.0
15	P052347+01	5 23 47.2	1 4 2.0	16	P052350+01	5 23 50.4	1 0 51.0
17	P052352+01	5 23 52.6	1 1 52.0	18	P052353+01	5 23 53.9	1 5 55.0
19	P052355+01	5 23 55.3	1 8 45.0	20	P052355+01	5 23 55.3	1 4 22.0
21	0101 1235	5 23 55.6	1 1 31.0	22	P052356+01	5 23 56.7	1 9 57.0
23	0101 0429	5 23 57.1	1 6 7.0	24	P052360+01	5 23 60.0	1 2 35.0
25	0101 0666	5 24 1.2	1 10 32.0				

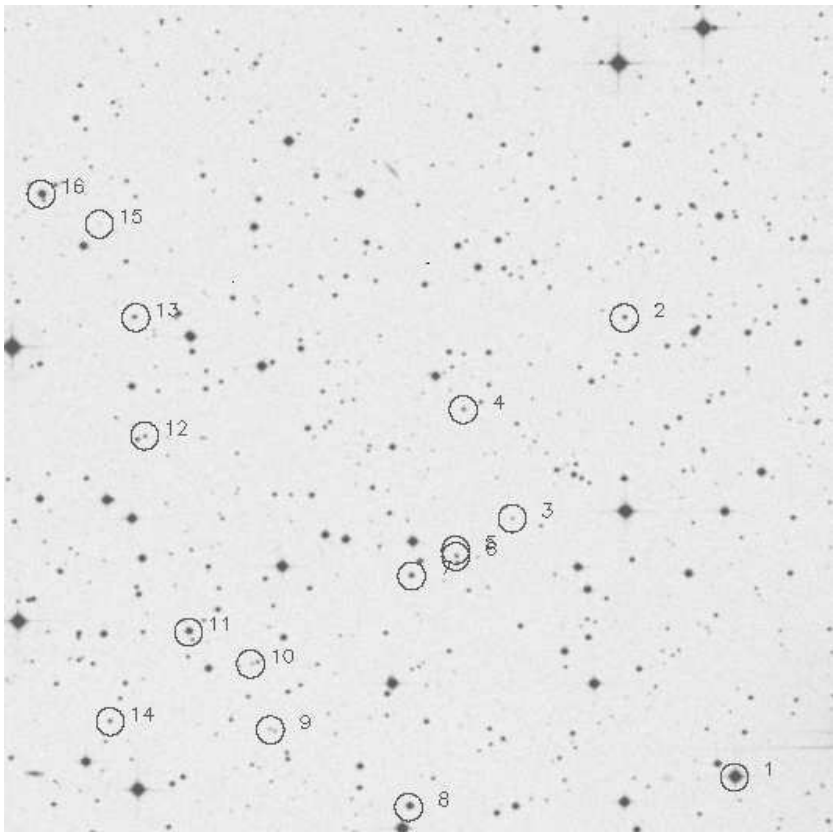

Figure A.21: PMS candidates which are not x-ray sources, located northwest of the belt of Orion (region 5).

Number	ID	RA(2000)	DEC(2000)	Number	ID	RA(2000)	DEC(2000)
1	0101 0518	5 23 21.7	1 7 51.0	2	P052329+01	5 23 29.5	1 16 12.0
3	P052337+01	5 23 37.7	1 12 34.0	4	P052341+01	5 23 41.2	1 14 33.0
5	P052341+01	5 23 41.8	1 12 0.0	6	P052341+01	5 23 41.8	1 11 53.0
7	P052345+01	5 23 45.0	1 11 32.0	8	0101 0497	5 23 45.3	1 7 20.0
9	P052355+01	5 23 55.3	1 8 45.0	10	P052356+01	5 23 56.7	1 9 57.0
11	0101 0666	5 24 1.2	1 10 32.0	12	P05244+01	5 24 4.3	1 14 6.0
13	P05244+01	5 24 4.9	1 16 15.0	14	P05246+01	5 24 6.9	1 8 55.0
15	P05247+01	5 24 7.5	1 17 57.0	16	P052411+01	5 24 11.7	1 18 30.0

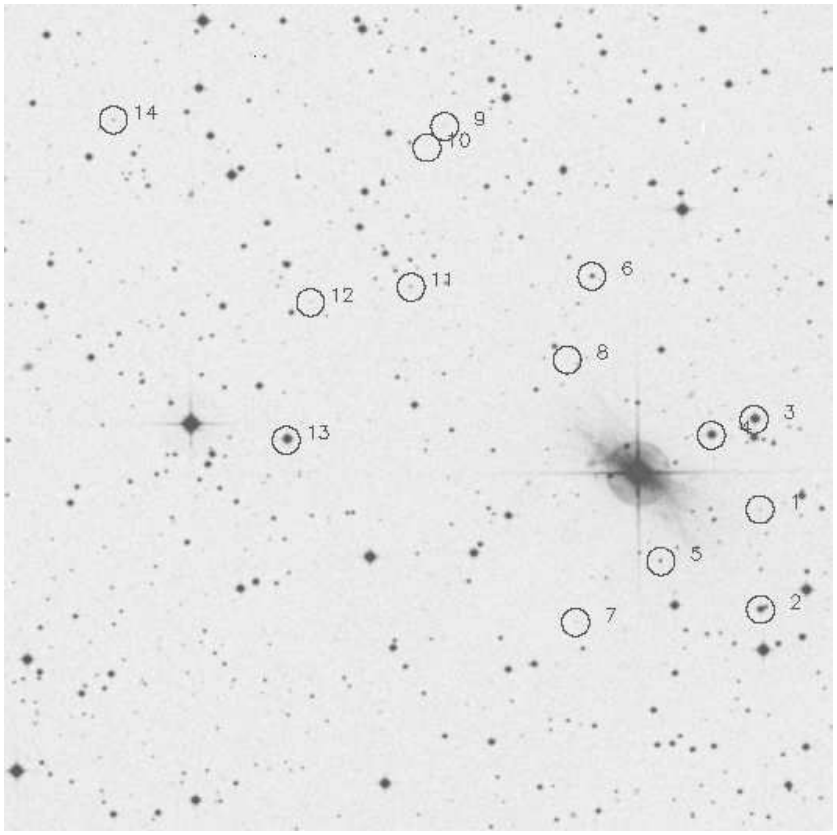

Figure A.22: PMS candidates which are not x-ray sources, located northwest of the belt of Orion (region 6).

Number	ID	RA(2000)	DEC(2000)	Number	ID	RA(2000)	DEC(2000)
1	P052342+00	5 23 42.5	0 51 6.0	2	0101 1151	5 23 42.5	0 49 17.0
3	0101 1242	5 23 42.9	0 52 44.0	4	0101 1191	5 23 46.0	0 52 27.0
5	P052349+00	5 23 49.7	0 50 10.0	6	P052354+00	5 23 54.6	0 55 21.0
7	P052355+00	5 23 55.9	0 49 4.0	8	P052356+00	5 23 56.4	0 53 50.0
9	P05245+00	5 24 5.2	0 58 5.0	10	P05246+00	5 24 6.5	0 57 42.0
11	P05247+00	5 24 7.7	0 55 10.0	12	P052415+00	5 24 15.0	0 54 54.0
13	0101 1184	5 24 16.8	0 52 24.0	14	P052429+00	5 24 29.2	0 58 14.0

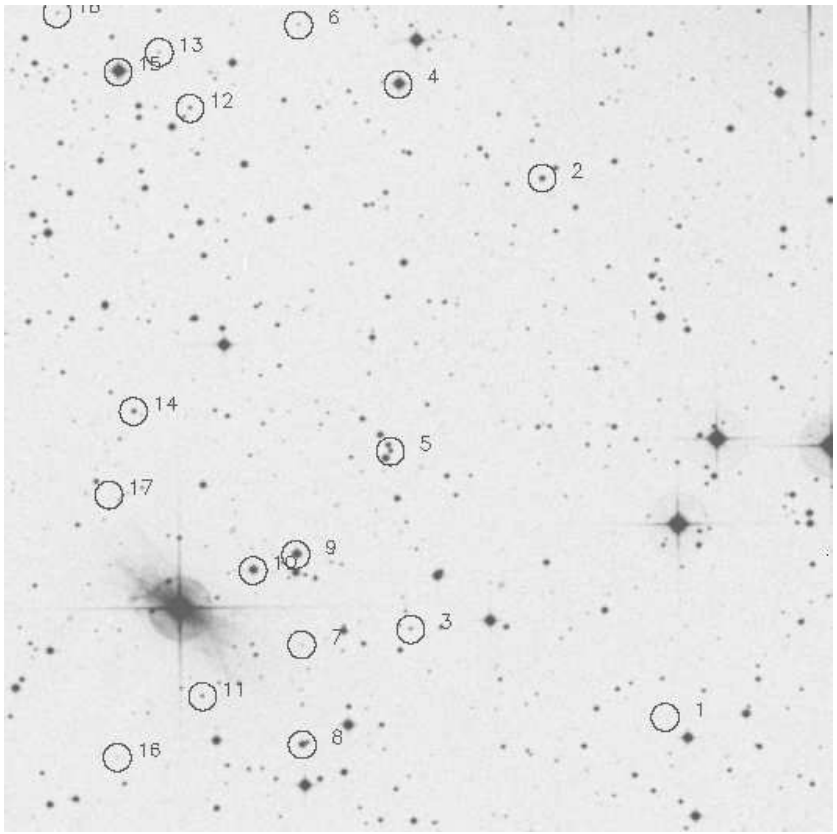

Figure A.23: PMS candidates which are not x-ray sources, located northwest of the belt of Orion (region 7).

Number	ID	RA(2000)	DEC(2000)	Number	ID	RA(2000)	DEC(2000)
1	P052316+00	5 23 16.2	0 49 45.0	2	P052324+00	5 23 24.9	0 59 33.0
3	P052334+00	5 23 34.6	0 51 22.0	4	0101 1252	5 23 35.3	1 1 16.0
5	P052336+00	5 23 36.0	0 54 36.0	6	P052342+01	5 23 42.5	1 2 21.0
7	P052342+00	5 23 42.5	0 51 6.0	8	0101 1151	5 23 42.5	0 49 17.0
9	0101 1242	5 23 42.9	0 52 44.0	10	0101 1191	5 23 46.0	0 52 27.0
11	P052349+00	5 23 49.7	0 50 10.0	12	P052350+01	5 23 50.4	1 0 51.0
13	P052352+01	5 23 52.6	1 1 52.0	14	P052354+00	5 23 54.6	0 55 21.0
15	0101 1235	5 23 55.6	1 1 31.0	16	P052355+00	5 23 55.9	0 49 4.0
17	P052356+00	5 23 56.4	0 53 50.0	18	P052360+01	5 23 60.0	1 2 35.0

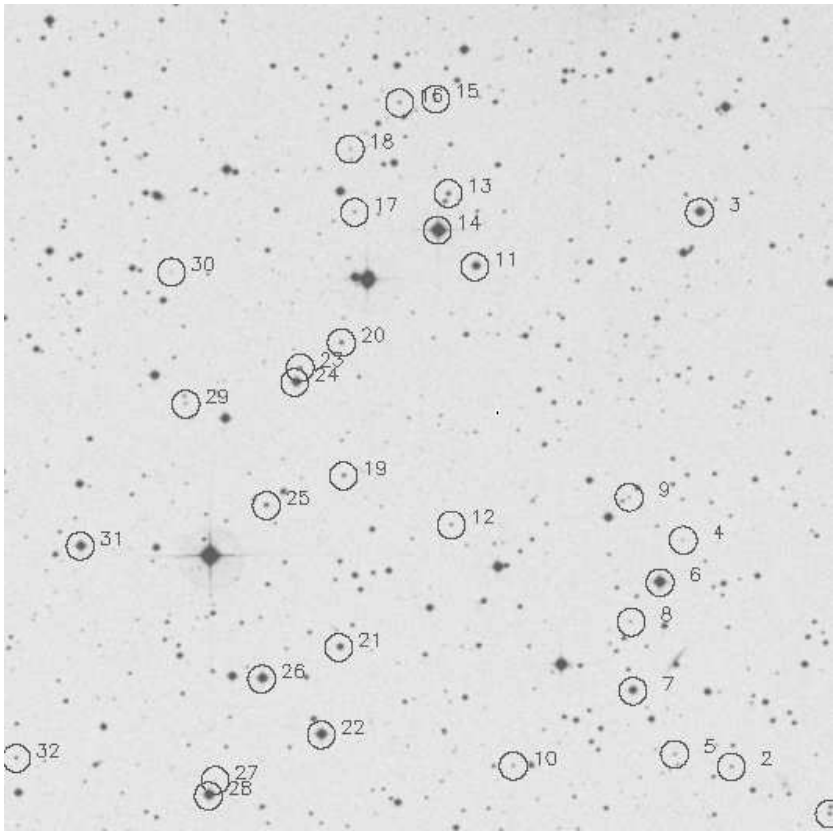

Figure A.24: PMS candidates which are not x-ray sources, located northwest of the belt of Orion (region 8).

Number	ID	RA(2000)	DEC(2000)	Number	ID	RA(2000)	DEC(2000)
1	P052426+01	5 24 26.8	1 28 45.0	2	P052433+01	5 24 33.9	1 29 37.0
3	0101 0296	5 24 36.0	1 39 41.0	4	P052437+01	5 24 37.3	1 33 44.0
5	P052438+01	5 24 38.0	1 29 51.0	6	0101 0746	5 24 39.0	1 32 58.0
7	0101 0889	5 24 41.0	1 31 0.0	8	P052441+01	5 24 41.1	1 32 15.0
9	P052441+01	5 24 41.2	1 34 31.0	10	P052449+01	5 24 49.7	1 29 39.0
11	0101 0320	5 24 52.3	1 38 43.0	12	P052454+01	5 24 54.1	1 34 2.0
13	P052454+01	5 24 54.2	1 40 3.0	14	0101 0300	5 24 55.0	1 39 23.0
15	P052455+01	5 24 55.1	1 41 46.0	16	P052457+01	5 24 57.7	1 41 42.0
17	P05251+01	5 25 1.0	1 39 43.0	18	P05251+01	5 25 1.3	1 40 52.0
19	P05251+01	5 25 1.9	1 34 56.0	20	P05252+01	5 25 2.0	1 37 21.0
21	0101 2527	5 25 2.3	1 31 49.0	22	0101 0932	5 25 3.6	1 30 14.0
23	P05255+01	5 25 5.0	1 36 54.0	24	0101 0431	5 25 5.4	1 36 38.0
25	P05257+01	5 25 7.5	1 34 24.0	26	0101 0876	5 25 7.9	1 31 15.0
27	P052511+01	5 25 11.3	1 29 25.0	28	0101 0977	5 25 11.8	1 29 8.0
29	P052513+01	5 25 13.3	1 36 15.0	30	P052514+01	5 25 14.3	1 38 39.0
31	0101 0685	5 25 21.0	1 33 41.0	32	P052525+01	5 25 25.7	1 29 50.0

Appendix B

Lightcurves and Observational Data

This section contains folded lightcurves and periodograms of all stars for which rotation periods were found. The light curves are broken up into three sections. The first section contains the highest quality light curves, those with FAP less than one percent. The second section contains those stars with FAPs of between one and five percent. The third section contains the lowest quality lightcurves – those with FAPs of between five and 20%. The calculation of the FAPs and periodograms is discussed in Chapter 3. The fits to the light curves are 7th order polynomial fits to two cycles of the data. The standard deviation of the data to the fit, the Mean magnitude and amplitude from the mean to peak are given in each left hand panel The Order of the light curves is the same as the ordering in Tables 4.1, 4.2 and 4.3 respectively.

B.1 Secure Rotation Period Determinations

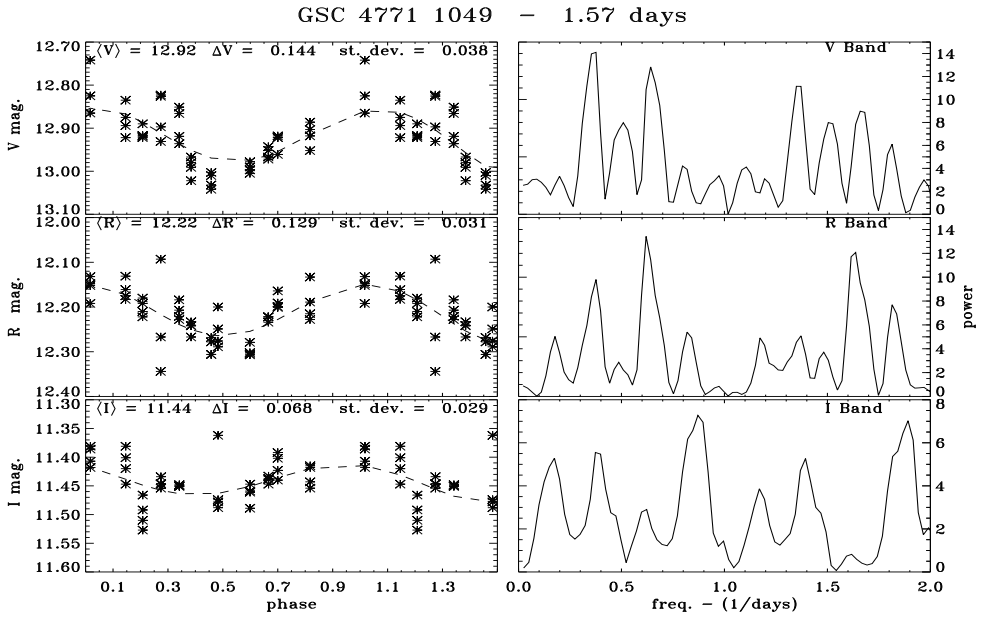

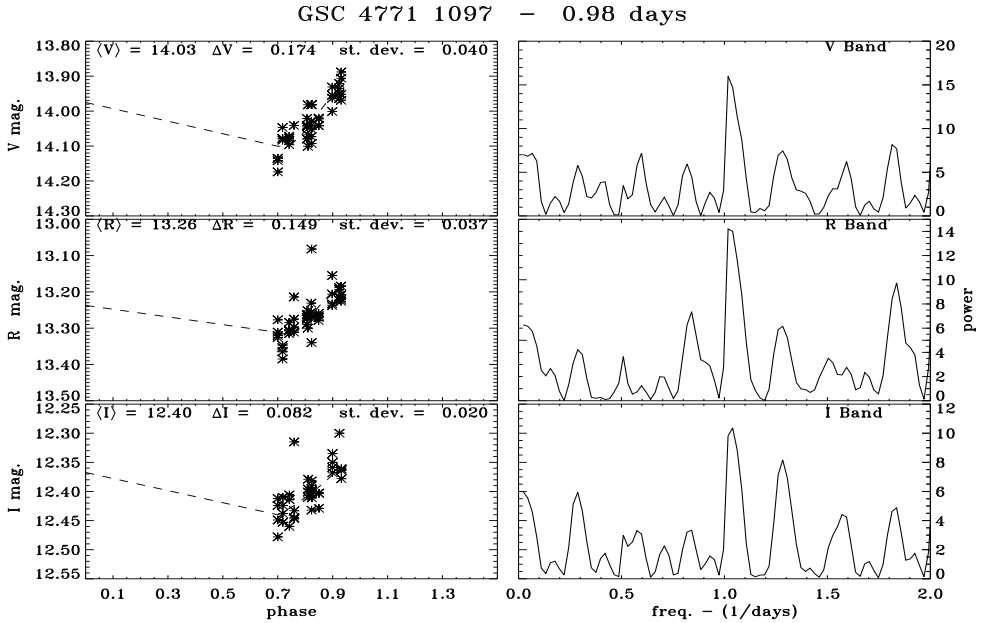

GSC 4771 0901 – 8.1 days

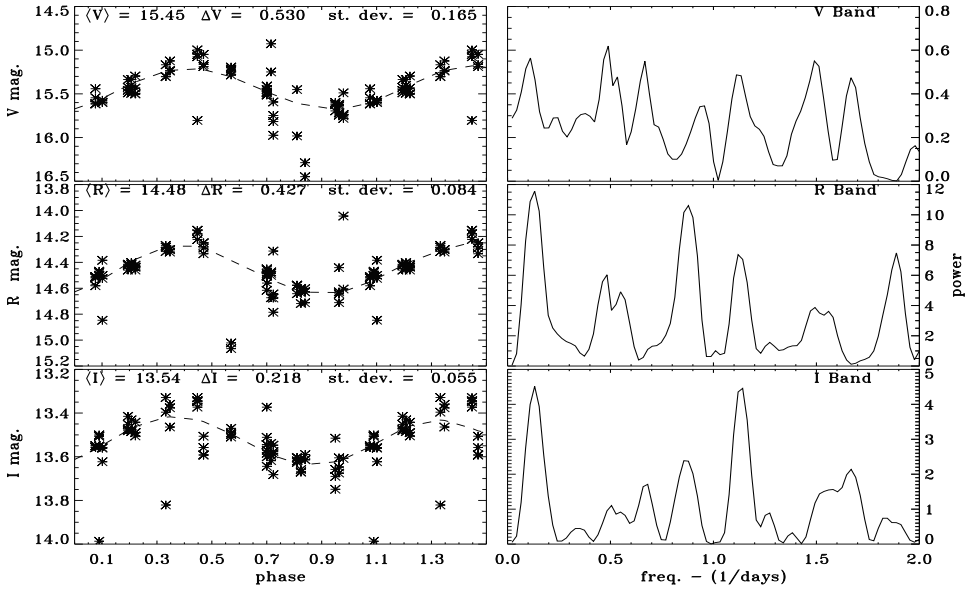

GSC 0101 2447 – 1.05 days

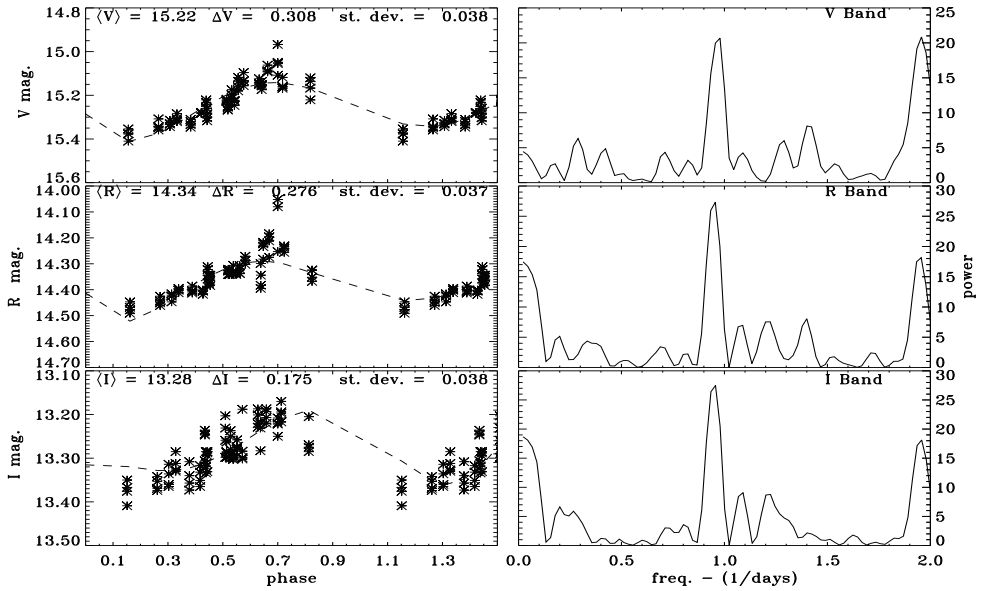

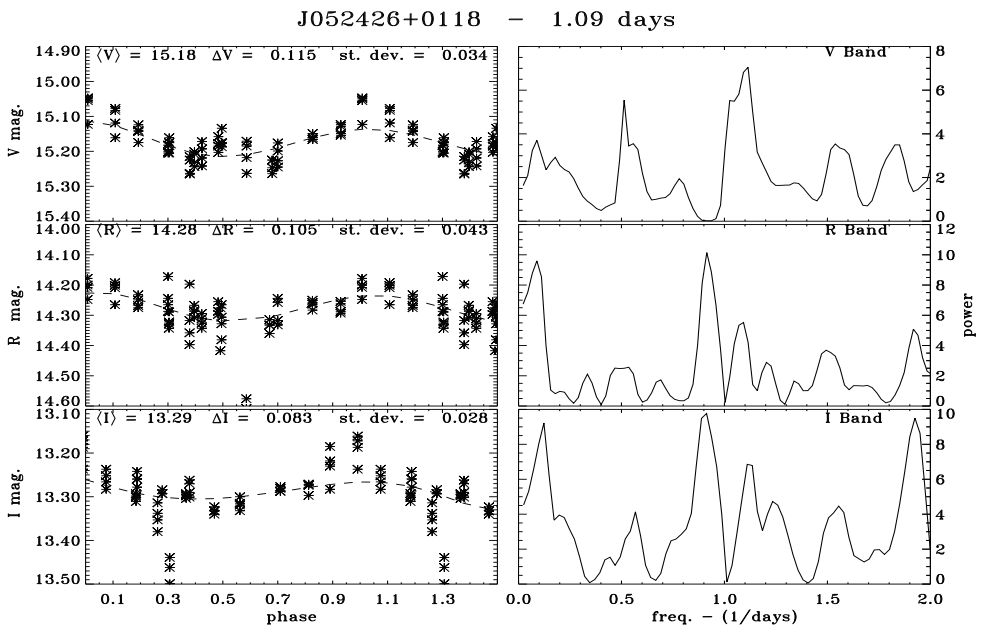
J052426+0118 − 1.09 days
⟨V⟩ = 15.18 ΔV = 0.115 st. dev. = 0.034
⟨R⟩ = 14.28 ΔR = 0.105 st. dev. = 0.043
⟨I⟩ = 13.29 ΔI = 0.083 st. dev. = 0.028
V mag.
R mag.
I mag.
phase
V Band
R Band
I Band
power
freq. − (1/days)

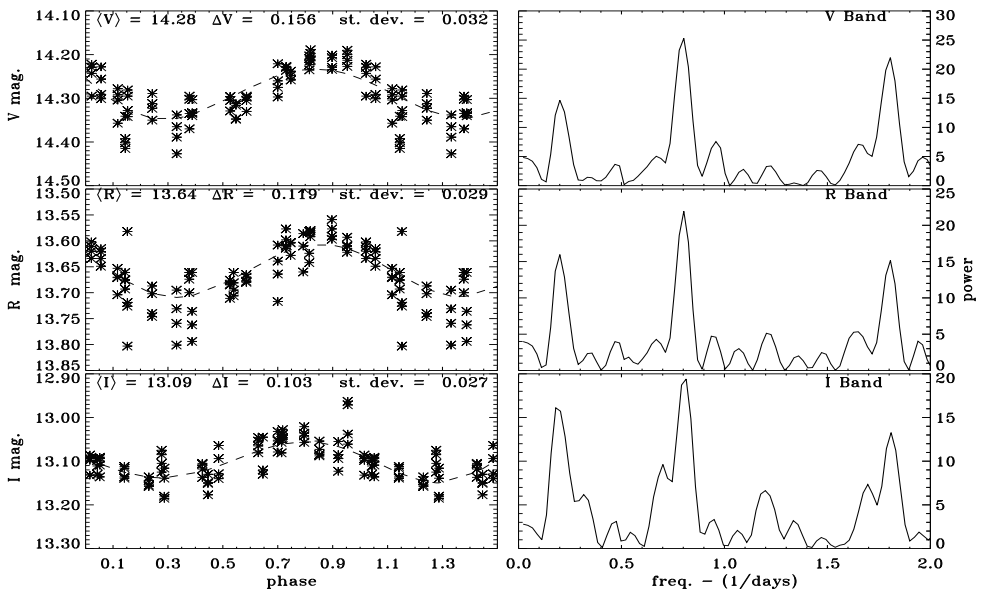
GSC 0101 0756 − 1.26 days
⟨V⟩ = 14.28 ΔV = 0.156 st. dev. = 0.032
⟨R⟩ = 13.64 ΔR = 0.119 st. dev. = 0.029
⟨I⟩ = 13.09 ΔI = 0.103 st. dev. = 0.027
V mag.
R mag.
I mag.
phase
V Band
R Band
I Band
power
freq. − (1/days)

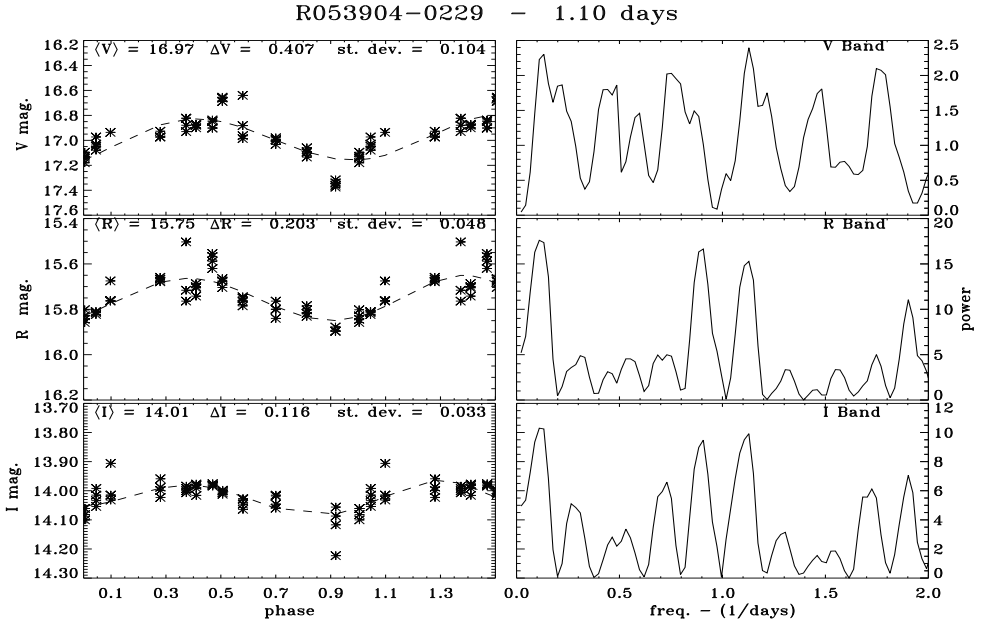
R053904−0229 − 1.10 days
⟨V⟩ = 16.97 ΔV = 0.407 st. dev. = 0.104
⟨R⟩ = 15.75 ΔR = 0.203 st. dev. = 0.048
⟨I⟩ = 14.01 ΔI = 0.116 st. dev. = 0.033
V mag.
R mag.
I mag.
phase
V Band
R Band
I Band
power
freq. − (1/days)

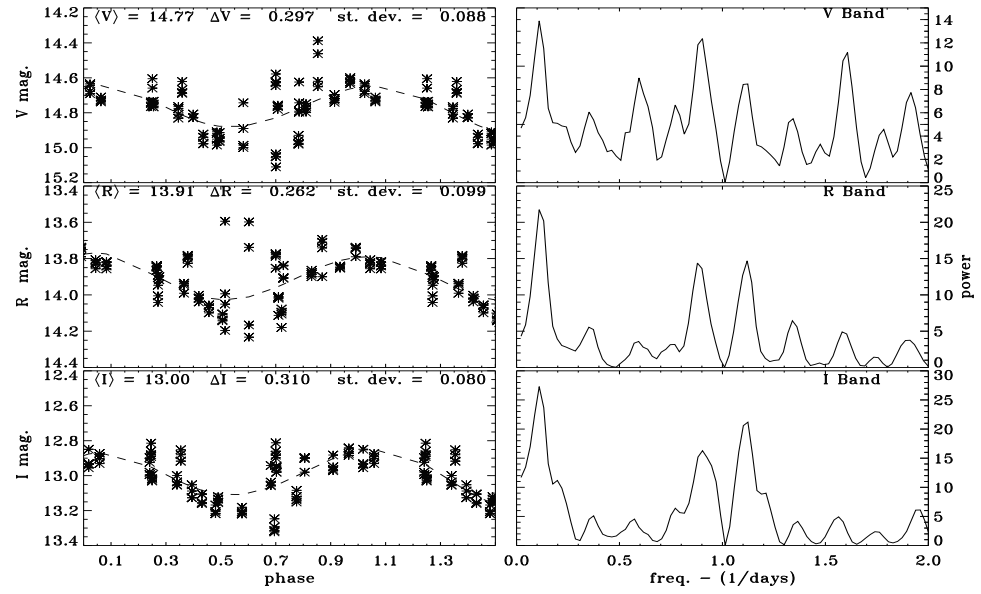
GSC 4771 0947 − 1.12 days
⟨V⟩ = 14.77 ΔV = 0.297 st. dev. = 0.088
⟨R⟩ = 13.91 ΔR = 0.262 st. dev. = 0.099
⟨I⟩ = 13.00 ΔI = 0.310 st. dev. = 0.080
V mag.
R mag.
I mag.
phase
V Band
R Band
I Band
power
freq. − (1/days)

B.2 Period Determinations of Moderate Confidence

GSC 4771 1051 – 12.2 days

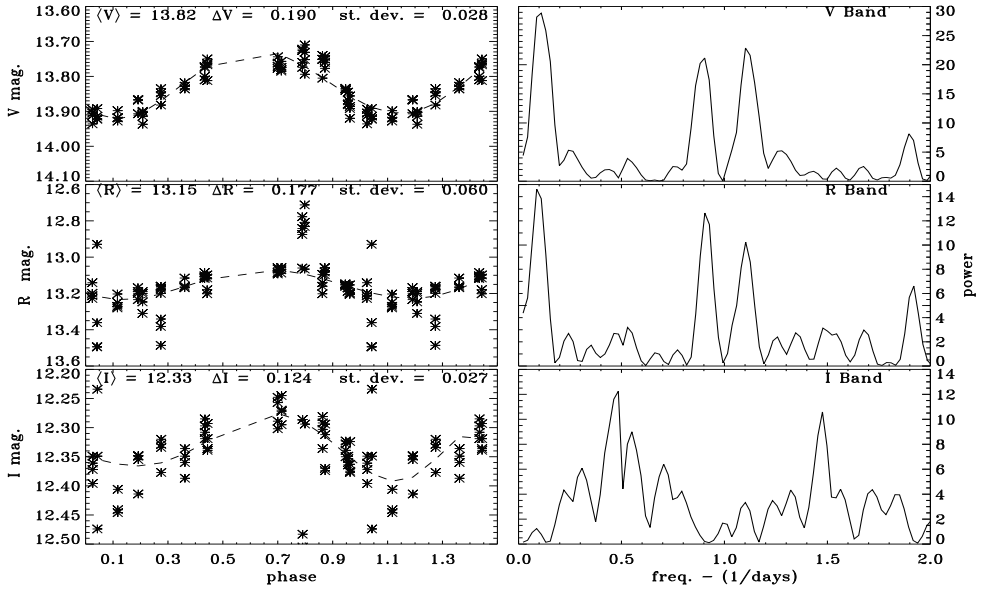

R053849−0238 – 12.9 days

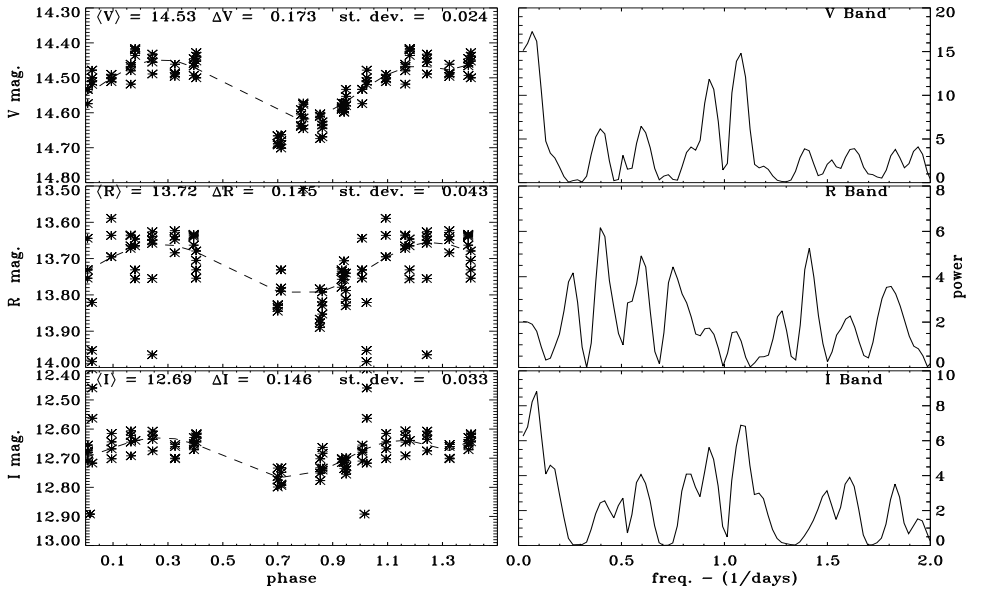

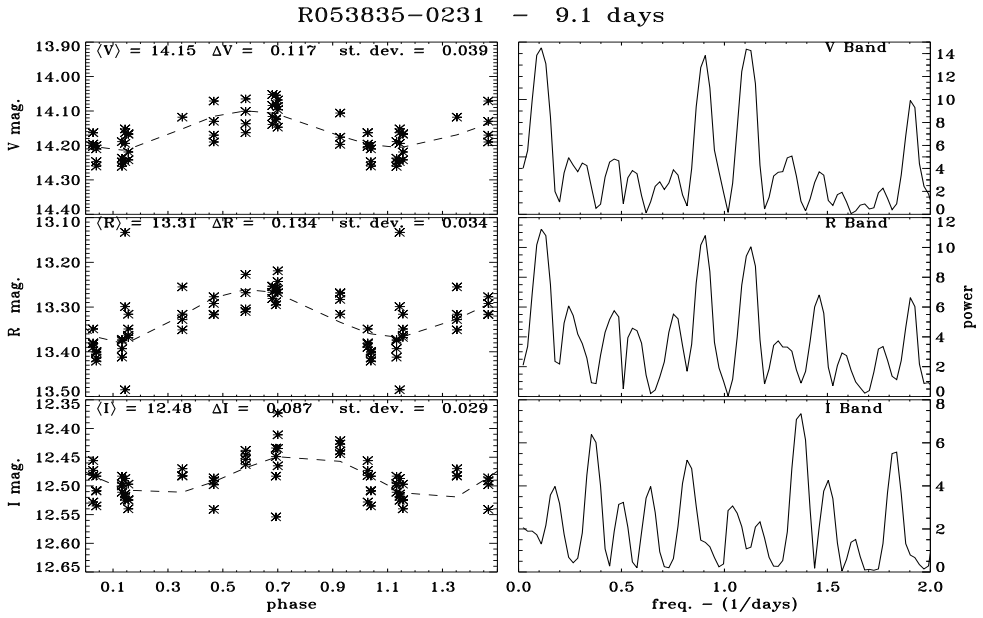
R053835−0231 − 9.1 days
⟨V⟩ = 14.15 ΔV = 0.117 st. dev. = 0.039
⟨R⟩ = 13.31 ΔR = 0.134 st. dev. = 0.034
⟨I⟩ = 12.48 ΔI = 0.087 st. dev. = 0.029
V mag.
R mag.
I mag.
phase
V Band
R Band
I Band
power
freq. − (1/days)

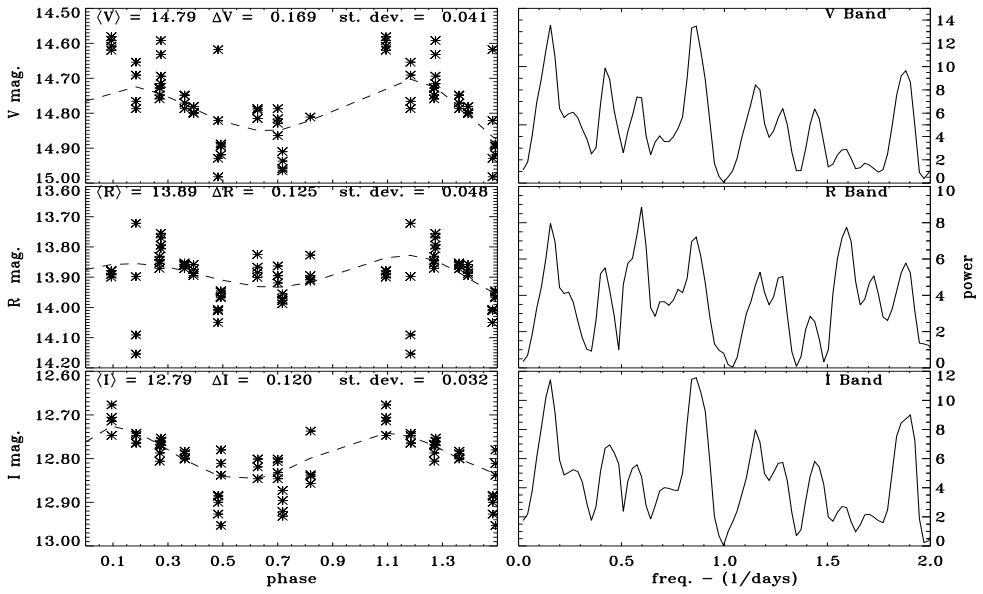
R053840−0230 − 1.16 days
⟨V⟩ = 14.79 ΔV = 0.169 st. dev. = 0.041
⟨R⟩ = 13.89 ΔR = 0.125 st. dev. = 0.048
⟨I⟩ = 12.79 ΔI = 0.120 st. dev. = 0.032
V mag.
R mag.
I mag.
phase
V Band
R Band
I Band
power
freq. − (1/days)

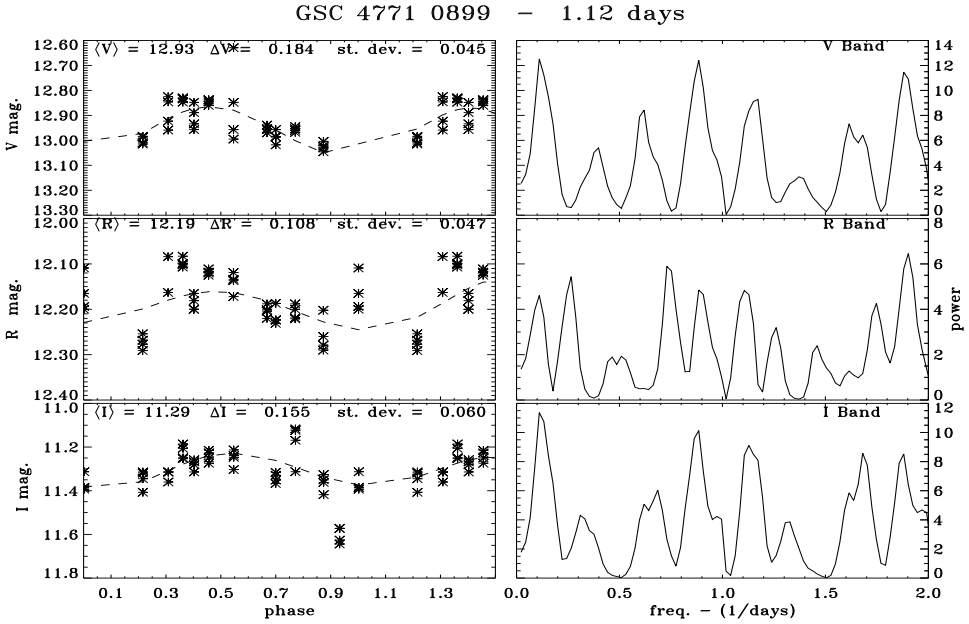
GSC 4771 0899 − 1.12 days
⟨V⟩ = 12.93 ΔV = 0.184 st. dev. = 0.045
⟨R⟩ = 12.19 ΔR = 0.108 st. dev. = 0.047
⟨I⟩ = 11.29 ΔI = 0.155 st. dev. = 0.060
V mag.
R mag.
I mag.
phase
V Band
R Band
I Band
power
freq. − (1/days)

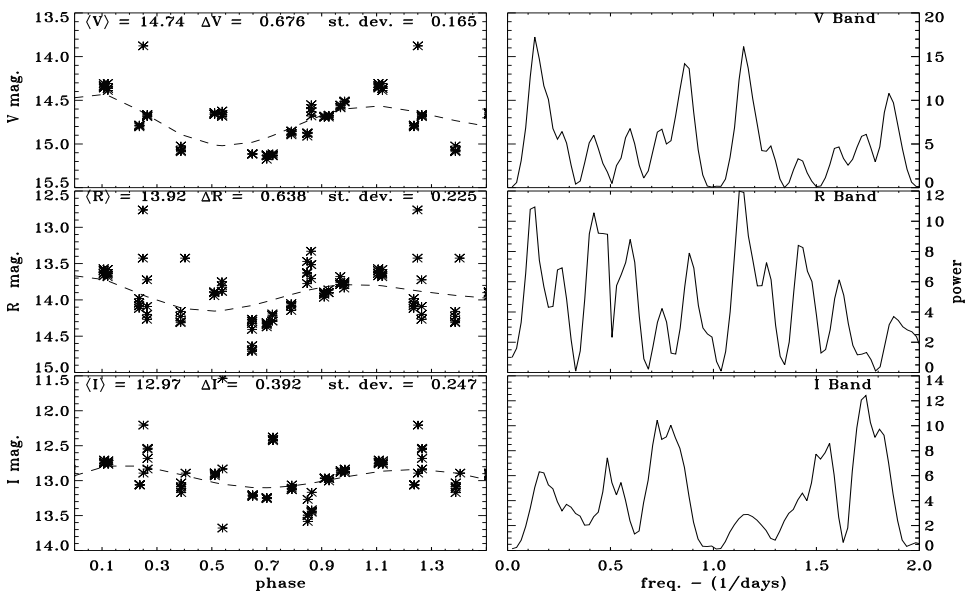
R053859−0247 − 7.40 days
⟨V⟩ = 14.74 ΔV = 0.676 st. dev. = 0.165
⟨R⟩ = 13.92 ΔR = 0.638 st. dev. = 0.225
⟨I⟩ = 12.97 ΔI = 0.392 st. dev. = 0.247
V mag.
R mag.
I mag.
phase
V Band
R Band
I Band
power
freq. − (1/days)

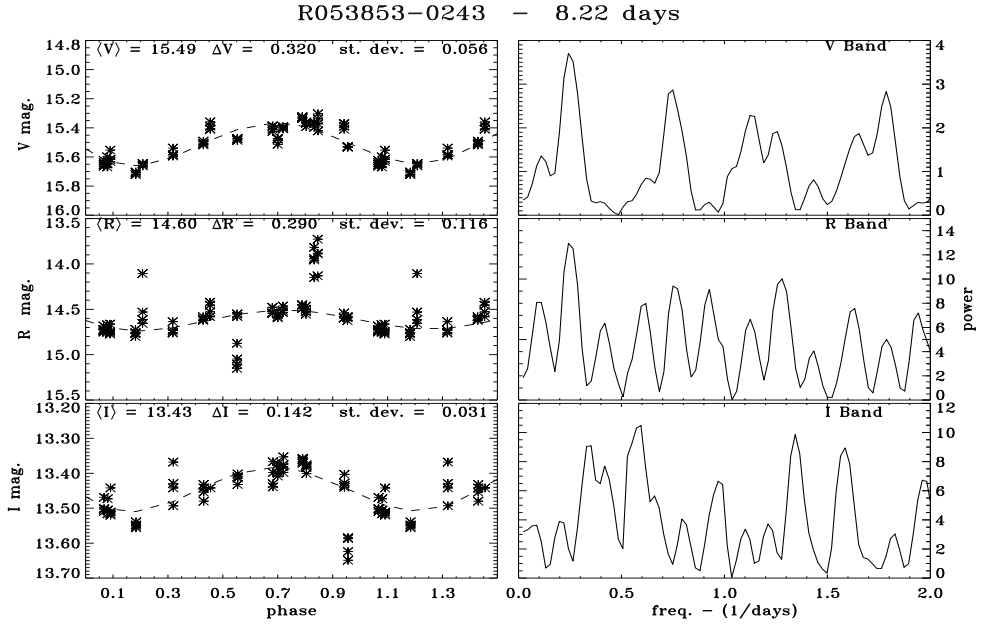
R053853−0243 − 8.22 days
⟨V⟩ = 15.49 ΔV = 0.320 st. dev. = 0.056
⟨R⟩ = 14.60 ΔR = 0.290 st. dev. = 0.116
⟨I⟩ = 13.43 ΔI = 0.142 st. dev. = 0.031
V mag.
R mag.
I mag.
phase
V Band
R Band
I Band
power
freq. − (1/days)

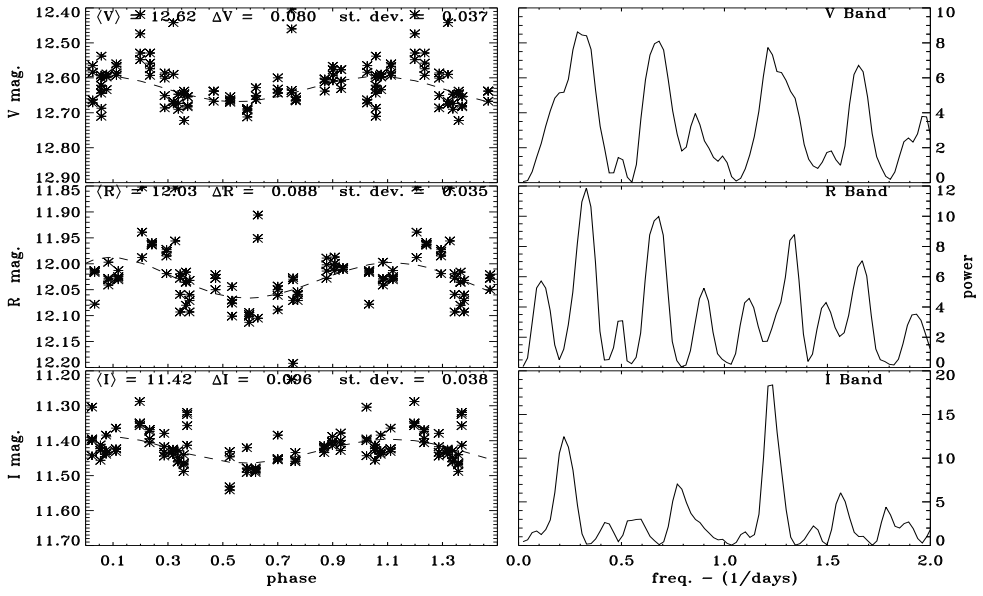
GSC 4771 0854 − 3.4 days
⟨V⟩ = 12.62 ΔV = 0.080 st. dev. = 0.037
⟨R⟩ = 12.03 ΔR = 0.088 st. dev. = 0.035
⟨I⟩ = 11.42 ΔI = 0.096 st. dev. = 0.038
V mag.
R mag.
I mag.
phase
V Band
R Band
I Band
power
freq. − (1/days)

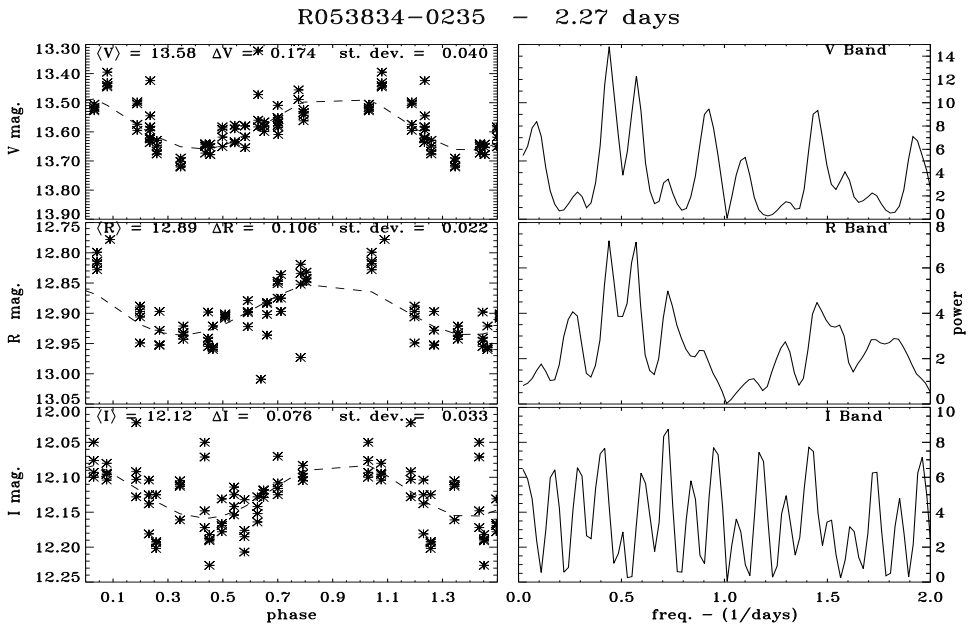
R053834−0235 − 2.27 days
⟨V⟩ = 13.58 ΔV = 0.174 st. dev. = 0.040
⟨R⟩ = 12.89 ΔR = 0.106 st. dev. = 0.022
⟨I⟩ = 12.12 ΔI = 0.076 st. dev. = 0.033
V mag.
R mag.
I mag.
phase
V Band
R Band
I Band
power
freq. − (1/days)

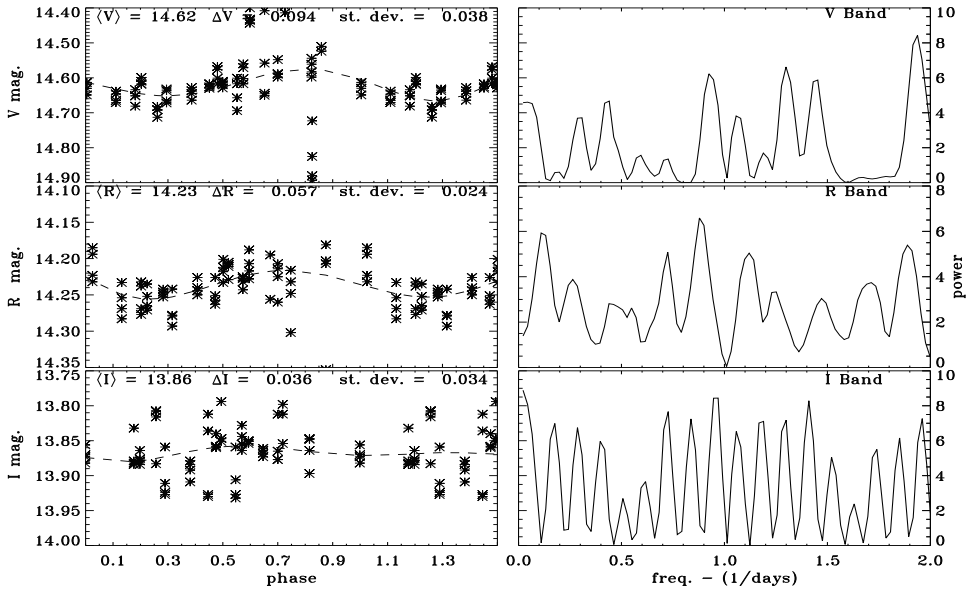
R053832−0235 − 1.08 days
⟨V⟩ = 14.62 ΔV = 0.094 st. dev. = 0.038
⟨R⟩ = 14.23 ΔR = 0.057 st. dev. = 0.024
⟨I⟩ = 13.86 ΔI = 0.036 st. dev. = 0.034
V mag.
R mag.
I mag.
phase
V Band
R Band
I Band
power
freq. − (1/days)

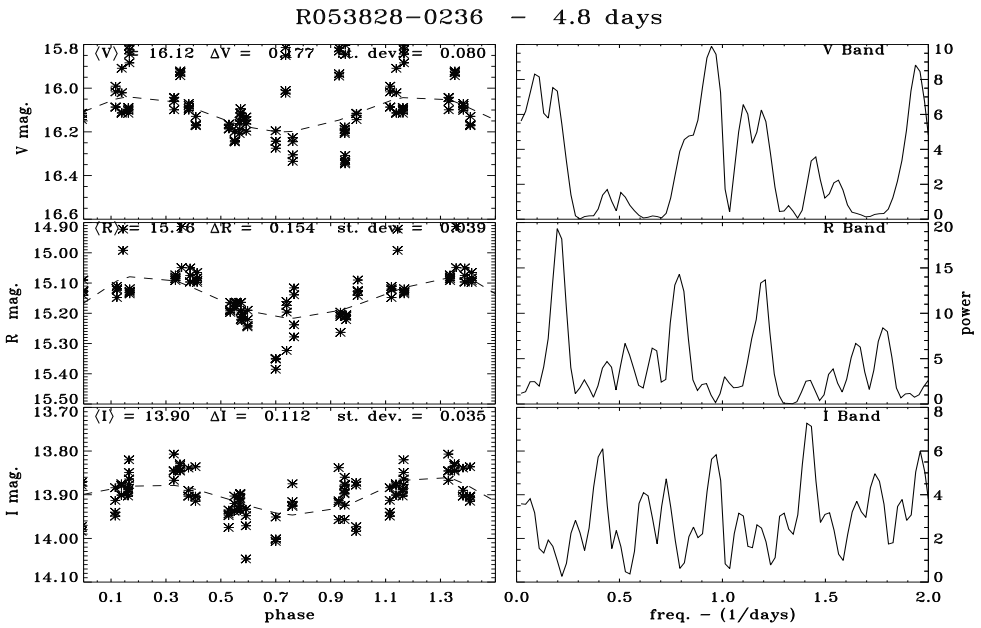
R053828−0236 − 4.8 days
⟨V⟩ = 16.12 ΔV = 0.177 st. dev. = 0.080
⟨R⟩ = 15.46 ΔR = 0.154 st. dev. = 0.039
⟨I⟩ = 13.90 ΔI = 0.112 st. dev. = 0.035
V mag.
R mag.
I mag.
phase
V Band
R Band
I Band
power
freq. − (1/days)

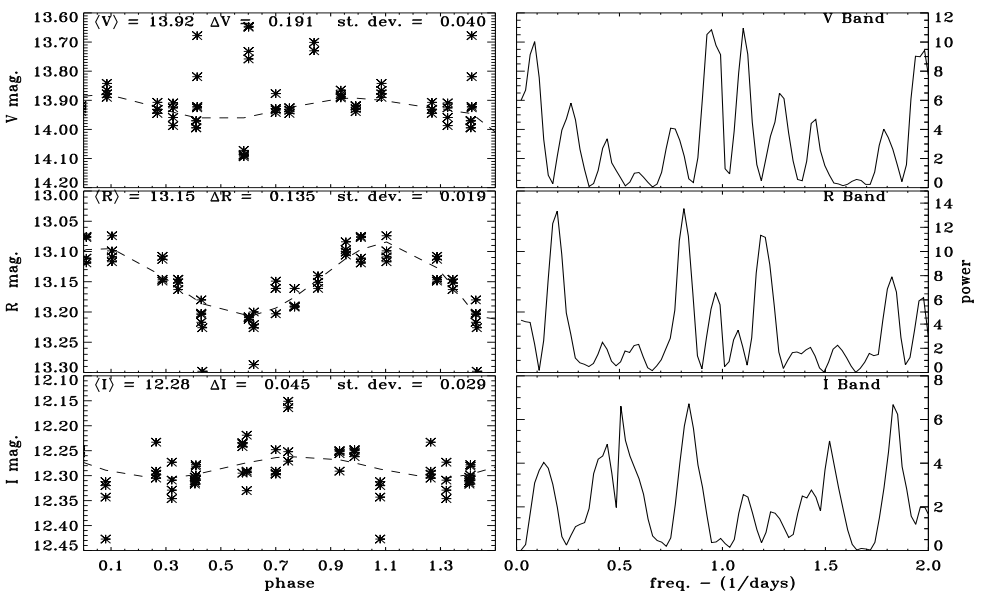
R053838−0236 − 1.23 days
⟨V⟩ = 13.92 ΔV = 0.191 st. dev. = 0.040
⟨R⟩ = 13.15 ΔR = 0.135 st. dev. = 0.019
⟨I⟩ = 12.28 ΔI = 0.045 st. dev. = 0.029
V mag.
R mag.
I mag.
phase
V Band
R Band
I Band
power
freq. − (1/days)

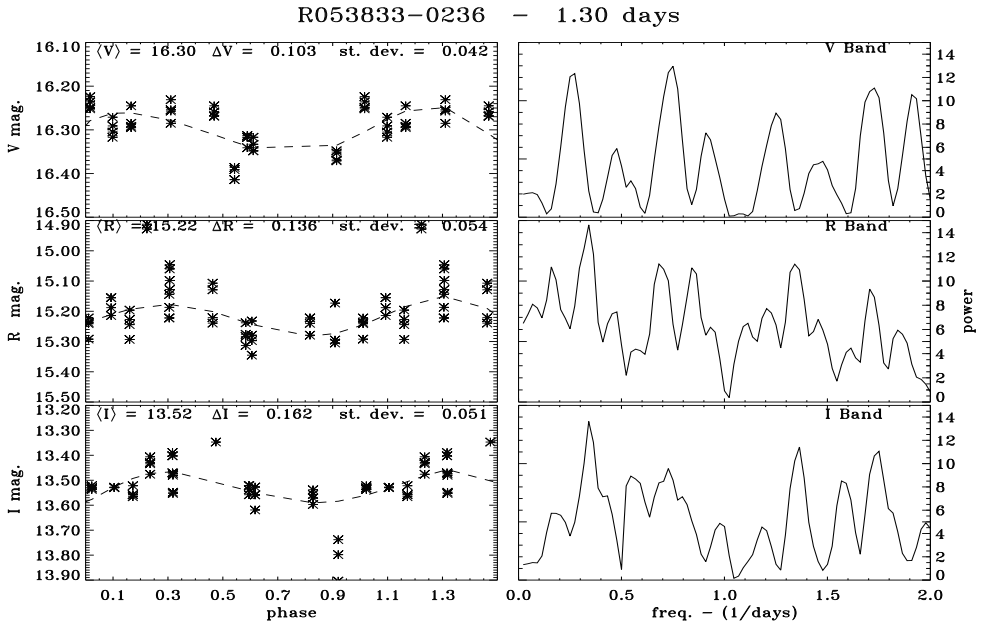
R053833−0236 − 1.30 days
⟨V⟩ = 16.30 ΔV = 0.103 st. dev. = 0.042
⟨R⟩ = 15.22 ΔR = 0.136 st. dev. = 0.054
⟨I⟩ = 13.52 ΔI = 0.162 st. dev. = 0.051
V mag.
R mag.
I mag.
phase
V Band
R Band
I Band
power
freq. − (1/days)

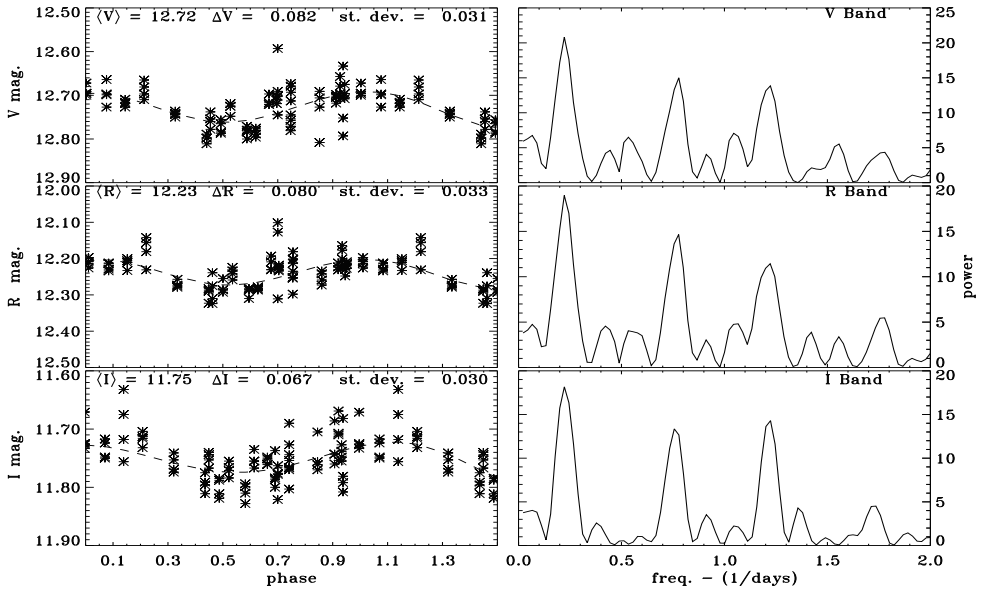
GSC 0101 1156 − 0.82 days
⟨V⟩ = 12.72 ΔV = 0.082 st. dev. = 0.031
⟨R⟩ = 12.23 ΔR = 0.080 st. dev. = 0.033
⟨I⟩ = 11.75 ΔI = 0.067 st. dev. = 0.030
V mag.
R mag.
I mag.
phase
V Band
R Band
I Band
power
freq. − (1/days)

R052422+0100 – 1.25 days

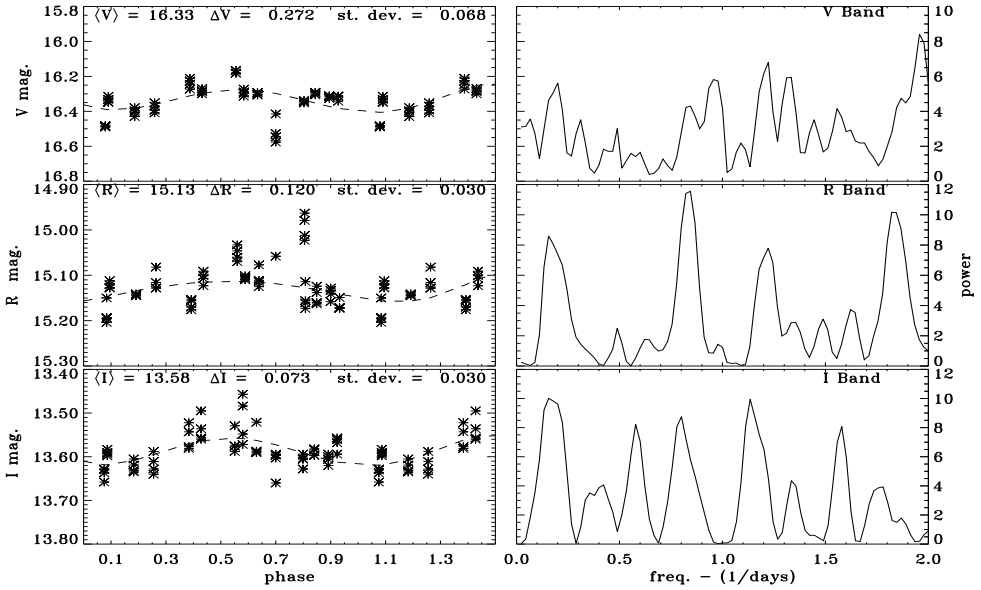

GSC 0101 0657 – 1.29 days

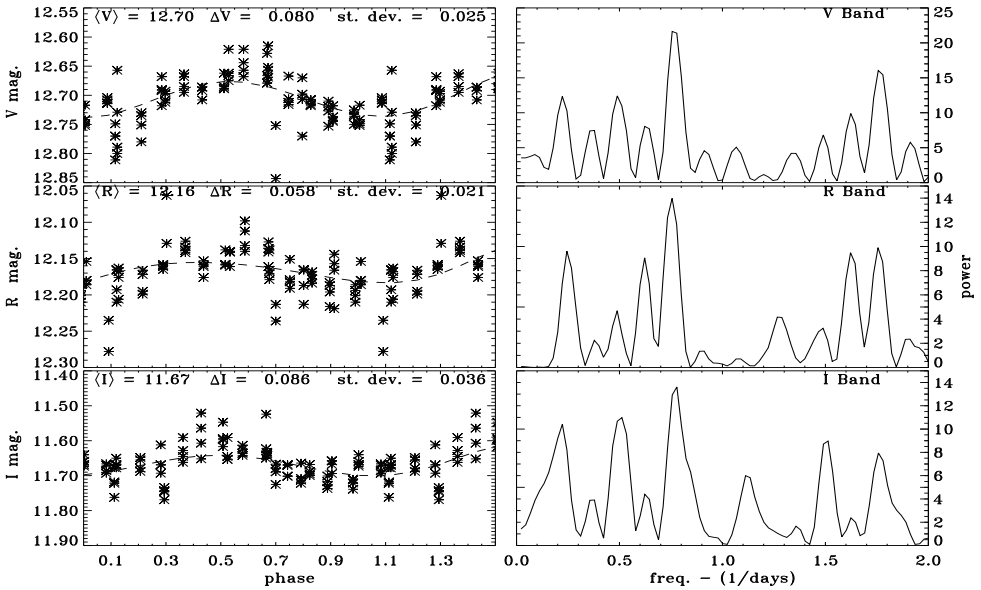

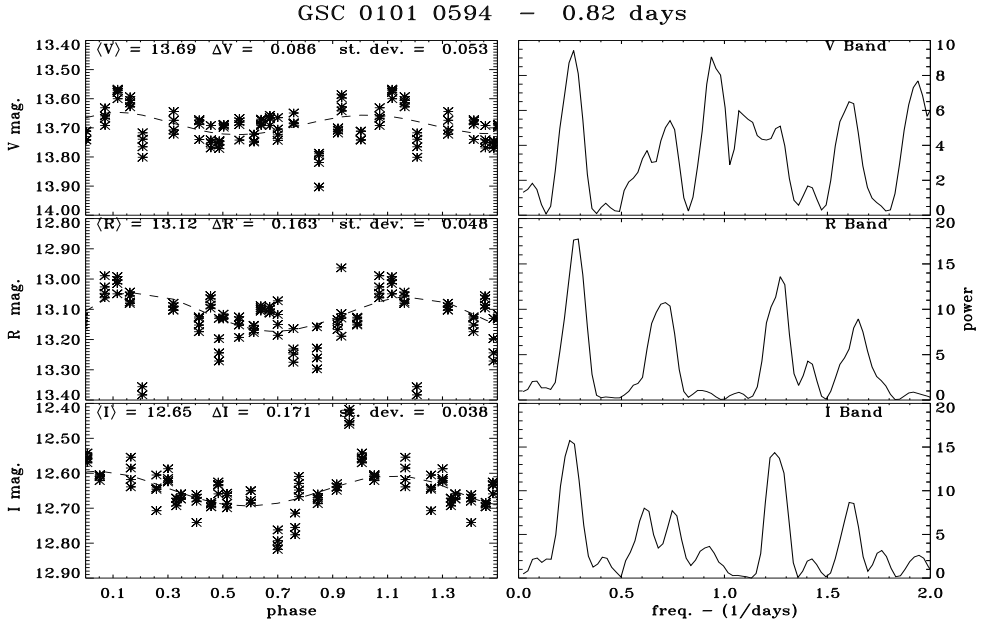
GSC 0101 0594 − 0.82 days
⟨V⟩ = 13.69 ΔV = 0.086 st. dev. = 0.053
⟨R⟩ = 13.12 ΔR = 0.163 st. dev. = 0.048
⟨I⟩ = 12.65 ΔI = 0.171 st. dev. = 0.038
V mag.
R mag.
I mag.
phase
V Band
R Band
I Band
power
freq. − (1/days)

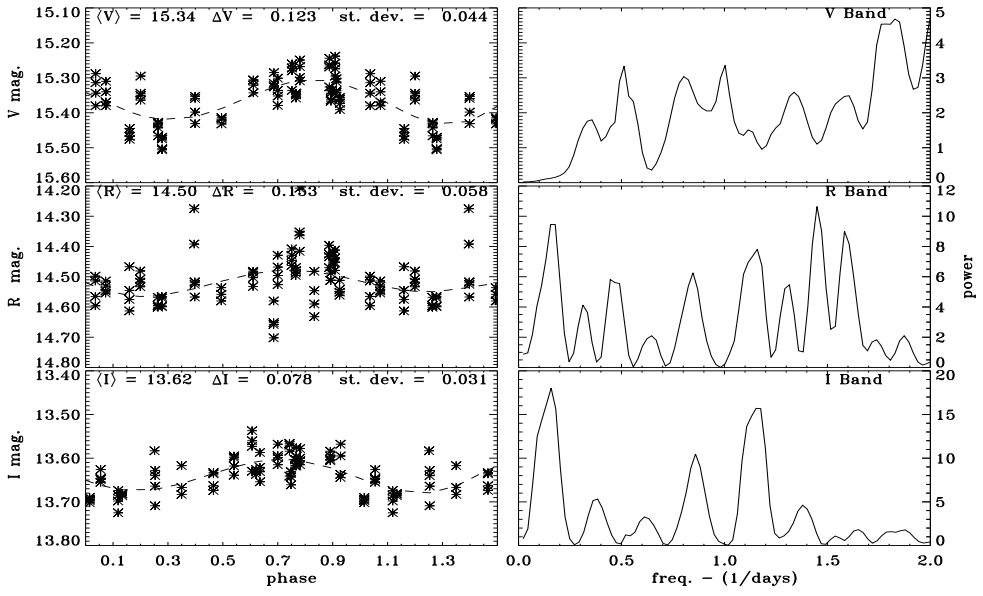
J052439+0121 − 0.88 days
⟨V⟩ = 15.34 ΔV = 0.123 st. dev. = 0.044
⟨R⟩ = 14.50 ΔR = 0.153 st. dev. = 0.058
⟨I⟩ = 13.62 ΔI = 0.078 st. dev. = 0.031
V mag.
R mag.
I mag.
phase
V Band
R Band
I Band
power
freq. − (1/days)

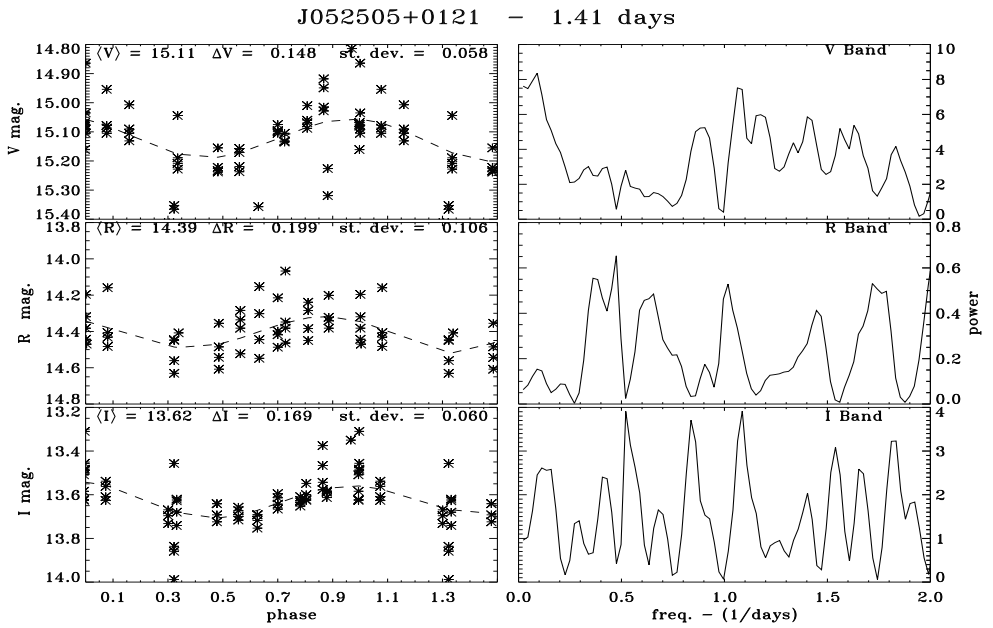
J052505+0121 − 1.41 days
⟨V⟩ = 15.11 ΔV = 0.148 st. dev. = 0.058
⟨R⟩ = 14.39 ΔR = 0.199 st. dev. = 0.106
⟨I⟩ = 13.62 ΔI = 0.169 st. dev. = 0.060
V mag.
R mag.
I mag.
phase
V Band
R Band
I Band
power
freq. − (1/days)

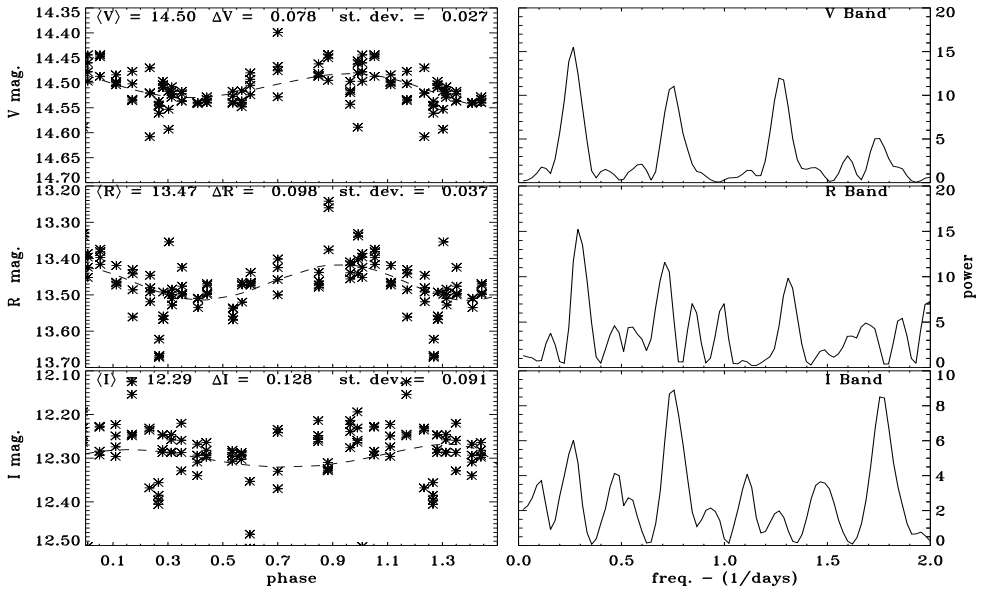
GSC 0101 1579 − 3.6 days
⟨V⟩ = 14.50 ΔV = 0.078 st. dev. = 0.027
⟨R⟩ = 13.47 ΔR = 0.098 st. dev. = 0.037
⟨I⟩ = 12.29 ΔI = 0.128 st. dev. = 0.091
V mag.
R mag.
I mag.
phase
V Band
R Band
I Band
power
freq. − (1/days)

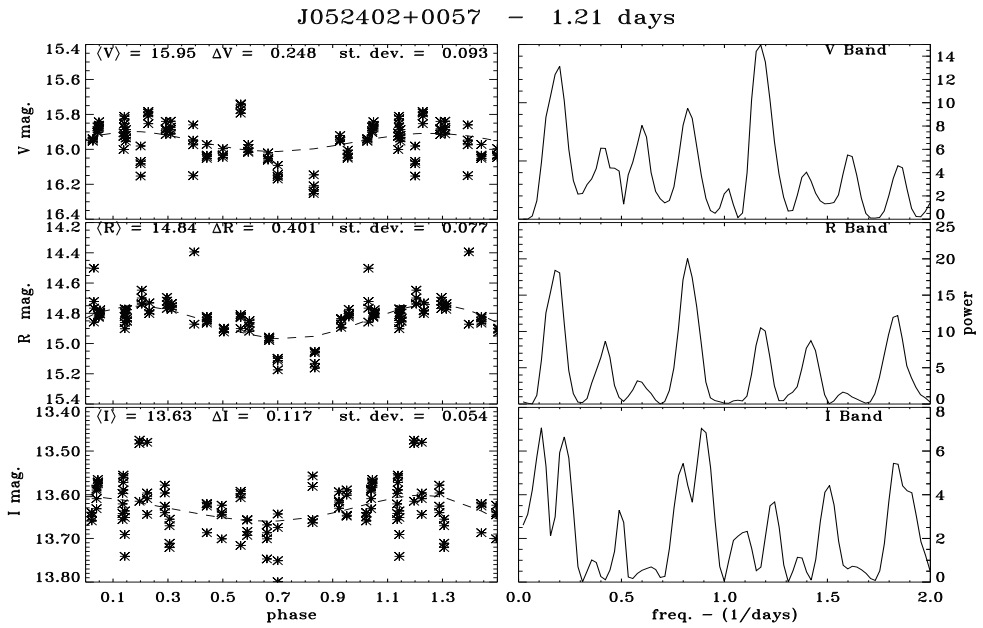
J052402+0057 − 1.21 days
⟨V⟩ = 15.95 ΔV = 0.248 st. dev. = 0.093
⟨R⟩ = 14.84 ΔR = 0.401 st. dev. = 0.077
⟨I⟩ = 13.63 ΔI = 0.117 st. dev. = 0.054
V mag.
R mag.
I mag.
phase
V Band
R Band
I Band
power
freq. − (1/days)

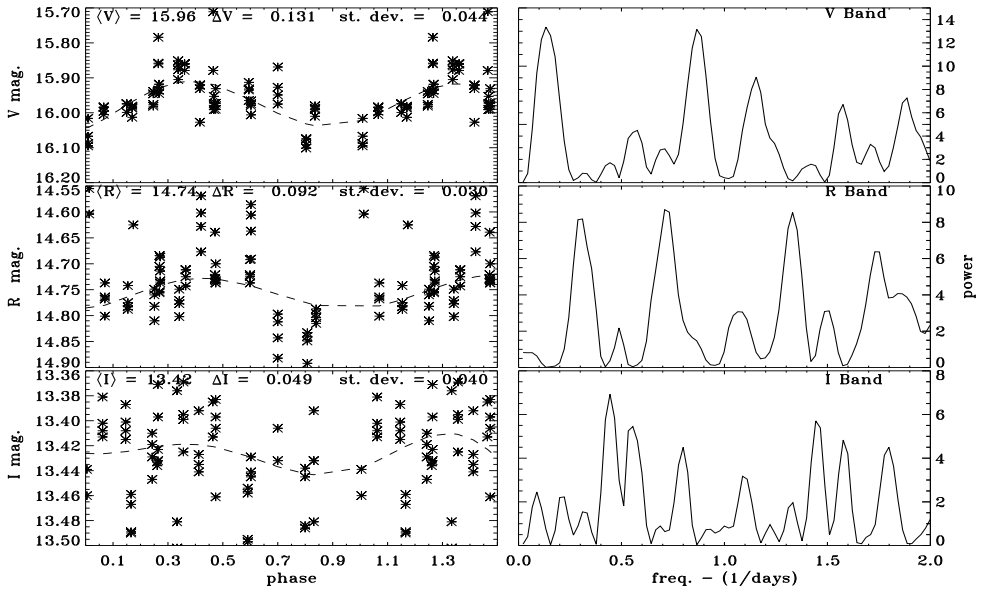
J052354+0055 − 1.16 days
⟨V⟩ = 15.96 ΔV = 0.131 st. dev. = 0.044
⟨R⟩ = 14.74 ΔR = 0.092 st. dev. = 0.030
⟨I⟩ = 13.42 ΔI = 0.049 st. dev. = 0.040
V mag.
R mag.
I mag.
phase
V Band
R Band
I Band
power
freq. − (1/days)

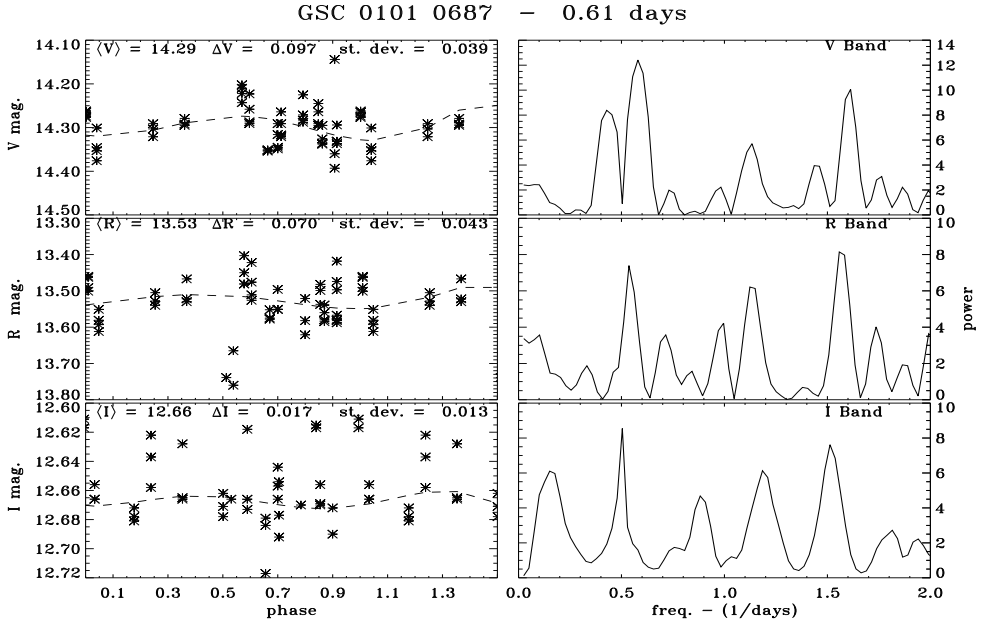
GSC 0101 0687 – 0.61 days
⟨V⟩ = 14.29 ΔV = 0.097 st. dev. = 0.039
⟨R⟩ = 13.53 ΔR = 0.070 st. dev. = 0.043
⟨I⟩ = 12.66 ΔI = 0.017 st. dev. = 0.013
V mag.
R mag.
I mag.
phase
V Band
R Band
I Band
power
freq. – (1/days)

B.3 Highly Uncertain Period Determinations

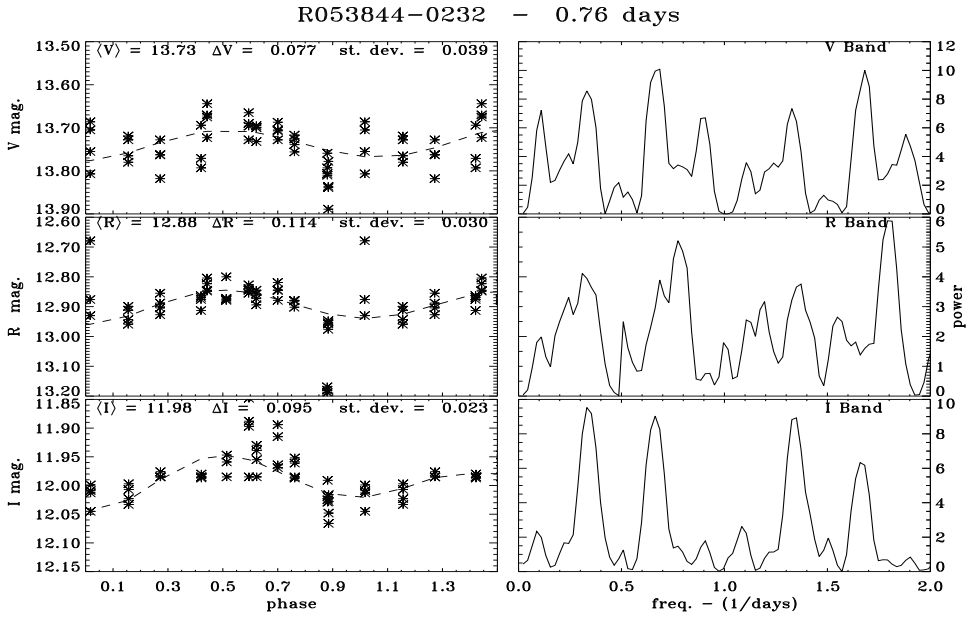

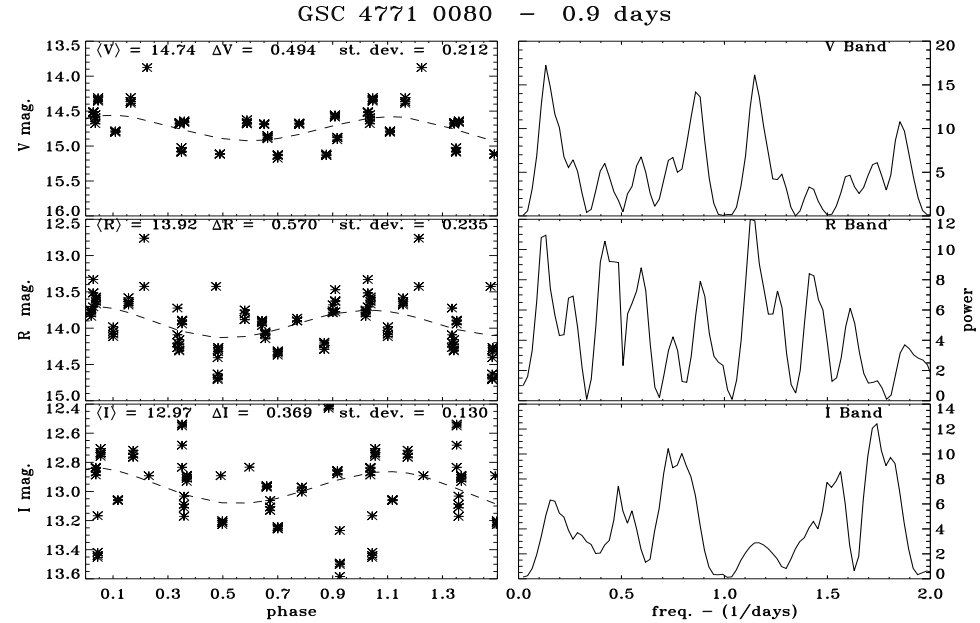

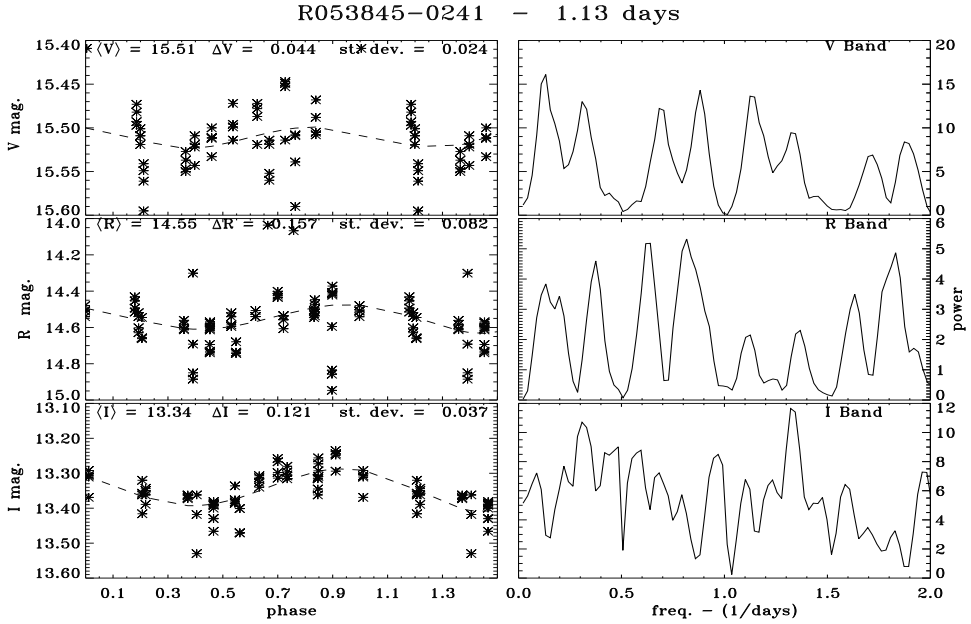
R053845−0241 − 1.13 days
⟨V⟩ = 15.51 ΔV = 0.044 st. dev. = 0.024
⟨R⟩ = 14.55 ΔR = 0.157 st. dev. = 0.082
⟨I⟩ = 13.34 ΔI = 0.121 st. dev. = 0.037
V mag.
R mag.
I mag.
phase
V Band
R Band
I Band
power
freq. − (1/days)

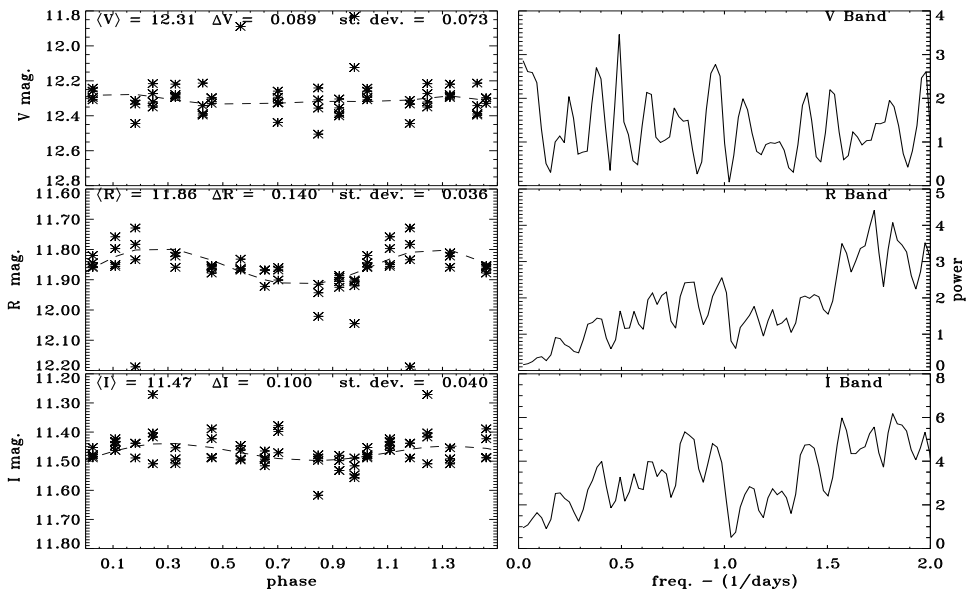
GSC 4771 0598 − 1.31 days
⟨V⟩ = 12.31 ΔV = 0.089 st. dev. = 0.073
⟨R⟩ = 11.86 ΔR = 0.140 st. dev. = 0.036
⟨I⟩ = 11.47 ΔI = 0.100 st. dev. = 0.040
V mag.
R mag.
I mag.
phase
V Band
R Band
I Band
power
freq. − (1/days)

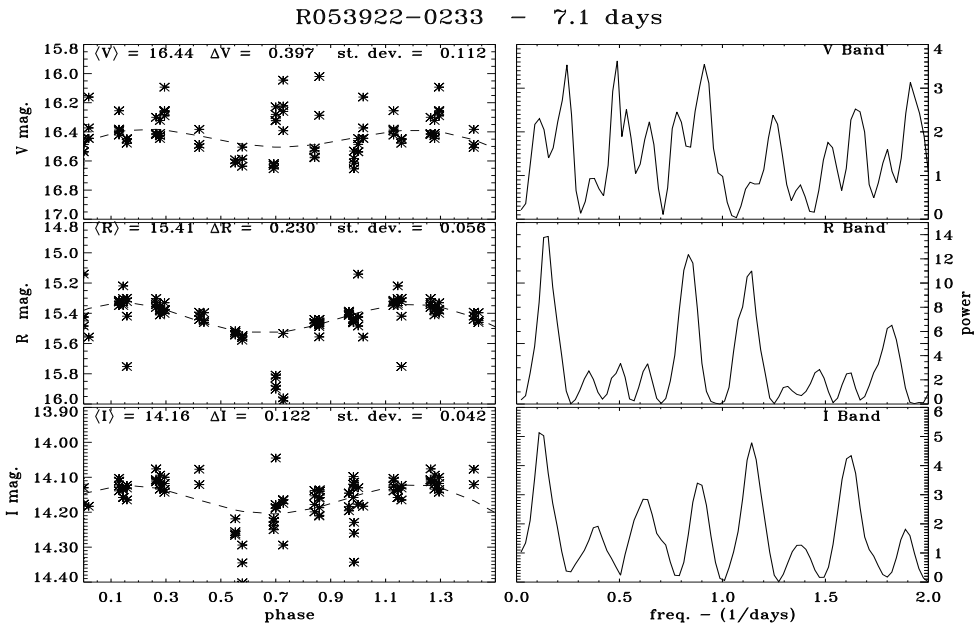
R053922−0233 − 7.1 days
⟨V⟩ = 16.44 ΔV = 0.397 st. dev. = 0.112
⟨R⟩ = 15.41 ΔR = 0.230 st. dev. = 0.056
⟨I⟩ = 14.16 ΔI = 0.122 st. dev. = 0.042
V mag.
R mag.
I mag.
phase
V Band
R Band
I Band
power
freq. − (1/days)

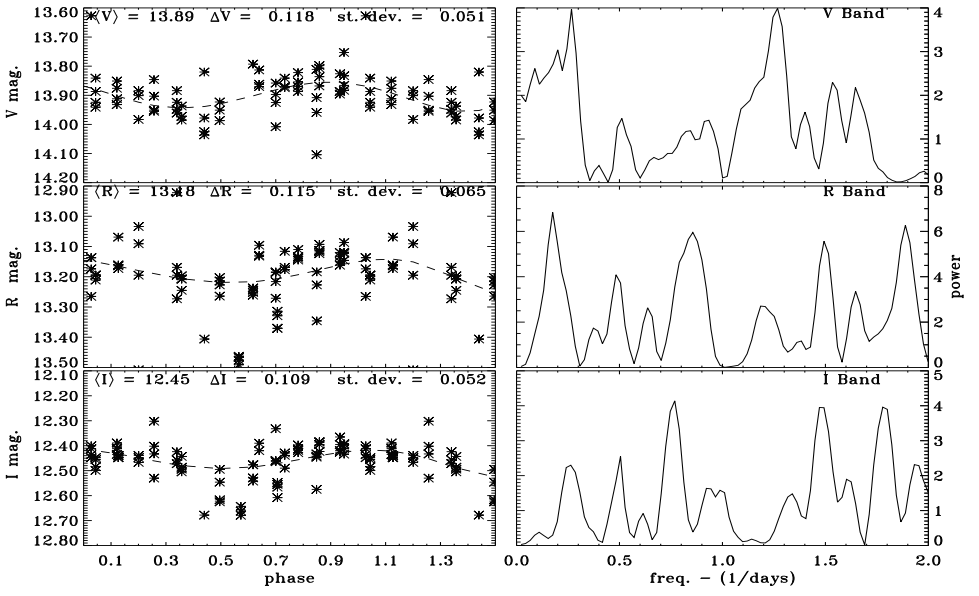
GSC 4771 1092 − 1.3 days
⟨V⟩ = 13.89 ΔV = 0.118 st. dev. = 0.051
⟨R⟩ = 13.18 ΔR = 0.115 st. dev. = 0.065
⟨I⟩ = 12.45 ΔI = 0.109 st. dev. = 0.052
V mag.
R mag.
I mag.
phase
V Band
R Band
I Band
power
freq. − (1/days)

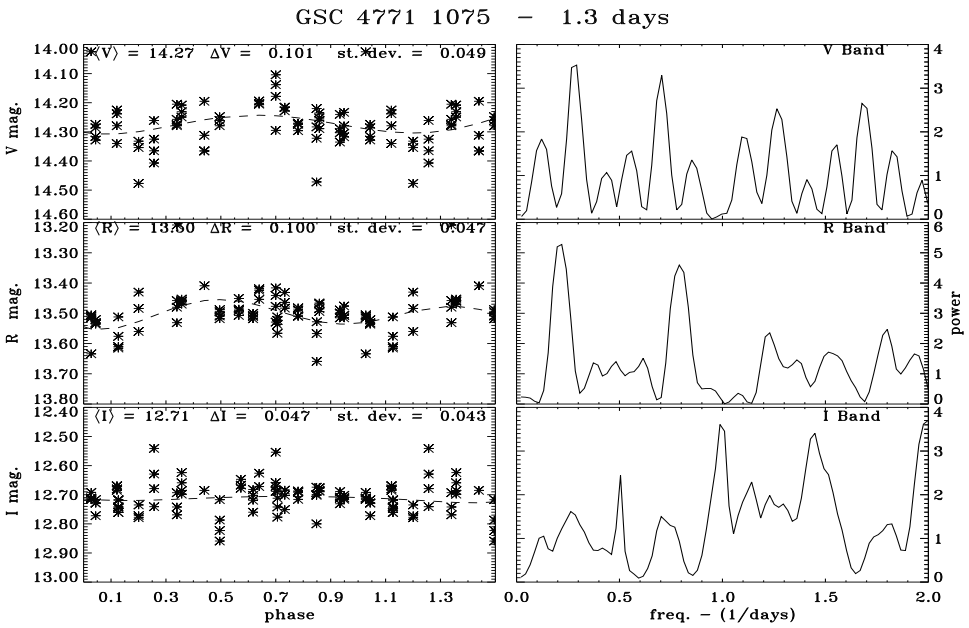
GSC 4771 1075 − 1.3 days
⟨V⟩ = 14.27 ΔV = 0.101 st. dev. = 0.049
⟨R⟩ = 13.60 ΔR = 0.100 st. dev. = 0.047
⟨I⟩ = 12.71 ΔI = 0.047 st. dev. = 0.043
V mag.
R mag.
I mag.
phase
V Band
R Band
I Band
power
freq. − (1/days)

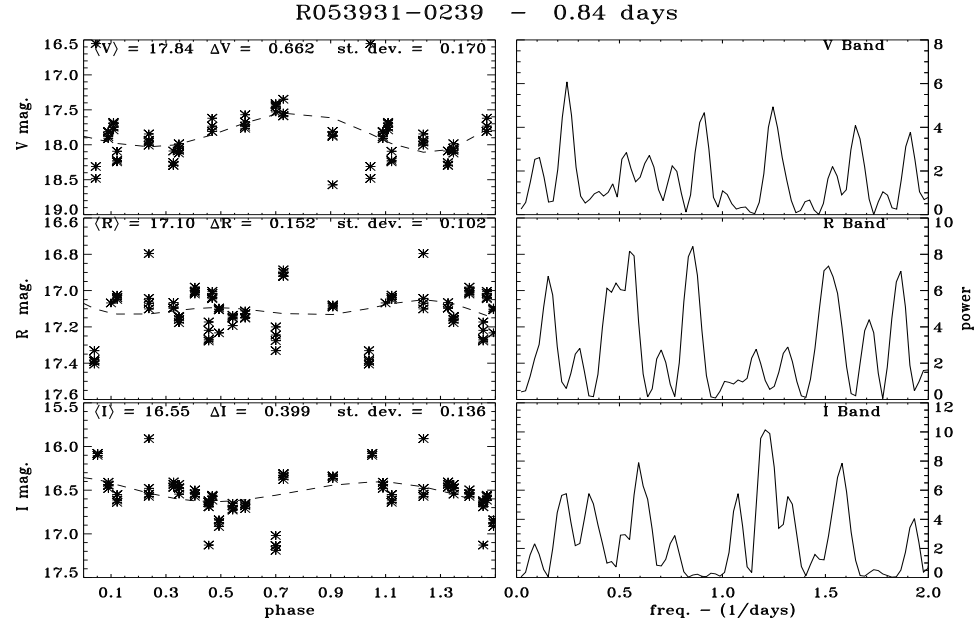
R053931−0239 − 0.84 days
⟨V⟩ = 17.84 ΔV = 0.662 st. dev. = 0.170
⟨R⟩ = 17.10 ΔR = 0.152 st. dev. = 0.102
⟨I⟩ = 16.55 ΔI = 0.399 st. dev. = 0.136
V mag.
R mag.
I mag.
phase
V Band
R Band
I Band
power
freq. − (1/days)

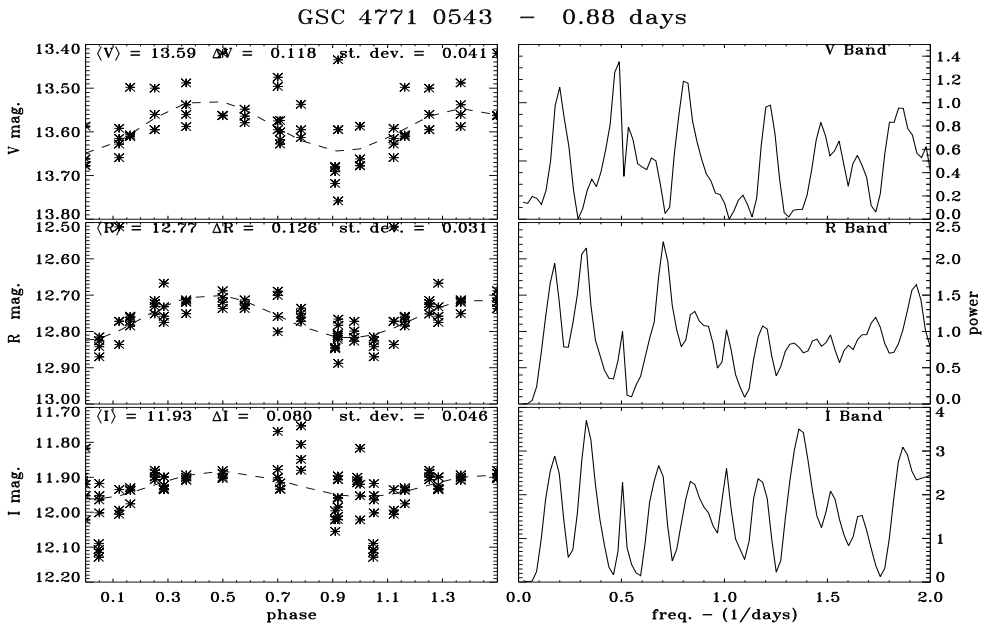
GSC 4771 0543 − 0.88 days
⟨V⟩ = 13.59 ΔV = 0.118 st. dev. = 0.041
⟨R⟩ = 12.77 ΔR = 0.126 st. dev. = 0.031
⟨I⟩ = 11.93 ΔI = 0.080 st. dev. = 0.046
V mag.
R mag.
I mag.
phase
V Band
R Band
I Band
power
freq. − (1/days)

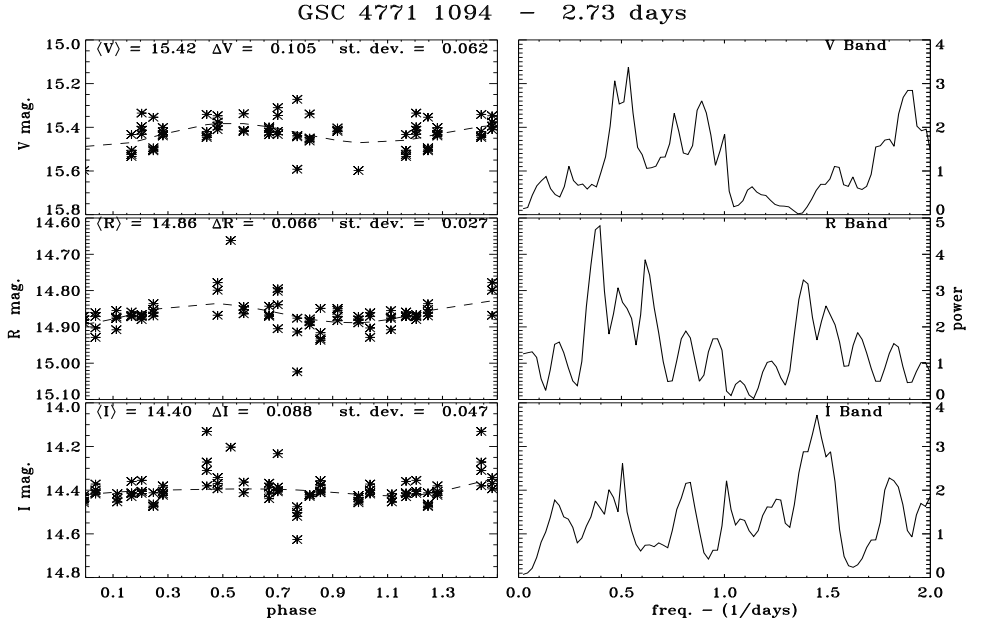
GSC 4771 1094 − 2.73 days
⟨V⟩ = 15.42 ΔV = 0.105 st. dev. = 0.062
⟨R⟩ = 14.86 ΔR = 0.066 st. dev. = 0.027
⟨I⟩ = 14.40 ΔI = 0.088 st. dev. = 0.047
V mag.
R mag.
I mag.
phase
V Band
R Band
I Band
power
freq. − (1/days)

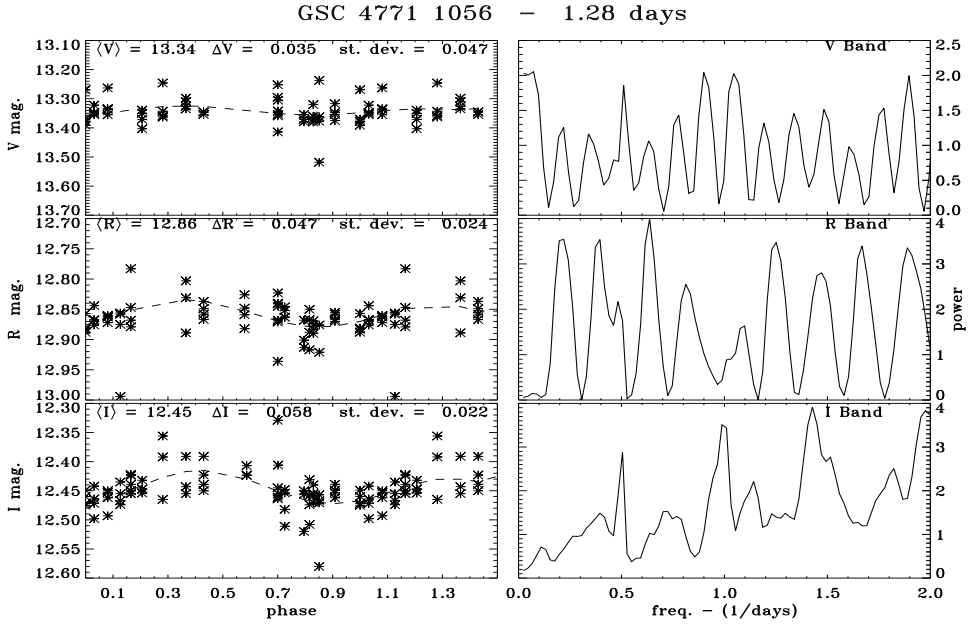
GSC 4771 1056 − 1.28 days
⟨V⟩ = 13.34 ΔV = 0.035 st. dev. = 0.047
⟨R⟩ = 12.86 ΔR = 0.047 st. dev. = 0.024
⟨I⟩ = 12.45 ΔI = 0.058 st. dev. = 0.022
V mag.
R mag.
I mag.
phase
V Band
R Band
I Band
power
freq. − (1/days)

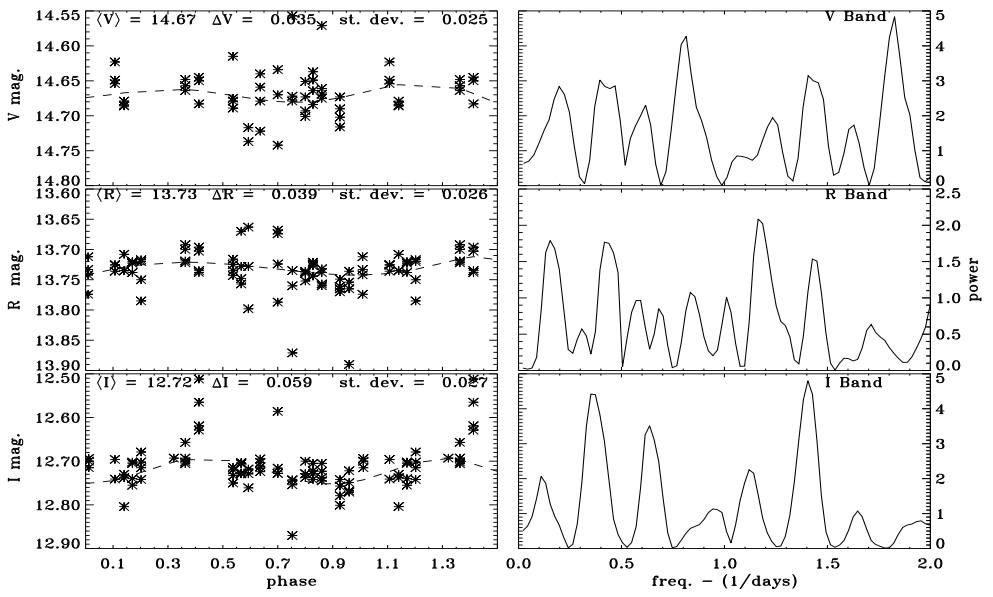
R053853−0238 − 3.64 days
⟨V⟩ = 14.67 ΔV = 0.035 st. dev. = 0.025
⟨R⟩ = 13.73 ΔR = 0.039 st. dev. = 0.026
⟨I⟩ = 12.72 ΔI = 0.059 st. dev. = 0.027
V mag.
R mag.
I mag.
phase
V Band
R Band
I Band
power
freq. − (1/days)

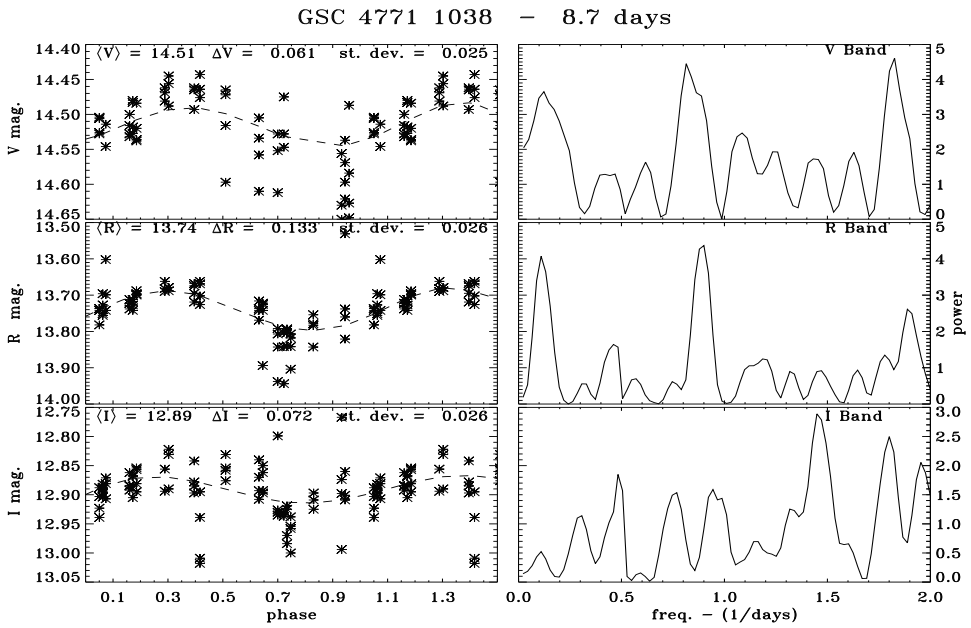
GSC 4771 1038 − 8.7 days
⟨V⟩ = 14.51 ΔV = 0.061 st. dev. = 0.025
⟨R⟩ = 13.74 ΔR = 0.133 st. dev. = 0.026
⟨I⟩ = 12.89 ΔI = 0.072 st. dev. = 0.026
V mag.
R mag.
I mag.
phase
V Band
R Band
I Band
power
freq. − (1/days)

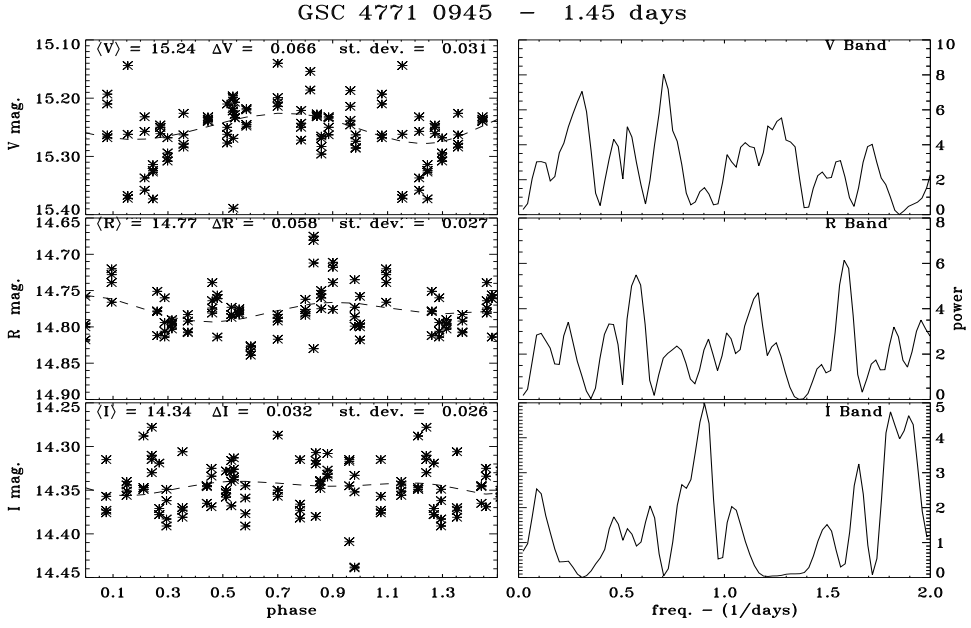
GSC 4771 0945 − 1.45 days
⟨V⟩ = 15.24 ΔV = 0.066 st. dev. = 0.031
⟨R⟩ = 14.77 ΔR = 0.058 st. dev. = 0.027
⟨I⟩ = 14.34 ΔI = 0.032 st. dev. = 0.026
V mag.
R mag.
I mag.
phase
V Band
R Band
I Band
power
freq. − (1/days)

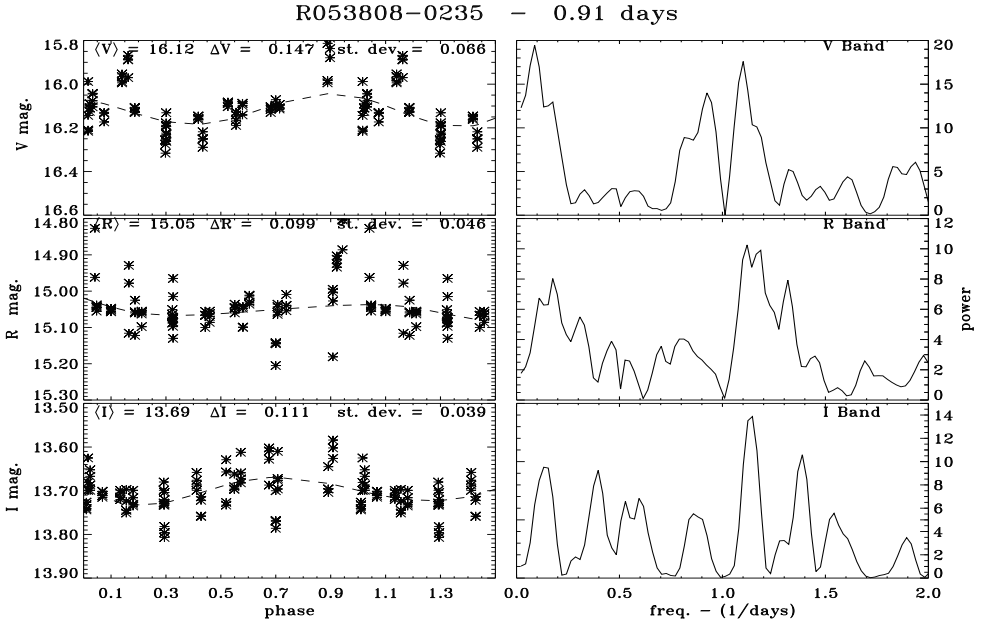
R053808−0235 − 0.91 days
⟨V⟩ = 16.12 ΔV = 0.147 st. dev. = 0.066
⟨R⟩ = 15.05 ΔR = 0.099 st. dev. = 0.046
⟨I⟩ = 13.69 ΔI = 0.111 st. dev. = 0.039
V mag.
R mag.
I mag.
phase
V Band
R Band
I Band
power
freq. − (1/days)

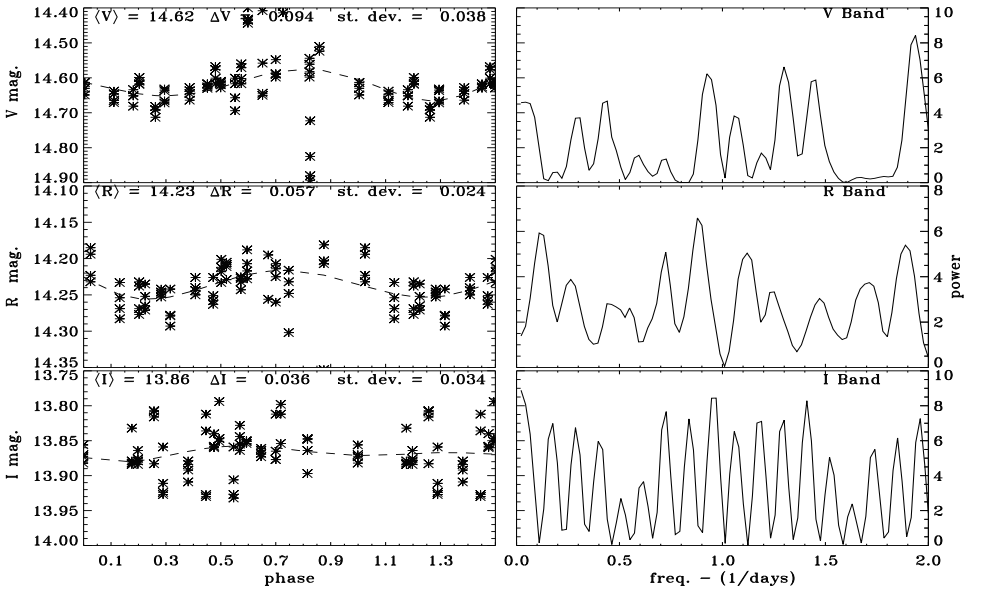
R053832−0235 − 1.08 days
⟨V⟩ = 14.62 ΔV = 0.094 st. dev. = 0.038
⟨R⟩ = 14.23 ΔR = 0.057 st. dev. = 0.024
⟨I⟩ = 13.86 ΔI = 0.036 st. dev. = 0.034
V mag.
R mag.
I mag.
phase
V Band
R Band
I Band
power
freq. − (1/days)

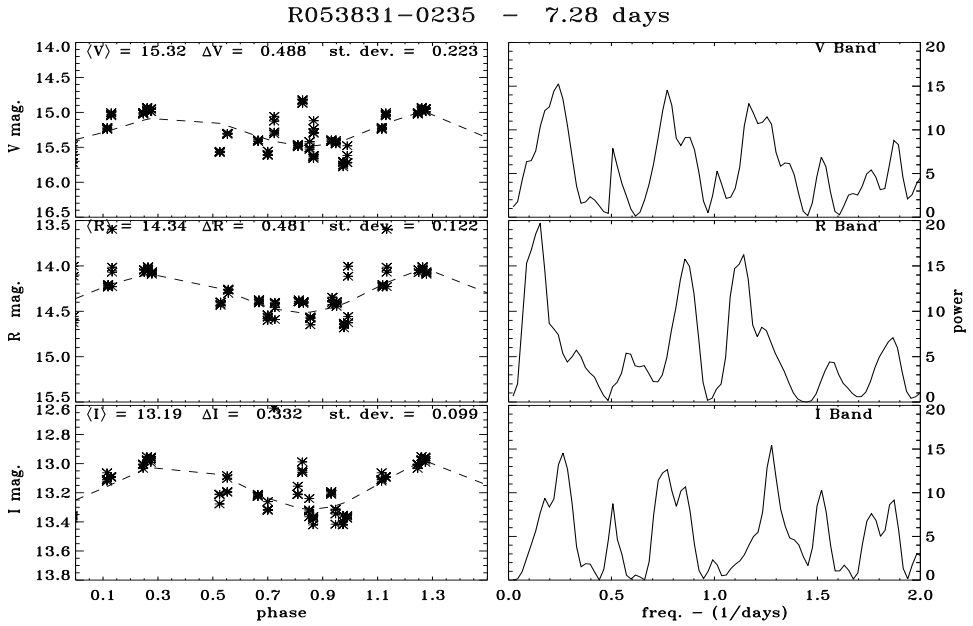
R053831−0235 − 7.28 days
⟨V⟩ = 15.32 ΔV = 0.488 st. dev. = 0.223
⟨R⟩ = 14.34 ΔR = 0.481 st. dev. = 0.122
⟨I⟩ = 13.19 ΔI = 0.332 st. dev. = 0.099
V mag.
R mag.
I mag.
phase
V Band
R Band
I Band
power
freq. − (1/days)

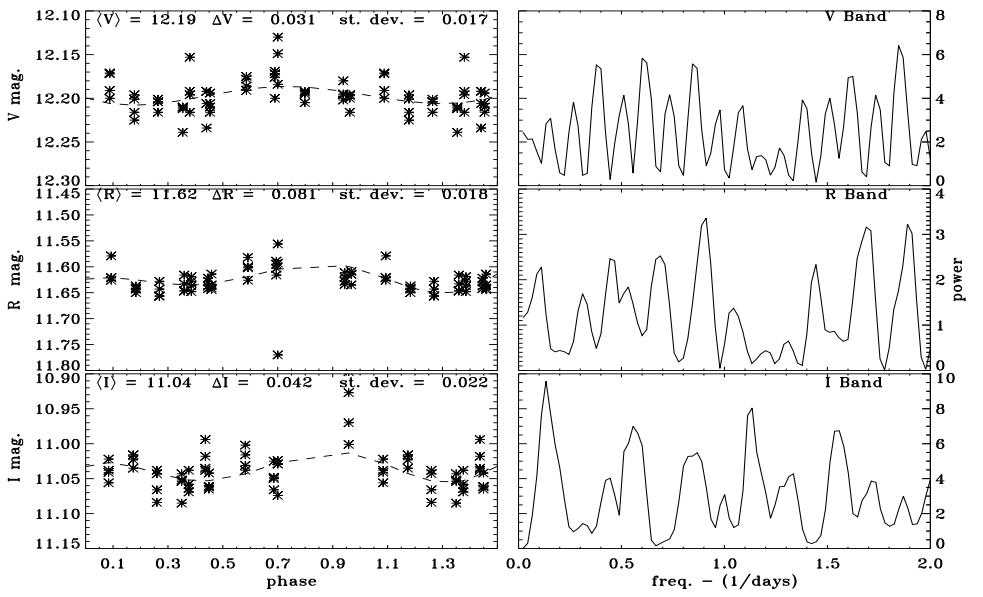
GSC 0101 1336 − 1.16 days
⟨V⟩ = 12.19 ΔV = 0.031 st. dev. = 0.017
⟨R⟩ = 11.62 ΔR = 0.081 st. dev. = 0.018
⟨I⟩ = 11.04 ΔI = 0.042 st. dev. = 0.022
V mag.
R mag.
I mag.
phase
V Band
R Band
I Band
power
freq. − (1/days)

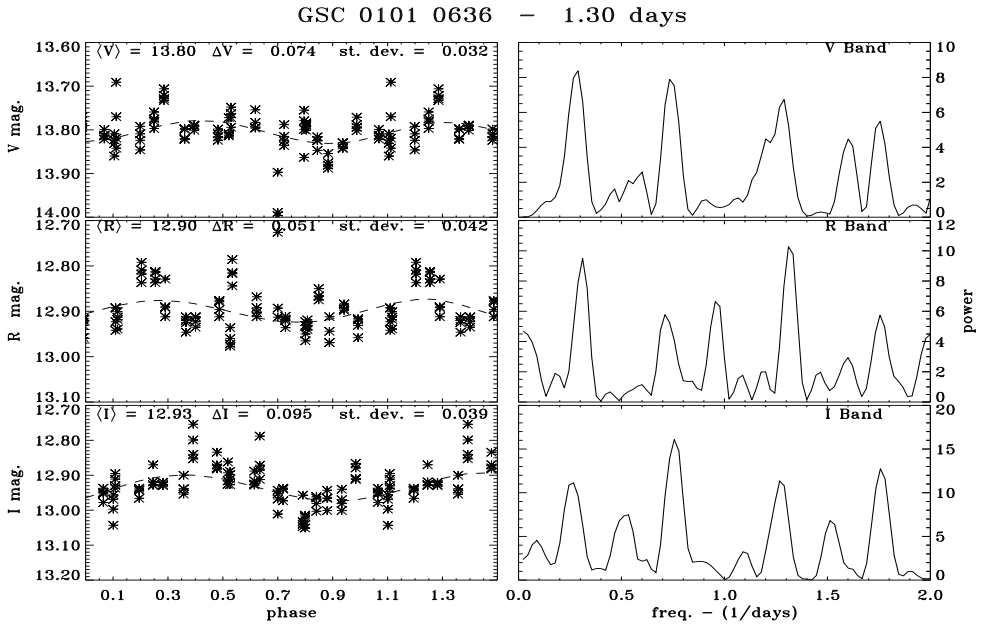
GSC 0101 0636 – 1.30 days
⟨V⟩ = 13.80 ΔV = 0.074 st. dev. = 0.032
⟨R⟩ = 12.90 ΔR = 0.051 st. dev. = 0.042
⟨I⟩ = 12.93 ΔI = 0.095 st. dev. = 0.039
V mag.
R mag.
I mag.
phase
V Band
R Band
I Band
power
freq. – (1/days)

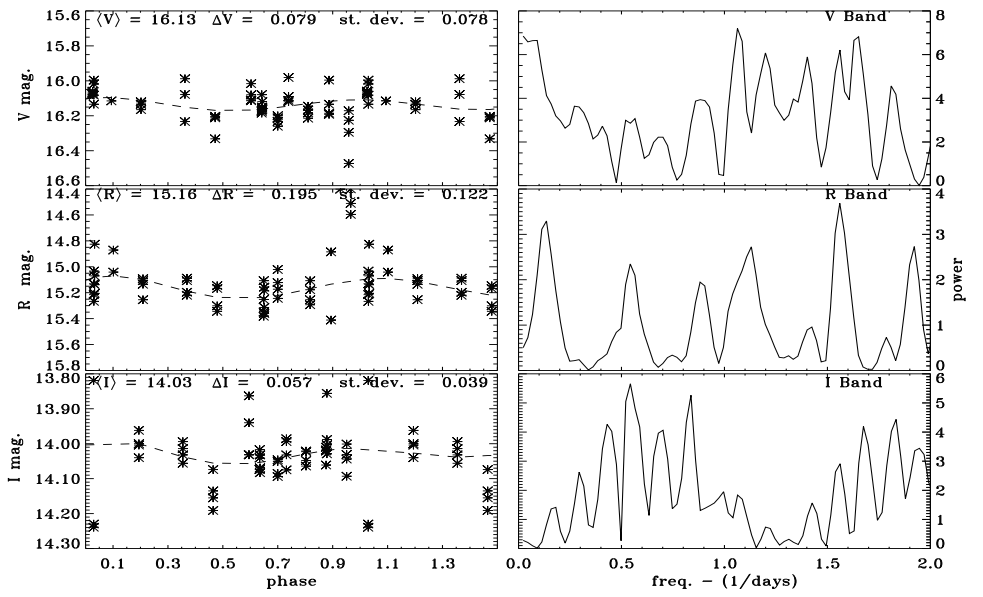
J052539+0125 – 0.66 days
⟨V⟩ = 16.13 ΔV = 0.079 st. dev. = 0.078
⟨R⟩ = 15.16 ΔR = 0.195 st. dev. = 0.122
⟨I⟩ = 14.03 ΔI = 0.057 st. dev. = 0.039
V mag.
R mag.
I mag.
phase
V Band
R Band
I Band
power
freq. – (1/days)

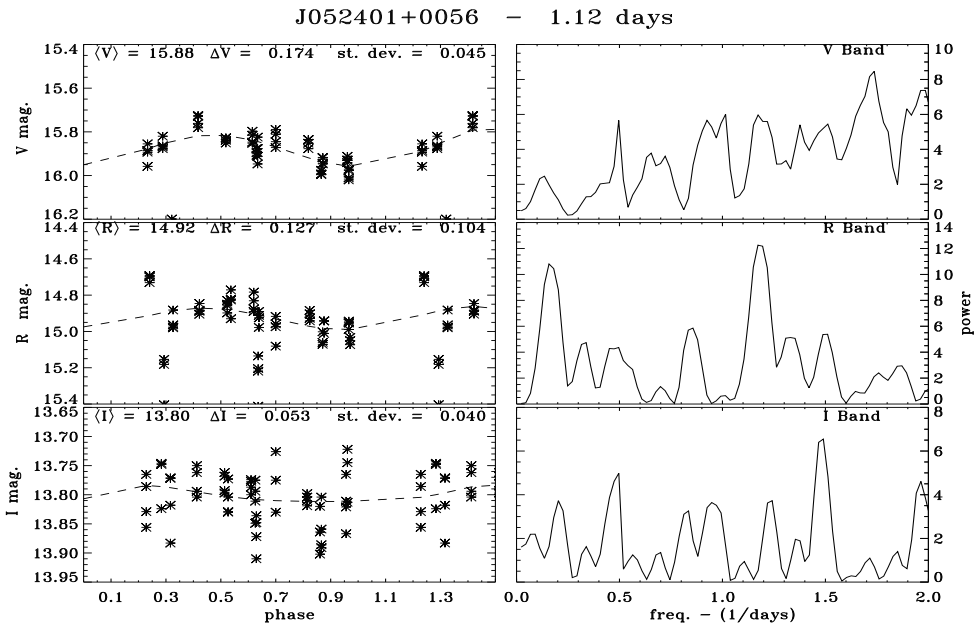
J052401+0056 – 1.12 days
⟨V⟩ = 15.88 ΔV = 0.174 st. dev. = 0.045
⟨R⟩ = 14.92 ΔR = 0.127 st. dev. = 0.104
⟨I⟩ = 13.80 ΔI = 0.053 st. dev. = 0.040
V mag.
R mag.
I mag.
phase
V Band
R Band
I Band
power
freq. – (1/days)

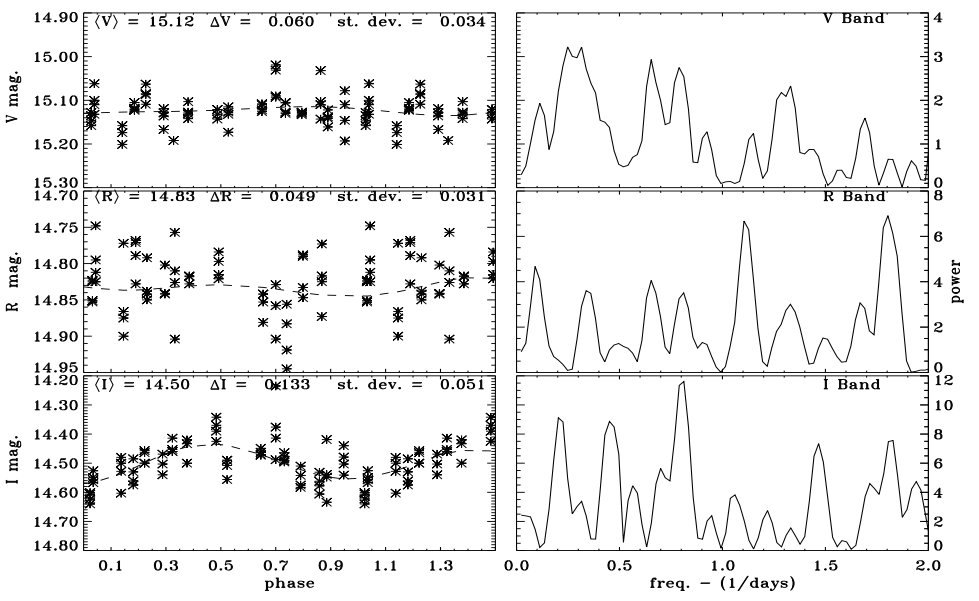
GSC 0101 1611 – 1.26 days
⟨V⟩ = 15.12 ΔV = 0.060 st. dev. = 0.034
⟨R⟩ = 14.83 ΔR = 0.049 st. dev. = 0.031
⟨I⟩ = 14.50 ΔI = 0.133 st. dev. = 0.051
V mag.
R mag.
I mag.
phase
V Band
R Band
I Band
power
freq. – (1/days)

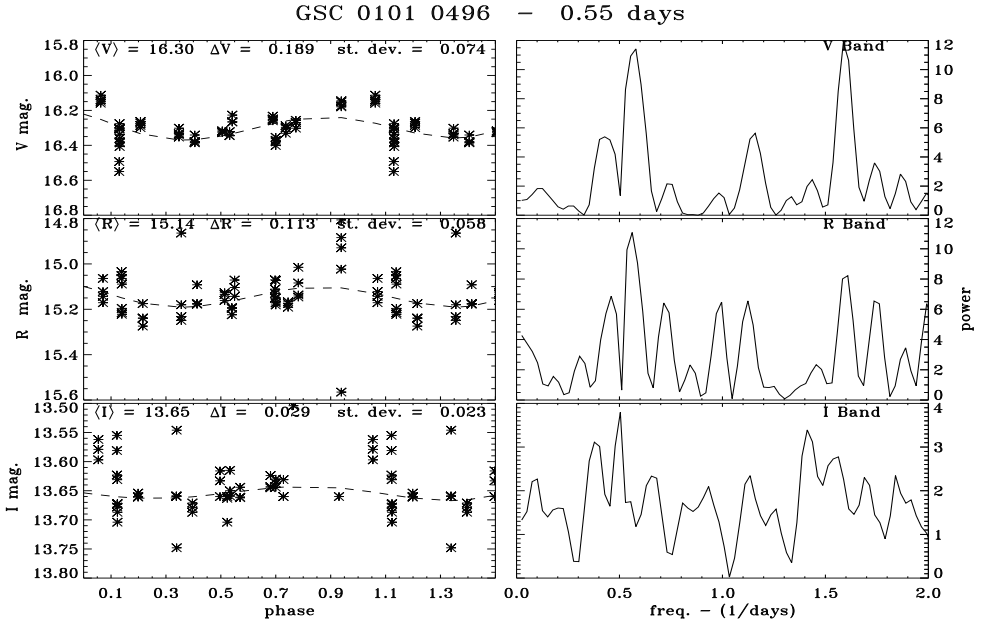
GSC 0101 0496 – 0.55 days
⟨V⟩ = 16.30 ΔV = 0.189 st. dev. = 0.074
⟨R⟩ = 15.14 ΔR = 0.113 st. dev. = 0.058
⟨I⟩ = 13.65 ΔI = 0.029 st. dev. = 0.023
V mag.
R mag.
I mag.
phase
V Band
R Band
I Band
power
freq. – (1/days)

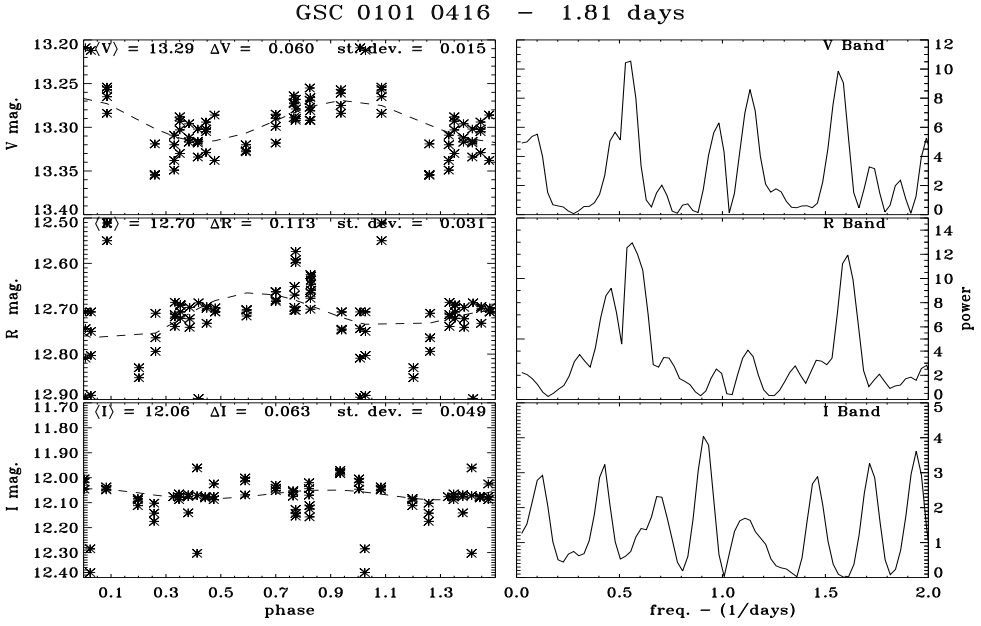
GSC 0101 0416 – 1.81 days
⟨V⟩ = 13.29 ΔV = 0.060 st. dev. = 0.015
⟨R⟩ = 12.70 ΔR = 0.113 st. dev. = 0.031
⟨I⟩ = 12.06 ΔI = 0.063 st. dev. = 0.049
V mag.
R mag.
I mag.
phase
V Band
R Band
I Band
power
freq. – (1/days)

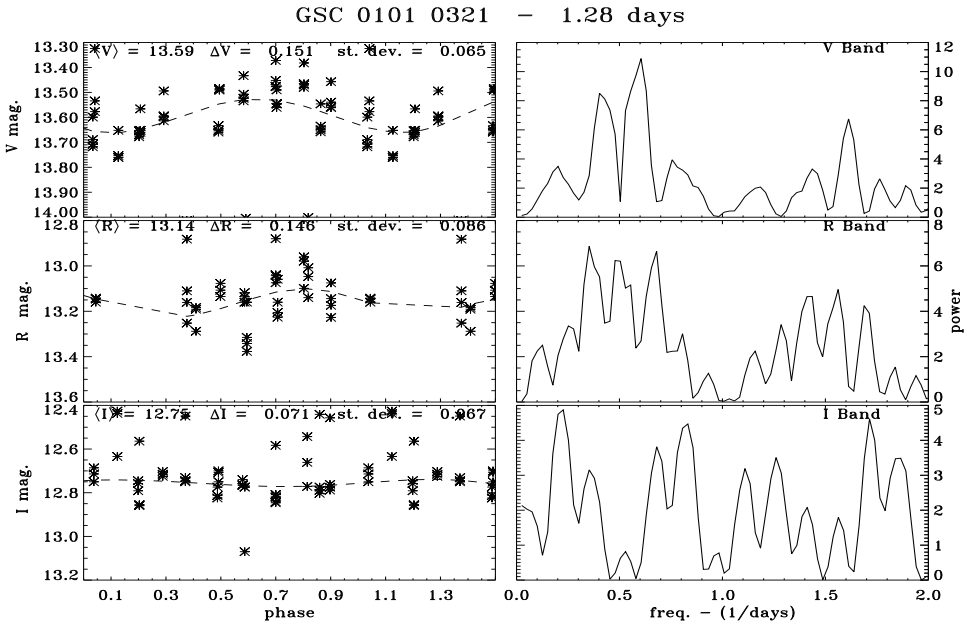
GSC 0101 0321 – 1.28 days
⟨V⟩ = 13.59 ΔV = 0.151 st. dev. = 0.065
⟨R⟩ = 13.14 ΔR = 0.146 st. dev. = 0.086
⟨I⟩ = 12.75 ΔI = 0.071 st. dev. = 0.067
V mag.
R mag.
I mag.
phase
V Band
R Band
I Band
power
freq. – (1/days)

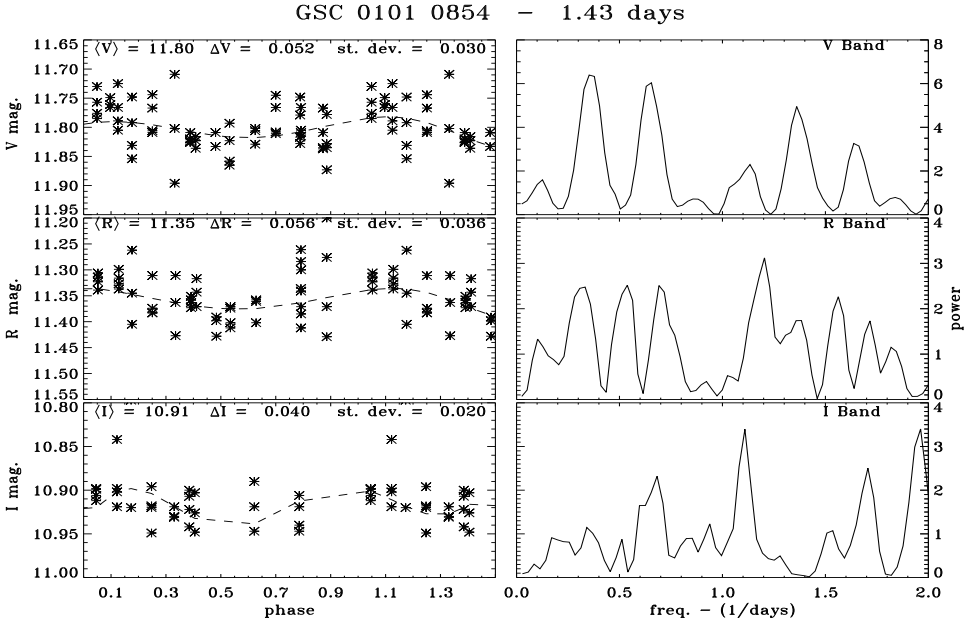
GSC 0101 0854 – 1.43 days
⟨V⟩ = 11.80 ΔV = 0.052 st. dev. = 0.030
⟨R⟩ = 11.35 ΔR = 0.056 st. dev. = 0.036
⟨I⟩ = 10.91 ΔI = 0.040 st. dev. = 0.020
V mag.
R mag.
I mag.
phase
V Band
R Band
I Band
power
freq. – (1/days)

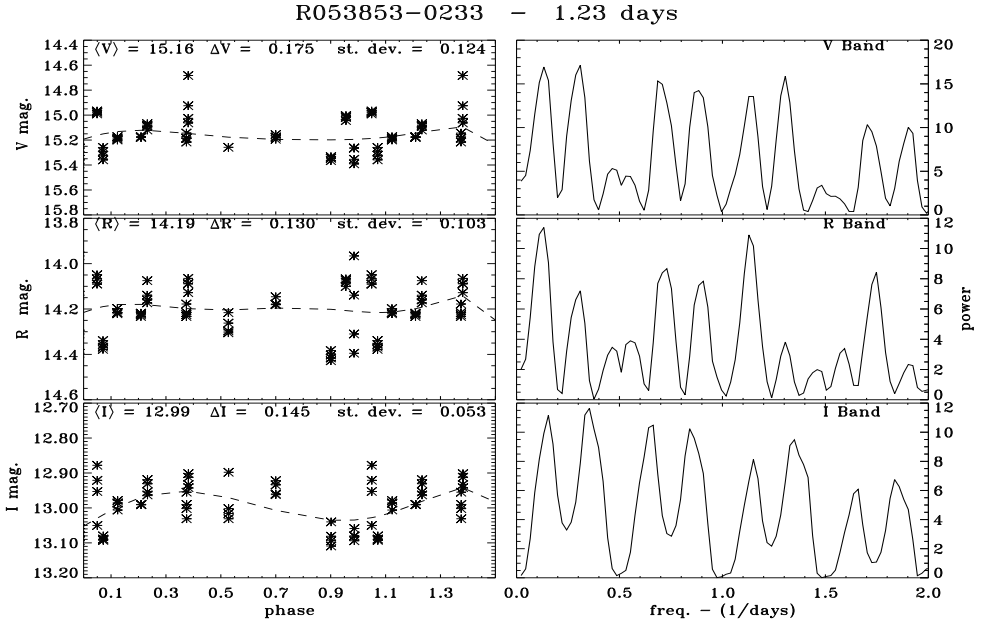
R053853−0233 − 1.23 days
⟨V⟩ = 15.16 ΔV = 0.175 st. dev. = 0.124
⟨R⟩ = 14.19 ΔR = 0.130 st. dev. = 0.103
⟨I⟩ = 12.99 ΔI = 0.145 st. dev. = 0.053
V mag.
R mag.
I mag.
phase
V Band
R Band
I Band
power
freq. − (1/days)

Appendix C

The Care and Feeding of the Mount Stony Brook Observatory

C.1 Introduction

This document is a manual, of sorts, for the equipment and software at SUNY at Stony Brook. The telescope is a nasty beast to care for and experience has shown that it needs to be treated properly. The material presented here is a collection of what has worked in the past for keeping the mighty beast happily collecting quality data. Although there are reminder sheets included at the end of this document, they are not meant to be a replacement for actually reading the manuals (RTFM!). There are formal manuals for the commercial equipment available in the warmroom, and these should be reviewed in conjunction with this paper.

C.2 The Telescope and Dome

For several years, the observatory at SUNY Stony Brook was used solely for undergraduate classes. Built in 1968, the observatory is located at the western end of the academic mall, atop the Earth and Space Sciences building. Exact coordinates are longitude 73^0 07'04" W latitude 40^0 54' 06" N, altitude $\approx$ 60 meters, time zone is +5 relative to Universal Time. The weather is not as bad as one might expect, base on statistics from 1991 through 1993 one can expect about 120 usable nights a year with about thirty of those being totally cloudless. The campus is approximately 40 miles from New York City. The location of the observatory makes it a very light polluted site. The sky brightness is 14 magnitudes per seeing disk with the seeing ranging between 3 and 5 arc seconds. This, along with the fact that the telescope drive motor is misgeared, made it difficult for the telescope to collect research data. The telescope now runs as an effective research facility. The changes are detailed below as the telescope was transformed from an old dinosaur to a more useful one.

The dome houses a 14" Celestron Schmidt-Cassegrain telescope that was installed in 1981. The telescope primary is a 14.25" diameter spherical mirror with a 60 inch radius of curvature. The secondary is slightly aspherical with a 3.5" diameter and a 17.6 inch radius of curvature. The effective focal length is 154 inches. An aspheric Schmidt corrector removes most of the spherical aberration. This telescope has some problems that make data collection arduous. The corrector plate is slightly skewed, the drive is misgeared, and the finding

scope is difficult to use in the winter. The finding scope is a 30mm refractor that tends to become misaligned with the 14" when exposed to cold weather due to shrinkage of the adjusting screws. To correct for this, a 3" refractor was added to this to the 14". This addition gives a deeper finding field and has a more stable alignment. The drive motor for the telescope cannot track objects for longer than fifteen seconds before the guiding error is greater than the seeing disk size.

In 1993, a hole was drilled through the roof to a laboratory on the fourth floor. Several cables were run from a warm room to the telescope. The operator of the telescope can observe from the fourth floor, only exposing himself to the cold when finding a new target. The operation of the dome and the telescope will be discussed in later sections.

C.3 The Computer Hardware and Relevant Equipment

Currently a 50MHz 486DX PCBrand personal computer, located on the fourth floor in the warm room in lab number 443C, is used to control the charge coupled devices (CCDs). The PC has 8 megabytes of RAM and a 325 megabyte hard drive which is useful for temporarily storing images taken with the CCD cameras. The PC also has 4 communications ports, 2 printer ports and an ethernet connection. The Colorado tape drive next to the PC is useful for backing the hard drives and storing data, but these tapes are not

compatible with the network tape drives. The PC runs on DOS 6.0 and uses version 3.1 of WINDOWS. Presently, data acquisition software should not be run through WINDOWS.

The PC is connected to a monitor and keyboard in the warm room and another pair in the dome itself. The active keyboard and monitor pair is selectable via the switch box in the warm room. The cables for the Lynxx, ST-6, ST-4, monitor, keyboard and the FW-1 filter wheel are run from the warm room, along the wall, and through the hole that is directly under the steps in the dome. The software for ST-4 and ST-6 is set so that the communication line for either camera is through communication port 1. Because they are operated through the same communication port the two cameras cannot currently be operated simultaneously. The Lynxx software runs from a card in one of the expansion slots, and the cabling is connected directly to a port on the card. Another cable running into the warm room is used to connect the PC via Kermit to the astronomy server. This connection can be used to upload data to any machine in the cluster at 19.2 kilobits per second (kps). However this line has been made obsolete by an ethernet connection that allows for File Transfer Protocol (FTP) to be used with data transfer proceeding at a much higher rate.

An intercom system simplifies communication between the dome and the warm room. Usually one of the intercoms in the dome is locked on channel b, so the observer in the warm room can hear what is happening in the dome. The second intercom in the dome is used for two way communication between the dome and the warm room.

	Lynxx	ST-4	ST-6
Pixel array	192×165	192×165	375×242
Pixel Size	13.75×16.00μm	13.75×16.00μm	23× 27μm
Active Area	2.5×2.5 mm	2.5×2.5 mm	8.63×6.53 mm
Dark Current (in e^-/sec/pixel)	100	160	30
Full Well	95,000 e^-	95,000 e^-	400,000 e^-
Field of View (in 14 inch)	2×2 arcmin	7×7 arcmin[a]	7×7 arcmin
Field of View (with a focal reducer)	4×4 arcmin	14×14 arcmin[b]	12×12 arcmin
Limiting Magnitude (1 min exposure)visible	15	9 [c]	18
Photometric Accuracy	5% at 8th mag.	N/A	5% at 13th mag.
Gain Available	23.2	150[d]	6.7
Read Out Noise	4.3	1[d]	4.5

Table C.1: Technical Specifications Of The CCD Cameras.

C.4 CCD Systems and Their Hardware

Currently, there are three CCD systems available at Mt. Stony Brook. The Santa Barbara Instrument Group (SBIG) ST-4 is an 8-bit camera used primarily for tracking. SpectraSource's Lynxx camera uses a 12-bit format, and the SBIG ST-6 follows a 16-bit format; both are used for imaging. All three cameras have focal reducer available, these are useful since both increase the field size and the signal to noise in each pixel. However depending on the exact specifications of the observation, it is possible to under sample the data when using a focal reducer. Each camera is utilized in different areas of data collection. Table 1 contains specifications of the cameras.

When working with the PC, all software packages are to be executed

outside of the WINDOWS. The reason for avoiding Windows with the Lynxx is because the PCBRAND BIOS chip is not compatible with the Lynxx software and the exposure times become distorted. For a listing of the exposure times for the Lynxx, see Appendix I. The more applications that are run on WINDOWS, the slower the clock runs, thus the exposure time becomes dependent on how many applications you are running. The ST-6 and ST-4 also should not run through WINDOWS as data transfer time is slowed. Within WINDOWS, the communication rate is set at 19.2 kbps, otherwise the communication rate can be 115 kbps.

C.4.1 The Lynxx

SpectraSource's Lynxx camera contains a Texas Instrument TI241 chip and is an array of 165 x 192 pixels, each pixel is approximately 13.75μm by 16μm. The chip is housed within the camera head which is cooled by a thermoelectric cooler (TEC) to approximately 30^o Celsius below the ambient temperature. The pixel size of the Lynxx's chip gives it the capability of very high angular resolution. The atmospheric seeing at Stony Brook does not allow it to be used to its full capability. The oversampling can be useful in some Fourier transform analysis. The Lynxx has a physical shutter creating a uniformly exposed picture. It has a fast image readout time: 1 second for 12 bit, .3 second for 8 bit and real time display. Therefore, Lynxx is better capable of observing asteroids, planets and occultations. Mounted on the Lynxx is a retrofit package that includes a flip mirror and filter box. This

allows the observer to see the targets, align them within a square reticle that overlaps the position of the CCD and take an image just by flipping the mirror out of the way. The alignment of the reticled eyepiece does have to be checked periodically. A set of Johnson BVRI filters are used with the Lynxx, and a clear filter is used to maintain the focus on the chip when the BVRI filters are not being used. The filter response curves are given in Appendix III. Undergraduates have used the Lynxx camera for research projects such as; asteroid light curves, periodicity of eclipsing binary stars (β Persei) and variable stars (W UMa). High school students also have used the camera as part of Westinghouse Research projects. These projects have included observations of weather patterns on Saturn, particle size distribution in the early Solar nebula by observing Lunar crater size and density and BVRI photometry of χ Persei.

C.4.2 The ST-4

The SBIG ST-4 uses the same CCD chip that is used by the Lynxx. The ST-4 uses a CPU box as opposed to a card that must be installed in the computer. This makes the ST-4 more portable than the Lynxx, since it can be run by a laptop computer for imaging, or with just the CPU box for guiding. At Mt. Stony Brook the ST-4 is used with the CPU box in the dome. The black CPU box is placed in the dome and can be connected to the computer currently through the 9 pin serial cable labeled ST-6. The chip is cooled by a TEC similar to the one in the Lynxx. This cooler lowers the temperature of the chip to approximately 20^0 Celsius below ambient temperature.

The ST-4 is also capable of moving the telescope. To do this, a relay box was built locally (for schematic diagram see figure 1). Its purpose is to allow the CCD computer to communicate with the telescope's drive. The relay box has three connecting cables. The standard grounded plug is connected to the power supply, the gray 15 pin female cable connects to the CPU box, and the gray 6 pin male polarized cable connects to the telescope's drive.[1] The telescope's drive has two speeds. The current relay box has been designed to work with the faster speed of the drive. To adapt the ST-4 to a different telescope, a new relay box would have to be designed.

CCDTRACK software is available to allow the ST-4 to track using an interactive image on a computer. The difficulty with this method is the computer can only operate one CCD at a time. If the ST-4 and the Lynxx are to be run simultaneously, the computer will interactively run the Lynxx, and the ST-4 will operate through the CPU box. The CPU box contains built in tracking software. Observations requiring a second tracking computer are possible but the user is responsible for providing the second PC.

In general, the ST-4 is used solely as a tracking device. The camera head is attached to the 3" telescope. A 36mm plössl eyepiece has approximately the same focus as the ST-4 in the 3" telescope and can be used to center a star for the ST-4 to track. In the track mode, the ST-4 will chose a star to track and move the telescope via the relay box to keep the star in its field of view at approximately the same position on the chip. This makes it possible to

[1]It is still possible to plug the cord to the drive in upside-down. The operator should take care in placing this plug.

take exposures longer than 15 seconds with the Lynxx camera. As mentioned earlier, the drive motor fails to track accurately after 15 seconds. With the ST-4 guiding the telescope, images of ten minutes and longer have been recorded. In many projects utilizing the Lynxx, the ST-4 is used to guide the telescope.

C.4.3 The ST-6

One SBIG upgrade from the ST-4 is the ST-6. The ST-6 utilizes a Texas Instrument TC241 chip. This is an array of 375 by 242 pixels each 23μm by 27μm. The components of the ST-6 system are similar to the ST-4. There is a CPU box, camera head, and the same relay box. This system also uses a motorized filter wheel made by Compuscope. The filter wheel contains BVRI Bessel filters and a clear filter. (See Appendix III for the response curves of the filters.) The TEC for this camera head is similar in operation to that of the Lynxx, however the ST-6 allows the temperature to be set. The ST-6 is usually set at -35^0 Celsius at Mt. Stony Brook Observatory.

The ST-6 is capable of simultaneous data acquisition and guiding. Used together with the ST-4, longer uninterrupted exposures are possible. The uninterrupted exposures will reduce read out noise since only one read-down occurs. This makes simultaneous use the preferred method of operation; however it is too cumbersome for regular use. A function in the software allows the operator to combine several short exposures to create a composite image. The basic idea of the *track and accumulate* function is to take a short image, and then chose a star for the telescope to track on. The software will take

short exposures and move the telescope to keep the star in the same region of the chip. Another image is taken, and the two images are aligned. This is the main data collection method. The track and accumulate function allows very deep exposures to be made. A 60-second exposure of a star forming region in Aurigae contained a 18th magnitude object in the infrared. The maximum magnitude detected by the Lynxx was 16th magnitude in 600 seconds. The ST-6 does not have a physical shutter. Instead of a physical shutter, an electronic shutter is used in conjunction with a vane. This can lead to short images not being exposed uniformly.

C.5 Data Acquisition

In this section the methods of data acquisition will be discussed. The means of finding targets is an important part to any observing program, and are included here. The operation of each camera is also covered, including some suggested settings that can be useful for the inexperienced user.

C.5.1 Target Finding

The main method of finding targets is a modified version of the classical star hopping method. It is critical that all three telescopes are well aligned before proceeding. Lock onto a bright star, no fainter than about third magnitude, which has a similar declination or right ascension as the target star and therefore it is necessary to slew in only one direction. The 30mm guide

telescope is used to acquire the bright starting star. The slew can be followed by observing in the 30mm.

General preparation would include several finder charts; a wide constellation field, the 30mm field, the 3" field and the of the 14" field. The charts were made using the Space Telescope Science Institute Guide Star Catalogue, and Tirion 2000. The 30mm has a field of view of 2.5 arcminutes, the 3" has a 40 arcsecond field of view; each camera's field of view is specified in Table 1. Once the target star has been found and centered in the 3", data acquisition can begin.

C.5.2 Data Acquisition with the Lynxx

The Lynxx software is under the D:\CCDS\LYNXX directory and the software package can be executed by entering CCD.

Once in the Lynxx Menu the first thing that must be done is the TEC must be turned on, the command to activate it is under *initialize*. The chip needs approximately fifteen minutes to cool sufficiently. The filepath for images to be stored will always be set to the default. This should be reset to F: each time the software is restarted. See Table 3 for the capacity of Lynxx images that can be held on various drives.

There are two methods to obtain an image using the Lynxx. Using the *expose* command will take a 12 bit image that has a readout time of .5 second. The second method is the *full-frame focus* command which utilizes the camera's ability to readout 8 bit images. This has the benefit of having a shorter

readout time, which is about one third of a second. Sub-frame images can be readout in .3 seconds and are 96 pixels high by 82 pixels wide as compared to 192x165 for the full frames.

When observing time dependent phenomena, it is useful to use the "green monitor" to video tape the observations. It is possible to tape images on the monitor, using the video port on a VCR. Simultaneously a connection with the radio broadcast of "WWV" (the time counter) using the audio port can be made. This setup will give an extremely accurate time-image correlation for observations.

All corrections made to an image are permanent, therefore it is not advised to use *stretch* or *log scale* until the image is saved or copied. *False color* is useful to enhance contrast in nebulous structure and between faint objects in an image while not affecting the actual image. The image can be saved using the *image save* command under *save/load*. The *image filepath* should be check to ensure the correct filepath. The format for saving images form the Lynxx is *******.ccd.

The Lynxx has six frame buffers so that multiple frames can be stored in RAM simultaneously, three of these buffers usually hold calibration data. Certain calibration frames, such as thermal frames, bias frames and flat field frames, should be taken because they play a key role in data reduction. Bias and thermal frames can be acquired by using the commands under the *initialize* menu. The thermal frames are always placed in the fourth frame and the bias frames are always placed in the fifth frame. The flat field frames are stored in the sixth frame. It is best to take five twilight flats in each filter using the

expose command. An alternative means of finding flats can be used at Stony Brook: sky flats. Sky flats are medianed images of a relatively starless field. The *get flat field* command is not recommended because the normalization process the Lynxx uses creates extra noise.

C.5.3 The ST-4

Since there are superior cameras and software packages for imaging at Stony Brook, the imaging software for the ST-4 will not be discussed. The tracking software is extremely important to data collection, and will be presented here. The tracking software is run from the CPU box. There are several controls including a menu that allows the operator to change parameters necessary for the tracking process. Table 2 includes a rough guide of settings for the ST-4. The *exposure adjust* will set the exposure time. *Calibration adjust* controls the period that the ST-4 moves each of the four relays during the calibration process. Each axis can be given its own time. The *scintillation adjust* allows for atmospheric turbulence. If the sky is turbulent when observing, this should be set at a fairly high number to track on a 'twinkling' star. The *brightness adjust* has two settings, average and faint. In the faint mode, the chip will take an average of a 3 by 3 pixel square and place the average in the center pixel. This helps find fainter stars, but will also increase the background. The *hysteresis* parameters can correct for backlash in the telescope's drive motor. The times are set in tenths of seconds and the ST-4 will use this time to set the motor in the correct direction before making a

Command		Value
EA	Exposure Adjust	3
b	Gain Boost	3
bA	Brightness Adjust	A
SA	Scintillation Adjust	2
FL	Focal Length	S
C1	Calibration Time, X Axis	1
C2	Calibration Time, Y Axis	3
H1	Hysteresis, X AXIS(.1 sec)	2
H2	Hysteresis, Y AXIS(.1 sec)	1
AA	Averaging Adjust	3
AL	Cycles Before Alarm	4

Table C.2: Sample settings for the ST-4 guiding on a 7^{th} magnitude star.

move. The last parameter is the *gain boost*. This increases the gain of the chip, but it is important to remember the background noise increases with the gain.

Once these parameters are set, a star can be found for tracking. As stated before, a 36mm plössl eyepiece has the same focus as the ST-4. This can be used to find a star in the region of interest to guide on. If the star is slightly out of center relative to the 14", there are two sets of adjustment screws which can be moved to center the 3" telescope on the star while not moving the 14". The camera can be replaced and the find and focus can start.

Find and focus will read down the brightness of the star on a scale where 99 is overexposed, along with the coordinates on the chip. The star can be found by using the four arrow keys to move the drive motor slightly. Once the display shows high counts, the focus of the three inch can be changed until the counts reach a maximum. Before tracking with the camera, the CPU and the

drive have to be calibrated. It is best to place the guide star near the position X=20, Y=80. When the calibration button is depressed, the telescope will be moved in all four directions. The CPU will determine how much time is necessary to move the telescope a certain number of pixels. Then when the star moves away from the centered position, the CPU will know how long to move the drive to get the star back in place.

After the drive is calibrated, the track button will set the ST-4 in a mode where it will track the star until it either loses track or the operator stops the track. The CPU box also contains a button to take a dark frame. If the dark frame is taken, a cover must be placed over the telescope. The ST-4 has neither a shutter, nor a vane that will block out the light.

C.5.4 ST-6 Data Collection

Like the Lynxx and the ST-4, this camera has a preferred orientation with the telescope (see figure 4). The software is located in the directory D:\CCDS\ST-6. The filter wheel can be started here with the command FW. Once the camera is attached to the telescope, and the several cables are set, the ST-6 software is started with the executable CCDOPS. The link between the computer and the camera will be established. The cooler can be set to a specific temperature. This is done by going to the *camera* menu, and selecting *setup*. The temperature control is contained in this menu. Mt. Stony Brook operates at a camera temperature of -35.00^0 Celsius.

Before taking images, the camera and the telescope have to be calibrated.

This process is similar in operation to the calibration with the ST-4. A star is placed near the center of the field, and the camera moves the drive to detect the times for each relay. These times change depending on the region of the sky that is being observed. After moving to a new target, the calibration should be done again. The commands for calibration are under the *track*menu.

Now the telescope is ready for imaging. The *focus* command allows the operator to find the target and then move the telescope to center the object. The focus mode is preferable to find a target since there is an option for a low resolution readout. This produces poor quality images, but they are readout faster than a normal image. Another advantage to the focus command is the ability to move the telescope. The a, s, w, and z keys will move the telescope in the -X, +X, -Y, and +Y directions respectively. This feature will only work in the focus mode.

There are two ways to collect images with the ST-6. The first is using the *grab* command. This will take an image for the requested time, and then download the image. This is the normal CCD camera image mode. The second method is the *track and accumulate* mode. In this mode, the camera takes several short images, and then adds them together to give an image that is comparable to the same total time image as taken by the grab function. The advantage of the second method is clear when using a telescope that cannot track well. At Mt. Stony Brook, a 60 second image under grab would have star trails throughout it due to the periodic guiding error (see figure 3). A 60-second track and accumulate image contains fairly round stars. The camera calculates how far the star has moved from the first image and will move the

telescope to compensate for the movement that occurred in between exposures. This is the nominal data collection method for the equipment at Mt. Stony Brook.

Another feature about the ST-6 is the dark frames can be removed from the image as the data is collected. Unlike the Lynxx, which creates a dark frame by taking an exposure of the shutter and then removing the bias level, the darks from the ST-6 include the bias level. In lieu of a shutter, the ST-6 has a vane that falls into place to collect a dark frame. When an image is taken, the electronics act as a shutter.

To save images under the ST-6 software, the *file* menu is used. The default *filepath* is usually D:\CCDS\ST-6. This should be changed to F:\. The filename can be eight characters long, and the operator has a choice of formats. The formats will be discussed in a later section. One important point: **save the tracklist.** After each track and accumulate image is taken, a tracklist is created. This records how far the telescope was moved each frame of the image. This must be saved to calculate the offsets needed for the flat corrections. The program prompts you for this after the track and accumulate sequence is taken.

C.6 Data Storage

All of the data are stored initially in the F:\ drive of the PC. About 25 ST-6 images or 172 Lynxx images can be saved here. Additional disk space is available for use in dire circumstances, but general use of other disks is

discouraged since it clutters the system. After all of the data for the night are collected, the data are transferred from the PC to the VAX mainframe in the department. The file transfer protocol link to the Astronomy group cluster is in general use with kermit link still an available backup. The data are saved in various formats depending on the software used. Appendix I contains the procedure for transferring data to the VAX.

C.6.1 Data Formats

There are several different ways for CCD images to be stored. Each software package has its own format for saving the data. The ST-4 can save data when used as an imaging camera. The format of the saved files is not discussed in the ST-4 manual.

The Lynxx saves data in a format that best uses its memory allocation. Since the Lynxx data is stored in 12 bits, the format rearranges the data to send 2 pixels of information in 3 bytes. This is really just a redistribution of data, so that it is sent faster and stored more efficiently. Two pixels can be represented as 3 bytes of information. The first byte contains the 8 least significant bits of pixel 1. The second byte carries two nibbles. The first nibble has the 4 most significant bits of pixel 1, and the second contains the 4 most significant bits of pixel 2. Finally the last byte contains the 8 least significant bits of pixel 2. The Lynxx manual suggests that data stored in this format be saved with a ccd extension.

The ST-6 offers its own format in compressed and uncompressed versions,

along with FITS (Flexible Image Transport System) and TIFF(Tagged Interchange File Format) formats. The ST-6 format saves data in 16 bit words for each pixel value. In the uncompressed version, the data is read down with each pixel being described by a 16 bit word. The compressed version saves the data in a slightly different manner. The first pixel in a row is described by a 16 bit word. The rest of the pixels are described by an 8 bit word, provided that the value varies from the first pixel by ± 127 counts. If the difference is more than ± 127 counts, that pixel's value will be described by a 16 bit word. Clearly, the compressed format will save the data in less space than the uncompressed format.

The other formats are FITS, a common astronomical format, and TIFF, a publication format. Under the FITS format, the user has the option of saving data in either a 16 bit or 8 bit mode. To save the original image, the data should be saved with 16 bits per pixel. When 8 bit is selected, the 16 bit image data will be reduced to 8 bits and will be photometrically useless. The ST-6 also allows the observer to record information about the image collection and comments about the collection. A word of caution for those using the FITS format, the ST-6 software will record the time of the FITS creation – not the time of the file creation. This information can be found in the comments.

The TIFF format under the ST-6 can only write in 8 bits while the ST-6 images are in a 16 bit format. This can be a disadvantage since this compresses the data and slightly alters it. This format is not suggested for images with astronomical data. This program also allows the observer to record collection conditions.

Camera	$5\frac{1}{4}$" HD	$5\frac{1}{4}$" DD	$3\frac{1}{2}$" HD	$3\frac{1}{2}$" DD	QIC-80
Lynxx	28 images	7 images	35 images	14 images	5000 images
ST-6 images	4 images	1 images	5 images	2 images	600 images

Table C.3: Storage Capacity For Lynxx and ST-6 Images.

C.6.2 Data Storage Media

There several backup systems to record the data if the VAX connection has failed or a disk on the VAX has failed. The first backup system is the use of floppy disks with the PC. Since all of the data are stored on the PC, the data can be sent directly from the F: drive to a floppy disk. The PC can read both $5\frac{1}{4}$" and $3\frac{1}{2}$" disks. Table 3 shows the disk capacity for each system. The data can then be stored on floppy disk until they can be sent to the VAX.

A second form of backup for the PC is a tape drive. The Colorado Memory Systems tape drive stores data on QIC-80 tapes. The QIC-80 tapes can store 250 megabytes of compressed data. From here several nights worth of data can be transferred to a single tape. This is a stronger system than the disks because the tape can hold 600 ST-6 images. The entire contents of the PC are backed using this system occasionally.

The data are also backed-up on the VAX with an 8mm or 4mm tape. A tape backup should occur once every month. This backup becomes important if the disk fails. A month's worth of data was lost when one of the VAX data disks failed. The disk in question had stored data from a year before the failure date, but they were stored on tape and recovered. The VAX has a routine that allows TAR procedures to run within VMS.

C.7 Data Processing

Once the data are collected and stored, the next logical step is to process the images. If photometry is desired, there are several tools available to make measurements from the images.

C.7.1 Quick Look Tools

Each program allows the operator to get a quick look at the data and do some processing. The ST-4 and ST-6 have the same basic tools, so only the ST-6 tools will be described here. Most of the tools are under the *display* menu. When an image is displayed in analysis mode, data can be roughly analyzed. Any process done under display will only alter the display and not the image itself.

The operator can use the *X-Hairs* to find the pixel coordinates and value. The average value of all pixels in a square area can be determined with the smooth command. This program will also give a relative magnitude of the star. An accurate magnitude can be determined if the telescope parameters are modified. If the object is a diffuse object such as a nebula, the diffuse magnitude is expressed in units of mag/square arcsecond. The separation in arcseconds and degrees can be determined between two stars.

Other operations include flipping the image horizontally and vertically, and a zoom that enlarges a section of the image by a factor of four. The image can also be cropped. If the image is not at a contrast that is desirable, the contrast can be manipulated by the operator. The image can be smoothed.

This is a process that removes the effects of rapidly varying pixels values. This is accomplished by replacing each pixel by the weighted average of a 3 by 3 square centered on the pixel. This can blur the details of an image, but can help bring out faint objects. A histogram can be displayed in either a text or graphical format for the ST-6. The ST-4 can only display a graphical histogram.

The ST-6 has a utilities menu that alters the image. The image should be saved before any processing is done to it. Several functions can be done here including *dark subtracting, co-adding frames, smoothing, sharpening,* and *flat fielding.* The *dark subtract* will remove the dark current and bias from the image. This removes background noise that is intrinsic to the chip. The *co-add* command allows two images to be added. This produces a third image with a better signal to noise ratio. *Smoothing* the image will have the same effect that it did before except now the image is permanently altered. Another form of filtering is the *sharpening.* This is a process called unsharp masking that brings out the details of the image. *Flat fielding* will remove the flat field from the image. This corrects for differences in gain from pixel to pixel and variations from the telescope. The tracklists must have been saved earlier if this tool is to be used in a track and accumulate image. Also under the *utilities* menu, the image can be rescaled. Cool and warm pixels can be removed.

The ST-4 allows some of these processes, but not all. Before using these commands, consult the manuals for these cameras.

C.7.2 The Lynxx Tools

The Lynxx software has its own quick analysis tools. Some processes are similar to the ST-6 tools. As previously discussed, the images can be rescaled, but if intensities are to be measured, the images should not be rescaled. The rescaling process destroys the raw data and makes intensity measurements inaccurate.

The processes for analysis are under the *analyze* menu. A histogram of the image can help decide if any part of the chip was over exposed. Changing the falsecolor of the image can also help in determining if a pixel is overexposed. The falsecolors display the image in a strongly varying colorbar that makes it easier to find out the counts in the pixel on examination. X and Y line scans can determine the focus of the image. When focusing the telescope, the lines scans can be a benefit to the focusing process. These procedures display the intensity along a chosen line. A zoom window is also available.

Before starting any analysis on an image, the calibration frames must be removed from the image. While these are generally carried out on the VAX using IRAF or IDL, the quick reduction methods included in the software are detailed here. The *process* menu contains the tools to remove the calibration frames. The *flat adjust* removes the bias stored in frame 5 (see figure 1 for frame positions). The flat stored in frame 6 is used to correct the image. The *therm adjust* process removes the dark current. This will correct for the dark in frame 4 in addition to the bias and the flat. When executing either of these procedures, the operator should place the correct flat frame and correct dark

frame in the buffers.

The remainder of the commands can be used for determining the intensity of the objects in the frame. *Meas intensity* is the command that will measure the intensity of the object in a square region around a star. The size of the square region can be changed with the command square size. A suggested size for the aperture is one that encloses all of the star and has a small section of sky around the star. After the star is measured, the background should also be removed. To do this, a square of the same size should be placed on a region that represents the background around the star. The difference between the two values is a more accurate representation of the relative intensity. An appendix to the Lynxx manual describes photometry with the Lynxx software.

A separate software package is The Personal Observatory. This is a package that allows the ST-6 and the filterwheel to be run simultaneously. Unfortunately, the track and accumulate mode will not work if the ST-6 is run by Personal Observatory. It is advised to use the SBIG software.

Although the camera cannot be operated by the Personal Observatory, it can be used for data reduction. Again, there are better processes in IRAF and IDL. This is a description for a quick look at the data. There are procedures for tricoloring images by using three images in different bands, and some photometry can be done in this software. The Adobe Photoshop can be used for color images also.

C.7.3 IDL

There are several IDL programs on file at Stony Brook. Several of these programs have been written locally to reduce the data collected. The programs cover a large range of functions, but all can be useful in the reduction of data. The help screens of all these programs are listed in Appendix II. IDL can run from either the astronomy mainframe, or from the PC. On the PC, IDL is located on the C: drive.

If the images being used were taken using the Lynxx the observer can use either IRAF or IDL to reduce the data. If IRAF is preferred there is an IDL routine CCD2FIT formatted image into a FITS format that is readable by IRAF. The *auto2fit* program is currently limited to approximately twenty-seven images, although it is being corrected.

If IDL is preferred, the CCD12BIT routine will reformat the .ccd images into an image that IDL can read as an array. The AUTOCCD routine will reformat a given list of .ccd images and convert it into an image cube that IDL can read. The CCD12BIT routine requires an image as the input, the directory where the image is located and a name for the output. This routine only works for one image. The AUTOCCD routine requires an image list as the input, the directory where the images are held and the name of the resulting image cube as the output.

Now that the images have been reformatted for use by IDL they can be displayed. IDL has several commands to view images; TV, TVSCL and BYTSCL. The TV command writes the image array to the display without

scaling it. The TVSCL command scales the image by a specified factor and displays the scaled version. The BYTSCL command allows one to scale the individual pixels using minimum and maximum operators for improved color contrast.

Before reduction of data can take place the calibration images must be dealt with properly. There is a routine available that helps with this process, MEDIAN. The MEDIAN routine takes the input image cube and finds the median value for each pixel position throughout the image cube. This new image, with every pixel value a median of all of the input frames, is the output. The main purpose for using this process of the removal of spurious high and low points that effectively reduces noise and therefore, the uncertainty.

Both biases and dark frames can be medianed easily using this routine. Flat fields are slightly more complicated. The flat field frames for a specific filter should be medianed together after which the medianed bias and dark frames should be removed. Flat fields must also be normalized. This is accomplished by weighing the medianed frames to the average value. To do this, set the scale to 1 when running the procedure. When this has been done for all filters, the reduction is almost complete.

The data frames must be reduced now. This involves subtracting the medianed bias and dark frames. They are subtracted because the CCD chip accumulates a thermally induced time dependent charge and operates with some background level of charge. The dark frame must be of the same time as the image since it is time dependent. The data frames should then be divided by the normalized flat field. This step smooths brightness gradients in the

image caused by variations in the chip.

If the images being used are from the Lynxx and the user wishes to use IRAF for reduction, the images can be rewritten into FITS format by the CCD2FITS procedure. Data reduction can be done in either IDL or IRAF.

There is an automatic reduction procedure called AUTORED2. This is currently programmed for Lynxx images. The program requires the operator to arrange the images in a certain order. Then the number of each type of image is input following the prompts from the computer, and the program removes the bias, darks and flats from the image cube. The flats used are premade, meaning that they were already medianed and weighted. The output is an image cube containing the corrected images.

There are two aperture photometry procedures. One is named APPHO, and the other is APPHOT. APPHO calculates the flux within a circle of a radius determined by the user. The error associated with the flux is also in the output. This is not really the flux from the star, but the counts in that area. To find the background, the cursor should be placed over a background position on the image. The two values can be subtracted to give the counts in the circle that belong to the star. This still is not the flux, but it gives an accurate measure of the counts from the star. To increase the accuracy of this process, it is advisable to take several measurements from the background and the star, and subtract the averages.

APPHOT is similar to APPHO, but has a minor adjustment that makes it easier to use. This program uses a centroid to center on the star, and calculates the flux in a circle around the star. In addition, a second circle of 1.5 times

the stellar aperture is drawn. This measures the background around the star and subtracts it from the inner aperture. The output is the counts from the star with the background already subtracted and the associated error. Future versions of this code will allow the operator to decide the size of the second aperture.

If the subject that is being studied is a periodic phenomenon, there are a few period finding programs. One of the programs, SHORTSTRING, works by taking an initial guess of the period, then the program detects periods that fit the points. From these periods, the one with the shortest path connecting all of the data points is the period returned. The operator may wish to plot the period array against the path array to help determine the true period since this procedure will always return a shortest path. A second period finding program also exists. This program, PERIODOGRAM, uses Fourier analysis to search for a period. The data points are fit to different sine curves. The probability of each curve being the best fit to the data points is then calculated. This program is based on Horne and Baliunas(1986).

To gain a better signal-to-noise ratio (S/N), two frames can be added. There is a program called SA, short for shift and add. This program takes two input images and asks for a star to center on in the first image. It then asks for the same star in the second image. The offset between the two images is calculated and the images are shifted. The pixel values for the two overlaid images are added for the output image. This procedure is important when working with faint sources. There are several variations of this program.

If a true color image is desired from series of blue, green, and red images,

the procedure MAKE_GIF can overlay the images and create a color bar so that the resultant image appears to have the true colors.

Another IDL procedure that can be useful, is the MULTICHART program. This program will read the guide star catalogue and plot out a field based on the input parameters of coordinates and field size. This is very helpful when searching for faint targets. Charts are created for the corresponding field of view and limiting magnitude for each telescope.

C.7.4 IRAF

The image reduction and analysis facility (IRAF) is a powerful tool for the reduction of images. This package is available on the VAX and UNIX machines in the astronomy cluster. Images start as FITS images and are converted to a format that IRAF can read. The images can then be calibrated and reduced. IRAF can make photometric measurements as well. This package is a major part of data reduction at Mt. Stony Brook. The details of IRAF's procedures are too lengthy to describe here. Figure 5 contains a flowchart to show the usual reduction procedure. There are many more tasks that can be completed by IRAF, and the manuals available in the department should be consulted.

C.8 A Night At The Telescope

A night at the Mt. Stony Brook Observatory begins not in the dome, but in the warm room. Here the computer that collects the data resides. The computer is set up so that the software for whatever camera is running and the

switch box set to channel B. This allows the monitor and keyboard upstairs to operate the computer.

Now the telescope can be set up. The dome is fairly simple to operate. In the North west of the dome, there is a motor that turns the dome. The dome opens with a motor that pulls the slit back. The switch for the slit motor is near the light switches. The slit motor must be plugged in before it is moved. The plug is an eight prong polarized plug that must be unplugged when the slit is open. The power cord is attached to the dome itself. A nice feature to the slit is a horizon shield that can be disconnected from the slit to block the lights from the campus. This also allows the telescope to view at zenith.

The next step is to mount the camera on the telescope. Each camera had a specific alignment with the telescope. This insures that the flat fields are in the same alignment as the images, and that images from night to night do not vary in orientation. The exact alignments are shown in figure 4, but it is important that a consistent alignment was used is.

Once the camera is attached and aligned, the cooler is started. This has been described in an earlier section for each camera. The observer usually has to wait for a fifteen minute period for the Lynxx to cool to temperature. The ST-4 and ST-6 cameras only take about 5 minutes to cool. When starting, the observer should check to make sure that the telescopes are in alignment with each other. Many hours of observing time have been lost by misaligned telescopes. The object of choice is the University Hospital. The lights on the roof provide a nice target to center in all three telescopes.

The first part of data collection is to take the flat fields. Evening twilight

flats are usually taken. The campus has a fairly turbulent atmosphere, so morning flats are not superior to these. The dome is placed in the east, and the telescope's drive is turned off. Three images in each filter are taken so that the chip is about 10% saturated. This is done approximately a half hour before sunset.

Once the target has risen, the observer can star hop to the target. This is described in an earlier section. Usually a focus frame is taken of a star to learn if the telescopes are aligned. Once at the target, the observer can go to the warmroom and run the cameras in a warm environment. With the ST-6, the filter wheel is entirely controllable from the warmroom. The Lynxx camera requires manual changing of the filters. The observer can be in contact with another observer via a set of intercoms. The intercoms allow the warmroom to monitor the dome. The ST-6 and ST-4 cameras can control the drive. If there is a malfunction, the person in the warmroom will hear the drive motor slewing the telescope, and he can stop the camera immediately before the telescope crashes into anything.

C.8.1 The End Of The Night

After all of the targets are found, data recorded and the sun has risen, the observer can begin the shut down. The drive is turned off and unplugged. All of the electronics are turned off and the items that belong in the warm room return there. Cables that remain in the dome are wrapped around the pedestal to prevent tripping. The telescope is stowed so the declination is reading 90

degrees. The 3" telescope should be on the east side of the 14" when properly stowed. This position serves two purposes. The first is to place even weight on the motors. The second is to allow the observer 12 hours to remember to turn off the drive. The motor will carry a balanced weight if the 3" is on the west side or the east side. By putting the telescope on the east side, the telescope's drive can be left on accidentally for approximately 12 hours longer before it crashes into the pier.

C.9 Training

The primary use of this telescope is as a training tool for both graduate and undergraduate observers. Toward this goal a 4 week training program has been designed and is outlined below. This program can be accelerated to 4 days, 4 hours or 40 minutes depending on the level of the student.

C.9.1 Week 1

This week three readings are handed out, including this document. *Sky on a Chip, The Fabulous CCD* (1987) Provides a simple overview of how any CCD works. *The Digital Darkroom* (1993) provides an introduction to data reduction. Copies of all these reading are on file in the warmroom. The main functions of the telescope are also explained.

C.9.2 Week 2

Now the student actually gets to use the telescope itself. Only an eyepiece is used. Students are given four targets to find. They start with a first magnitude star. This can be difficult even for graduate students if they have never used a telescope before. Secondly, a bright planet or easy double star such as Alcor is given. The third assignment is any Messier object, and the last is a non discript eighth or ninth magnitude star. The projects are designed to be of increasing difficulty and to get the student to an adequate level at which they can point the telescope comfortably. The last week's reading is reviewed and relevant sections of the telescope manuals are handed out.

C.9.3 Week 3

Mounting and dismounting of the CCDs is demonstrated. After a review of the previous week's reading, students operate the PC. They practice the process of taking, manipulating and storing data. The students also transfer data to disks on the cluster.

C.9.4 Week 4

A quick oral quiz is in order, "What are flats? What are zeros? How are data corrected?" Then the student is ready to go. They install the camera, point the telescope to the same sequence of targets used in week 2. Then they acquire, process and store the data. Now the students are ready to use the 14" for scientific applications. It should be noted that none of the students

are perfect with the system, and periodic discussions about the maintenance and operation of the telescope should be held over an observing season.

C.10 Maintenance

As with any system, there must be maintenance preformed occasionally. The main points of maintenance at Mt. Stony Brook include the dome motors, and the cameras. The slit motor was replaced in 1993. The rotation motor is currently the original motor. The motor has shown considerable amounts of hysteresis, and to move the dome to west, one must first let it move to the east, the try to move it west. The track for the dome rotation must also be oiled occasionally. Once an observing season is recommended.

The cameras need to be maintained as well as the dome. The filters need to be cleaned once a week, as they are wonderful lint collectors. The window above the chip should also be cleaned once a week. Dust on the filters or window will be extremely apparent when examining flat field exposures.

The telescope must not be forgotten either. The declination lock wears itself loose over a few weeks. This should be checked as often as possible. The lock is easily tightened. An important note for the serious observer is moisture. The telescope is not sealed so water can condense on the corrector plate. If this happens in winter, the water will freeze. A hairdryer is stored in the warmroom for just this problem. In 30 minutes or less, the ice can be melted and the water evaporated. At least once a semester the collimation should be check. The directions for this are located on page 22 of the Celestron

Cable	Connects...	Quantity	Part No.
25' keyboard	dome keyborad to PC	2	HK0277M/F
25' VGA cable	dome VGA and Lynxx to PC	4	HK0307M/F
25' 9-Pin serial	SBIG cameras to PC[a]	2	HK0235M/F[b]
25' RJ-12	filter wheel to PC	2	HK0206-25 [b]
10BASE2 Cable	PC to cluster	1	[c]
50' 25 pin serial	PC to cluster	1	[c]

Table C.4: Cables fundamental to the operation of Mt. Stony Brook.

14 operating manual located in the warm room.

The biggest maintenance issue with the observatory is cabling. There are at least 7 cables connecting the dome to the PC. Exposure to the elements and time make failure of these cables inevitable. Failure in any cable can cause the entire system to go down. The following table list the cable types, their purpose and part number in the Misco catalog:

These are the major problems with maintenance have occurred in the past. As with any experiment, one has to periodically check for problems.

C.11 Future Improvements

The system is not yet perfect. Some improvements for the future are listed in this section. The Compuscope filter wheel can be attached to the Lynxx camera. This has not been done yet, but may be a consideration for the future. The filter wheel also has three empty positions. Additional filters would be useful. Suggestions for Hα and [OIII] have been made. A bigger screen is required to properly take advantage of the Xterminal capabilities of

the PC. A second PC would be useful, since the observer could use the ST-4 to see the guide star as he is imaging with the Lynxx or ST-6. This would prevent lost hours from trying to find the star that the ST-4 was tracking on. A second PC would also allow the filter wheel to be run in a different mode. Presently, the filter wheel is run in a pop-up window mode. This does not tell the operator which filter is in position. The other program with the filter wheel would show that information.

Better reduction and camera software would be an improvement to the current system. A beta test version of new data Acquisition software, called The Sky is on order. More analysis programs that are user friendly would be helpful to the current library. This is being worked on. An upgrade to the WINDOWS operating system would also be helpful. WINDOWS 95 and Windows for Workgroups are capable of more efficient multitasking and faster data transfer rates than currently available under WINDOWS. WINDOWS itself, or any of the upgrades can run more efficiently if the computer had more than 8 megabytes of memory. Sixteen megabytes of RAM is the minimum suggested memory for a machine running the number of processes we expect the machine to be running during data acquisition in the near future (e.g. Windows for Workgroups operating system, SkyPro data acquisition, IDL data analysis, QVTNET FTP utility.)

A final consideration would be electronic setting circles. With these circles, observed could simply align the telescopes, calibrate the circles, and then type in the numbers for the target. This system would make observing a much shorter routine, but the thrill of finding a target is gone.

C.12 Help Sheets For Operation Of The PC

C.12.1 Lynxx Time Sheet

When using the PC out of the WINDOWS mode, use this conversion sheet to run the Lynxx camera.

Time	Type	Time	Type	Time	Type
1 sec	3 sec	15 sec	57.0 sec	6 min	1368 sec
2 sec	7 sec	20 sec	76.0 sec	7 min	1596 sec
3 sec	11.5 s	25 sec	94.5 sec	8 min	1824 sec
4 sec	15.0 s	30 sec	114 sec	9 min	2052 sec
5 sec	19.0 s	45 sec	171 sec	10 min	2280 sec
6 sec	22.5 s	60 sec	228 sec		
7 sec	26.5 s	2 min	456 sec		
8 sec	30.5 s	3 min	684 sec		
9 sec	34.5 s	4 min	912 sec		
10 sec	37.5 s	5 min	1140 sec		

To get any time that is not printed here, you can add, subtract, multiply and divided at will to get the desired time. i.e.) 2.5 min=2 min+30 sec= 456+114=570 so you would type in 570 for a 2.5 min exposure. You must be out of windows for these times to work.

C.12.2 PC To VAX FTP Commands

At the end of each night, send the data you have collected over to the VAX cluster. Here is how to do it:

1. In the program manger is a group called INTERNET in this group there is an item called QVTNET. Double-click on QVTNET and then choose the FTP option

2. Using the dialog box login to the OBSERVER account on sbast3. Once there, type:
   cd \home\sbast92\observer.
   This will put you into the data directory.

3. Type mkdir and create a new directory under mtsb named for the month and the date after midnight. (ie. for the night of November 2 to the morning of the 3, use NOV_3. Cd into the new directory (eg. cd NOV_3)

4. Check to make sure you are in the right directory by typing path. \home\sbast92\observer\NOV_3 is what you would see if you used the example from above. If you are not, use the CD command to changethe directory.

5. Now you can transfer data. Type:
   binary
   to set the data type.

6. Now type

   mput F:*.*

   This will send everything from the F:\ drive to the directory you are in FTP.

When the files have finished the transfer (this takes about 10 minutes) you exit the process. To do this: Simply select the exit option under the FILE pull-down.

C.12.3 14" Telescope Shut Down Check Sheet

This is a check list for how to leave the telescope at the end of the night. Please make sure you have completed all of the following steps.

1. Turn off the drive to the telescope and unplug.
2. Unplug all electronics, including the Lynxx, the autoguider and its many components, and any other pieces of equipment you may have used. Replace any filters etc. to their boxes.
3. Remove any eyepieces and cover the eyepiece openings (there should be some film containers to use for this purpose). Also, the telescope should be covered now.
4. Return the telescope to the stowed position. (With the 3 inch on the EAST side of the 14 inch)
5. Rotate the dome so that the slit is above the door. Close the slit and unplug the motor to the slit.
6. Turn off the monitor, the lights and lock the dome.
7. Replace all equipment and the keys to the warm room.
8. Rotate the dome so that the slit is above the door. Close the slit and unplug the motor to the slit.
9. Turn off the monitor, the lights and lock the dome.
10. Replace all equipment and the keys to the warm room.

11. Reset the computer to warm room control.

C.13 IDL Program Help Pages

CCD2FITS: CONVERSION OF CCD FILES TO FITS FORMAT

CCD2FITS,file,ofile

FILE: File to be read

OFILE:Name of output file

Procedure to convert three 8 bit words to two 12 bit words

Writes out in FITS

AUTO2FITS: AUTOMATIC CCD TO FITS CONVERTER

AUTO2FITS,ccdfiles,fitsfiles

CCDFILES: file containing list of files to be read

FITSFILES: file containing list of files to be written

Converts several CCD format files to FITS

CCD12BIT: LYNXX IMAGE READER

CCD12BIT,file,pix2

FILE:file to be read

PIX2:output filename

Procedure to convert three 8 bit words to two 12 bit words

AUTOCCD: MULTIPLE CCD FILE READER

AUTOCCD,filenames,dir,imagecube

FILENAMES: file containing list of files to be read

DIR: string containing location of source directory

IMAGECUBE: name of output image vector

MEDIAN: IMAGE MEDIANS

MEDIAN,imagecube,m,scale

IMAGECUBE: images to find median of

M: name of output image

SCALE: =1 for normalized images, =0 for non-normailized

AUTORED2: LYNXX AUTOMATIC REDUCTION

The operator is queried for all inputs

The image cube must be filled so that the bias images

are first, then the dark15,dark30 and dark60 images.

Then the colors are filled with red, infrared,visible

and blue. Each color should have the 15,30 and 60 second

images in that order.

APPHO:APERTURE PHOTOMETRY

APPHO,image,rad,cts,nbins,x,y or

APPHO,image,rad,counts,xvec,yvec,col=col,resize=resize

RAD: radius of square in pixels; def=3

X,Y: center for remote call

KEYWORDS:

COL: color for circle

RESIZE: expand the image by a factor

APPHOT:APERTURE PHOTOMETRY AND BACKGROUND SUBTRACTION

APPHOT,image,rad,cts,nbins,x,y

APPHOT,image,rad,counts,xvec,yvec,col=col,resize=resize

RAD: radius of square in pixels; def=3

X,Y: center for remote call

KEYWORDS:

COL: color for circle

RESIZE: expand the image by a factor

PERIODOGRAM:PERIOD FINDING PROGRAM

PERIODOGRAM,t,v,p1,p2,np,title

T: observation times

V: observed values

P1,P2: first and last periods to be tested

NP: number of points to be tested

TITLE: optional plot title

OUTPUTS:

pdgm: power(p1 or p2)

p1: frequency

p2: period

finds periods in timed magnitude data

SA: SHIFT AND ADD IMAGES

SA,image1,image2,image3,dispmin,dispmax

IMAGE1,IMAGE2: images to be added

IMAGE3: output image

DISPMIN,DISPMAX: limits to the byte scale of the images

shifts and adds two images together

MAKE_GIF: SHIFT AND ADD THREE BAND IMAGES TO PRODUCE

TRUE COLOR IMAGE. WRITTEN INTO A GIF FILE

MAKE_GIF,ri,gi,bi,fileout,warp=warp

RI: red image

GI: green image

BI: blue image

FILEOUT: name of output image without .gif

WARP: If set will poly warp the fields, only needed for SQIID data

MULTICHART: AUTOMATICALLY READ GSC AND PRINTS FINDER CHARTS

MULTICHART,filename,hard=hard

FILENAME: file containing star name,RA in h,m,s DEC in d,m,s

HARD: if set will produce a hard copy of the charts

SHORTSTRING: FIND THE PERIOD FOR A DATA SET

SHORTSTRING,time,deltamag,guess

TIME: the time array to be plotted folded over the period

DELTAMAG: the magnitude array to be plotted

GUESS: intial guess at period

Appendix D

The Epsilon Aurigae Secondary: A Hydrostatically Supported Disk

D.1 Introduction

Disks are among the most common of astrophysical systems. They range in size from galaxies, through protostellar/circumstellar disks, down to the rings around planets. A powerful technique for observing disk systems is stellar occultations. This method has been applied with great success to planetary rings (e.g., Lane et al. 1982, Holberg et al. 1982), the best understood astrophysical disk systems. The ϵ Aurigæ system allows us to apply this technique to an entirely new class of disks.

Epsilon Aurigæ is an F0 Ia star with an enigmatic companion which partially eclipses the visible star for $\sim$ 2 years every 27.1 years. The maximum fraction of the primary that is eclipsed is about 48%. The eclipse light curve has a long, flat minimum (Figure D.1), implying that the secondary is not

appreciably convex. The eclipse is fairly colorless (hereafter "gray") over the range of 4000 Å to 5 μm. The smaller eclipse depth that is observed at longer wavelengths has been attributed to thermal radiation from the secondary with a color temperature of $\sim$ 500 K (Backman et al. 1984). During eclipse, absorption lines are seen, presumably due to cool, optically thin material in the secondary passing in front of the primary. However, these lines are much more prominent after mid-eclipse than prior to it (Lambert and Sawyer 1986, Hinkle and Simon 1987), in contrast to the fairly symmetric light curve.

Huang (1965) suggested that the secondary is a thick opaque disk which we view edge-on. In most subsequent studies of ϵ Aurigæ, the secondary has been modeled as a completely opaque disk viewed edge-on or nearly so. Such a disk is unphysical. A realistic disk would have a finite optical depth with a maximum value in the midplane ($z = 0$) and decreasing values along lines of sight traversing the disk at larger $|z|$. In this paper, we develop a hydrostatic/quasi-hydrodynamic model of the secondary disk which is constrained by the observational data.

Analysis of the ϵ Aurigæ system is complicated by diverse data of varying quality. The mass function, period and eclipse timing are well known, as is the angular size of the primary. The solid angle subtended by the secondary, the eccentricity of the orbit, the orbital velocity of material at the edge of the secondary disk, and the distance of the system from Earth have all been measured, but uncertainties are larger on these quantities. We summarize the relevant system characteristics in Section D.2.

A rotating disk supported by centrifugal force and gas pressure against

gravitational collapse will have a concave shape. That is, it will have greater vertical (z) extent at its outer radius than near its center (Figure D.3). For certain density distributions, more blockage of light would occur at 2^{nd} and 3^{rd} contacts than at mid-eclipse. In principle, this effect may offer an explanation for the small central brightening observed during the broad light minimum. We develop hydrostatic models for the ϵ Aurigæ secondary in Section D.3 and present synthetic eclipse light curves calculated using these models in Section D.4.

Thermal heating of the portion of the secondary exposed to the radiation field of the primary increases the secondary's z extent at the edge facing the primary. This thermal expansion from "morning" (post-star "rise") to "afternoon" offers an explanation for the observed temporal asymmetry in the strength of absorption line profiles relative to mid-eclipse. We study this hypothesis quantitatively using a quasi-hydrodynamic model of the disk edge in Section D.5. Our results are summarized in Section D.6.

D.2 Characteristics of the ϵ Aurigæ System

The size, mass and distance to the system are inter-dependent and uncertain. Constraints derived using the mass function, stellar evolution models and various other data suggest either a high-mass system ($M_1 \sim 20$ M$_\odot$, $M_2 \sim 15$ M$_\odot$) at a distance of ~ 1200 pc or a low-mass system ($M_1 < 2$ M$_\odot$, $M_2 < 5$ M$_\odot$) at ~ 600 pc (Webbink 1985). Note that in the low-mass model, the "secondary" is more massive than the visible "primary";

however, we shall follow the convention used in most of the ϵ Aurigæ literature and continue to refer to the F star as the primary because it is clearly the primary source of luminosity of the system. Doppler shifts of absorption lines seen during eclipse imply an orbital velocity at the edge of the secondary more compatible with the low-mass model (Saitō et al. 1987, Lambert and Sawyer 1986). A distance estimate based on astrometry of the primary's orbit of $\sim 580 \pm 30$ pc (van de Kamp 1978) also supports the low-mass system; however, this result must be interpreted with caution due to the difficulty of obtaining such an estimate from the ground; other evidence suggests a distance of ~ 1000 pc (cf. Carroll et al. 1991). The *HIPPARCOS* spacecraft is expected to provide a more accurate estimate of, or lower bound to, the distance to the ϵ Aurigæ system.

Many characteristic quantities can be derived for ϵ Aurigæ that are independent of the system's absolute scale. These scale-independent quantities include the ratios between the secondary's length, the primary's diameter, the component separation, and the system's distance from Earth, the ratio of the bolometric luminosities of the components, the radiative flux at the secondary due to the primary, and the color of the eclipse. Our approach is to separate scale-dependent from scale-independent quantities, and rely on the latter as much as possible to construct the model framework. The scale-dependent quantities (e.g., the thickness of the disk as a function of temperature, mass of the secondary and the system's dimensions) then allow us, in principle, to discriminate between the high- and low-mass systems. A resolution between the two alternative models is crucial to determining whether the disk is

a remnant of post-main sequence mass transfer (Eggleton and Pringle 1985) or a protostellar/protoplanetary disk (Carroll et al. 1991). Results in this paper (Section D.4) lend some support to the high-mass model, but the scale-independence of our calculations allows them to be directly applied to either high- or low-mass systems.

The best known parameters of the ϵ Aurigæ system are the mass function,

$$f = \sin^3 i \frac{M_2^3}{(M_1 + M_2)^2} = 3.12 \text{ M}_\odot \tag{1}$$

(Morris 1962); the orbital period, $P = 9890$ days (e.g., Carroll et al. 1991); the eclipse depth, 48% of the primary's light blocked at visual (≈ 0.7 magnitudes extinction; Schmidtke 1985); and the angular size of the primary, 8×10^{-17} str. The mean eclipse depth varies by $\leq 1\%$ from 1.25 μm – 4.8 μm (Backman 1985). The upper limit to the color variations is almost as severe within the visible (Schmidtke 1985), but possible differences between visible and IR depths are less well constrained because the data were obtained at different times. The fact that we can see the eclipse means that the orbital inclination with respect to the plane of the sky, i, is close to 90°.

Quantitative timing estimates vary from one eclipse to another. Typical eclipse durations are: 1^{st} – 4^{th} contact ≈ 670 days, 2^{nd} – 3^{rd} contact ≈ 394 days, these numbers are uncertain and possibly changing (Schmidtke 1985). The time between 1^{st} and 3^{rd} (or 2^{nd} and 4^{th}) contacts implies the secondary's "length" (i.e., its extent parallel to its orbit) is

$$\ell = 2\pi a F_{ecl}(1 + e\cos\omega) = 0.338a(1 + e\cos\omega)$$

$$= 4.6 \times 10^{13}(1 + e\cos\omega)\Big(\frac{M_2^{1/2}}{{\rm M_\odot}^{1/3} f^{1/6}}\Big)\ {\rm cm}, \qquad (2)$$

where a is the semimajor axis of the primary's orbit around the center of mass, e the orbital eccentricity (roughly equal to 0.2, Wright 1970), ω the angle between periapsis and the line of sight (periapse is estimated to be 14° before we observe mid-eclipse; Wright 1970) and F_{ecl} is the fraction of the system's orbital period which lies between first and third contacts. Terms of second order in e or F_{ecl} have been omitted, and only those quantities well known from eclipse observations have been evaluated numerically.

Regarding the geometry of the cross-section of the secondary in view during eclipse, there are several alternatives. A) The secondary may be a sharp-edged thick disk that is parallel to its orbital plane and this plane may also contain our line of sight. This model yields the minimum projected area for the disk. B) The disk could lie parallel to its orbit about the F star and be viewed along a line-of-sight somewhat inclined to that plane, subtending a solid angle larger than the minimum. C) The disk could be warped or inclined to its orbit plane and the line of sight, and be larger in cross-section during eclipse than the minimum size.

The timing between 1^{st} and 2^{nd} contact and between 3^{rd} and 4^{th} contact gives the primary's radius, $R_1 = (1/2) \times \ell \times 138/532 = 0.13\ \ell$. The depth of the eclipse implies a minimum height (extent perpendicular to its orbit) of

the secondary of $H \geq 0.82R_1$, with the equality holding if and only if Earth is in the orbital plane of the system. Thus, if the secondary is a thick opaque disk (Huang 1965), the area of the secondary as viewed from the Earth is $\geq$ 2.0 times that of the primary.

If we are viewing the eclipse from out of the orbital plane ($i \neq 90°$), then the most extreme viewing angle consistent with the observed eclipse depth implies that the secondary blocks the light from (almost exactly) one hemisphere of the primary and one edge of the secondary passes nearly across the center of the primary. A thin secondary in the orbital plane cannot block the center of the primary unless it extends to the primary's center, which is impossible. A secondary of thickness H and disk radius $R_d = \ell/2$ just eclipses the primary's center if $\tan i = (2a - \ell)/H$. The area presented to us in such a configuration is

$$\pi(\ell/2)^2 \cos i + H\ell \sin i \approx \pi(\ell/2)^2 \frac{H}{2a - \ell} + H\ell \approx 1.5H\ell. \qquad (3)$$

This area is twice that presented in Huang's model if $H = 1.1R_1$ and $i = 88°$.

Comparison of data taken during eclipse with post-eclipse observations (Backman et al. 1984, Backman and Gillett 1985) seemed to imply that the IR fluxes require a larger companion disk than would be consistent with cases A or B. Alternatively, these data could be fit by a smaller secondary which was substantially more transparent at 20 μm than at 4.8 μm, but we show in Section D.4 that such a possibility is very unlikely given the colorlessness of the eclipse at shorter wavelengths. However, recent reanalysis of the

thermal-IR data from mid- and post-eclipse (Backman et al. 1996) indicates that the pre-eclipse 20 μm brightnesses were too low, and the projected area of the disk companion is possibly only twice the minimum area allowed by Huang's model. Models have been proposed of a disk that is substantially warped or inclined to its orbital plane (e.g. Kumar 1987) due, for example, to the presence of a secondary binary inside (Lissauer and Backman 1984, Eggleton and Pringle 1985). Such a disk might require a hole in its center (Wilson 1971, Eggleton and Pringle 1985) in order to be consistent with the flat-bottomed eclipse profile. These sorts of systems are difficult to model because the available data do not adequately constrain the conceivable parameter space. In the remainder of this paper, we will restrict our analysis to models of disk with midplanes parallel to the orbital plane about the F star, which either lie within our line of sight (case A), or are inclined (case B) at angles as high as 3.5°.

D.3 Vertical Structure of the Secondary: Hydrostatic Model

In this section, we develop a physical model of the secondary as a disk that is centrifugally supported in the radial direction and hydrostatically supported in the vertical direction. We assume that the disk is vertically isothermal and well mixed. If heating occurs predominantly near the midplane of the disk, e.g. as a result of viscous dissipation, the temperature would be expected to

drop with height. However, assuming that the exposed regions are in radiative equilibrium, the material above the disk's photosphere is optically thin in the thermal-IR so it may be expected to be roughly isothermal in z, in analogy with planetary atmospheres (Chamberlain and Hunten 1987). As the visible opacity is likely to be larger than the mid-IR opacity, the assumption of vertical isothermality is likely to hold for the portions of the disk partially transparent to visible and near-IR radiation. Our eclipse profiles are most sensitive to the thermal structure in these regions. If the star(s) at (near) the center of the secondary illuminate(s) and heat(s) the faces of the disk, scattering and absorption at high z in the disk may produce temperature gradients in the optically thin regions of the disk. However, these temperature gradients depend on unknown system parameters; moreover, they are unlikely to be large enough to appreciably affect our analysis.

We use a right-handed Cartesian coordinate system in which the z axis is perpendicular to the plane of the disk and the line of sight from the Earth runs from $-y$ to $+y$, perpendicular to z. The vertical component of the momentum equation for a "thin" (i.e., centrifugally supported) disk is:

$$\frac{\partial v_z}{\partial t} + v_z \frac{\partial v_z}{\partial z} = -\frac{1}{\rho}\frac{\partial p}{\partial z} - z\Omega^2 \tag{4}$$

where v_z is the velocity of the gas, t is time, ρ signifies density, p refers to pressure and Ω is the angular frequency of the material relative to the center of the disk. In equilibrium, $v_z = 0 = \partial v_z/\partial t$. If we further assume that the disk is isothermal in the vertical direction and use the perfect gas law, then

eq. (4) can be integrated to yield

$$\rho = \rho_o \; e^{\left(\frac{-z^2}{h^2}\right)}. \tag{5a}$$

The Gaussian scale height of the disk is:

$$h = \frac{1}{\Omega}\Big(\frac{2kT}{\mu}\Big)^{1/2} = 9.6 \times 10^{11}\Big(\frac{T}{500}\Big)^{1/2} P_{disk} \text{ cm}, \tag{5b}$$

where μ is the mean molecular mass of the gas, P_{disk} is the orbital period at the outer edge of the disk in years, and all of the mass of the secondary has been assumed to be concentrated near its center, so the Keplerian approximation is valid.

The "dynamical aspect ratio" of the disk, h_o/R_d, where h_o is the scale height at the disk's outer edge, can be computed using eqs. (1), (2) and (5) and the orbital parameters of the system:

$$\frac{h_o}{R_d} = \Big(\frac{2kTR_d}{\mu G M_2}\Big)^{1/2} = (2\pi)^{1/6}\Big(\frac{kT}{\mu}F_{ecl}(1+e\cos\omega)\Big)^{1/2}\Big(\frac{P}{G}\Big)^{1/3}\Big(\frac{\sin i}{M_2}\Big)^{1/4}\frac{1}{f^{1/12}}$$

$$= 0.119\Big(\frac{m_{\rm H}}{\mu}\;\frac{T}{500}\;(1+e\cos\omega)\Big)^{1/2}\Big(\frac{\rm M_\odot}{M_2}\Big)^{1/4}\Big(\frac{\rm M_\odot}{f}\Big)^{1/12}$$

$$= 0.079\Big(\frac{\mu_{sn}}{\mu}\Big)^{1/2}\Big(\frac{\rm M_\odot}{M_2}\Big)^{1/4}\Big(\frac{T}{500}\Big)^{1/2} \tag{6}$$

where m_H is the mass of a hydrogen atom and $\mu_{sn} = 2.25\ m_H$ is the mean molecular weight of a solar composition gas. The factors contributing to the largest uncertainties to h_o/R_d are, in decreasing order, M_2, T, $e\cos\omega$ and μ. The mean molecular weight of the gaseous disk is probably similar to μ_{sn} because the gas of which the disk is composed is likely to be unprocessed ISM material or mass transferred from the primary when the star overflowed its Roche lobe; both stellar evolution models (Webbink 1985) and the line spectrum of ϵ Aurigæ (Castelli 1978) suggest that such gas would be hydrogen-rich. As stated earlier, model estimates of h_o/R_d can therefore be useful in estimating M_2 and thus in discriminating between the high- and low-mass models of the ϵ Aurigæ system.

The radial structure of a centrifugally supported disk is less well defined. Radial profiles for a disk which has settled into a quasi-equilibrium configuration depend on the form of the viscosity law. Temperature profiles are also model-dependent. In an effort to reduce the parameters to a reasonable number, for most of our simulations the surface mass density of the disk, σ, is assumed to be constant from an inner hole radius R_H (which may be zero) out to the disk radius R_d, beyond which it is zero. We also performed a few runs in which σ varies as r^{-2}.

The scale height of the disk is assumed to be proportional to the distance from the center (equivalently, $\Omega \propto r^{-3/2}$ and $T \propto r^{-1}$). The opacity of the gas/dust mixture, κ (in units of cm^2/g), is a function of wavelength only. If we also assume that we are viewing the eclipse exactly in the orbital plane, then the optical depth which we observe through the disk at a given point on

the projected surface is

$$\tau(x,z) = \frac{2\kappa\sigma R_d}{\sqrt{2\pi}h_o} \int_{\Re e(\sqrt{R_H^2-x^2})}^{\sqrt{1-x^2}} \frac{e^{\frac{-z^2}{x^2+y^2}}}{(x^2+y^2)^{1/2}} dy, \qquad [\sigma = \text{constant}] \qquad (7a)$$

or

$$\tau(x,z) = \frac{2\kappa\sigma_o R_d}{\sqrt{2\pi}h_o} \int_{\Re e(\sqrt{R_H^2-x^2})}^{\sqrt{1-x^2}} \frac{e^{\frac{-z^2}{x^2+y^2}}}{(x^2+y^2)^{3/2}} dy, \qquad [\sigma(r) = \left(\frac{R_d}{r}\right)^2 \sigma_o] \qquad (7b)$$

where the origin of the rectangular coordinate system is the center of the disk, the y axis points toward Earth (see Figure D.3) and the coordinates x, y and z and hole size R_H have been made nondimensional via division by R_d, R_d, h_o and R_d respectively.

If we are not viewing the disk exactly in the orbital plane, the situation becomes somewhat more complicated. We continue to define the z axis to be perpendicular to the Earth-star line, but the y axis no longer points directly at the Earth. For a given line of sight through the disk, the z coordinate of a ray from the primary to the Earth changes as the ray traverses the disk:

$$z = z_o - \frac{a(1-e^2)}{h_o(1+e\cos\omega)} \cot i - \frac{R_d y \cot i}{h_o}. \qquad (8)$$

In equation (8), z_o is the z coordinate of the point on the star from which the ray emanates and i is defined relative to the "plane" of the sky, i.e., $i = 90°$ when the system is viewed edge-on. Note that we have defined the sign of z such that the center of the primary is at $z \geq 0$.

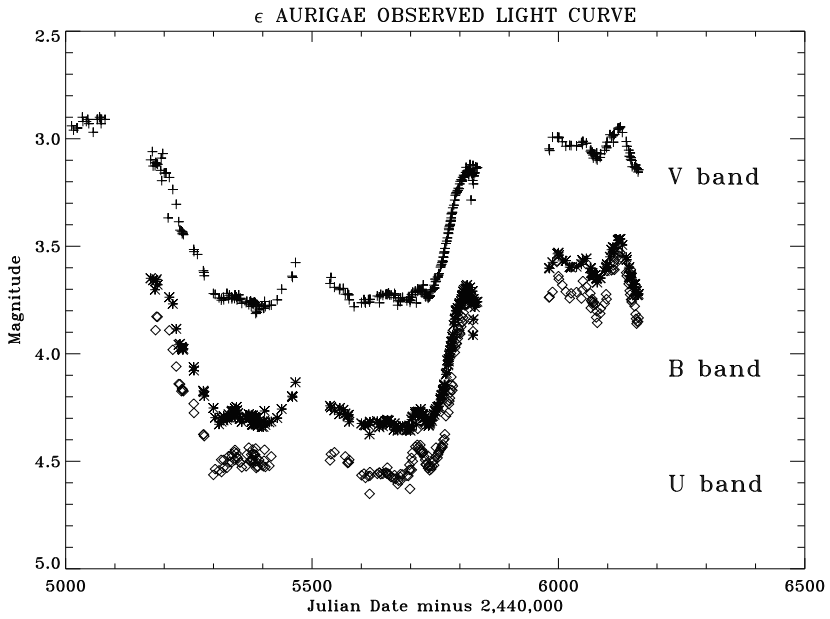

Figure D.1: Light curves of ϵ Aurigæ, 1982 – 1984, showing the eclipse at $\lambda = 0.55$ μm (crosses), $\lambda = 0.44$ μm (asterisks) and $\lambda = 0.36$ μm (diamonds) (from Hopkins 1995). The large gaps are caused by the star's annual passage behind the Sun. The short term irregular variations are thought to be caused by pulsations of the primary (cf. Carroll et al. 1991).

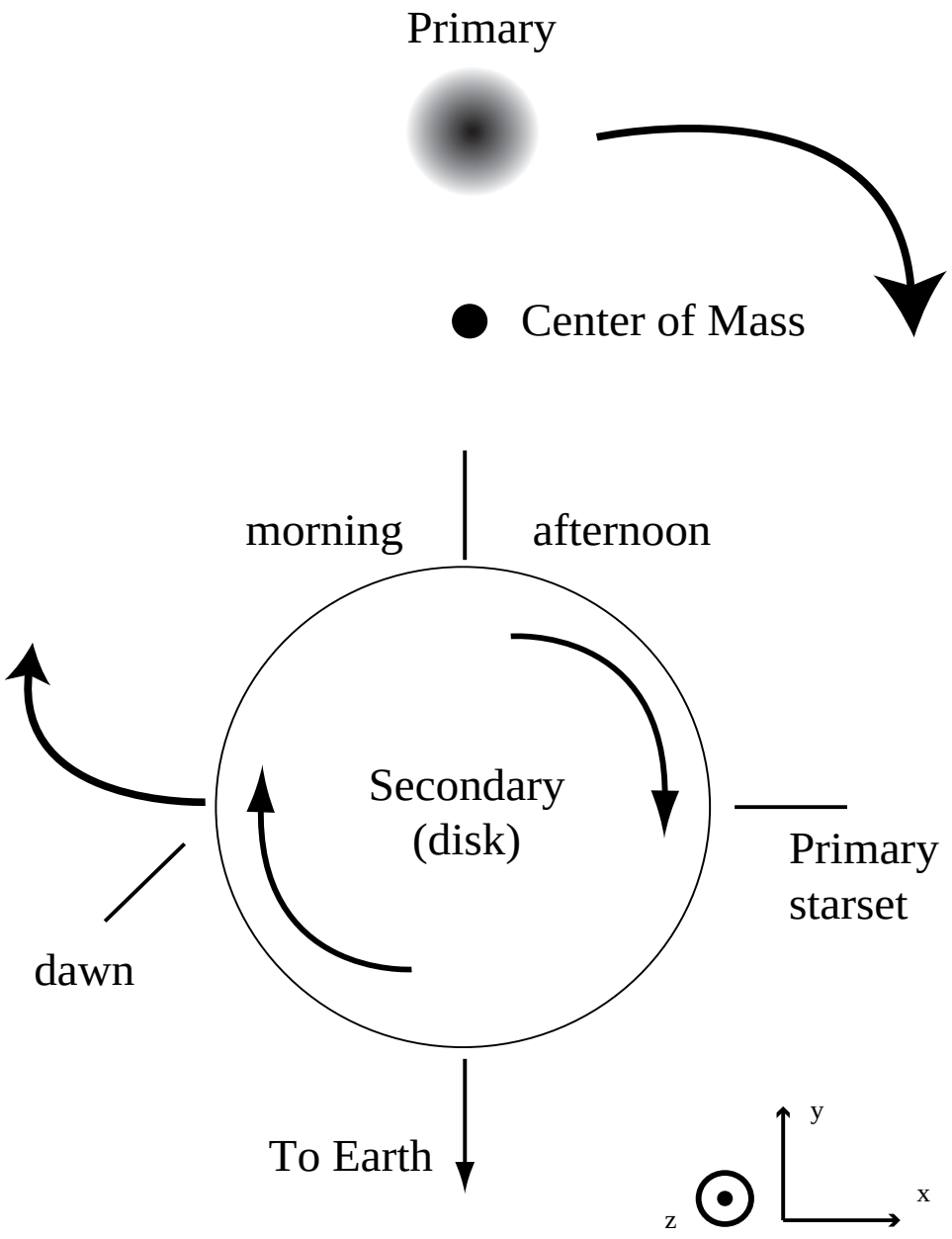

Figure D.2: View of the ϵ Aurigæ system from well above the orbital plane, at a time when a terrestrial observer would see the secondary (partially) eclipsing the primary. The wide arrows show orbital motions of the primary star and the secondary disk about their mutual center of mass. The thin arrows denote the orbital direction of material at the edge of the secondary.

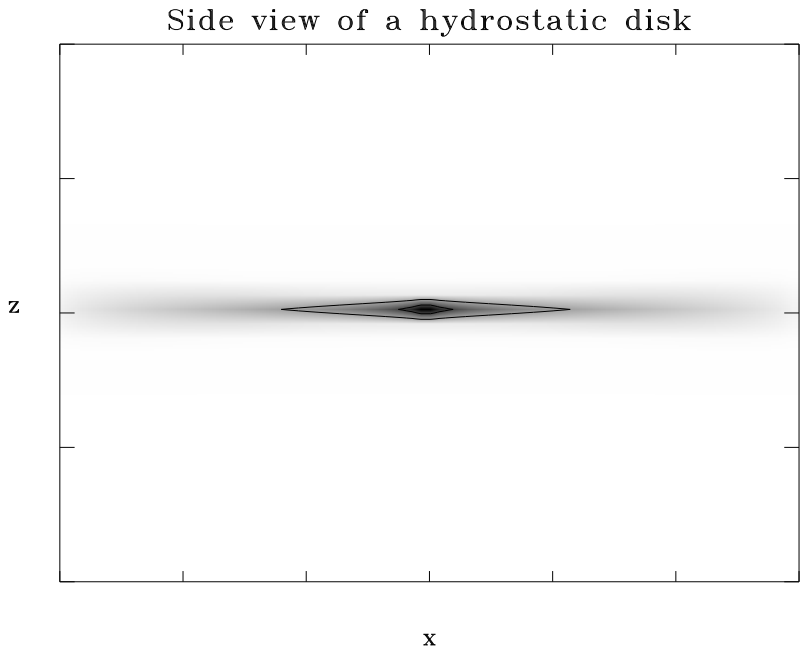

Figure D.3: Isodensity contours of a thin slice cut through the center of the secondary perpendicular to the disk's midplane.

D.4 Eclipse Lightcurves for the Hydrostatic Model

We have generated synthetic eclipse profiles from equation (7) with z given by equation (8). The values of the orbital elements e and ω were those given in Section D.2. Throughout this section, we assume the disk to be cylindrically symmetric. We model disks with and without central holes and use a variety of midplane opacities and temperatures.

The disk was modeled on a rectangular grid of 101 elements in the z direction and 505 elements in both x and y. The opacity at each grid point was then calculated. The eclipse lightcurve was computed on a grid of 505 time steps separated by approximately 1.3 days, for a range of values of the disk scale height, h_o, the inclination, i, and central hole radius, R_H. The opacity parameter, approximately equal to the "vertical" optical depth of the disk, is:

$$K \equiv \kappa\sigma\frac{R_d}{h_o}, \qquad [\sigma = \text{constant}] \tag{9a}$$

or

$$K \equiv \kappa\sigma_o\frac{R_d}{h_o}, \qquad \left[\sigma(r) = \left(\frac{R_d}{r}\right)^2\sigma_o\right] \tag{9b}$$

was calculated iteratively to reproduce the maximum eclipse depth of 48% for each combination of h, i and R_H that we modeled. If the disk's mass is 0.1 $M_\odot$ and its opacity is similar to that of interstellar matter, then $K \sim 10^6$ in the near-IR. A more massive disk, or one made of a more opaque material,

could increase K, but realistically only by a few orders of magnitude. No equivalent lower bound on K exists because substantial grain growth, settling of the grains to the midplane and extremely low-mass disks cannot be ruled out. (See Weidenschilling and Cuzzi (1993) for a review of grain growth within protoplanetary disks.) Line of sight optical depth profiles through six of our model disks are shown in Figures D.4 and D.5.

Tables D.1 and D.2 describe the values of the parameters chosen for our simulations and the primary quantitative results.[1] The constant σ models are numbered consecutively, but the $\sigma = \sigma_o(R_d/r)^2$ models are given numbers 100 greater than the constant σ runs with otherwise identical parameters. We present two measures of the dependence of the eclipse depth, D, upon opacity. The "δ-color" is defined as $\delta_c \equiv D(10K)/D(K)$, evaluated at the phase where $D(K)$ reached its maximum. The "δ-opacity", δ_K, is the factor by which the nominal opacity must be multiplied to give $D_{max} = 50\%$. These parameters allow comparison of model predictions and observations with functions of particle opacity vs. wavelength. A value of $\delta_c = 1$ signifies completely gray, since this implies that D_{max} is the same for both opacities. A value of $\delta_K = \infty$ also signifies completely gray, since infinite opacity differential means there is no opacity which increases D_{max} by 2%. Second contact is defined as the first time (in days after first contact) that the eclipse depth $D = 46\%$ (vs.

[1]The accuracy of the results presented Tables D.1 and D.2 is often limited by the resolution of the grid used for our simulations. In many cases, the last digit tabulated should not be regarded as significant, so results which appear to be identical to four places despite differing input parameters may only have been the same to three places if a higher resolution code were used. However, given the scatter in the observational data, we do not believe that more precise modeling is warranted.

Hydrostatic Model Simulations

Model #	INPUT PARAMETERS: Scale height h_o/R_d	Inclination i	Hole size R_h/R_d	CALCULATED PARAMETERS: Opacity[1] K	δ-color $\delta_c \equiv \frac{D_{max}(10K)}{D_{max}(K)}$	δ-Opacity[2] δ_K	Second contact[3]	Mid-eclipse depth D_{mid}
1	0.02	90.0	0.0	1.05×10^{11}	1.038	3.30	135	0.4748
2	0.02	90.0	0.9	1.05×10^{11}	1.038	3.31	135	0.4748
3	0.02	89.0	0.0	1.18×10^{9}	1.045	2.98	143	0.4800
4	0.02	89.0	0.9	1.19×10^{9}	1.045	2.97	143	0.4800
5	0.025	90.0	0.0	1.53×10^{7}	1.059	2.52	135	0.4720
6	0.025	90.0	0.9	1.57×10^{7}	1.059	2.51	135	0.4719
7	0.025	89.0	0.0	1.36×10^{6}	1.068	2.51	140	0.4800
8	0.025	89.0	0.9	1.40×10^{6}	1.068	2.51	140	0.4800
9	0.03	90.0	0.0	1.19×10^{5}	1.086	2.14	135	0.4694
10	0.03	90.0	0.5	1.19×10^{5}	1.086	2.14	135	0.4694
11	0.03	90.0	0.9	1.29×10^{5}	1.087	2.10	135	0.4691
12	0.03	89.0	0.0	3.08×10^{4}	1.094	2.23	139	0.4800
13	0.03	89.0	0.5	3.08×10^{4}	1.094	2.23	139	0.4800
14	0.03	89.0	0.9	3.37×10^{4}	1.095	2.21	139	0.4800
15	0.03	87.5	0.0	2.93×10^{6}	1.021	40.9	163	0.4800
16	0.03	87.5	0.5	2.93×10^{6}	1.021	40.9	163	0.4800
17	0.03	87.5	0.9	3.00×10^{6}	1.021	40.7	163	0.4800
18	0.04	90.0	0.0	7.68×10^{2}	1.149	1.80	135	0.4619
19	0.04	90.0	0.5	7.68×10^{2}	1.149	1.80	135	0.4619
20	0.04	90.0	0.9	9.71×10^{2}	1.155	1.76	135	0.4601
21	0.04	89.0	0.0	5.86×10^{2}	1.156	1.83	135	0.4800
22	0.04	89.0	0.5	5.86×10^{2}	1.156	1.83	135	0.4800
23	0.04	89.0	0.9	8.91×10^{2}	1.175	1.83	133	0.4800
24	0.04	87.5	0.0	1.28×10^{4}	1.059	4.85	179	0.4800
25	0.04	87.5	0.5	1.28×10^{4}	1.059	4.85	179	0.4800
26	0.04	87.5	0.9	1.40×10^{4}	1.060	4.64	179	0.4800
27	0.05	90.0	0.0	6.53×10^{1}	1.230	1.54	135	0.4535
28	0.05	90.0	0.5	6.53×10^{1}	1.230	1.54	135	0.4535
29	0.05	90.0	0.9	1.01×10^{2}	1.249	1.48	135	0.4479
30	0.05	89.0	0.0	7.32×10^{1}	1.219	1.59	133	0.4751

Table D.1: Results of disk simulations.

a maximum depth of 48%). The fifth calculated quantity is the fraction of the primary's light which is blocked by the disk at mid-eclipse. Owing to the disk's projected "bow-tie" shape, the deepest part of the eclipse usually occurs near second and third contacts, with mid-eclipse brightening in between. The central brightness is a measure of how "pinched" the center of the disk appears at the given viewing angle. Representative eclipse profiles at a variety of wavelengths are shown in Figures D.6 and D.7; additional profiles are presented in Figures D.8 through D.14.

Hydrostatic Model Simulations - Continued

Model #	INPUT PARAMETERS: Scale height h_o/R_d	Inclination i	Hole size R_h/R_d	CALCULATED PARAMETERS: Opacity[1] K	δ-color $\delta_c \equiv \frac{D_{max}(10K)}{D_{max}(K)}$	δ-Opacity[2] δ_K	Second contact[3]	Mid-eclipse depth D_{mid}
31	0.05	89.0	0.5	7.32×10^{1}	1.219	1.59	133	0.4751
32	0.05	89.0	0.9	1.09×10^{2}	1.237	1.52	132	0.4686
33	0.05	87.5	0.0	7.70×10^{2}	1.099	2.43	175	0.4800
34	0.05	87.5	0.5	7.70×10^{2}	1.099	2.43	175	0.4800
35	0.05	87.5	0.9	9.44×10^{2}	1.114	2.34	171	0.4800
36	0.10	90.0	0.0	1.91×10^{0}	2.102	1.15	144	0.4450
37	0.10	90.0	0.5	1.97×10^{0}	2.126	1.18	141	0.4239
38	0.10	90.0	0.9	5.99×10^{0}	2.566	1.11	132	0.3605
39	0.10	89.0	0.0	2.11×10^{0}	1.871	1.12	143	0.4466
40	0.10	89.0	0.5	2.16×10^{0}	1.883	1.15	141	0.4275
41	0.10	89.0	0.9	6.56×10^{0}	2.182	1.12	131	0.3664
42	0.10	87.5	0.0	7.93×10^{0}	1.317	1.37	132	0.4800
43	0.10	87.5	0.5	7.93×10^{0}	1.317	1.37	132	0.4800
44	0.10	87.5	0.9	1.73×10^{1}	1.388	1.26	129	0.4479
45	0.03	87.0	0.0	6.45×10^{9}	1.003	105.	197	0.4800
46	0.04	87.0	0.0	1.30×10^{6}	1.057	9.19	177	0.4800
47	0.04	86.5	0.0	1.92×10^{8}	1.049	15.7	193	0.4800
101[4]	0.02	90.0	0.0	1.00×10^{11}	1.042	3.30	135	0.4716
109	0.03	90.0	0.0	1.09×10^{5}	1.088	2.11	135	0.4649
115	0.03	87.5	0.0	5.58×10^{6}	1.021	44.8	178	0.4800
118	0.04	90.0	0.0	6.71×10^{2}	1.114	1.81	135	0.4626
120	0.04	90.0	0.9	8.93×10^{2}	1.115	1.76	135	0.4607
136	0.10	90.0	0.0	1.01×10^{0}	1.807	1.19	153	0.4606
139	0.10	89.0	0.0	1.23×10^{0}	1.699	1.20	153	0.4628

[1] Determined so that $D_{max} = 48\%$.
[2] Factor opacity must be multiplied by to give $D_{max} = 50\%$.
[3] Number of days after first contact when $D \geq 46\%$ for the first time.
[4] Models with # > 100 assume $\sigma \propto r^{-2}$, other models assume $\sigma = const.$

Table D.2: Results of disk simulations (continued).

Our principal conclusion based upon the results presented in Tables D.1 and D.2 and Figures D.6 and D.7 is that the particles providing the bulk of the opacity in the ϵ Aurigæ secondary are much larger than typical interstellar grains (0.01 – 0.1 μm) and are thus probably the result of a process of solid accretion. Observations of the eclipse imply that the fractional difference in depth from $\sim$ 1.25 μm to 4.8 μm is $< 2\%$ (Backman 1985). For an interstellar extinction law, $\kappa \propto \lambda^{-1.8}$ from 1 – 5 μm (Rieke and Lebovsky 1985; this appears to be a robust result, with far less variability than the

visible opacity, Whittet 1992). Thus, if the disk's opacity is produced by particles similar to interstellar grains, then the observed colorlessness of the eclipse in the near-IR would imply $\delta_c \leq 1.02$; we can only come close to reproducing this value for extremely high opacity disks with small scale heights (compare Figure D.6(c) with Figure D.7(e)). This would imply an extremely massive and cold disk as $K \sim 10^7 M_d/\mathrm{M}_\odot$. If $\geq 98\%$ of the opacity at 1.25 μm is produced by particles large enough to block radiation with $\lambda \approx$ 4.8 μm, then the opacity differential does not provide any constraints on K. However, if the fractional opacity at 1.25 μm provided by small particles is S, then $K(1.25\ \mu\mathrm{m})/K(4.8\ \mu\mathrm{m}) \approx 1/(1-S)$. For plausible particle size distributions, the observed eclipse colorlessness still constrains K from being too small. Thus, unless $K(20\ \mu\mathrm{m}) \ll K(4.8\ \mu\mathrm{m})$, the principal cause of the decrease in eclipse depth from 4.8 μm to 20 μm cannot be increased transparency of the secondary. This reinforces our confidence in temperature estimates of the secondary derived using infrared colors.

If K is small, then the sides of the disk, viewed edge-on, are as much as 10% more effective in blocking light then the center due to a longer path length in the thicker outer portion of the disk. Such a disk produces an eclipse light curve with two minima after 2^{nd} and before 3^{rd} contact, and a local maximum at mid-eclipse. Substantial mid-eclipse brightening occurs in our synthetic eclipses *only* if the opacity parameter is small, whereas dense disks appear sharp-edged, producing flat-bottomed light curves. Mid-eclipse brightening has arguably been observed in each of the last three eclipses (e.g., Carroll et al. 1991 and references therein). However, the eclipse depth cannot be

precisely measured over periods of less than a few months due to irregular light variations on this time scale, probably caused by pulsations of the primary (Burki 1978, Ferro 1985, Donahue et al. 1985, Carroll et al. 1991). In addition, the apparent mid-eclipse brightening occurs on a time scale more analogous to that of the observed stellar variations than to the gradual change seen in our synthetic profiles. For the cases of low opacity and significant mid-eclipse brightening, color constraints imply that the disk's opacity must be provided almost entirely by particles larger than ~ 5 μm.

A 1° disk tilt ($i = 89^\circ$) has little effect on the eclipse profile, although the slight central brightening seen in edge-on disks at moderate to high opacity is eliminated (compare, e.g., models 18 and 21 in Table D.1). Greater tilt implies that a disk with given physical parameters covers a larger solid angle in the sky plane. Thus, a slightly tilted ($i \geq 89^\circ$) thin ($h_o/R_d \leq 0.04$) disk can produce the observed eclipse depth with a lower opacity parameter than an edge-on disk with the same scale height. However, in the cases where the disk is more significantly tilted and/or thinner, a substantial amount of the disk material does not block the primary, so a larger opacity parameter is needed. We did not even compute eclipse profiles for $i = 87.5^\circ$ and $h_o/R_d \leq 0.025$ because the required values of K are too large. The marginal case of $i = 87.5^\circ$, $h_o/R_d = 0.03$ produces a nearly colorless eclipse because of the sharp cutoff in the optical depth of the projected disk. While a significantly tilted disk with high opacity could produce the observed colorlessness (model #47), it would also produce a very rounded eclipse bottom (Figure D.6(b)) and thus is ruled out by observation. Therefore, we conclude that $i \geq 87^\circ$.

Our results are not sensitive to the radial dependence of the surface density (compare Figures D.6(c) and D.7(f)), unless the opacity parameter is very low (e.g., model 39 vs. model 139). Likewise, central holes, even as large as $0.9R_d$, have little influence on eclipse profiles except for low opacity disks, because the optical depth of the outer edge near the midplane remains high enough to block most of the light (Figure D.5(d)). Central holes might have more of an effect on the eclipse light curve if the disk is inclined because this could allow us to see directly through the clear central region (Wilson 1971, Eggleton and Pringle 1985, Kumar 1987, Ferluga (1990). A disk inclined to the system's orbital plane would result in a warp (Kumar 1987) that would make seeing through the central hole difficult if the particles providing the opacity are coupled to the (presumed) gaseous component of the disk.

The models presented above do not depend directly on the size and scale of the ϵ Aurigæ system. However, the ratio of the scale height of the disk to its radius as given by eq. (6) depends upon the mass of the secondary as well as the temperature of the outer portion of the disk. Our best matches to observations, using parameters which we consider reasonable, are obtained for $h_o/R_d \approx 0.03$ (Figure D.4(c) and D.6(c)). Thus, using the temperature of the disk's outer edge measured during the 1982 – 1984 eclipse by Backman et al. (1984), our results appear to be more consistent with the high-mass model ($M_2 \approx 15$ M$_\odot$) than with the low-mass model ($M_2 \leq 5$ M$_\odot$); however, because of various modeling and observational uncertainties involved, we do not view this result as definitive.

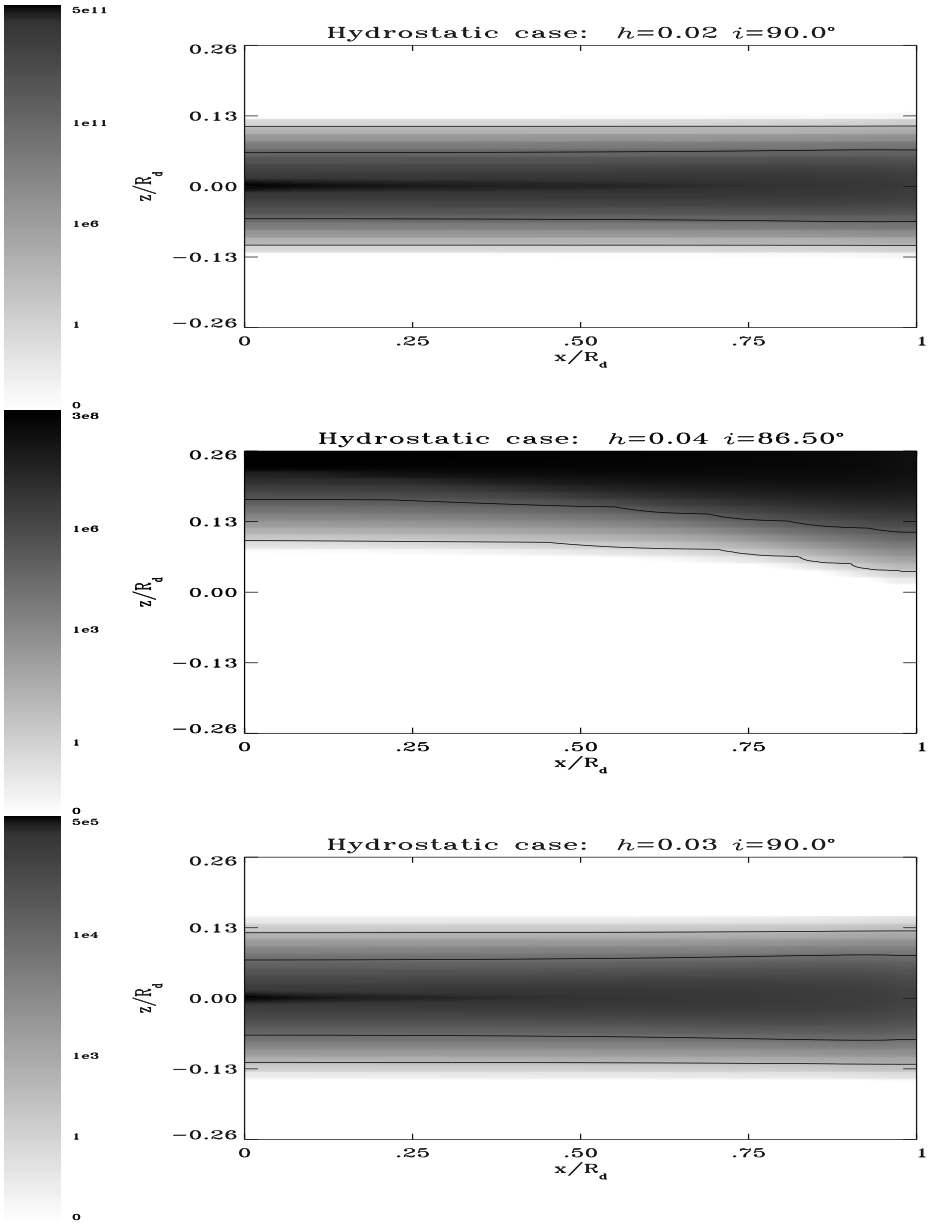

Figure D.4: Optical depth profile for the disk in the sky plane. Only half of the disk is shown, as the disk is symmetric about the z axis in our hydrostatic model. Density is scaled logarithmically. The surface density of the disk (perpendicular to its midplane) is assumed to be constant unless otherwise stated. All models have been normalized to give a mid-eclipse depth of 48%. Note that the scale for the optical depth is logarithmic and differs from frame to frame. (a) The very high opacity case viewed from within the plane of the disk (corresponding to model #1 in Table D.1). (b) Model #47, a high opacity case with a 3.5° tilt of the disk relative to the viewing plane ($i = 86.5°$). (c) A moderately high opacity disk viewed from the disk's midplane (model #9).

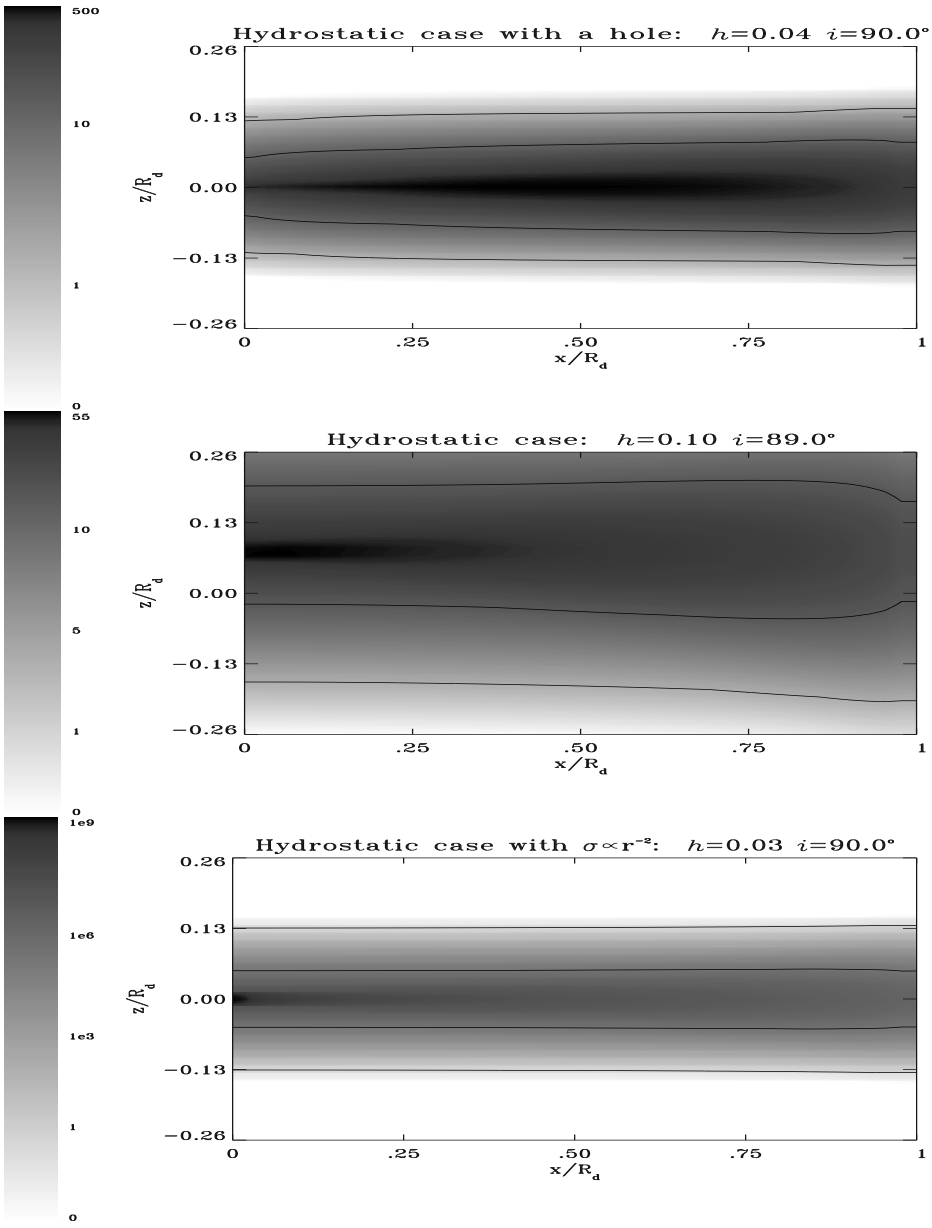

Figure D.5: More optical depth profile for the disk in the sky plane. (d) A medium opacity case with a central hole of radius 0.9 R_d viewed from the plane of the disk (model #20). (e) Low opacity case viewed at $i = 89°$ (model #39). (f) A disk with surface mass density $\sigma \propto r^{-2}$, viewed from the plane of the disk (model #109).

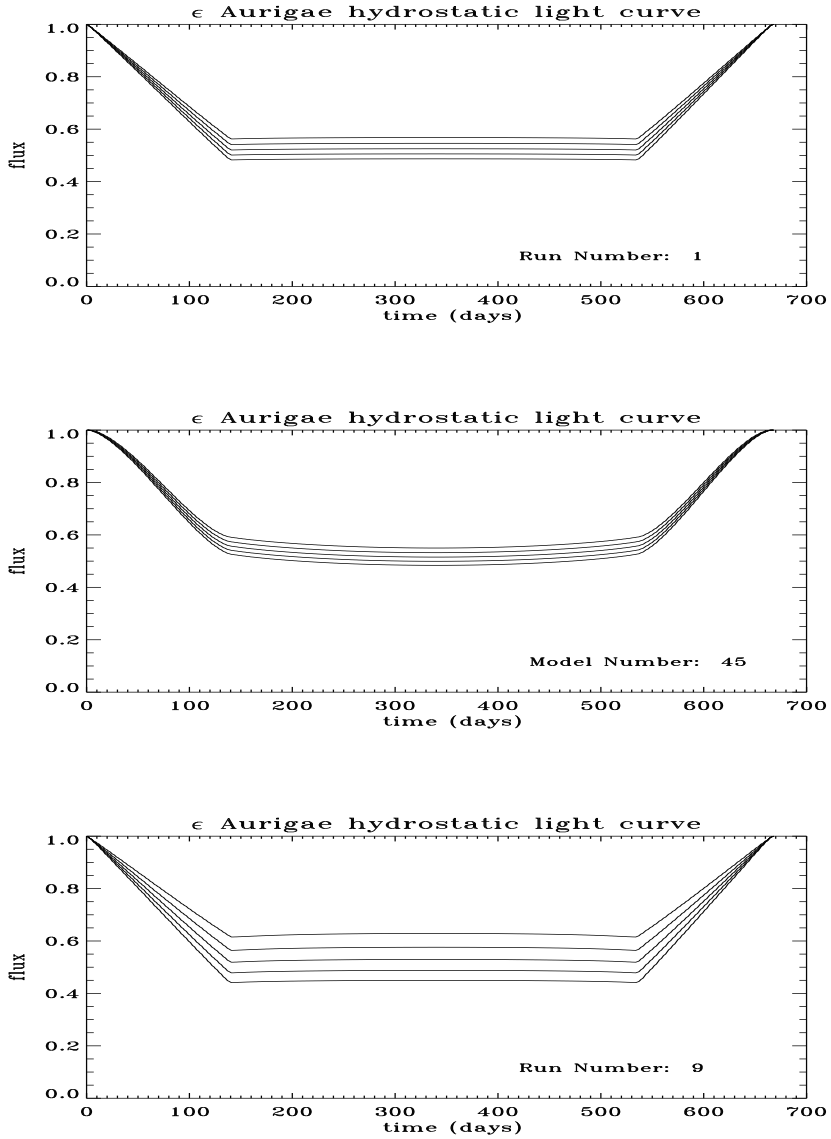

Figure D.6: These panels show synthetic light curves produced by the disk models shown in Figure D.4 passing in front of the primary. In each plot, the bold line indicates the profile obtained using an opacity parameter K ($\equiv \kappa\sigma R_d/h_o$) which has been adjusted to give the eclipse a maximum depth of 48%. The other lines indicate eclipse profiles obtained when the opacity has been increased or decreased by factors of 10 and 100 from this reference value. The differences among these curves can be used to relate the (presently unknown) particle extinction spectrum to observable small color changes or limits to changes during eclipses.

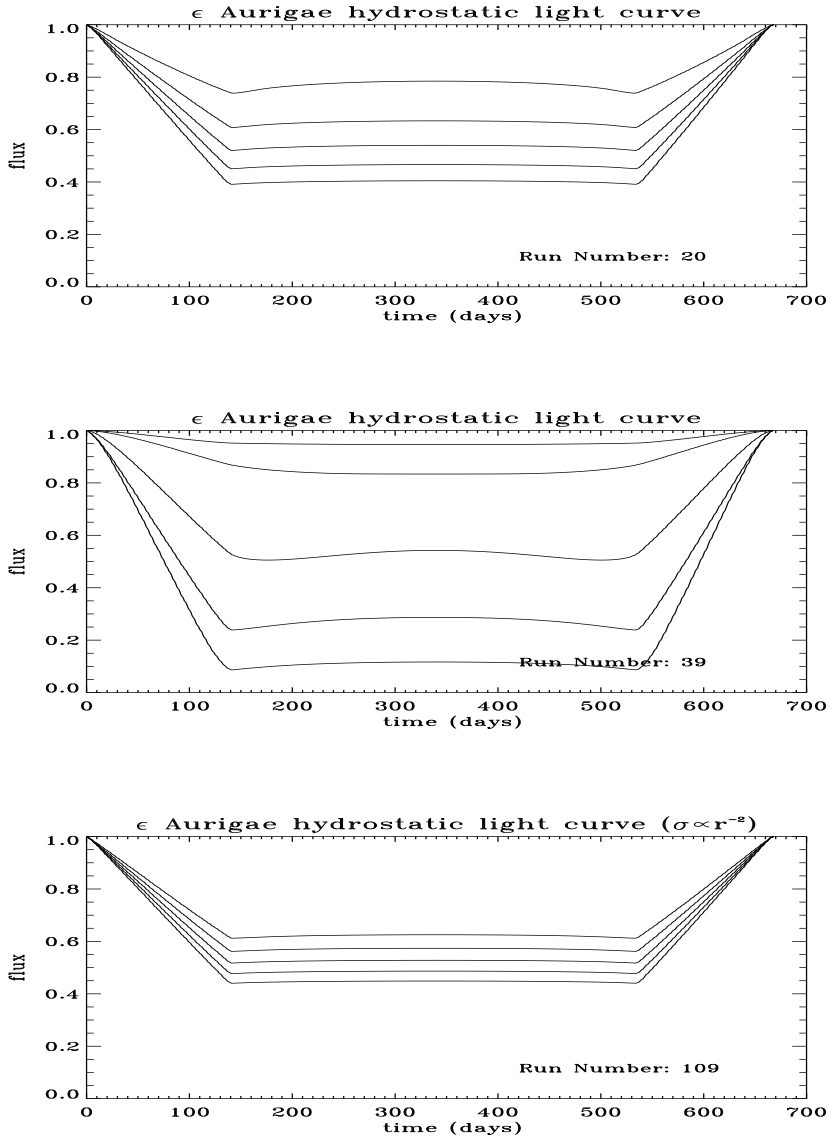

Figure D.7: These panels as similar to the previous figure. They show synthetic light curves produced by the disk models shown in Figure D.5 passing in front of the primary.

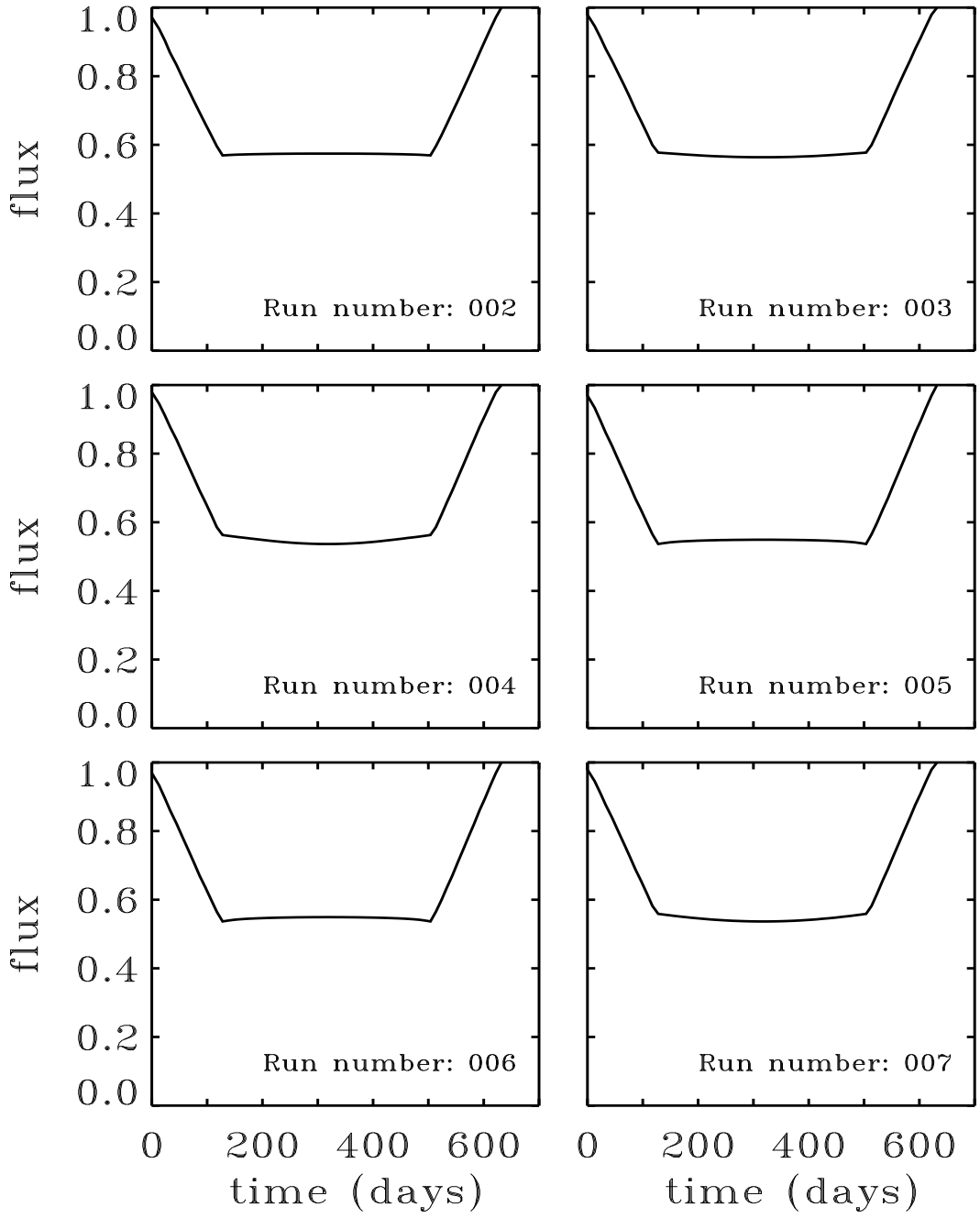

Figure D.8: These panels show synthetic light curves produced by many of the disk models shown given in Tables D.1 and D.2 and not shown in the previous 2 figures.

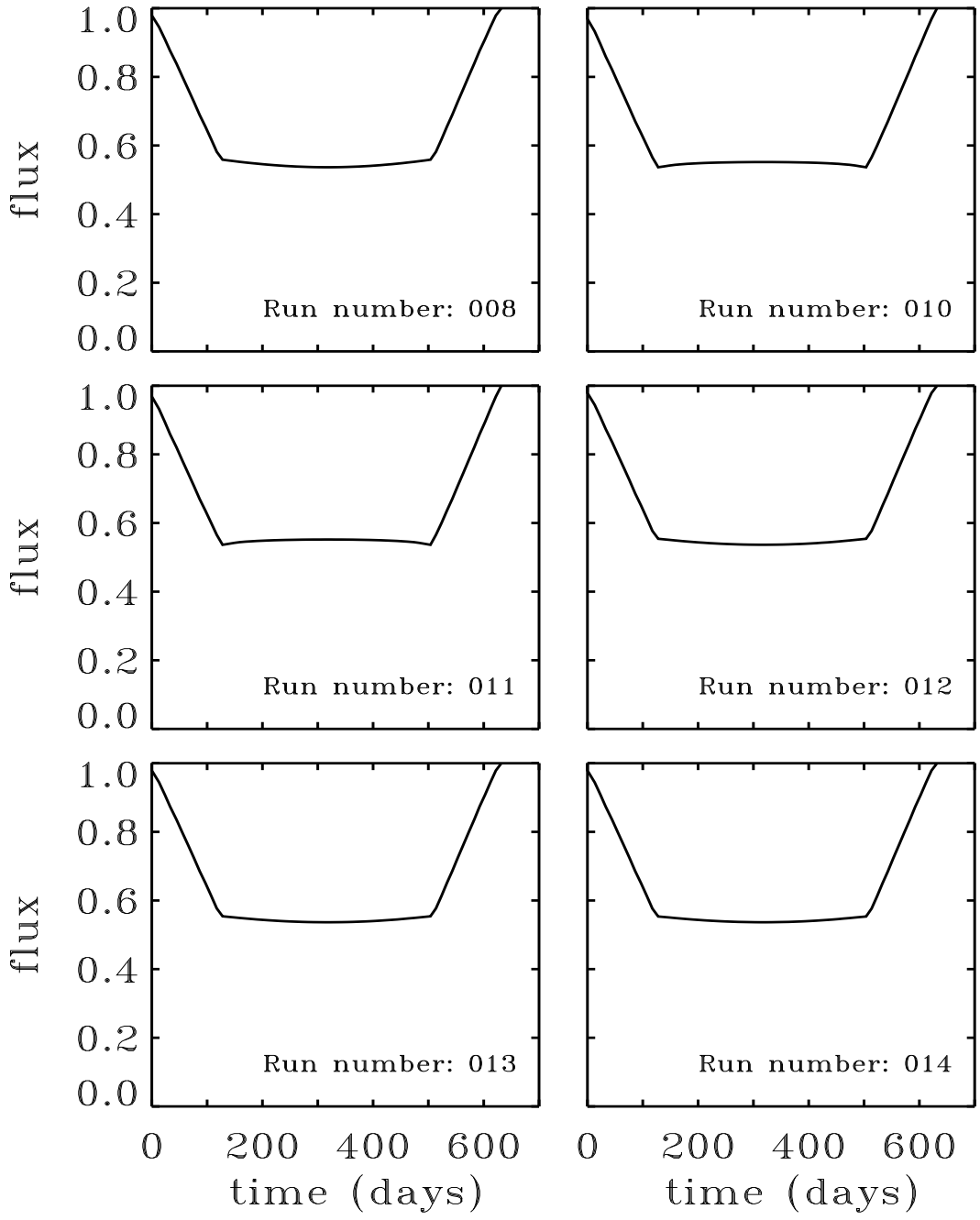

Figure D.9: Continuation of previous figure.

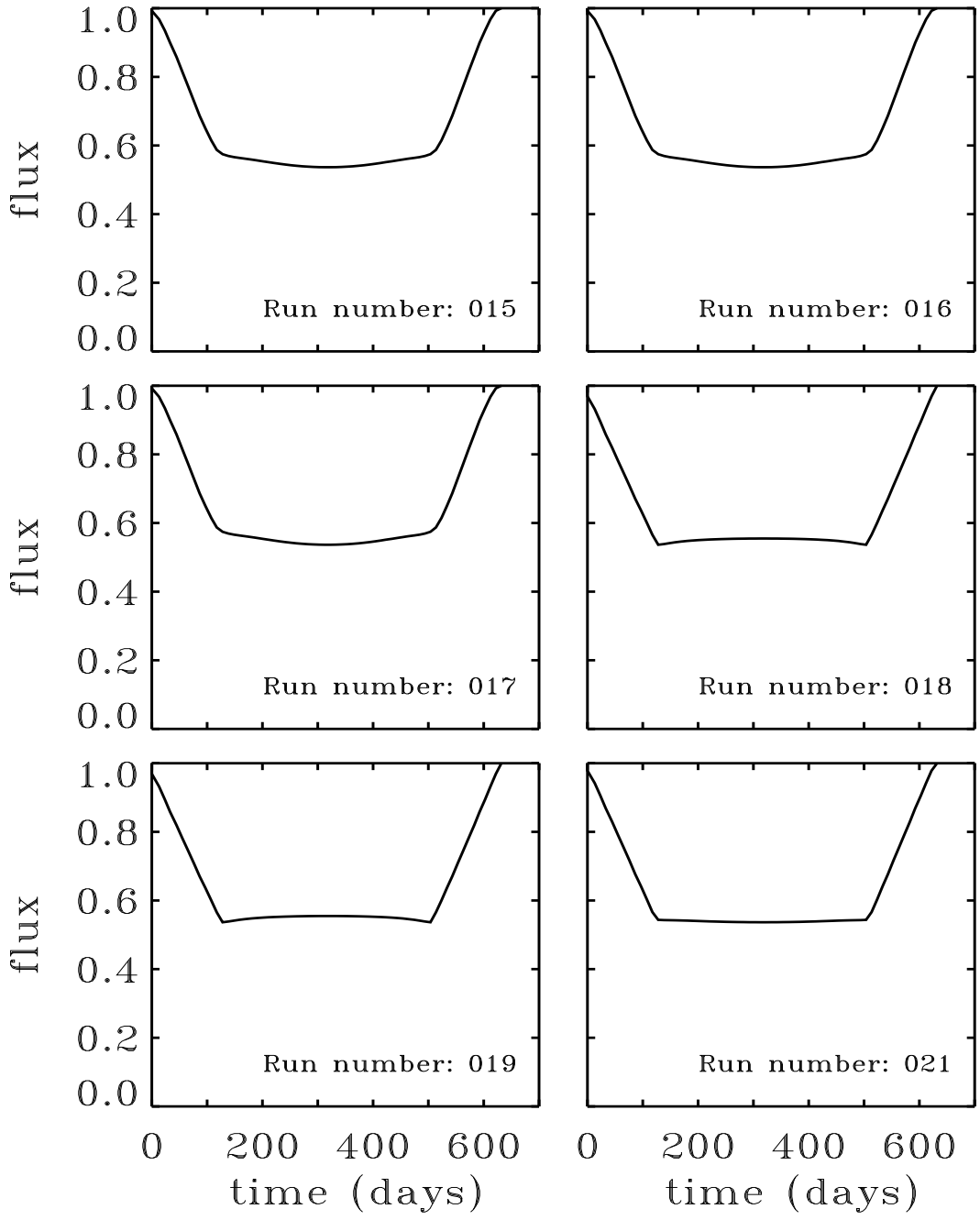

Figure D.10: Continuation of previous figure.

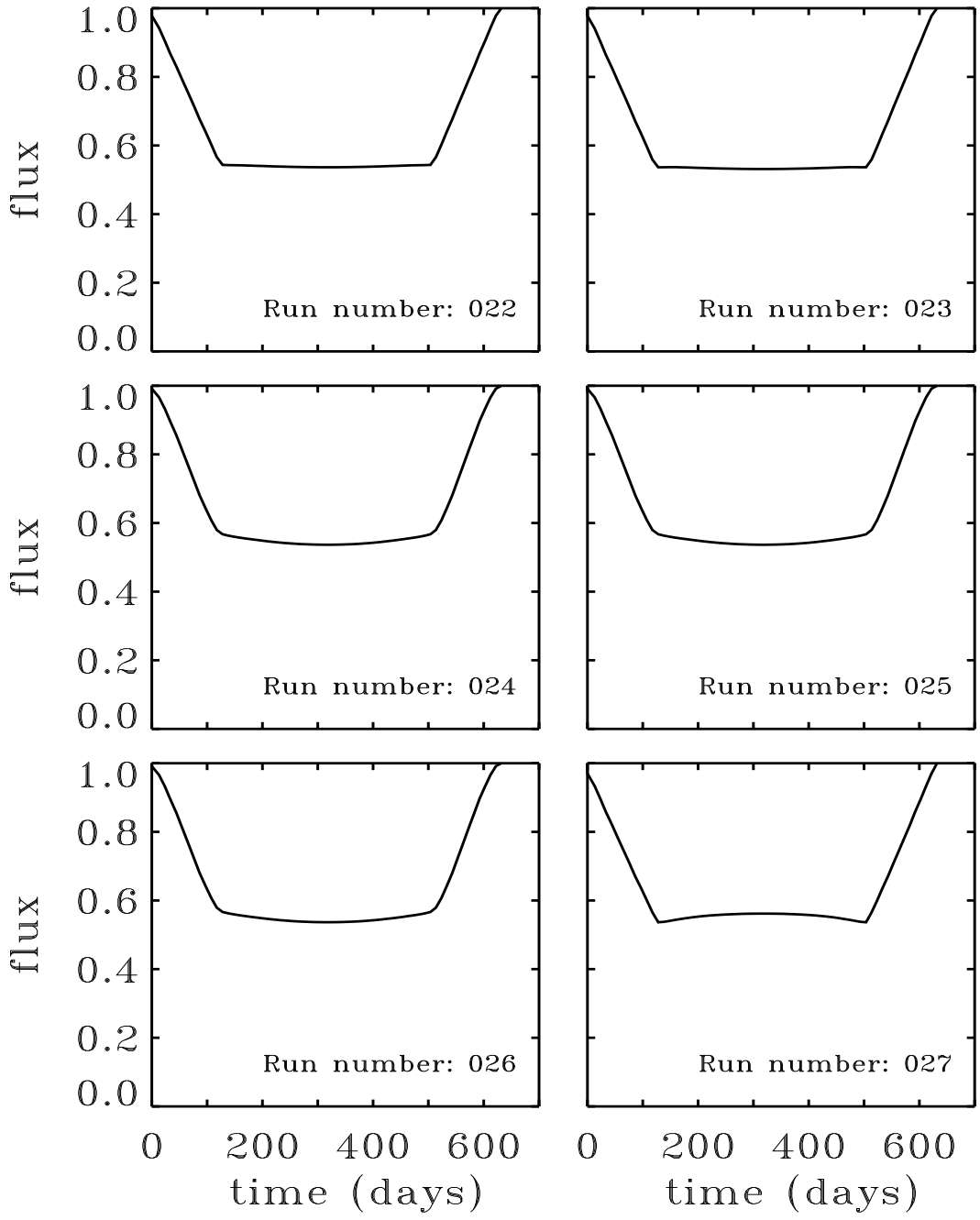

Figure D.11: Continuation of previous figure.

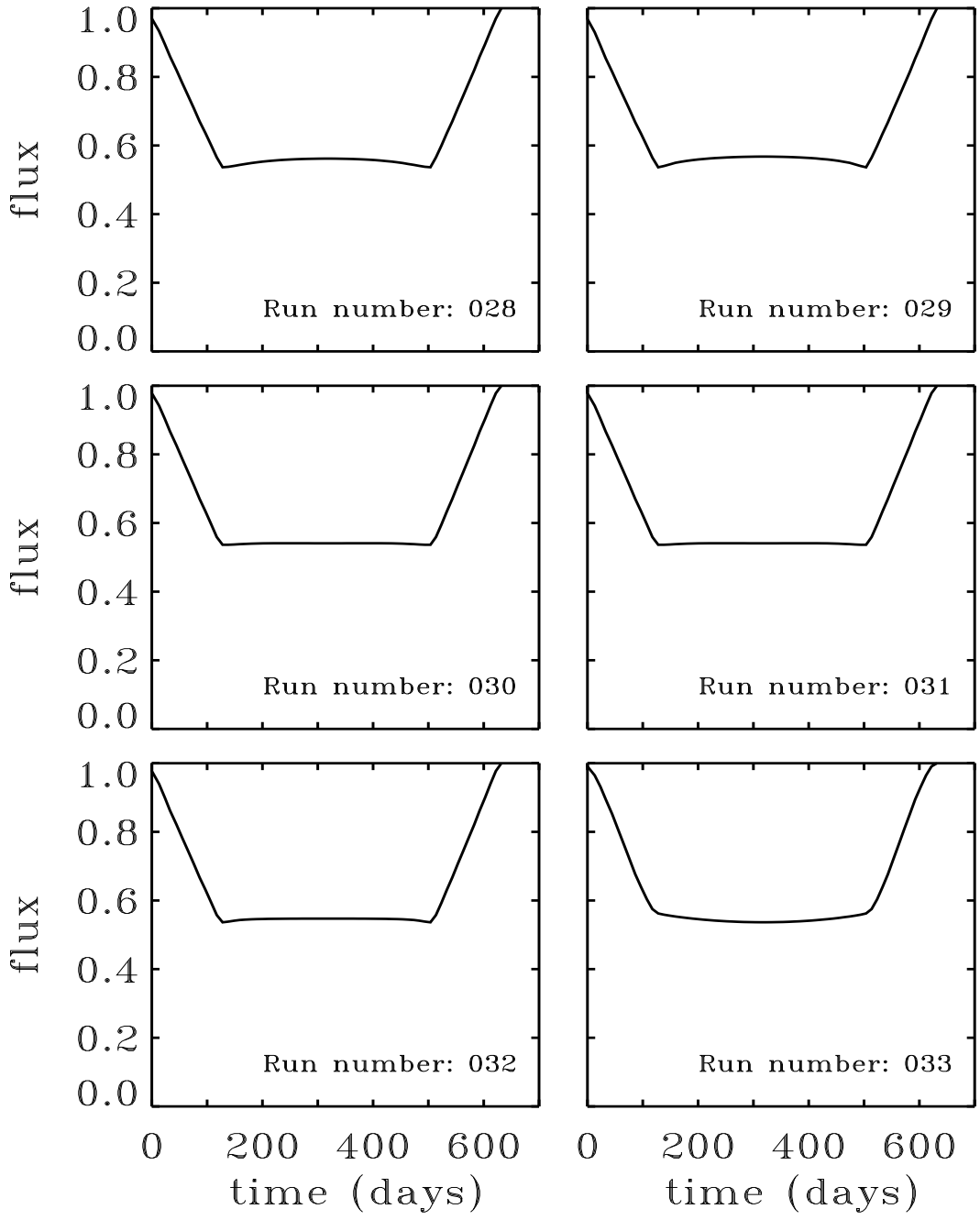

Figure D.12: Continuation of previous figure.

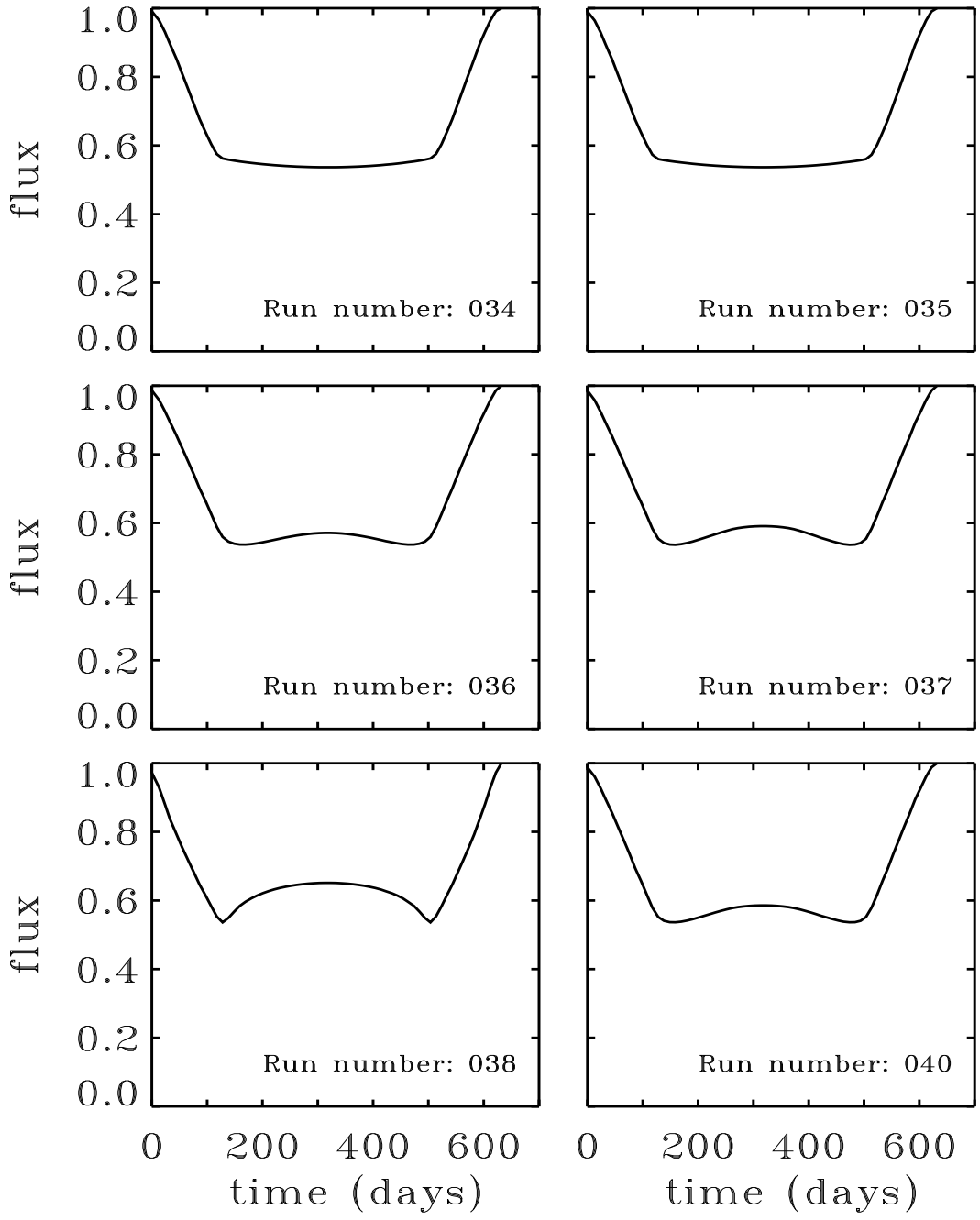

Figure D.13: Continuation of previous figure.

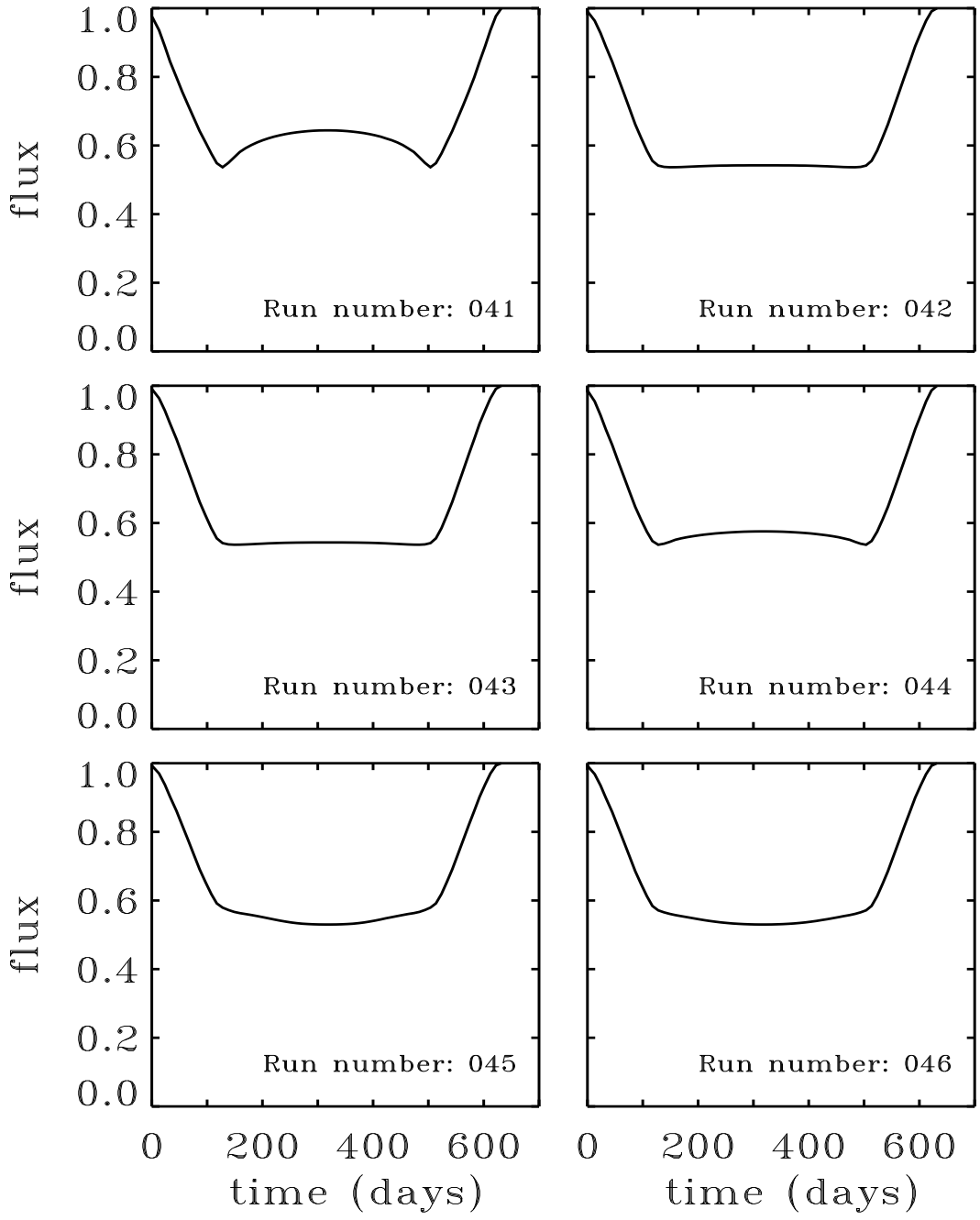

Figure D.14: Continuation of previous figure.

D.5 Disk Expansion and Absorption Line Profiles

In this section, we attempt to account for the observed asymmetry in absorption line profiles by using a crude model of the thermal expansion of the outer edge of the disk as it rotates into the radiation field of the primary. The preceeding analysis can be extended to model the temporal variations in the observed absorption line profiles. Ignoring scattering and the emission from the secondary, the fractional depth of an absorption line is equal to

$$\frac{\int\int e^{-\tau}(1-e^{-\tau_A})dxdz,}{\int\int e^{-\tau}dxdz} \tag{10}$$

where τ is the continuum optical depth, τ_A is the optical depth of the absorbing species and the integral is taken over the disk of the primary. For a homogeneous disk, $\tau_A \propto \tau$, assuming that the line is not saturated. Synthetic profiles can be computed from the above equations for a given constant of proportionality. However, for an azimuthally symmetric disk these computed line strengths will be symmetric about the eclipse center, apart from slight differences resulting from the eccentricity of the orbit.

Hinkle and Simon (1987) proposed that the asymmetries in the pre- and post-central eclipse line profiles are a consequence of the vaporization of grains caused by heating from the primary. Infrared observations of the system at quadrature indicate that the primary heats the side of the disk facing it to an equilibrium temperature of $\sim$ 1000 K (Backman et al. 1996). This value

is much hotter than the $\sim$ 500 K temperature observed on the back side of the disk during eclipse (Backman et al. 1984, Backman and Gillett 1985). At these high "daytime" temperatures, some grain destruction should occur. The velocities of the lines imply the disk rotates in a prograde direction (Lambert and Sawyer 1986), so the "late night/morning" regions block the primary during ingress, and the "afternoon/evening" regions are in front of the primary during egress (Figure D.2).

Hinkle and Simon's conjecture thus explains the observations in a qualitatively correct manner; however, we believe that it is quantitatively inadequate for the following reasons. First, although the temperature range is large, it does not include the condensation temperatures of the most cosmically abundant grain constituents; ices condense at well below 500 K, whereas most silicates remain in grain form up to at least 1200 K (Lewis 1974). Second, the orbital period at the outer edge of the secondary is given by (cf. eq. 2):

$$P_{disk} = 1.9(1 + e\cos\omega)^{3/2}\left(\frac{M_2}{f}\right)^{1/4}\text{yr}. \qquad (11)$$

The length of a "day" with respect to the primary is slightly longer, because the disk rotates in a prograde direction. Evaporation times of small grains are so short that exposed grains of intermediate volatility are rapidly destroyed in the "early morning". Finally, this model does not explain the persistence of absorption profiles well past 4th contact (Lambert and Sawyer 1986).

We agree with Hinkle and Simon (1987) that heating by the primary probably produced the temporal asymmetry in the absorption lines, but we believe that the mechanism is thermal expansion of the disk rather than grain

destruction. Pressure is proportional to the temperature, and thus rises rapidly in the region of the disk's edge rotating into view of the primary. This increases the RHS of equation (4) (for $z > 0$) and must be balanced by an acceleration of the gas in the vertical direction. (The second term of the LHS of eq. (4) is quadratic in v_z, and as $v_z \approx 0$ at "dawn", this term is small in the "early morning".) The disk's edge thickens until a pressure balance is restored, at which time the scale height has expanded by a factor of $\sim (1000/500)^{1/2} \sim 1.4$. The time required to restore a balance can be crudely estimated using dimensional arguments. Eventual thickening is of order unity, thus

$$\Delta z \sim v_z \Delta t \sim z. \tag{12}$$

Prior to "dawn", both terms on the LHS of eq. (4) are ≈ 0, assuming the disk has had time to settle into a static "night" equilibrium. Therefore, the terms of the RHS must be approximately equal in magnitude just before "dawn". During the "early morning", the first term on the RHS of eq. (4) increases by a factor of ≈ 2. Thus, ignoring the quadratic term on the LHS,

$$\frac{\partial v_z}{\partial t} \approx -\frac{1}{\rho}\frac{\partial p}{\partial z} - z\Omega^2 \sim z\Omega^2, \tag{13}$$

$$\Delta z \sim z\Omega^2 (\Delta t)^2. \tag{14}$$

The scalings (12 and 14) can be combined to give

$$\Delta t \sim 1/\Omega. \tag{15}$$

(The second term of the LHS of eq. (4) grows from zero to the order of the first term during the "morning" expansion and therefore has only an effect of order unity, i.e., it does not alter the above dimensional arguments.) Disk thickening thus can occur on the required timescale. The disk does not expand immediately at "dawn", but it thickens by a factor of ~ 1.4 by "mid-afternoon". Contraction at "night" occurs on the same timescale. This follows immediately from a sign change in the above scalings, or directly from the realization that when pressure support is removed, gas molecules and dust travel on free-fall orbits, which must intersect the disk midplane exactly twice each orbit and thus require 1/4 orbit from peak to node.

A full treatment of the thermal expansion of the disk would be very complicated, involving 3-D numerical hydrodynamics and radiative transfer. An analysis of disk expansion requires solution of the three components of the momentum equation and the continuity equation, plus computation of temperature using radiative transfer models. These models require input of an optical depth scale consistent with the dynamics. Such a system of coupled nonlinear partial differential equations in three dimensions is prohibitively difficult to solve, even numerically. The uncertainties in many of the required input parameters and the paucity of the observational constraints would make any quantitative results of questionable value. We thus restrict our numerical simulations to the following simple model based on the qualitative arguments presented above: (1) The thickness of the outer edge of the disk is increased as this portion of the disk is exposed to stellar radiation during the "day"; (2) At "night" it cools and contracts. Specifically, we define the outer portion of

the disk to be material in the outer 0.1% of the disk radius. We have linearly increased the scale height of the outermost portion of the disk from its nominal value used in Sections D.3 and D.4 at "6 a.m." to 1.4 times that value at "3 p.m." (cf. the discussion prior to eq. 12). Then we linearly decrease the value with the same slope until the quiescent "night" value is reached at "midnight." As our hydrodynamic simulation is quite sensitive to variations in a thin outer layer of the disk, we increased the resolution of the grid in the x and y directions by a factor of ten.

In order to estimate the depths of the absorption lines, we must include in our models the ratio of line opacity to that in the neighboring continuum. The persistence of the lines after the end of the continuum eclipse implies that this ratio is at least of order unity, and possibly much greater. This contrasts to the situation in the ISM, where the continuum dust opacity is the larger. The difference is not surprising, as metals are highly depleted in the gaseous phase in the cold ISM environment, and are thus are probably substantially more abundant in the much warmer gas of the ϵ Aurigæ disk. Moreover, the larger grain sizes in the ϵ Aurigæ secondary (Section D.4) imply a smaller continuum opacity than in the ISM. For illustrative purposes, we consider that lower-abundance metal lines might be several orders of magnitude weaker than Hα which would have a line-center opacity about 10^9 times that in the neighboring continuum for a Doppler width corresponding to 1000 K and ISM-like composition. The larger grain sizes in ϵ Aurigæ relative to the ISM would also make the continuum opacity weaker. We consider line opacities per mass 10^2, 10^4 and 10^6 times as large as that of the continuum.

Figures D.15, D.16, D.17 and D.18 illustrate the results of adding thermal expansion to one of our disk models. The observed gross temporal asymmetry of the line strength about the midpoint of the eclipse (Lambert and Sawyer 1986, Hinkle and Simon 1987) is readily reproduced. The persistence of the absorption signatures after 4^{th} contact could be accounted for in a qualitative manner by allowing the optically thin outer edge of the disk to also expand in the horizontal direction as a result of heating by the primary; however, the observation of TiII for an entire year after fourth contact (Lambert and Sawyer 1986) exceeds the duration that would result from an expansion in the horizontal direction comparable in size to the vertical scale height of the disk. An optically thin (in the continuum) annulus exterior to the optically thick disk which expands in the daytime and contracts at night would help explain both the longevity of the absorption after fourth contact and the decrease in the absorption strength observed just following second contact. An alternative explanation for this latter feature is gas vertically extended above the disk's outer edge.

D.6 Summary

The principal characteristics of the eclipsing ϵ Aurigæ star system can be reproduced by assuming that the optically unseen secondary is a disk of gas and dust which is in centrifugal balance in the radial direction and is hydrostatically supported perpendicular to its midplane. Several of the basic characteristics including ingress time, egress time, and the general flat shape

of the minimum are well accounted for. The geometry of the eclipse implies that the disk midplane is tilted by $< 3°$ from the line of sight.

The wavelength-independence of the observed eclipse depth in the visual and near-IR provides important constraints on the properties of the disk. This colorlessness implies that the particles responsible for the bulk of the opacity of the disk are $\geq$ 5 μm in radius. If, in contrast, an ISM particle distribution were assumed, the eclipse would be much deeper in the blue than in the red and the near-IR. This conclusion is stronger and more quantitative than that of Kopal (1971), who also noted that the grayness of the eclipse implies large particles. Unless particles of radius < 5 μm are almost totally absent from the secondary, the scale height at the outer edge of the disk must be quite small, $\leq$ 3% of the disk's radius. The low ratio of the scale height to the disk's radius lends some support to the high-mass model of the ϵ Aurigæ system.

Our analysis assumes that the gas and dusk in the disk are well mixed. If instead virtually all of the particles in the disk are settled into a significantly thinner dust zone, the secondary could present a sharp-edged profile that produces a colorless eclipse even with an ISM opacity law. However, even a small quantity of submicron-sized dust remaining well above the midplane would color the eclipse.

Our model can produce a significant mid-eclipse brightening only if the optical depth of the disk is small. A central hole can increase the magnitude of this mid-eclipse brightening. However, the duration of the model's mid-eclipse brightening is longer than that observed. In addition, a model disk optically thick enough to reproduce the mid-eclipse brightening in single-color

data would only produce a "gray" eclipse if virtually all the particles in the disk are much larger than 5 μm in radius.

Absorption lines seen during and immediately after the F star eclipse are probably produced by a thin layer of gas in the outer portion of the disk companion secondary which expands when it is heated by radiation from the F star and contracts when it is shielded.

The above analysis demonstrates that the ϵ Aurigæ disk is well-modeled by a gas/dust disk with a scale height at its outer edge that is $\sim 3\%$ of the disk's radius. Such a disk contains particles characteristically much larger than interstellar dust. Our results will provide more valuable information on the process of planet formation when *HIPPARCOS* parallax measurements become available. Once the distance to the system is known, the mass and evolutionary state of the primary will be better understood (Webbink 1985). The masses of the components and the geometry of the ϵ Aurigæ system will then provide a lower bound on the maximum size of a (quasi-) stable circumstellar disk within a binary system of known dimensions. If the system turns out to be young (Carroll et al. 1991), then the disk properties that we have derived become directly applicable to models of protoplanetary disks. If the ϵ Aurigæ disk was produced by recent ($< 10^4$ years) mass transfer (Eggleton and Pringle 1985), then the lack of small grains would imply that rapid grain growth can occur within circumstellar disks and pre-planetary processes may also occur in this context.

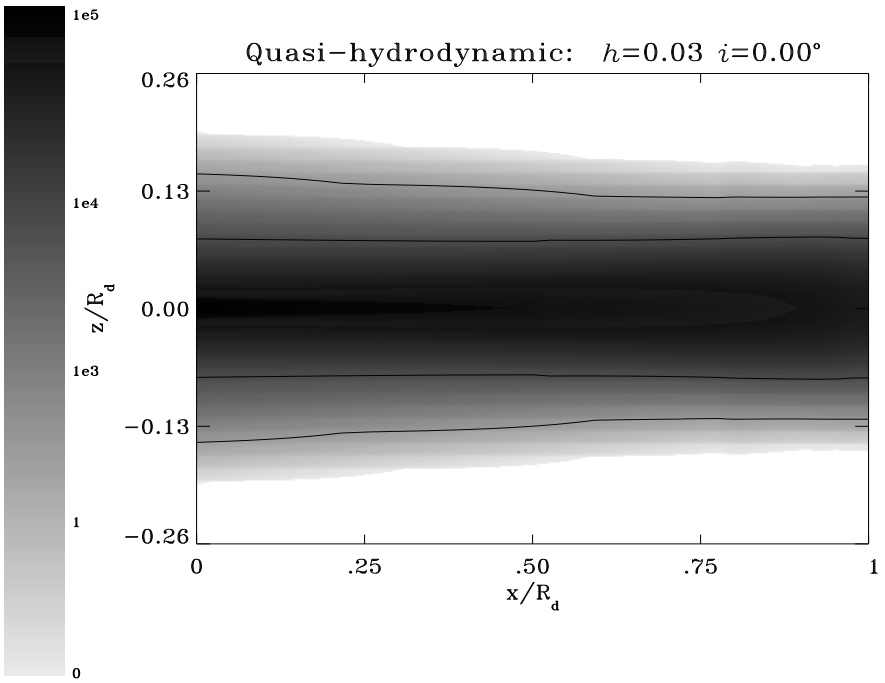

Figure D.15: Optical depth profile of the leading half of the disk in the sky plane for a quasi-hydrodynamic model of the ϵ Aurigæ secondary with thermal expansion of the outer layer of the disk facing the primary star. The "pre-dawn" hydrostatic structure was assumed to be identical to that given in Figure D.4. The scale height of the outermost 0.1% of the disk expanded linearly in time by a factor of 1.4 between "6 a.m." and "3 p.m." and then contracted linearly until "midnight." Note that this optical depth profile is very similar to that of the hydrostatic disk shown in Figure D.4(c), with the principal difference evident near the disk's leading edge at high $|z|$.

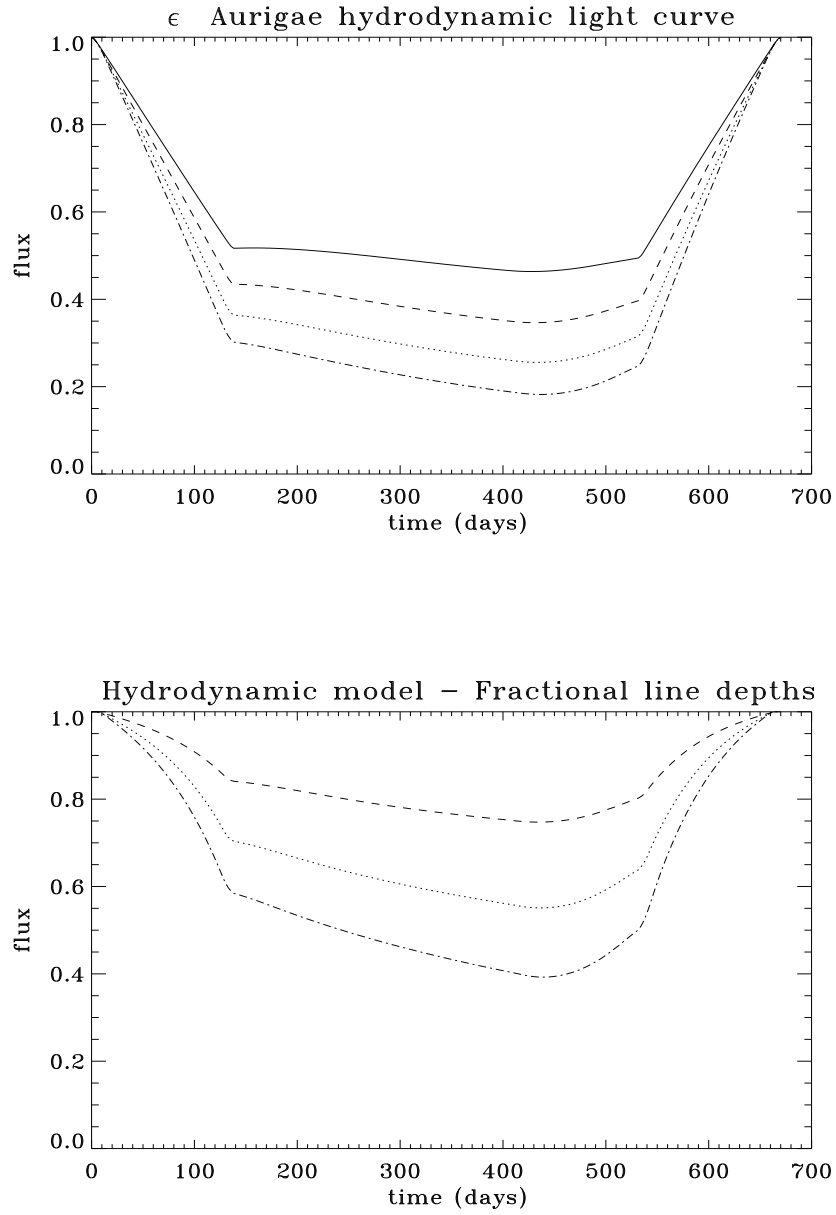

Figure D.16: Lightcurves produced by the occultation of the primary by the disk shown in Figure D.15. (a) The solid curve represents the fraction of the primary's continuum light observable. The dashed curve gives the fraction of light from an absorption line whose opacity is 100 times as large as the continuum opacity, the dotted curve and the dot-dashed curve show the light in lines whose opacities are 10^4 and 10^6 as large as the continuum opacity respectively. (b) Fractional line depths as a function of time corresponding to the same conditions as part (a).

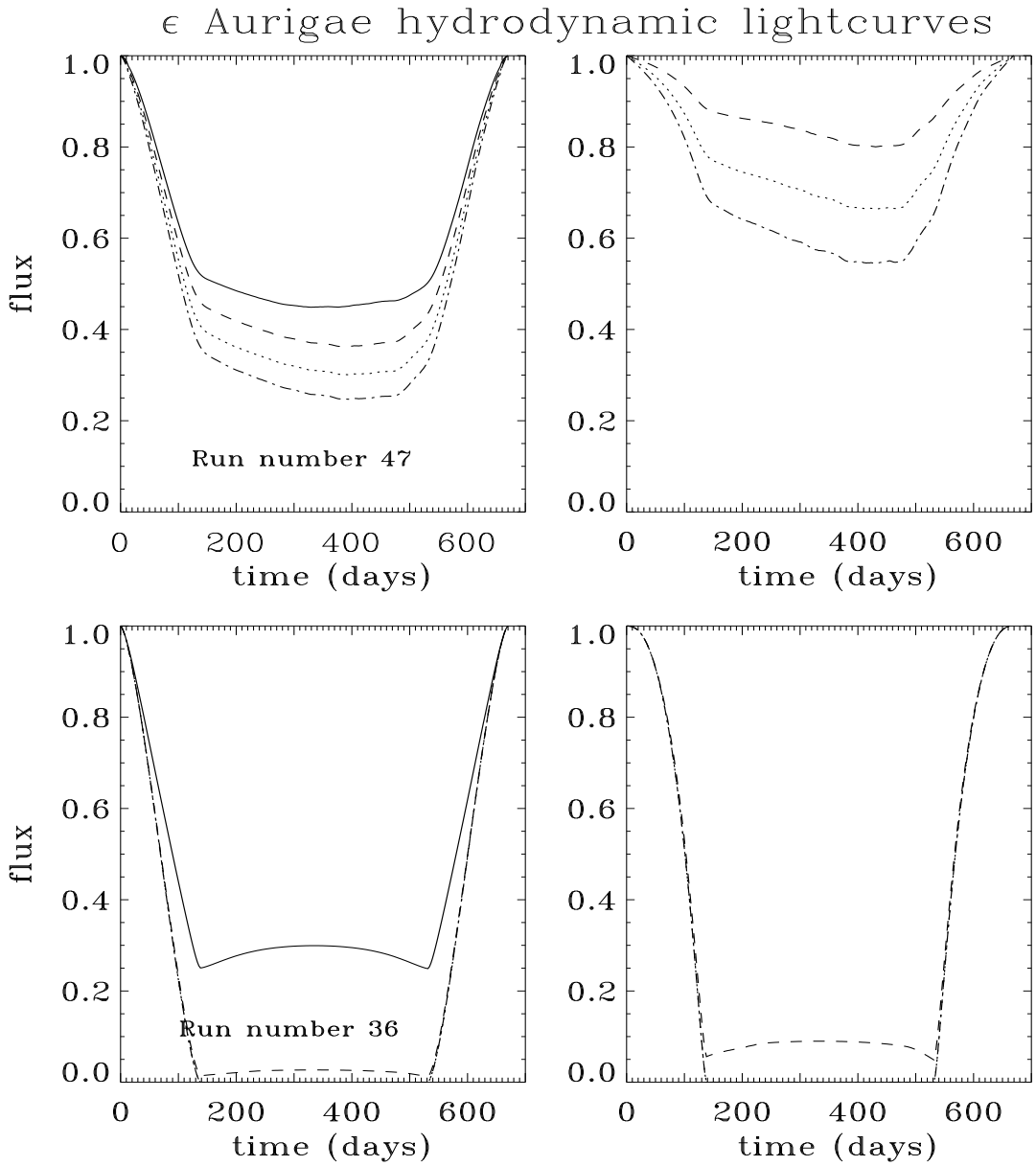

Figure D.17: Lightcurves similar to those shown in Figure D.16. The initial conditions were modified to correspond with run numbers 47 and 36 as given in Tables D.1 and D.2. Lightcurves on the right hand side show the fraction of the primary's continuum light observable from absorption lines of the same strength as those in the top half of Figure D.16. Curves on the left hand side are the fractional line depths corresponding to the same conditions as the right hand side.

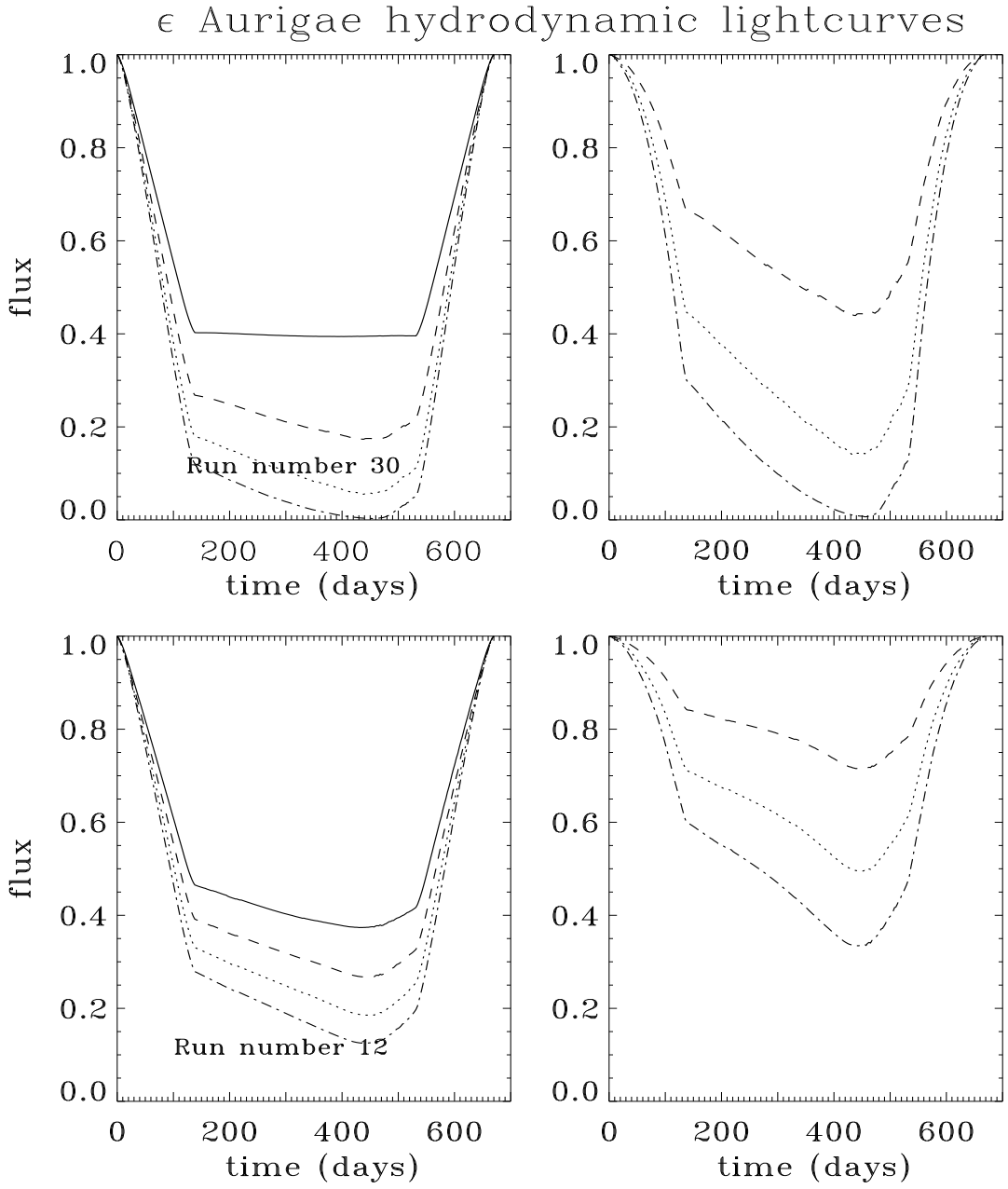

Figure D.18: Same as previous figure. In these cases, the initial conditions are taken from run numbers 30 (top) and 12 (bottom).

References

Adams, N.R. 1995, M.S. Thesis, SUNY at Stony Brook

Adams, N.R., Wolk, S.J.& Walter, F.M. 1996 in preparation

Alexander, D.R., Augason, G.C. & Johnson, H.R. 1989, ApJ, 345 1014.

Allen, C. W 1973. *Astrophysical Quantities* (London: Athlone Press).

Attridge, J. & Herbst, W. 1992, ApJ, 398, L61.

Backman, D.E. 1985, in 1982-84 Eclipse of Epsilon Aurigæ, NASA Conf. Publ. 2384, ed. Stencel (NASA: Washington), 23.

Backman, D.E., Becklin, E.E., Cruikshank, D.P., Joyce, R.R., Simon, T., & Tokunaga, A., 1984, ApJ, 284, 799.

Backman, D.E., Das, S.R., Witteborn, F.C., Graps, A.L., & Lissauer, J.J., 1996 in preparation.

Backman, D.E., & Gillett, F.C., 1985, ApJ, 299, L99.

Barnes, S. & Sofia, S. 1996 ApJ, 462, 746.

Barnes, S. 1996 Private communication.

Barry, D.C. 1988, ApJ, 334, 436.

Basri, G. 1987, in *Cool Stars, Stellar Systems and the Sun – the Fifth Cambridge Workshop* J. Linsky and R Stencel eds. (New York: Springer–Verlag) 411.

Bertout, C., Basri, G. & Bouvier, J. 1988, ApJ, 330, 350.

Bessell, M.S. 1979, PASP, 91, 589.

Bessell, M.S. & Brett, J. M. 1988, PASP, 100, 1134.

Bessell, M.S. 1990, PASP 102, 1181.

Blaauw, A. 1964, ARAA, 2, 213.

Blaauw, A. 1991, in *The Physics of Star Formation and Early Stellar Evolution*, C.J. Lada & N. D. Kylafis eds. (Kluwer, Dordrecht) 125.

Bouvier, J. 1986, in *Advances in Space Research*, vol. 6, no. 8, p. 175.

Bouvier, J. & Bertout, C. 1989, A&A, 211, 99.

Bouvier J. 1990, in *Angular Momentum Evolution of Young Stars*, eds. S. Catalano and J. R. Stauffer, 41.

Bouvier, J., Cabrit, S., Fernadez, M., Martin, E. & Matthews, J. 1993, A&A, 272, 176.(COYOTES I)

Bouvier, J., Covino, E., Kovo, O., Martin, E.L., Matthews, J.M., Terranegra, L., & Beck, S.C. 1995, A&A, 299, 89. (COYOTES II)

Brown, A. 1996, *Stellar Content and evolution of OB Associations* (Amsterdam: Thesis Publishers).

Burki, G. 1978, A&A 65, 357.

Burrows, A. Hubbard, W.B. & Lunine, J.I 1989, ApJ, 345, 939.

Burrows, A. Hubbard, W.B., Saumon, D. & Lunine, J.I 1993 ApJ, 406, 158.

Canuto, V.M. & Mazzitelli, I. 1990, ApJ, 370, 295.

Carney, B.W. 1983, AJ, 88, 623.

Carroll S.M., Guinan, E.F., McCook G.P., & Donahue, R.A., 1991, ApJ, 367, 278.

Casali, M.M. & Hawarden, T.G. 1992, JCMT-UKIRT Newsletter, 3, 33.

Castelli, F. 1978, A&A 69, 23.

Chamberlain, J.W. & Hunten, D.M. 1987, Theory of Planetary Atmospheres (Academic Press: Orlando).

Choi, P.I. & Herbst, W. 1996, AJ, 111, 283.

Comeron, F., Rieke, G.H., Burrows, A. & Rieke, M.J. 1993, ApJ, 416, 185.

Cousins, A.W.J. 1980, S.Afr.Astron.Obs.Circ., 1, 234.

D'Antona, F. & Mazzitelli, I. 1994, ApJS 90, 467.

Deeming, T.J. 1975, A&SS, 36, 137.

Donahue, R.A., Guinan, E.F., & McCook, G.P. 1985, in 1982-84 Eclipse of Epsilon Aurigæ, NASA Conf. Publ. 2384, ed. R. Stencel (NASA: Washington), 77.

Dorren, J.D., Guedel, M. & Guinan, E.F. 1995, ApJ, 448, 431.

Duncan, D.K. 1981, ApJ, 248, 651.

Dworetsky, M.M. 1983, MNRAS, 203, 917.

Eaton, N.L., Herbst, W. & Hillenbrand, L.A., 1995, AJ, 110, 1735.

Edwards, S., Strom, S.E., Hartigan, P., Strom, K.M., Hillenbrand, L.A., Herbst, W., Attridge, J., Merrill, K.M., Probst, R. & Gatley, I. 1993, ApJ, 106, 372.

Eggleton, P.P., and Pringle, J.E., 1985, ApJ, 288, 275.

Elston, R. 1995, *Introduction to the CTIO Infrared Imager*.

Endal, A.S. & Sofia S. 1981, ApJ, 243 625.

Feigelson, E.D. & Decampli, W.M. 1981, ApJ, 243, L89.

Feigelson, E.D. & Kriss, G.A. 1981, ApJ, 248, L35.

Feigelson, E.D., Jackson, J.M., Mathieu, R.D., Myers, P.C. & Walter, F.M. 1987, AJ, 94, 1251.

Ferluga, S. 1990, A&A, 238, 270.

Ferro, A.A. 1985, MNRAS, 216, 571

Gahm, G. F. 1980, ApJ, 242, L163.

Gilliland, R.L. 1985, ApJ, 299, 286.

Goodman, A.A., Jones, T.J., Lada, E.A. & Myers, P.C. 1992, ApJ, 399, 108.

Goodman, A.A., Jones, T.J., Lada, E.A. & Myers, P.C. 1995, ApJ, 448, 748.

Grankin K.N. 1993 IBVS, No. 3823.

Grankin K.N. 1994 IBVS, No. 4042.

Hartmann, L., Hewett, R., Stahler, S. & Mathieu, R.D. 1986, ApJ, 309, 275.

Herbig, G. H. 1957, ApJ, 125, 612.

Herbig, G.H. 1978, in Problems of Physics and Evolution of the Universe, edited by L.V. Mirzoyan (Academy of Sciences of the Armenian SSR, Yervan), 171.

Herbig, G.H., & Bell, K.R. 1988, Third Catalog of Emission-Line Stars of the Orion Population, Lick Obs. Bull. No.1111.

Herbst, W., Herbst, D.K. & Grossman, E.J. 1994, AJ, 108, 1906.

Herbst, W., 1996, private communication.

Heyer, M.H., Vrba, F.J., Snell, R.L., Schloerb, F.P., Strom, S.E., Goldsmith, P.F. & Strom, K.M. 1987, ApJ, 321, 855.

Hinkle, K.H., & Simon, T. 1987, ApJ, 315, 296.

Holberg, J.B., Forrester, W.T., & Lissauer, J.J. 1982, Nature 297, 115.

Hopkins, J.L., 1995 private communication.

Horne, J.H. & Baliunas, S.L. 1986, ApJ, 302, 757.

Huang, S.S. 1965, ApJ, 141, 976.

Johnson, H.L. 1963, Basic Astronomical Data, edited by K. Aa. Strand, (Univ. of Chicago Press, Chicago), 204.

Jones, B.F. & Walker, M.F. 1988, PASP, 95, 1755.

Kraft, R.P. 1970. In *Spectroscopic Astrophysics*, G.H. Herbig ed. (Berkeley: U of California Press) 385.

Königl, A. 1991, ApJ, 370, L39.

Kopal, Z. 1971, ApSS 10, 332.

Ku, W.H.M. & Chanan, G.A. 1979, ApJ, 234, L59.

Kumar, S. 1987, MNRAS 225, 823.

Laird, J.B. 1985, ApJS, 57, 389.

Lambert, D.L. and Sawyer, S.R. 1986, PASP 98, 389.

Landolt, A.U. 1992, AJ, 104, 372.

Lane, A.L., Pomphrey, R.B., Morris, R.B., Hord, C.W., West, R.A., Esposito, L.W., Simmons, K.E., Coffeen, D. L. & Saitō, M. 1982, Science 215, 537.

Lang, K. R. 1992, *Astrophysical Data* (New York: Springer-Verlag).

Lasker, B.M., Sturch, C.R., Mclean, B.J., Russell, J.L., Jenkner, H. 1990, AJ, 99, 2019.

Lewis, J.S. 1974, Science 186, 440.

Li, J. & Collier-Cameron, A. 1993, MNRAS, 261 766.

Linsky, J. & Saar, S. 1987, In *Cool Stars, Stellar Systems and the Sun – the Fifth Cambridge Workshop* J. Linsky and R Stencel eds. (New York: Springer–Verlag) 44.

Lissauer, J.J., & Backman, D.E. 1984, ApJ, 286, L39.

Lomb, N.R, 1976, A&SS, 39, 447.

Lynden-Bell, D. & Pringle, J.E. 1972, MNRAS 168, 603.

Mayor, M. & Mermilliod, J.C. 1991, in *Angular Momentum Evoultion of Young Stars* S.Catalano and J.R. Stauffer eds. (Dordrecht: Kluwer) 143.

Miller, G.E. & Scalo, J.M. 1979, ApJS, 41 513.

Morris, S.C. 1962, JRASC 56, 210.

Mundt, R., Walter, F.M., Feigelson, E.D., Finkenzeller, U.,Herbig, G.H. & O'Dell, A.P. 1983, ApJ, 269, 229.

Neuhäeuser, R., Preibisch, T., Alcalá, J. M. & Schmitt, J.H.M.M. 1995, in Stellar Surface Structure Strassmeier, K.G. ed. (Wein: IAU) 197.

Noyes, R. W., Weiss, N.O. & Vaughan, A.H. 1984, Apj, 287, 769.

Preibisch, T., Neuhäeuser, R. & Alcalá, J. M. 1995, A&A, 304, 13.

Press, W.H., Teukolsky, S.A., Vetterling, W.T. & Flannery, B.P. 1992, *Numerical Recipes* (Cambridge: Cambridge University Press).

Prosser, C.F. 1992, AJ, 103, 488.

Prosser, C.F., Schild, R.E. Stauffer, J.R. & Jones, B.F. 1993a, PASP, 105, 269.

Prosser, C.F., Shetrone, M.D. Marilli,E., Catalano,S., Williams, S.D., Backman, D.E. Laaksonen, B.D., Adige, V., Marschall, L.A. & Stauffer, J.R. 1993b, PASP, 105, 1407.

Prosser, C.F., Shetrone, M.D, Dasgupta, A., Backman, D.E.,Laaksonen, B.D., Baker, S.W., Marschall, L.A., Whitney, B.A., Kuijken, K. & Stauffer, J.R. 1995, PASP, 107, 211.

Radick, R.R., Thompson, D.T., Lockwood, G.W., Duncan, D.K. & Baggett, W.E. 1987, ApJ, 321, 459.

Rieke, G.H., and Lebofsky, M.J., 1985, ApJ, 288, 618.

Rogers, F.J. & Iglesias, C.A. 1992, ApJS, 79, 507.

Rydgren, A.E. & Vrba, F.J. 1983, ApJ, 267, 191.

Saitō, M., Kawabata, S., Saijo, K., and Sato, H. 1987, PASJ 39, 135.

Scargle, J.D. 1982, ApJ, 263, 835.

Schaller, G., Schaerer, D., Meynet, G. & Maeder, A. 1992, A&AS, 96, 269.

Schmidtke, P. 1985, in 1982-84 Eclipse of Epsilon Aurigæ, NASA Conf. Publ. 2384, ed. R. Stencel (NASA: Washington), 65.

Seaton, M.J. 1979, MNRAS, 187, 73.

Shu, F., Najita, J., Ostriker, E., Wilkin, F., Ruden, S. & Lizano, S. 1994, ApJ, 429, 781.

Simon, M., Ghez, A.M. & Leinert, C. 1993. ApJ, 408, L33.

Skumanich, A. 1972. ApJ, 171, 565.

Skrutskie, M.F., Dutkevitch, D., Strom, S.E., Edwards, S. Strom, K.M. & Shure, M.A. 1990, AJ, 99, 1187.

Soderblom D.R. 1996, in *Cool Stars, Stellar Systems and the Sun – the Ninth Cambridge Workshop* R. Pallavicini and A. Dupree eds. in press.

Soderblom, D.R. Stauffer, J.R., MacGregor, K.B. & Jones, B.F. 1993. ApJ, 409, 624.

Stahler, S.W. 1983, ApJ, 274, 822.

Stauffer, J.R., Liebert, J., Giampapa, M., Macintosh, B., Reid, N. & Hamilton, D. 1994, AJ, 108, 160.

Stauffer, J.R., 1996, private communication.

Stellingwerf, R.F., 1978, ApJ, 224, 953.

Sterzik, M.F., Neuhäeuser, R. & Röser, S. 1996, in *Cool Stars, Stellar Systems and the Sun – the Ninth Cambridge Workshop* R. Pallavicini and A. Dupree eds. in press.

Strassmeier, K.G., Welty, A.D. & Rice, J.B. 1994, A&A 285, 17.

Strom, S.E. 1994, in *Cool Stars, Stellar Systems and the Sun – the Eighth Cambridge Workshop*, J.P. Caillault ed. (San Francisco: ASP) 211.

Swenson, F.J. 1996, ApJ, in press.

Trumpler, J.E. 1983 Adv. Space Res. 2, 241.

Vandenberg, D.A. 1985, ApJS, 58, 711.

Van De Kamp, P. 1978, ApJ, 83, 975.

Vogel, S.N. & Kuhi L.V. 1981, ApJ, 245, 960.

Vrba, F.J., Herbst, W. & Booth, J.F. 1988, AJ, 96, 1032.

Walter, F.M. & Kuhi, L.V. 1981, ApJ, 250, 254.

Walter, F.M. & Kuhi, L.V. 1984, ApJ, 284, 194.

Walter, F.M. 1986, ApJ, 306, 573.

Walter, F.M. 1987, in *Cool Stars, Stellar Systems and the Sun – the Fifth Cambridge Workshop* J. Linsky and R Stencel eds. (New York: Springer–Verlag) 422.

Walter, F.M., Brown, A., Mathieu, R.D., Myers, P.C. & Vrba, F.J. 1988, AJ, 96, 297.

Walter, F.M. & Barry, D.C. 1991 in *The Sun in Time* C.P. Sonett, M.S. Giampapa, M.S. Matthews, eds. (Tucson: University of Arizona) 633.

Walter, F.M. 1992, *The ICUR Spectral Analysis Package.*

Walter, F.M. 1993, *RX, An IDL-Based ROSAT Data Analysis Package.*

Walter, F.M., Vrba, F.J., Mathieu, R.D., Brown, A. & Myers, P.C. 1994, AJ, 107, 692.

Warren, W.H. & Hesser, J.E. 1977, ApJS, 34, 115.

Warren, W.H. & Hesser, J.E. 1978, ApJS, 36, 497.

Weaver, W.M. 1987, ApJ, 319, L89.

Weidenschilling, S.J. & Cuzzi, J.N. 1993, in Protostars and Planets III, eds. E.H. Levy & J.I. Lunine (Univ. Arizona Press: Tucson), 1031.

Whittet, D.C.B. 1992, Dust in the Galactic Environment (I.O.P.: Bristol, U.K.).

Wilson, R.E. 1971, ApJ, 170, 529.

Wolk, S.J. & Walter, F.M. 1996, AJ, 111, 2066.

Wright, K.O. 1970, Vistas in Astronomy, 12, 147.